DOCTOR OF PHILOSOPHY

Multiscale Mathematical Modelling of Cancer Invasion

Peng, Lu

Award date:
2015

Multiscale Mathematical Modelling of Cancer Invasion

Lu Peng

June 2015

Contents

Acknowledgements

I would like to thank my supervisor Prof. Mark Chaplain, second supervisor Dr. Dumitru Trucu and all the friends in the department who made my PhD study successful and delightful.

A big thank you to my parents and beloved ones in China who love me too much to keep me by their side and give me the freedom to follow my heart. Also, thanks to my brothers and sisters in UK who bless me a lot through the love of Christ.

Thank Lord Jesus Christ for being with me through the whole journey and bringing these precious people into my life.

Declaration

I declare that the following thesis is my own composition and that it has not been submitted before in application for a higher degree.

Lu Peng

Certification

This is to certify that Lu Peng has complied with all the requirements for the submission of this Doctor of Philosophy thesis to the University of Dundee.

Prof. Mark A. J. Chaplain

Dr. Dumitru Trucu

Abstract

Invasion of the surrounding tissue is one of the hallmarks of cancer. Solid tumours have a reciprocal relationship with the surrounding microenvironment, a complex tissue composed of extracellular matrix and other multiple distinct cell types. Proteolytic degradation and remodelling of the extracellular matrix is essential for cancer cells to be able to invade. Important matrix degrading enzymes include the matrix metalloproteases (MMP) and the urokinase plasminogen activator (uPA).

This thesis has investigated the complex process of cancer growth and spread that occur across several different spatial scales, in order to gain a better understanding of the key processes involved during invasion. At first, we tested our modelling concept by applying a level-set method to a moving boundary problem. Later, a multi-scale mathematical model of cancer invasion was developed by coupling the urokinase plasminogen activation (uPA) system with a two-scale computational modelling technique. This approach allows us to investigate cancer invasion not only at the macroscopic tissue level, but also at the microscopic cellular level. Our computational simulation results demonstrate a range of heterogeneous dynamics which are qualitatively similar to the invasive growth patterns observed in a number of different types of cancer known as tumour infiltrative growth patterns (INF).

Chapter 1

Introduction

Cancer cells are defined by two heritable properties: (1) they break the rules of normal cell growth and division with uncontrolled reproduction; (2) invade and colonise territories in other tissues (Alberts et al., 2008). Invasion of the surrounding tissue transforms a localised solid tumour (benign) into a systemic, metastatic and fatal disease (malignant). Solid tumours have a reciprocal relationship with the surrounding microenvironment, a complex tissue composed of extracellular matrix and other multiple distinct cell types. The extracellular matrix especially not only plays the role of a scaffold for tissues and cells and a physical barrier during cell migration, but also involves in biological signalling pathways that create distinct cellular microenvironments. This microenvironment locally regulates cell migration, proliferation and differentiation. Thus, proteolytic degradation and remodelling of the extracellular matrix is essential for cancer cells to be able to invade. Important matrix degrading enzymes include the matrix metalloproteases (MMP) and the urokinase plasminogen activator (uPA).

This thesis seeks to investigate the complex process of cancer growth and spread that occur across several different spatial scales, in order to gain a better understand-

ing of the key processes involved during invasion. Chapter 2 provides brief biological background of cancer cell invasion and migration. Chapter 3 reviews some of the key mathematical models that contribute to the understanding of the processes of cancer growth and invasion, which also contribute to the development of modelling techniques.

Chapter 4 examines the modelling concept that PDE systems with heterogeneous solutions are used to describe the dynamics of the tumour cell community, and couple a level-set method (Macklin and Lowengrub, 2008) to calculate the position of the moving boundary of the tumour. In the previous models of tumour growth that involves level-set technique (Macklin and Lowengrub, 2005, 2006, 2007, 2008), linear and nonlinear quasi-steady reaction-diffusion equations with curvature-dependent boundary conditions were used to model the dynamics (e.g. nutrients transport, membrane pressure of the tumour boundary) in the tumour microenvironment. In order to extend and develop the previous models, we investigate PDE systems that model the interactions in and around the tumour region, in which we intend to approach the modelling of cancer invasion from different aspects, such as proteolytic activities, interactions between cancer cells and surrounding tissue. We first test our modelling concept without biological relevance by coupling a two-PDE equation system, i.e. Schnakenberg system, with level-set method. Then we used an enzymatic system, i.e. the urokinase plasminogen activation (uPA) system, to model the interactions between cancer cells, the extracellular matrix (ECM), the urokinase plasminogen activator (uPA), uPA inhibitors, and the ECM degrading enzyme plasmin. In this model, we introduced more details of the dynamics in the tumour microenvironment than the previous models. Also, the movement of the tumour boundary depend only on the dynamics of the distribution of plasmin (the ECM degrading enzyme), not the curvature of the boundary. In this way, our model focus

more on the mutual effects between cancer cells and ECM, biological signalling, and proteolytic activities. Since we are modelling a collective mode of cancer cells, unlike single cell mode in which there is a well-defined and continuous cell membrane, we believe it is more biologically relevant to consider all those cellular and molecular interactions mentioned above than the modelling methods in which the deformations of tumour boundary is curvature-driven.

Chapter 5 and 6 extend a two-scale model of cancer invasion by coupling the urokinase plasminogen activation (uPA) system (Chaplain and Lolas, 2005; Andasari et al., 2011) with a computational modelling technique introduced in Trucu et al. (2013). The modelling technique allows us to investigate the protease-dependent cancer invasion on the macroscopic (tissue) level and on the microscopic (cellular) level. In this model, we not only include more details of the dynamics at the tissue level in the tumour microenvironment by applying the uPA system mentioned in Chapter 4, but also more details are provided at the cellular level around the tumour boundary by using the two-scale modelling technique, in which proper amount of microdomains around the tumour boundary are formed to obtain more information of the molecular interactions in uPA system and the determinants of movements of cells on the moving boundary. Our computational simulation results demonstrate a range of heterogeneous dynamics which are qualitatively similar to the invasive growth patterns observed in a number of different types of cancer known as tumour infiltrative growth patterns (INF).

Finally, chapter 7 discusses the findings and conclusions of the thesis. A few directions of future work are also included in the chapter.

Chapter 2

Cancer cell invasion and migration

2.1 Introduction

Cancer is a generic term used to describe a group of diseases sharing common cellular hallmarks, such as sustaining proliferative signalling, evading growth suppressors, activating invasion and metastasis, enabling replicative immortality, inducing angiogenesis and resisting cell death (Hanahan and Weinberg, 2000). Due to the growing knowledge of the disease in last decade, more revelations have been added to this picture, i.e., avoiding destruction by the immune system, tumour-promoting inflammation, genome instability and mutation and deregulating cellular energetics (Hanahan and Weinberg, 2011). As one of the hallmarks of cancer, cancer invasion and metastasis are landmark events that transform a locally growing tumour into a systemic, metastatic and fatal disease. Therefore, a lot of effort has been made by researchers to get a better understanding of the processes during cancer invasion in order to obtain effective therapies.

There is more and more evidence supporting the observation that a malignant tumour is not just a collection of relatively homogeneous cancer cells but a complex

tissue composed of extracellular matrix and multiple distinct cell types, e.g. fibroblasts, endothelial cells and macrophages. The recruited normal cells are not "innocent bystanders", they actively participate in carcinogenesis by forming tumour-associated stroma. Furthermore, it is increasingly apparent that crosstalk between cancer cells and cells in the peritumoural stroma is involved during cancer invasion (Hanahan and Weinberg, 2011; Mikala et al., 2010; Qian and Pollard, 2010; Joyce and Pollard, 2009; Kalluri and Zeisberg, 2006) (Figure 2.1).

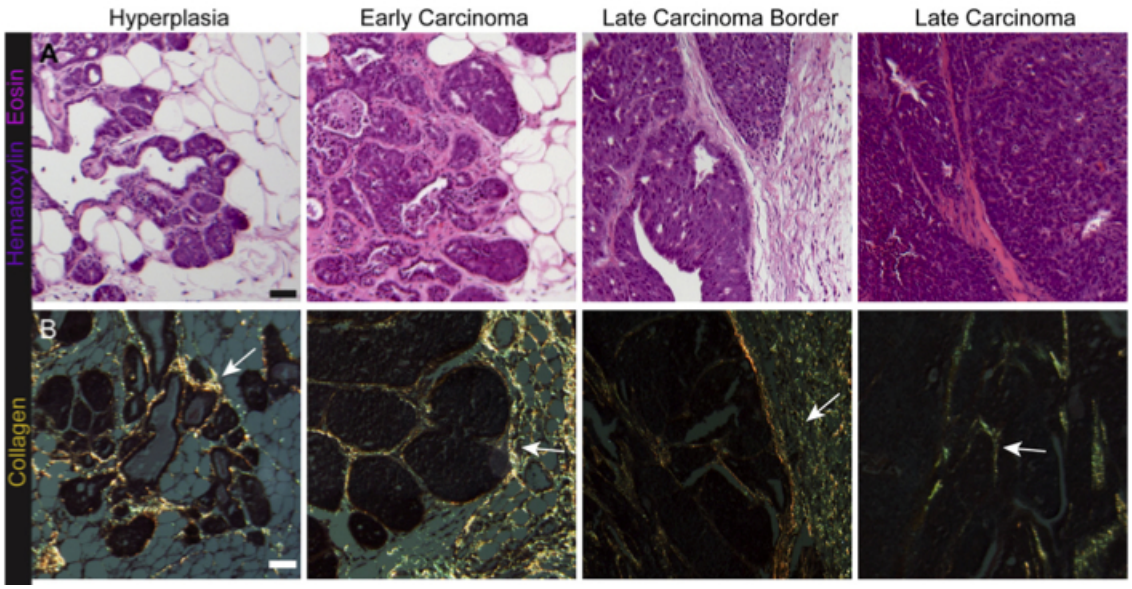

Figure 2.1: *Evolutions of cancer cells and its microenvironment during tumour progression: (A) evolutions in overall tissue composition in different progression stages. (B) evolutions in extracellular matrix in different progression stages. Copyright permission requested. Mikala et al. (2010)*

From image (A) in Figure 2.1 we can see that with tumour progression, the architecture of carcinoma cells bears less and less resemblance to the architecture of the tissue from which it was derived. The stromal tissue also changes. For example, the stromal tissue used to be dominated by fatty cells, however, as the tumour progression proceeds, it becomes more and more dominated by extracellular matrix,

fibroblasts, and immune cells. Image (B) shows that fibrillar collagen accumulates at the invasive edge of the tumour and surrounding nests of cancer cells, and it also indicates that the collagen fibres must be degraded to allow the tumour to occupy more space inside the tissue.

Thus, knowledge of how the reactive tumour microenvironment influences cancer invasion is indispensable. When developing mathematical models of cancer invasion, we must take into consideration the determinants that stem from the peritumoural extracellular matrix composition and structure, protease activities, cell-cell and cell-matrix adhesion and so on.

2.2 The Extracellular Matrix (ECM)

The extracellular space between cells inside tissues is occupied by extracellular matrix and it has been recognised that there is a reciprocal relationship between cells and the extracellular matrix: cells make extracellular matrix, organise it and degrade it and the matrix in turn exerts powerful influences on the cells, no matter if the cells are normal or neoplastic (Wolf et al., 2013; Wolf and Friedl, 2011; Papini et al., 2007). Therefore, ECM not only plays the role as a scaffold for the tissues and physical barriers during cell migration but also provides signals that, together with soluble factors, may create distinct cellular microenvironments that locally regulate cell migration, proliferation and differentiation.

The ECM renders an amazing diversity of materials in different tissues. The variations do not come from the classes of macromolecules constituting the ECM but from the relative amounts of these molecules and the ways in which they are organised. These various components of ECM play different roles to meet the requirement of a particular tissue, and we can classify them into two main categories: (1) glycosaminoglycan polysaccharide chains; (2) and fibrous proteins (Alberts et al.,

2008).

Glycosaminoglycans (GAGs) Glycosaminoglycans (GAG) polysaccharide chains are unbranched polysaccharide chains which are too stiff to fold up and also strongly hydrophilic. Thus, GAGs are usually large relative to their mass as they tend to adopt highly extended conformations, and they can form gel even at very low concentrations. The porous hydrated gels they form is negatively charged. Therefore, GAGs not only fill most of the extracellular space but also help to attract cations, especially sodium (Na^+), leading to water moving into the matrix. The swelling pressure created by this process enables the matrix to withstand compressive forces. On the other hand, these gels can change pore size and charge density, so GAGs are very likely to regulate the traffic of molecules and cells according to their size and charge.

Most GAGs are covalently attached to proteins as proteoglycans, and they can regulate the activities of secreted proteins so that they play an important part in chemical signalling between cells. For example, proteoglycans can bind to fibroblast growth factors (FGFs) that stimulate many kinds of cell types to proliferate. They also bind and regulate the activities of proteolytic enzymes and protease inhibitors, which are essential components controlling both the assembly and the degradation of the ECM (Alberts et al., 2008).

Fibrous proteins Fibrous proteins are also very important since they give the matrix strength and resilience, and also form structures that cells can be anchored to.

Collagen The collagen family contains the major proteins of the ECM and it includes many types of collagens. For instance, fibrillar collagens type I, II,III,V and

XI are rope-like, triple-stranded helical molecules that aggregate into long fibrils which provide tensile strength and act as barriers to cell migrations and cancer invasion; collagen type IX and XII are fibril-associated collagens, since they link fibrils to one another and to other components of ECM, and these fibrils decorate the surface of the fibril-associated collagens (Alberts et al., 2008).

Elastin Elastin is the main component of elastic fibres that gives tissues their elasticity, such as skin, blood vessels, and lungs. It is the dominant protein in arteries (Alberts et al., 2008).

Fibronectin Fibronectin is an extracellular protein that helps cells attach to the matrix through their multiple binding sites for integrins on the cell surface (Alberts et al., 2008).

Laminin Laminin is another extracellular protein that has similar functions to fibronectin and it is mainly found in basal lamina (Alberts et al., 2008).

The ECM renders different morphologies in different tissues. For example, there are tight calcified collagens in bones and teeth, and in perimuscular stroma there are wide gaps and trails with parallel interfaces, and so on. In the following subsections we introduce two main types of ECM: basal lamina (2D) and the ECM of animal connective tissues (3D).

2.2.1 The basal lamina

The basal lamina, also called basement membrane, is a thin tough sheet of extracellular matrix that closely underlies epithelia in all multicellular animals and its key components are laminin, type IV collagen, nidogen and the proteoglycan perlecan (Alberts et al., 2008). Besides these components, fibronectin and other collagens,

e.g. collagen XVIII, can be found in the basal lamina as well. Schematic and experimental pictures can be found in Figure 2.2 showing the structure of the basal lamina and its main components.

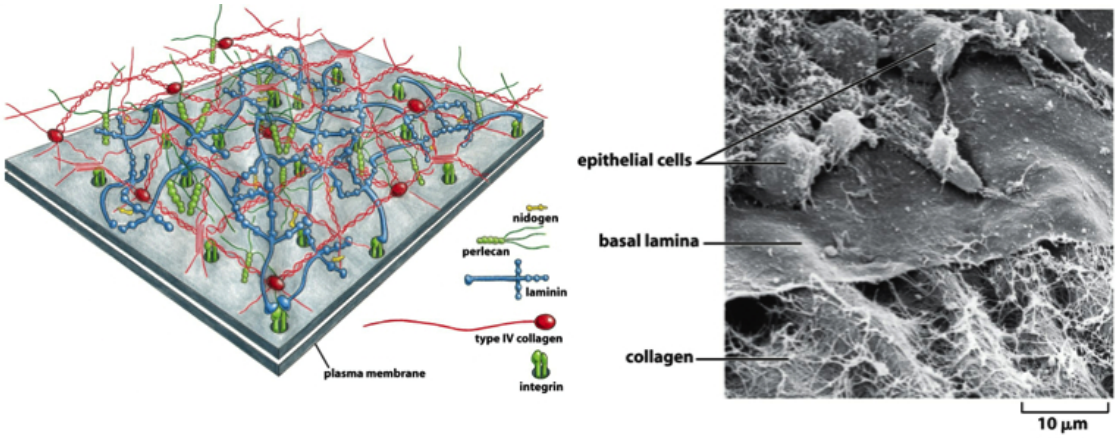

Figure 2.2: *The basal lamina: (1) on the left is a model of the molecular structure of a basal lamina; (2) on the right shows the basal lamina in the cornea of a chick embryo. Copyright permission requested Alberts et al. (2008).*

The basal lamina provides mechanical support for epithelia and forms the interface and the attachment between epithelia and connective tissue. It also has the functions of the other types of ECM in general that are mentioned above.

2.2.2 The ECM of animal connective tissue

Unlike the basal lamina, which is a sheet-like mesh formed by fibril proteins and proteoglycan, i.e., a two-dimensional structure, the ECM in connective tissue is a three-dimensional structure. It contains various protein fibres (e.g. collagen fibres and elastic fibres), interwoven in a hydrated gel composed of a network of glycosaminoglycan (GAG) chains. Figure 2.3 shows schematically the components of the matrix in connective tissue and also an experimental image is presented giving us a better idea as to what the matrix looks like *in vivo*. The most abundant and

important component of the matrix in connective tissue is collagen type I, which is the principal collagen of skin and bone. Collagen type I molecules secreted into the extracellular space usually assemble into higher-order polymers called collagen fibrils. Moreover, these collagen fibrils often aggregate into larger cable-like bundles that can be easily observed with a light microscope (Figure 2.3) (Alberts et al., 2008).

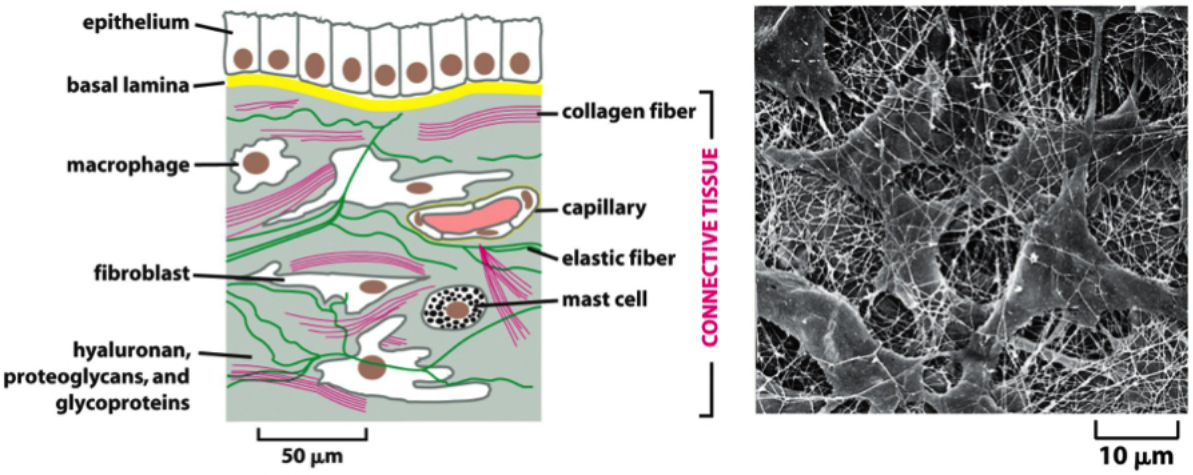

Figure 2.3: *On the left: a schematic picture of the connective tissue underlying the epithelium, which contains a variety of cells and extracellular matrix components. The predominant cell type that secretes abundant extracellular matrix is fibroblast. On the right: a scanning electron micrograph shows tissue from the cornea of a rat. The cells in the graph are fibroblasts and the surrounding extracellular matrix is composed largely of collagen fibrils. Copyright permission requested Alberts et al. (2008).*

2.3 Modes of cell migration

Cell migration, a multi-step process that requires the integration of complex biochemical and biophysical cell functions, is fundamental to cell and tissue dynamics in morphogenesis, the immune defence, wound healing as well as cancer invasion

and metastasis. There are two major ways for normal or neoplastic cells to migrate – individually or collectively – according to the cell type and tissue environment, e.g. whether cell-cell adhesion is strong enough or not.(Friedl and Alexander, 2011; Friedl and Wolf, 2009, 2008) (Figure 2.4). On the other hand, if we consider the pericellular proteolytic activities, we can classify cell migration into another two modes: proteolytic or non-proteolytic cell migration. However, migration of cells does not always use one mode. For example, if the cell-cell adhesion, or traction force generated via integrins and the cytoskeleton, is modified by changing ECM composition and density, cells can shift from highly adhesive to low adhesive migration (e.g. epithelia-mesenchymal transition), or from proteolytic to non-proteolytic migration (e.g. mesenchymal-amoeboid transition) and so on. Such adaptation responses is known as the plasticity of cell migration (Friedl and Alexander, 2011; Friedl and Wolf, 2010; Friedl and Gilmour, 2009; Friedl and Wolf, 2003).

Single-cell migration The cyclic process of single-cell migration mainly involves five steps that change the cell shape, its position and the surrounding tissue structure (Friedl and Alexander, 2011; Sheetz et al., 1999; Lauffenburger and Horwitz, 1996) (Figure 2.4A). They are: (1) actin polymerisation-dependent pseudopod protrusion at the leading edge (Ridley et al., 2003); (2) integrin-mediated adhesion to ECM; (3) pericellular proteolytic ECM cleavage and remodelling; (4) small GTPase Rho activation of myosin II, and contraction mediated by actomyosin, which generates tension inside the cell; (5) contraction and translocation of the cell body (Wolf et al., 2013; Friedl and Alexander, 2011; Poincloux et al., 2011; Estecha et al., 2009; Friedl and Wolf, 2009; Ridley et al., 2003; Friedl et al., 1997).

Amoeboid migration Amoeboid migration usually refers to the the movement of rounded or ellipsoid cells with low adhesion force or high actomyosin-

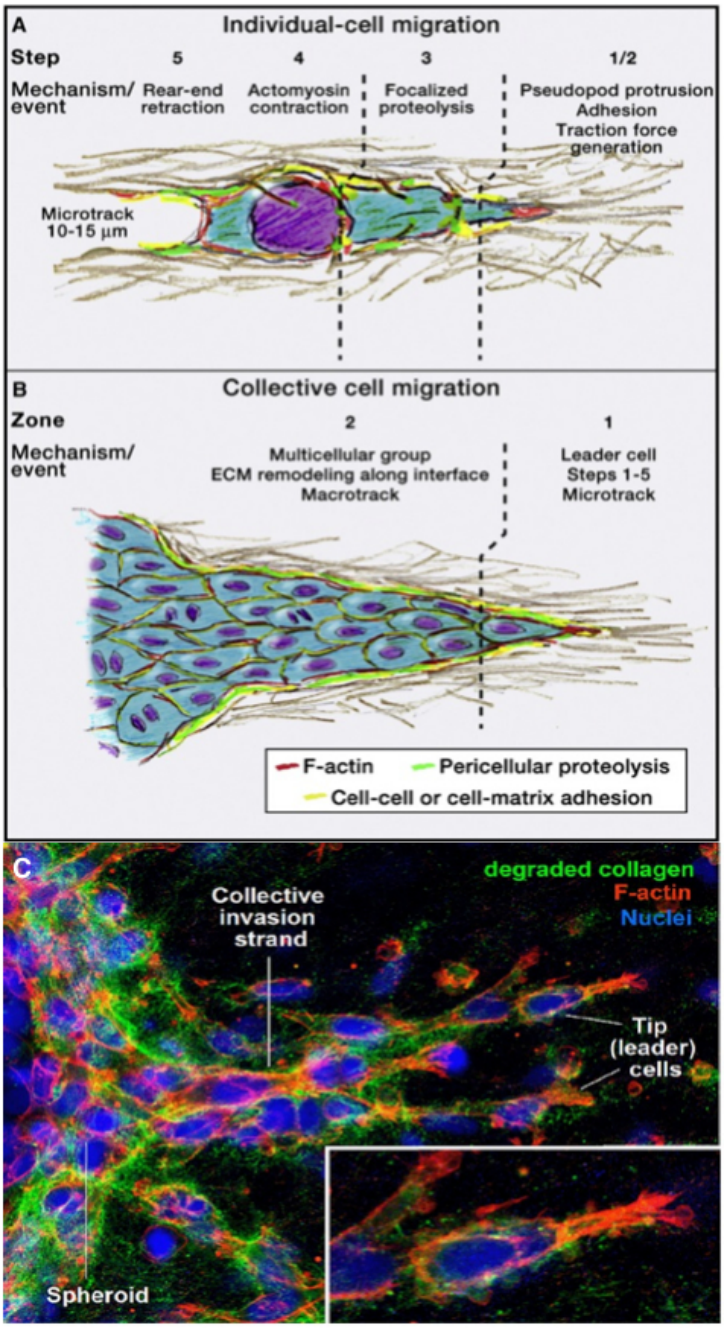

Figure 2.4: *Schematic illustration showing the cell migration processes: (A) five steps of single-cell migration that change the cell shape, its position, and the tissue structure; (B) there are two major zones in the process of collective cell migration: in zone 1, a "leader cell" generates a proteolytic micro-track at the front of the migrating group, and in zone 2 the subsequent cells then widen this micro-track to form a larger macro-track. Copyright permission requested (Friedl and Alexander, 2011). (C)an experimental image showing individual and collective invasion from three-dimensional spheroid cultured within a three-dimensional collagen lattice. Copyright permission requested (Friedl and Wolf, 2008).*

mediated contractility. The characteristics of amoeboid migration are well established through studies of the single-cell amoeba, *Dictyostelium discoideum* (Friedl et al., 2001; Firtel and Meili, 2000; Devreotes and Zigmond, 1988), including rounded morphology with membrane blebbing, proteolysis-independent or low matrix metalloproteinases (MMPs) activity, high Rho-Rock activity, high cellular contractility and cortical tension, weak attachment to ECM.

Mesenchymal migration Mesenchymal cells move via the five-step migration cycle mentioned earlier, and is predominantly found in cells from connective tissues. Its characteristics are quite different from those of amoeboid migration, i.e., proteolysis-dependent or high MMPs activity, low Rho-Rock activity, elongated morphology with lamellipodial protrusions and strong attachment to ECM via focal adhesions.

Collective migration Collective migration is essential in building, shaping and remodelling complex tissues and tissue compartments, such as epithelia, ducts, glands, and vessels, but also contributes to cancer progression by local invasion (Friedl and Wolf, 2010). During collective migration, cell-cell adhesion and multicellular coordination are required and cells move as sheets, strands, clusters or ducts rather than individually (Friedl and Gilmour, 2009) (Figure 2.4B). There are mainly two types of collective migration: (1) one or several leader cells with mesenchymal characteristics form the tip of multicellular strands and generate forward traction and pericellular proteolysis toward the tissue structure (Figure 2.4c); (2) a blunt bud-like tip protrudes along the tissue space consisting of multiple cells that variably change position, lacking defined leader cells (Figure 2.5).

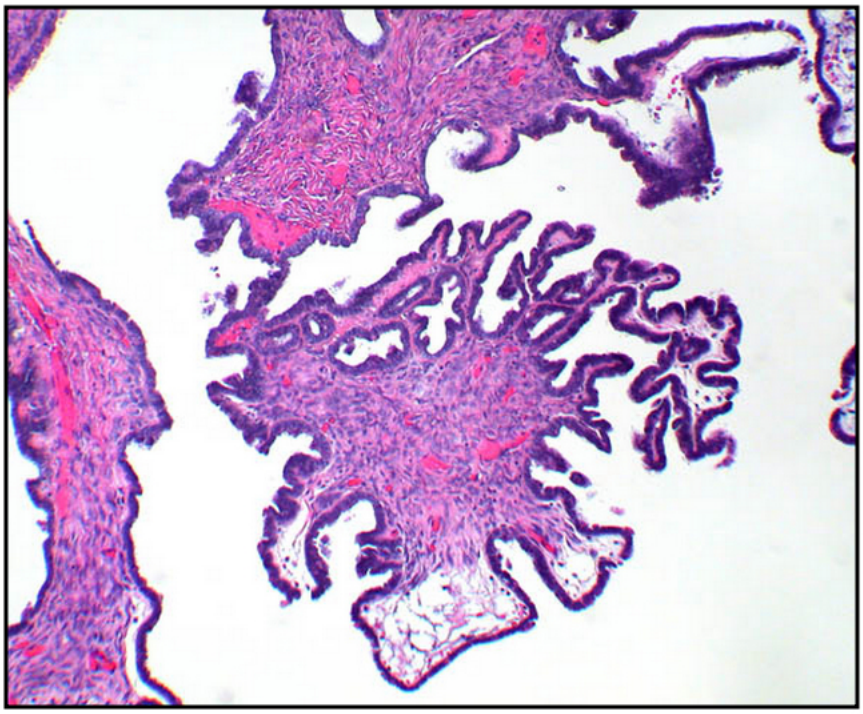

Figure 2.5: *An experimental image of borderline cystadenofibroma showing infiltrative growth patterns (INF). Copyright permission requested (The digital atlas of gynecologic pathology by Meenakshi Singh, MD on the internet).*

2.4 Determinants of cancer cell invasion and migration

Cancer cell invasion is now regarded as a heterogeneous and adaptive process, and physical, cellular, and molecular determinants adapt and react altogether for this process throughout the progression of the disease. The plasticity in cell adhesion, cytoskeletal dynamics and mechanotransduction tunes and perpetuates migration under diverse structural, molecular and even adverse microenvironmental conditions (Friedl and Alexander, 2011; Sanz-Moreno and Marshall, 2010; Friedl and Wolf, 2010; Sahai, 2007).

2.4.1 ECM determinants of cell migration

The extracellular matrix has a big influence on cell migration modes by its diverse macromolecular and structural organisation, such as dimension, density, stiffness and orientation.

Dimension Extracellular tissue structures encountered by moving cells are either flat 2D sheets (e.g., the basal lamina in Figure 2.2) or 3D tissue networks (e.g., the matrix in connective tissue in Figure 2.3). 2D surfaces almost allow cells a barrier-free migration as long as they have stable-enough but transient attachment to the substrate, and the cells usually adopt a flattened, spread-out morphology guided by a leading lamellipodia. However, in 3D structures, cells have a spindle-like shape when travelling through the network of interwoven collagen fibres. Also, instead of lamellipodia formation as in 2D, cells form thin tip-like cylindrical pseudopodia at the leading edges that orient in three dimensions. Moreover, the cell either deforms its shape to accommodate small tissue gaps or remodels the ECM structure by pericellular proteolysis (Friedl and Alexander, 2011; Wolf and Friedl, 2011; Friedl and Wolf, 2010). *In vivo*, most 2D surfaces are encountered in a 3D scaffold.

Density and gap size In 3D matrix structures, the density and gap size determine whether there is enough spaces between ECM fibres or within the filter pore that can accommodate the migrating cell body. Large pore sizes favour cell rounding, allowing non-proteolytic amoeboid migration, whereas the confinement of the ECM makes moving cells stretch into a spindle-like shape to reduce their cell diameter, and most of the time, pericellular proteolysis is required to create more space. Here, we might also need to consider the deformability of nucleus of the moving cells in response to space constraints (Wolf et al., 2013).

Stiffness ECM stiffness depends on molecular properties of the tissue and cells detect matrix rigidity via integrin-mediated adhesions and downstream protein signalling. Similar to chemotaxis, cells tend to migrate toward substrate of greater stiffness, a process called durotaxis (Friedl and Wolf, 2010).

Orientation Connective tissues could have loose and random structures and also highly aligned ones, and cells tend to align in parallel along oriented structural discontinuities. The aligned fibre orientation in collagen-rich ECM might not influence cell shape, but it helps multicellular streaming in chainlike patterns in 3D tissue and migration of 2D cell sheets along tissue clefts (Friedl and Wolf, 2010).

Thus, the extracellular matrix provides different conditions that modulate cell adhesion and cytoskeletal organisation, which in turn impacts cell shape and modes of migration. However, the matrix does not complete the modulation process alone. There are other physical and molecular determinants that cooperate with it, which will be introduced in the next subsection.

2.4.2 Physical and molecular determinants of cell migration

Integrins (cell-matrix adhesion) Cell-matrix adhesion is one of the important factors that determine which cell shapes and forces are generated during migration. This is predominantly generated by integrins, which function as transmembrane linkers between the extracellular matrix and the cytoskeletal proteins inside the cell (Friedl and Wolf, 2010; Weaver, 2006; Alberts et al., 2008; Ridley et al., 2003).

High integrin expression levels tend to result in slow and mesenchymal-type cell migration because of the high attachment forces and slow turnover of the adhesion sites, which promote cell contractility and formation of elongated or spindle-shaped

morphologies in various cell types, such as fibroblasts, smooth muscle cells and neoplastic cells. Whereas, if the integrin-talin axis, focal adhesions and stress fibres do not form or do not reach full maturation, cell adhesion strength is moderate or low. The cells then generate relatively smaller lamellipodia and pseudopodia compared with the large deformations observed while the attachment force is strong (such as lymphocytes and neutrophils whose adhesion to the ECM exists but no focal adhesions or stress fibres are formed). Furthermore, if cell adhesion strength is very low, cells cannot form unilateral attachments to two-dimensional ECM so that no lamellipodia will be formed and the cells will not move. However, in 3D, cells can move using the amoeboid blebbing mode of migration.

Cadherins (cell-cell adhesion) Cadherins are the main mediators for cell-cell adhesion (a key determinant of whether cells move either individually or collectively), including E-cadherin in epithelial cells, VE-cadherin in endothelial cells and N-cadherin in stromal cells (Friedl and Wolf, 2010; Friedl and Gilmour, 2009; Vitorino and Meyer, 2008; Ewald et al., 2008). Collective migration requires the presence of cell-cell junctions and coordinated cycles of protrusion and rear retraction of the leading cells as well as of cells inside the group, and the absence of cell-cell adhesion causes cells to move independently. Thus, whether or not the cell-cell adhesion exists and how stable are the cell-cell junctions determines whether collective translocation, cell streaming or single-cell migration will be generated.

Rac activity and Rho/ROCK signalling (cell protrusion and rounding) The Rho family of small GTPases are key regulators of both cell adhesion and the cytoskeleton. The best studied members of the Rho GTPases family are Cdc42, Rac1 and RhoA. Rac1 can promote the formation of large membrane protrusions (lamellipodia) so that Rac activity also plays an important role in the morphologies

of migrating cells and the migration mode. High Rac activity leads to leading edge extension, elongated morphology and focal integrin engagement. Whereas active RhoA and RhoC can recruit the ROCK (or Rho kinase) family that phosphorylate cytoskeletal proteins, which promotes the formation of actin stress fibres and the generation of contractile force. Active Rho/ROCK signalling in the presence of little or no RAC activity promotes rounded cell shapes and amoeboid migration. Moreover, Rac activity and Rho/ROCK signalling forms a negative feedback loop, counterbalancing each other (Friedl and Wolf, 2010; Sanz-Moreno et al., 2008; Sahai and Marshall, 2003).

Actin polymerisation-driven propulsion and actomyosin-based contractility (force generation) The forces for cells to move are mainly generated by two physical mechanisms: actin polymerisation-driven propulsion that push the cell body forward and the pulling force exerted on ECM substrate generated by actomyosin-based contractility at the rear of the cell. Almost all types of cell migration will involve actin polymerisation-driven propulsion at the leading edges. However, the pulling force is dependent on the cell-matrix adhesion strength, meaning that in some migration modes, for instance, amoeboid migration, we might expect little or no actomyosin-based contractility and adhesive pulling of the ECM.

Proteases (proteolysis and extracellular matrix degradation) Another molecular determinant of cell migration is pericellular proteolysis activity executed by protease systems, which include MMPs (matrix metalloproteases), ADAMs (a disintegrin and metalloproteases), cathepsins, uPA (urokinase plasminogen activator) and its receptor uPAR (urokinase plasminogen activator receptor), etc. These proteases are usually produced by cancer cells and cells in the tumour microenvironment, such as fibroblasts, lymphocytes, macrophages, pericytes and neutrophils (Mason

and Joyce, 2011) (Figure 2.6).

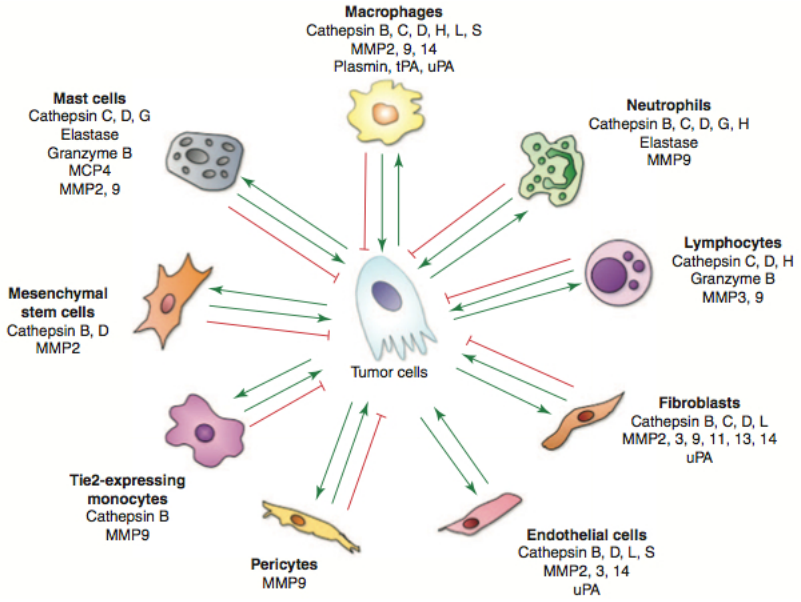

Figure 2.6: *Proteolytic contributions from different stromal cells in the tumour microenvironment. Copyright permission requested Mason and Joyce (2011).*

uPA (urokinase plasminogen activator) system The urokinase plasminogen activator occupies a prominent location in the proteolytic network with its ability to convert plasminogen into plasmin. After the binding of uPA or pro-uPA to their receptor uPAR, there is a positive feedback loop between uPA and plasmin. Although it is believed that, during cell trafficking, plasmin might not directly degrade the fibrous proteins in the ECM which acts as physical barriers to cells' movement (Rowe and Weiss, 2009), plasmin still plays an important role in the degradation of other proteins in the matrix, such as fibronectin, laminin, vitronectin and thrombospondin. In addition, the uPA system is involved in the activation of MMP2 via a mechanism dependent on contributions from stromal fibroblasts and also overexpression of uPA and uPAR in the basal epidermis and hair follicles. This leads to increased activation of MMP2 and MMP9 (Mason and Joyce, 2011), and thus

the uPA system indirectly promotes the pericellular proteolysis and degradation of ECM.

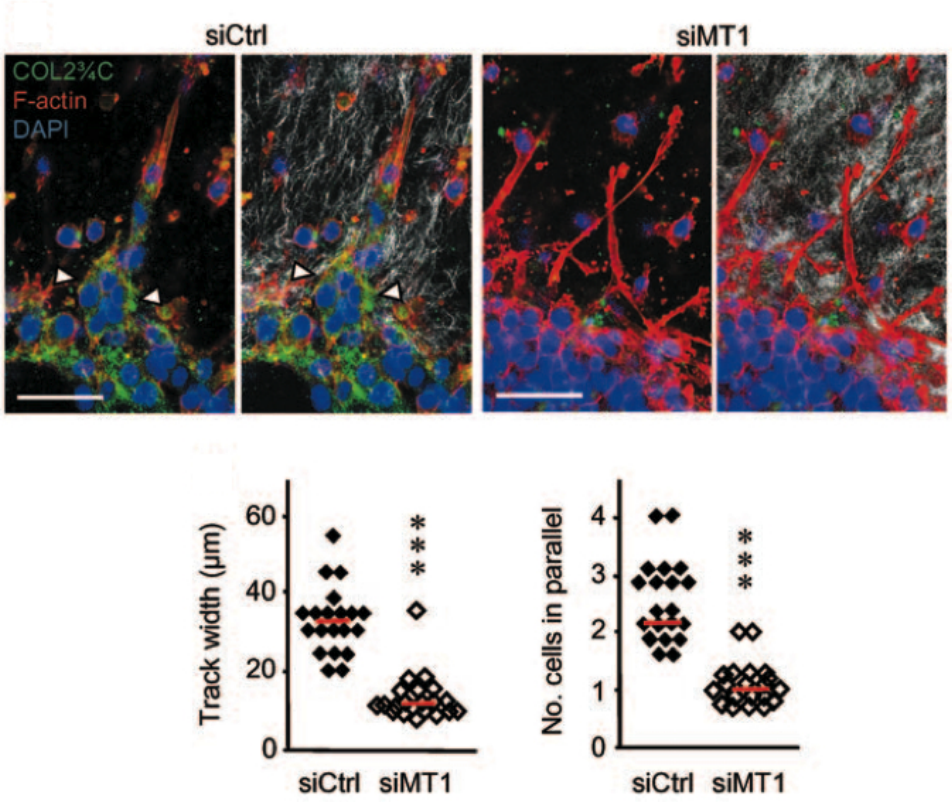

Figure 2.7: *Experimental images showing that the formation of collagenolytic track stops if the inhibitor of MT1-MMP is present. Then the cells change the modes of migration from collective invasion (the first image) to individual invasion (the second image). The third and fourth images show that track width and the number of cells will reduce after knockdown of MT1-MMP. Copyright permission requested (Wolf et al., 2007).*

MMPs (matrix metalloproteases) The over-expression of MMPs is frequently observed in many types of cancers due to their ability to degrade various components of ECM, which makes them the most extensively studied proteases in cancer biology. As a large family of proteases, multiple and distinct mechanisms exist for the activation of different MMPs (Mason and Joyce, 2011), even single one

MMP might have more than one pathway for its activation. During cancer cell invasion and migration, several MMPs are involved in proteolysis activity and degrade ECM components, such as MMP1, 2, 8, 9 (Inaba et al., 2014; Ordoñez et al., 2014; Akgu et al., 2005), MT1-MMP/MMP14 and so on.

In particular, MT1-MMP, a membrane-anchored metalloproteases, is thought to be an absolute requirement for cancer invasion in 3D (Sabeh et al., 2009) and more and more evidence demonstrate that the inhibition of MT1-MMP almost completely prevent collagen type I (the main fibrous protein of the matrix in 3D) degradation (Wolf et al., 2013; Rowe and Weiss, 2009; Sabeh et al., 2009; Wolf et al., 2007). Moreover, it is believed to be further involved in the remodelling of already existing trails to even larger "macro-tracks" in collagen-rich interstitial tissue, which then accommodate the collective invasion of multicellular strands. Blocking fibre cleavage by protease inhibitors causes cell squeezing (Wolf et al., 2007). Therefore, inhibition of MT1-MMP will force the cells to stop the collective migration and they then might adopt the non-proteolytic individual migration mode (Figure 2.7).

2.5 Plasticity of cancer cell invasion and migration

As described above, cancer cell invasion is a plastic and adaptive process. The divergent degree of ECM remodelling capability, molecular receptors and cytoskeletal regulators for cell-cell and cell-matrix adhesion, various protease systems, together form an "orchestra" that plays the "symphony" of cancer cell invasion and migration. Moreover, these processes control the cell migration mode and efficiency not in a discrete "on" and "off" manner but a continuous one. Thus, they "tune" cell behaviours during migration by increasing or decreasing their input (Friedl and Alexander, 2011;

Friedl and Wolf, 2010, 2003) (Figure 2.8). Therefore, some modes of cell migration have known as transition modes, such as the epithelial-to-mesenchymal transition, the collective-to-individual cell transition and the mesenchymal-to-amoeboid transition.

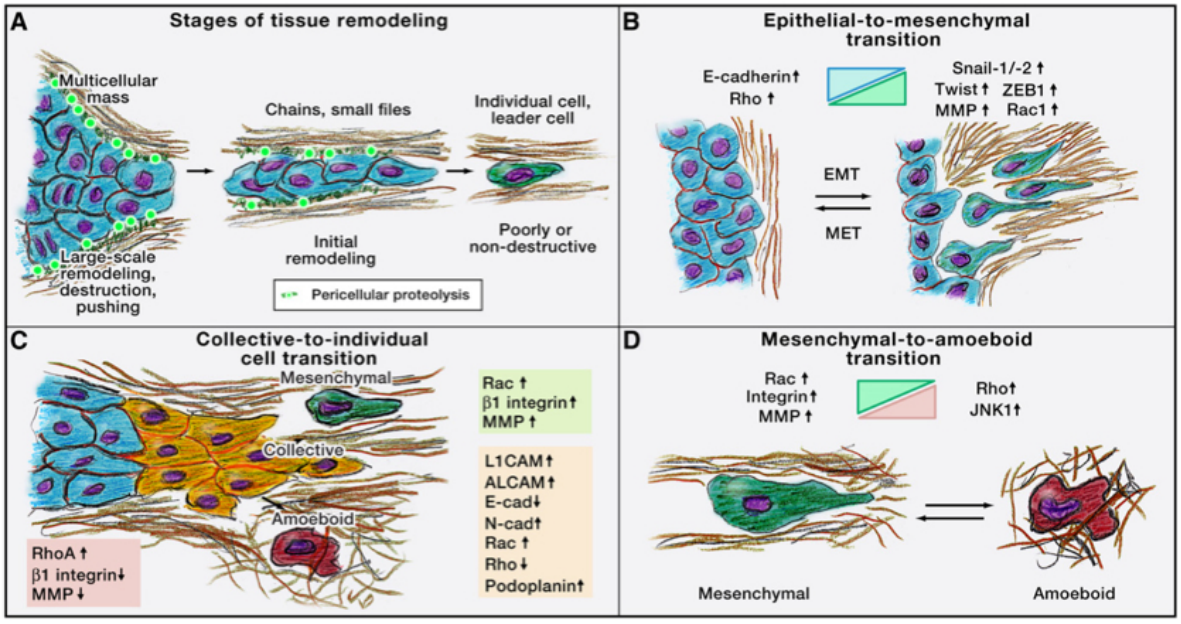

Figure 2.8: *Schematic illustration of plasticity of cell-matrix Interaction, invasion, and tissue remodelling. Copyright permission requested (Friedl and Alexander, 2011).*

Epithelial-to-mesenchymal transition (EMT) The EMT is a central programme enhancing tumour invasion in response to the changes of the peritumoural environment, and it can arise in the epithelial cancers of breast, colon, lung and prostate tissue. The transition occurs when cells start losing their cell-cell junctions (E-cadherin expression is diminished) via some mechanisms triggered by local Rac1 engagement. Cells then will be allowed to detach from the epithelium and acquire a mobile mesenchymal phenotype. However, cells also undergo the reverse mesenchymal-to-epithelial transition when they lose the local upstream signalling

after metastatic seeding in a secondary organ (Figure 2.8B).

Collective-to-individual cell transition The process of collective-to-individual cell transition is similar to that of EMT, i.e. collective migrating cells gain the ability of detachment by losing cell-cell adhesion triggered by Rac activity. A difference between the two is not only that the mesenchymal migration of single cells can happen, but also β1-integrin-independent amoeboid migration can occur after the disruption of cell-cell links, the mode of low integrin-mediated (cell and matrix) adhesion and high Rho-mediated cortical actomyosin contractility (Figure 2.8C).

Mesenchymal-to-amoeboid transition Under certain circumstances, cancer cells can undergo conversion from mesenchymal migration to amoeboid migration, via a decrease in Rac activity and activation of Rho-mediated actomyosin contractility. Also, the inhibition of MMPs can promote amoeboid migration as it can prompt the cells to change to a non-proteolytic mode to bypass narrow ECM barriers without the pericellular activities executed by MMPs. Likewise, amoeboid migration can convert back to mesenchymal migration when the environment provides high Rac activity, increasing cell-matrix adhesion and in the presence of proteolytic activities (Figure 2.8D).

Chapter 3

Mathematical modelling of tumour growth and invasion

3.1 Overview

Cancer is a complex disease that involves genetic mutations, dynamical interactions among the cancer cells, and also, between the cells and the microenvironment in the vicinity of the tumour. Its initiation and development mainly includes avascular growth, tumour-induced angiogenesis, and invasive growth and metastasis. Although experimental and clinical observations have been the main methods used to study the disease, mathematical modelling at multiple temporal and spatial scales can also contribute to a greater understanding of the prevention, diagnosis and treatment of cancer.

The first attempts of using mathematical models to help cancer research can be dated back as early as the 1950s, when informative descriptions of *in vitro* avascular growth of a human lung cancer were provided by a mathematical model proposed by Thomlinson and Gray (1955). In this earliest stage, tumour growth is considered

to be regulated by direct diffusion of nutrients (e.g. oxygen) from the surrounding tissue and limited by the finite nutrient supply. Two decades later, inspired by the work of Thomlinson and Gray (1955) and Burton (1966), Greenspan (1976) proposed a continuum model on the growth and stability of cell cultures and solid tumour in which the tumour was treated as an incompressible fluid. Not only cell death and birth and nutrient supply were taken into consideration, but also conditions were established in the model for the unstable development of a colony when internal pressure overcomes surface tension and adhesion. Since then, an increasing number of mathematical models describing solid tumour growth have appeared (Adam, 1986, 1987a,b; Chaplain et al., 1994; Byrne and Chaplain, 1995a, 1997, 1998; Chaplain et al., 2001, 2006a), each starting from a different aspect of tumour growth and examining various biomechanical and chemical factors (e.g. cell movement through diffusion, convection, chemotaxis and haptotaxis; cell proliferation and apoptosis; cell-cell adhesion; growth factors and inhibitors, etc.), resulting in a more comprehensive understanding of the subject.

Due to the limitations of experimental and numerical techniques, the majority of early mathematical models focus on the early stage growth of an avascular tumour or multicellular spheroid. However, as knowledge of both cancer biology and computational techniques has increased rapidly in last two decades, mathematical models that described angiogenesis and vascular tumour growth have also been developed(Chaplain and Stuart, 1993; Byrne and Chaplain, 1995b; Orme and Chaplain, 1996; Chaplain and Anderson, 1996; Anderson et al., 2000; Chaplain et al., 2006c). In the paper by Chaplain (1996), mathematical models of spherical tumour growth through the stages of avascular growth, angiogenesis, and vascularisation were presented. In the early 2000s, based on classic tumour models, Cristini et al. (2003) broke through the limitation of mathematical linear analyses and spherical

geometries, which not only enabled the nonlinear modelling of complex tumour morphologies but also predicted the conditions that separate noninvasive growth from invasive progression. Therefore, it was suggested that the morphology of a tumour plays an important role in cancer invasion.

As one of the hallmarks of cancer, invasion of the surrounding tissue is a landmark event that transforms a localised solid tumour into a systemic, metastatic and fatal disease. Therefore, investigation of cancer invasion is very meaningful and necessary, and as a useful tool, mathematical modelling also contributes to the understanding of the process. In the following sections, we will introduce and discuss mathematical models of cancer invasion that use different modelling techniques: continuum models, discrete models and hybrid (discrete-continuum or continuum-discrete) models, all of which describe the invasion process on different spatial and temporal scales.

3.2 Models of cancer invasion

One of the first attempts to describe cancer invasion was the model proposed by Gatenby and Gawlinski (1996). This model uses a reaction-diffusion system to model the interaction between malignant and normal cells, and excess H^+ ion concentration, based on the hypothesis that tumour-induced alteration of microenvironmental pH may provide a mechanism for cancer invasion. The model consists of three coupled reaction-diffusion equations describing the spatial distribution in spatial domain W and temporal evolution $t \in [0, T]$ of three variables, the dimensionless form of which were written as,

$$\frac{\partial \eta_1}{\partial t} = \eta_1(1-\eta_1) - \delta_1 \Lambda \eta_1, \quad \mathbf{x} \in W, \tag{3.1}$$

$$\frac{\partial \eta_2}{\partial t} = \rho_2 \eta_2(1-\eta_2) + \nabla \cdot (\Delta_2(1-\eta_1)\nabla \eta_2), \quad \mathbf{x} \in W, \tag{3.2}$$

$$\frac{\partial \Lambda}{\partial t} = \delta_3(\eta_2 - \Lambda) + \nabla^2 \Lambda, \quad \mathbf{x} \in W, \tag{3.3}$$

where η_1, η_2 and Λ are the dimensionless variables representing the density of normal tissue, the density of neoplastic tissue and the excess concentration of H^+ ions respectively.

Simulation results shows that a very crucial parameter of the system is δ_1 in equation (3.1): when $\delta_1 > 1$, an appreciable hypocellular interstitial gap develops between the advancing tumour edge and the retreating heathy tissue, which is consistent with clinical observations; whereas, for $\delta_1 < 1$ the healthy tissue profile is coincident with the tumour edge. Since the dimensionless δ_1 is determined by the carrying capacity of the tumour population, the production rate of acid by the tumour and the reabsorption rate of acid, the model demonstrates and predicts: (1) the transition from benign to malignant growth of a tumour could be controlled by parameters such as the acquisition of angiogenesis; (2) transformation-induced reversion to glycolytic metabolism provides a mechanism for invasive tumour growth; (3) the normal cells, instead of the tumour cells, are intolerant of acidic interstitial pH in the range typically found within the acidic pH gradient extending into the peritumoural normal tissue. Finally, another prediction is that a tumour-host interface that is infiltrative indicates a better prognosis than one having a well-defined, sharp interface (i.e., a hypocellular interstitial gap between normal tissue and tumour cells can be found in some malignancies). These conclusions drawn from this model are well-supported by clinical studies and other aspects of cancer biology.

The model was later on extended and developed in Gatenby and Gawlinski (2003) and Gatenby et al. (2006).

In the same year, Perumpanani et al. (1996) first introduced haptotaxis into the modelling of cancer cell migration. The model is a reaction-diffusion-taxis system that consists of six PDE equations. The six components of the system are: the invasive cancer cells $u(\mathbf{x}, t)$, noninvasive cancer cells $m(\mathbf{x}, t)$, generic ECM proteins $c(\mathbf{x}, t)$ (fixed to the surrounding tissue), soluble ECM molecules $s(\mathbf{x}, t)$ (the resultant product of proteolytic digestion of the ECM protein) and the proteases $p(\mathbf{x}, t)$. The invasive cancer cells are modelled by the equation in the spatial domain W and temporal domain $[0, T]$:

$$\frac{\partial u}{\partial t} = \underbrace{u f_2(n, m, u)}_{\text{production}} + \nabla \cdot \left[\Theta(c) \left(\underbrace{\Gamma_u(n, m, u) \nabla u}_{\text{diffusion}} - \underbrace{u \chi(c) \nabla c}_{\text{haptotaxis}} - \underbrace{u \psi(s) \nabla s}_{\text{chemotaxis}} \right) \right], \quad (3.4)$$

where $\mathbf{x} \in W,\ t \in [0, T]$ and $\Theta(c)$ is a decreasing ramp function that models the effects of accumulating ECM retarding the movement of cells, $\Gamma_u(n, m, u)$ models changes in the chemokinesis and cell-cell adhesion, and coefficients for responsiveness to fixed gradients (haptotaxis) and soluble gradients (chemotaxis) are modulated by $\chi(c)$ and $\psi(s)$ respectively.

Five other differential reaction-diffusion equations for the other components in

the system complete the model:

$$\frac{\partial n}{\partial t} = n f_1(n,m,u) + \nabla \cdot \left[\Theta(c) \left(\Gamma_n(u,m,n) \nabla n \right) \right], \tag{3.5}$$

$$\frac{\partial m}{\partial t} = m f_2(n,m,u) + \nabla \cdot \left[\Theta(c) \left(\Gamma_n(u,m,n) \nabla m \right) \right], \tag{3.6}$$

$$\begin{aligned} \frac{\partial c}{\partial t} &= g(p,c) + \nabla \cdot K \Big[c\Theta(c) \Big(\Gamma_n(\nabla u + \nabla m) + \Gamma_u(n,m,u) \nabla u \\ &\quad - u\chi(c) \nabla c - u\psi(s) \nabla s \Big) \Big], \end{aligned} \tag{3.7}$$

$$\frac{\partial s}{\partial t} = h(p,c) + D_s \nabla^2 s, \tag{3.8}$$

$$\frac{\partial p}{\partial t} = l_1(u,c) - l_2(u,p,c) + D_p \nabla^2 p, \tag{3.9}$$

where $\mathbf{x} \in W,\ t \in [0,T]$. The model gave results (i.e. invading travelling waves of cancer cells) suggesting that movement of cells under the simultaneous effects of a haptotactic gradient and a concomitantly created chemotactic gradient is oscillatory with respect to both the speed of invasion and the wave profile of the invasive cells. Cell-matrix adhesion also plays an important role in the process. Later on, this work inspired many modellers to study the effects of haptotactic gradients resulting from proteolysis of the extracellular matrix as part of the mechanism of cell migration (Perumpanani et al., 1998; Byrne et al., 2001).

Cell-cell and cell-matrix adhesion which facilitate the movements of cells by the binding and unbinding of cell surface molecules to other cells and components in extracellular matrix (ECM) respectively are also important. In Byrne and Chaplain (1996), the role of cell-cell adhesion in the growth and development of carcinomas was modelled by using the Gibbs-Thomson relation which relates the change in nutrient concentration across the tumour boundary to the local curvature (this theoretically and analytically developed the previous work by Greenspan (1976)). The evolution of nutrient concentration at a point inside the tumour, $c(\mathbf{r},t)$, is described

by a reaction-diffusion equation, i.e.,

$$0 = \nabla^2 c - \lambda(c), \quad \text{inside } \Gamma(\mathbf{r}, t) = 0, \tag{3.10}$$

where the outer surface of the tumour colony is denoted by the free boundary $\Gamma(\mathbf{r}, t) = 0$, i.e.,

$$\Gamma(\mathbf{r}, t) = \mathbf{r} - R(\theta, \phi, t). \tag{3.11}$$

The tumour here is regarded as an incompressible fluid, and it was assumed that the motion of neighbouring cells is induced by the birth and death of cells. Thus, applying mass conservation, the cell velocity denoted by $\mathbf{u}(\mathbf{r}, t)$ and the net proliferation rate $S(c)$ (expressed in terms of the nutrient concentration) satisfy the equation:

$$\nabla \cdot \mathbf{u} = S(c), \quad \text{on } \Gamma(\mathbf{r}, t) = 0. \tag{3.12}$$

The equation of motion of a point on the boundary $\Gamma(\mathbf{r}, t) = 0$ is given by,

$$\hat{\mathbf{n}} \cdot \frac{d\mathbf{r}}{dt} = \mathbf{u} \cdot \hat{\mathbf{n}}, \tag{3.13}$$

where $\hat{\mathbf{n}}$ is an outward unit normal.

Based on the assumption that $\mathbf{u}$ is related to the internal pressure p via Darcy's Law, i.e., $\mathbf{u} = -\mu \nabla p$ (μ denotes the motility of the tumour cells), the cell velocity $\mathbf{u}$ can be eliminated from the system. Thus, the system introduced above that defines the evolution of the nutrient concentration inside the tumour boundary, the cell

velocity at the outer tumour boundary, can be reformulated as:

$$0 = \nabla^2 c - \lambda(c), \qquad \text{inside } \Gamma(\mathbf{r}, t) = 0, \tag{3.14}$$

$$\mu \nabla^2 p = -S(c), \qquad \text{on } \Gamma(\mathbf{r}, t) = 0 \tag{3.15}$$

$$\hat{\mathbf{n}} \cdot \frac{d\mathbf{r}}{dt} = -\mu \nabla p \cdot \hat{\mathbf{n}}, \qquad \text{on } \Gamma(\mathbf{r}, t) = 0 \tag{3.16}$$

The boundary and initial conditions imposed on the system were as follows:

$$\frac{\partial c}{\partial t} = 0, \qquad \text{at } \mathbf{r} = 0, \tag{3.17}$$

$$\frac{\partial p}{\partial t} = 0, \qquad \text{at } \mathbf{r} = 0, \tag{3.18}$$

$$c = c_\infty (1 - 2\gamma\kappa), \qquad \text{on } \Gamma(\mathbf{r}, t) = 0, \tag{3.19}$$

$$p = p_\infty, \qquad \text{on } \Gamma(\mathbf{r}, t) = 0, \tag{3.20}$$

where $t \in [0, T]$ and c_∞ is the constant nutrient concentration on the tumour boundary, p_∞ is value that matches continuously with the external pressure field, κ is the mean curvature, and γ is the surface tension coefficient. In particular, via the second term (i.e., $2c_\infty\gamma\kappa$) in (3.19), cell-cell adhesion was for the first time incorporated using the Gibbs-Thomson relation, accounting for the energy consumed by cells on the periphery to preserve the tumour's compactness. Solutions of the model under conditions of spherical symmetry supported the conclusion that if cell-cell adhesion is sufficiently strong, then the tumour is likely to disappear. By contrast, if the bonds between the cells are weak, then the tumour will persist and eventually develop into a highly structured entity, with distinct regions of necrosis and quiescence.

By studying how small asymmetric perturbations from a radically symmetry solution evolve over time, the analysis shows that in the absence of cell-cell adhesion,

all asymmetric modes grow in time. However, only a finite number of these asymmetric modes will be excited when cell-cell adhesion is included, and this number depends upon the relative strengths of the restraining cell-cell adhesion force and the expansive cell proliferation force. These predictions of the instability of the asymmetric perturbations might give a clue as to how the shape of the tumour changes and gives rise to configurations which are reminiscent of invasive carcinomas. Therefore, the model demonstrated the important role of cell-cell adhesion in estimating a tumour's ability to invade.

With the further development of modelling techniques, hybrid models that combine both continuum and discrete descriptions of cancer invasion appeared. These models investigated the processes not only at the tumour tissue level but also at the individual cell level and in most of the cases, tumours or parts of a tumour are represented as the sum total of discrete individual cells while the cell substrates (e.g. nutrients, growth factors, matrix degrading enzymes, etc.) and ECM are described by continuum variables (Anderson et al., 2000; Anderson, 2005; Kim et al., 2007; Stolarska et al., 2009; Kim and Othmer, 2013). In Anderson et al. (2000), two types of models were presented: a continuum, deterministic model and a discrete, quasi-stochastic model. The continuum model focused on three key variables in cancer invasion, namely, tumour cells (denoted by $n(x,t)$), extracellular matrix (denoted by $f(x,t)$) and matrix degrading enzymes (denoted by $m(x,t)$). The full system was calculated on some spatial domain Ω (a region of tissue) and temporal domain

T, which consists of three nonlinear PDEs as follows:

$$\frac{\partial n}{\partial t} = \underbrace{D_n \nabla^2 n}_{\text{random motility}} - \underbrace{\chi \nabla \cdot (n \nabla f)}_{\text{cell-matrix adhesion}}, \quad \mathbf{x} \in \Omega, \tag{3.21}$$

$$\frac{\partial f}{\partial t} = \underbrace{-\delta m f}_{\text{degradation}}, \quad \mathbf{x} \in \Omega, \tag{3.22}$$

$$\frac{\partial m}{\partial t} = \underbrace{D_m \nabla^2 m}_{\text{diffusion}} + \underbrace{\mu n}_{\text{production}} - \underbrace{\lambda m}_{\text{decay}}, \quad \mathbf{x} \in \Omega, \tag{3.23}$$

where $t \in T$. Travelling wave solutions of the system in one-dimension and two-dimensions indicate the importance of haptotaxis as a mechanism of invasion, which in turn emphasises the importance of ECM gradients caused by proteolytic activities. In addition, one dimensional results also indicate that the initial cluster of tumour cells may be able to break into two separate clusters. In two dimensions, ECM heterogeneity appears as another factor governing the final tumour cell density distribution. These results are in qualitative agreement with clinical observations that small clusters can invade further probably leading to metastasis when breaking away from the central mass of the tumour.

The discrete modelling part of the paper involves discretising the partial differential equations (3.21)-(3.23), and a biased random walk governing the motion of a single tumour cell was derived where cell movement was modelled in response to a chemical stimulus. For example, the discrete equation for tumour cell can be written in the form:

$$n_{i,j}^{q+1} = n_{i,j}^{q} P_0 + n_{i+1,j}^{q} P_1 + n_{i-1,j}^{q} P_2 + n_{i,j+1}^{q} P_3 + n_{i,j-1}^{q} P_4, \tag{3.24}$$

where i, j, q are positive parameters that specify the location on the grid and the time step. The coefficients P_0 to P_4 are considered as being proportional to the

probabilities of the tumour cell being stationary (P_0) or moving left (P_1), right (P_2), up (P_3) or down (P_4), and each of the coefficients P_1 to P_4 consists of two components:

$$P_n = \text{Random movement} + \text{Haptotaxis}, \quad n = 1, 2, 3, 4. \tag{3.25}$$

Cell proliferation was accounted for in the discrete model under the assumption that each individual cell is able to produce two daughter cells on the conditions: (1) the parent cell has reached maturity and (2) there is sufficient space for the new cells to move into. The results of the discrete model confirm the predictions of the continuum model that haptotaxis is important for both invasion and metastasis. Later on, the continuum-discrete model mentioned above was further extended and developed in Anderson (2005), in which the dynamics of the nutrients (i.e. oxygen) was modelled in addition to tumour cell density, ECM proteins and matrix degrading enzymes.

Although a lot of models of cancer invasion used continuum or hybrid approaches, there are also discrete models to describe the behaviour of individual cells during malignant invasion (Ramis-Conde et al., 2008a; Turner and Sherratt, 2002; Drasdo, 2003; Araujo and Mcelwain, 2004; Ramis-Conde et al., 2008b; Lowengrub et al., 2010; Schluter et al., 2012; Scianna and Preziosi, 2012). In Turner and Sherratt (2002), a cellular Potts model is used to simulate a population of malignant cells including interactions due to both homotypic and heterotypic adhesion, proteolytic activities and a haptotactic gradient. The cellular Potts model has a regular lattice comprised of pixels with each cell, and cells are not regarded as single points but as spatial objects that allow for a change in shape and size. Each lattice site is represented by a vector of integers (i, j). In the model, a collection of biological cells was represented by being attached to each lattice pixel (i, j) of a square lattice

labelled σ_{ij}. The simulation progresses through a series of Monte Carlo steps (MCS) by attempts of generalised cells to extend their boundaris in an effort to minimise the effective energy. In this model of Turner and Sherratt (2002), the effective energy term that includes surface energy and mechanical deformations was written as:

$$\begin{aligned} H = & \sum_{ij} \sum_{i'j'} J_{\tau(\sigma_{i,j}),\tau(\sigma_{i'j'})}\{1 - \delta_{\sigma_{i,j},\sigma_{i'j'}}\} \\ & + \sum_{\sigma} \lambda(\nu_\sigma - V_T)^2, \end{aligned} \tag{3.26}$$

where $J_{\sigma_{i,j},\sigma_{i'j'}}$ are the constants that quantifies the strength of the interaction between adjacent lattice pixels and V_T is the "target" volume of the cell. Energy is required if the cell is expanded or compressed above or below the "target" volume. At each MCS, attempts are made to transform the neighbouring pixels at the boundary of each cell to increase its volume. A Monte Carlo Step (MCS) is completed when every lattice site has made an index-copy attempt. To start an index-copy attempt, a pixel (i, j) is randomly selected, and then one of its nearest neighbour site is chosen to be a source pixel (i', j'). if they are in the same cell, no calculation is needed and another index-copy attempt will carry out; if the selected site (i, j) and its neighbour (i', j') are in different cells, the probability of a successful index-copy attempt that changes σ_{ij} to $\sigma_{i'j'}$ is:

$$p(\sigma_{ij} \to \sigma_{i'j'}) = \begin{cases} 1, & \text{if } \Delta H \leq 0, \\ e^{-\Delta H/\beta}, & \text{if } \Delta H > 0, \end{cases} \tag{3.27}$$

where ΔH is the change in effective energy that consists of three parts, i.e.,

$$\Delta H = \Delta H_1 + \Delta H_2 + \Delta H_3. \tag{3.28}$$

Here ΔH_1, ΔH_2 and ΔH_3 are the energy changes associated with alterations in cell-cell adhesion, mechanical deformation and haptotaxis respectively. Thus, ΔH_1 represents the change of the first term in equation (3.26) and ΔH_2 represents the change of the second term in equation (3.26). Haptotaxis (cell movement along ECM gradients) was considered in the model by attaching a parameter f_{ij} to lattice pixel (i, j) that represents local ECM concentration, so that the change of the effective energy that is associated with ECM gradients was described as $\Delta H_3 = k_H(f_{i'j'} - f_{ij})$, and k_H influences the strength of haptotaxis.

The simulation results of this discrete model showed that the morphology of the invading front is influenced by changes in the adhesiveness, and cell-matrix adhesion has a greater impact on the cancer invasion compared with cell-cell adhesion. Also, when proliferation is present in the model, it was seen that the tumour grow further into the tissue but reduce the ability to produce fingered patterns. In addition, increases both proteolytic enzyme secretion rate and haptotaxis strength promote cancer invasion.

From the models mentioned so far (Perumpanani et al., 1996, 1998; Anderson et al., 2000; Turner and Sherratt, 2002), we see that proteolytic activities are highly involved in tumour acidity. Webb et al. (1999) proposed a model suggesting a critical role for proteinase activities in tumour invasive behaviour. However, in most of models the protease dynamics were modelled either by a simple term in discrete models or in the continuum approach by a reaction-diffusion equation that includes random motility, production and decay terms. However, Chaplain and Lolas (2005) investigated the role of a protease system, namely the urokinase plasminogen activation (uPA) system, by a system of reaction-diffusion-taxis partial differential equations. uPA secreted by cancer cells initiates the activation of an enzymatic cascade that primarily involves the activation of plasminogen which then is turned

into the matrix degrading protein, plasmin. Therefore, the model mainly described interactions between cancer cells, urokinase plasminogen activator (uPA), uPA inhibitors, plasmin and the host tissue. The dimensionless model is calculated on some spacial domain Y and temporal domain T, which is written as follows:

$$\frac{\partial c}{\partial t} = \underbrace{D_c \Delta c}_{\text{diffusion}} - \nabla \cdot [\underbrace{\chi_u c \nabla u}_{\text{uPA-chemo}} + \underbrace{\chi_p c \nabla p}_{\text{PAI-1-chemo}} + \underbrace{\chi_v c \nabla v}_{\text{VN-hapo}}] + \underbrace{\mu_1 c(1-c)}_{\text{profieration}}, \ \mathbf{x} \in Y, \tag{3.29}$$

$$\frac{\partial v}{\partial t} = - \underbrace{\delta v m}_{\text{degradation}} + \underbrace{\phi_{21} u p}_{\text{uPA/PAI-1}} - \underbrace{\phi_{22} v p}_{\text{PAI-1/VN}} + \underbrace{\mu_2 v(1-v)}_{\text{proliferation}}, \ \mathbf{x} \in Y, \tag{3.30}$$

$$\frac{\partial u}{\partial t} = \underbrace{D_u \Delta u}_{\text{diffusion}} - \underbrace{\phi_{31} p u}_{\text{uPA/PAI-1}} - \underbrace{\phi_{33} c u}_{\text{uPA/uPAR}} + \underbrace{\alpha_{31} c}_{\text{production}}, \ \mathbf{x} \in Y, \tag{3.31}$$

$$\frac{\partial p}{\partial t} = \underbrace{D_p \Delta p}_{\text{diffusion}} - \underbrace{\phi_{41} p u}_{\text{uPA/PAI-1}} - \underbrace{\phi_{42} p v}_{\text{PAI-1/VN}} + \underbrace{\alpha_{41} m}_{\text{production}}, \ \mathbf{x} \in Y, \tag{3.32}$$

$$\frac{\partial m}{\partial t} = \underbrace{D_m \Delta m}_{\text{diffusion}} + \underbrace{\phi_{52} p v}_{\text{PAI-1/VN}} + \underbrace{\phi_{53} c u}_{\text{uPA/uPAR}} - \underbrace{\phi_{54} m}_{\text{degradation}}, \ \mathbf{x} \in Y, \tag{3.33}$$

where $t \in T$ and we denote cancer cell density by c, the extracellular matrix (ECM, vitronectin) substrate density by v, urokinase plasminogen activator (uPA) concentration by u, plasminogen activator inhibitor (PAI-1) concentration by p and plasmin concentration by m. The simulation results of the model exhibit a very rich dynamic behaviour, and show that the spatio-temporal heterogeneities in the distributions of cancer cells can arise from the interactions between proliferative effects (i.e., cancer cell proliferation and matrix remodelling) and gradient driven migration. The results are in line with experimental results that in the presence of malignant breast cells, plasmin is activated on the membrane of cancer cells and the morphology of the tumour is changed from sheet-like structures to multicellular heterogeneous masses.

There are some recent mathematical models that also emphasise the role of

proteolytic activities of some hydrolytic enzymes such as urokinase plasminogen activator (uPA) and matrix metalloproteinases (MMPs) in tumour invasive behaviour (Andasari et al., 2011; Deakin and Chaplain, 2013). Each of these models adopted a continuum approach, using systems of partial differential equations (PDE) of a generic chemotaxis/haptotaxis nature.

Since capturing features of the growth of a tumour can be considered as a moving boundary problem, certain numerical techniques facilitate the modelling of cancer invasion. In a series of papers by Zheng et al. (2005); Frieboes et al. (2006); Macklin and Lowengrub (2005, 2006, 2007), a level-set method was used to study solid tumour morphology changes in homogeneous and heterogeneous microenvironments. In the paper of Macklin and Lowengrub (2007), previous tumour growth models (Greenspan, 1976; Byrne and Chaplain, 1996; Cristini et al., 2003; Macklin and Lowengrub, 2005; Zheng et al., 2005) were extended by including more details of the microenvironment, i.e., allowing variability in the nutrient (denoted by σ) availability and the response to proliferation-induced mechanical pressure (denoted by p) in the peri-tumourous tissue. The dimensionless equations for nutrient concentration σ in different regions of the domain (i.e., tumour region Ω that is composed of a viable region Ω_V and a necrotic region Ω_N, healthy tissue region Ω_H, and the boundary of tumour and its necrotic core Σ and Σ_N accordingly) are written as:

$$\begin{cases} D\nabla^2\sigma = 0, & \mathbf{x} \in \Omega_H, \\ \nabla^2\sigma = \sigma, & \mathbf{x} \in \Omega, \\ [\sigma] = 0, & \mathbf{x} \in \Sigma, \\ D\nabla\sigma|_{\Omega} \cdot \mathbf{n} = D\nabla\sigma|_{\Omega_H} \cdot \mathbf{n}, & \mathbf{x} \in \Sigma, \\ \sigma \equiv 1, & \mathbf{x} \in \partial(\Omega \cup \Omega_H). \end{cases} \tag{3.34}$$

Here, $D = D_H/D_T$ (where, D_H and D_T are the nutrient diffusion rates in heathy

tissue and tumour respectively) provides a measure of the nutrient richness of the tumour microenvironment relative the tumour. Once the nutrient concentration profile is known by solving equations (3.34), the radius of the necrotic core R_N at time t is defined, since the value of $R_N(t)$ is completely determined by the known radius of the tumour R at the current time and a parameter N that gives the critical nutrient concentration level for tumour cell necrosis.

The pressure in the different regions of the domain satisfies the following system of equations:

$$\begin{cases} \mu\nabla^2 p = 0, & \mathbf{x} \in \Omega_H, \\ -\mu\nabla^2 p = G(\sigma - A), & \mathbf{x} \in \Omega_V, \\ -\mu\nabla^2 p = -GG_N, & \mathbf{x} \in \Omega_N, \\ [p] = \kappa, & \mathbf{x} \in \Sigma, \\ \mu\nabla p|_{\Omega} \cdot \mathbf{n} = \mu\nabla p|_{\Omega_H} \cdot \mathbf{n}, & \mathbf{x} \in \Sigma, \\ \sigma \equiv 1, & \mathbf{x} \in \partial(\Omega \cup \Omega_H). \end{cases} \tag{3.35}$$

Similarly, the diffusion coefficient $\mu = \mu_H/\mu_T$ is a measure of the relative ability of the external tissue to respond to the pressure compared to the biomechanical response of the tumour; G measures the tumour aggressiveness; A measures the susceptibility of tumour cells to apoptosis; and G_N measures the enzymatic breakdown of necrotic tumour cells. The normal velocity functions F is defined as:

$$F = \begin{cases} -\mu\nabla p|_{\Omega_H} \cdot \mathbf{n}, & \mathbf{x} \text{ on } \Sigma_N, \\ -\mu\nabla p|_{\Omega} \cdot \mathbf{n}, & \mathbf{x} \text{ on } \Sigma, \\ 0, & \text{otherwise.} \end{cases} \tag{3.36}$$

Solving equations (3.35) gives us the spatial distribution of p, so that we can calculate the normal velocity on the necrotic core boundary and tumour boundary by equations (3.36). This normal velocity F is used to update the tumour boundary

position by solving the PDE for the level set function φ, which is written as:

$$\frac{\partial \varphi}{\partial t} + \widetilde{F}|\nabla \varphi| = 0, \quad \mathbf{x} \in \Omega \cup \Omega_H, \tag{3.37}$$

where $\widetilde{F}(\mathbf{x}, t)$ is an extension of F off the tumour boundary Σ (see section 4.2.4 for details about the velocity extension).

The simulation results show that the qualitative features of tumour morphologies are mainly determined by the microenvironmental parameters, i.e., D and μ. Quantitive aspects of the tumour progression (size, the amount of invasive cells, growth rate,morphological instability degree) are generally affected by the parameters that characterise the tumour genetics, i.e., G, G_N, N, and A. Also, it was found that the internal structure of the tumours depends primarily upon D, G_N and N, and very little upon μ and G. Moreover, these volume fractions tend toward constant values even during growth, which is in contrast to the case of tumour spheroids where the volume fraction is only stabilised once a global steady state is established.

In addition, three distinct morphologies were observed through the model: fragmenting, invasive/fingering, and compact/hollow growth. If the microenvironment is nutrient poor, tumours tend to break into small fragments regardless of cellular mobility; the invasive fingering morphology can be found in the microenvironment of nutrient-rich and low mobility; and tumours growing into nutrient-rich, high-mobility tissues develop compact/hollow morphologies. These results have important implications for therapy and treatment for various types of cancer.

A new ghost cell/level set method was later developed in Macklin and Lowengrub (2008) which was applied to models of tumour invasive growth in complex, heterogeneous tissues. The model consists of a nonlinear nutrient equation and a pressure equation with geometry-dependent jump boundary conditions. This model was then further extended into an improved model of vascular tumour invasion including the

process of tumour-induced angiogenesis (Macklin et al., 2009).

Multiphase mixture models are also used to investigate tumour growth problems. (Byrne and Preziosi, 2003; Chaplain et al., 2006b; Preziosi and Tosin, 2009; Wise et al., 2011), where the tumour tissue is regarded as a system consisting of different phases (e.g. cellular phase, liquid phase, etc) and the development of a solid tumour is modelled by exploring the mass and momentum balances alongside constitutive laws that distinguish the phases in the system. The diffuse interface method is another successful technique used to study tumour invasive behaviour (Wise et al., 2008; Frieboes et al., 2010).

Another continuum approach for cancer invasion was proposed by Gerisch and Chaplain (2008) which explicitly incorporates the important biological processes of cell-cell and cell-matrix adhesion through the inclusion of nonlocal terms in a system of PDEs. It introduced a sensing radius R for cells to detect their environment.

The system held on some spacial domain Ω and temporal domain T takes the form:

$$\frac{\partial c}{\partial t} = \nabla \cdot [D_1 \nabla c - c\mathscr{A}\{\underline{u}(t,\cdot)\}] + \mu_1 c(1-c-v), \quad \mathbf{x} \in \Omega, \tag{3.38}$$

$$\frac{\partial v}{\partial t} = -\gamma m v + \mu_2(1-c-v), \quad \mathbf{x} \in \Omega, \tag{3.39}$$

$$\frac{\partial m}{\partial t} = \nabla \cdot [D_3 \nabla m] + \alpha c - \lambda m, \quad \mathbf{x} \in \Omega, \tag{3.40}$$

where $t \in T$ and $c(\mathbf{x},t)$, $v(\mathbf{x},t)$ and $m(\mathbf{x},t)$ represent the concentration of cancer cells, extracellular matrix and matrix degradation enzymes respectively. In the cancer cell equation there is a non-local flux term that models cell-cell and cell-matrix adhesion. The random motility and haptotaxis are included as the mechanisms that drive cancer cell migration as in Anderson et al. (2000). However, the haptotaxis

term in equation (3.38) is not local, and takes the form in 1D as:

$$\mathscr{A}\{\underline{u}(t,\cdot)\}(\mathbf{x}) = \frac{1}{R}\int_0^R \sum_{k=0}^{1} \underline{\eta}(k)\cdot\Omega(r)g(\underline{u}(t,\underline{x}+r\underline{\eta}(k)))dr, \tag{3.41}$$

with right and let unit outer normal vector $\underline{\eta}(k) = (-1)^k, k = 0, 1$. For 2D, the non-local term is written as:

$$\mathscr{A}\{\underline{u}(t,\cdot)\}(\mathbf{x}) = \frac{1}{R}\int_0^R r\int_0^{2\pi} \sum_{k=0}^{1} \underline{\eta}(\theta)\cdot\Omega(r)g(\underline{u}(t,\underline{x}+r\underline{\eta}(\theta)))d\theta dr, \tag{3.42}$$

with $\underline{\eta}(\theta) = (\cos(\theta), \sin(\theta))^T$ denoting the unit outer normal vector corresponding to angle θ. In the nonlocal terms (3.41) and (3.42), $R > 0$ is the sensing radius; $\Omega(r)$ is referred to as the radial dependency function; and $g(\underline{u}(t,\underline{x}+r\underline{\eta}))$ represents the velocity of the cancer cells at time t and spatial point $\underline{x}$ due to their adhesion to themselves and the ECM sampled over the sensing region at $\underline{x}$. It was proved that in the limit as $R \to 0$ the nonlocal model converges to a related local system of reaction-diffusion-taxis equations, which is written as:

$$\frac{\partial c}{\partial t} = \nabla\cdot[D_1\nabla c - \chi_{12}(1-c-v)c\nabla v] + \mu_1 c(1-c-v), \quad \mathbf{x}\in\Omega, \tag{3.43}$$

$$\frac{\partial v}{\partial t} = -\gamma m v + \mu_2(1-c-v), \quad \mathbf{x}\in\Omega, \tag{3.44}$$

$$\frac{\partial m}{\partial t} = \nabla\cdot[D_3\nabla m] + \alpha c - \lambda m, \quad \mathbf{x}\in\Omega. \tag{3.45}$$

In order to solve the equations computationally, an efficient numerical technique was developed in Gerisch (2010), which implemented a fast evaluation of the quadrature rule to deal with the nonlocal terms in the equations allowing for 2D simulations to be carried out with high spatial accuracy within a reasonable computation time. In certain circumstances, solutions of the local and nonlocal models were

travelling-wave like in nature, and for some parameter sets, cancer cells split into two subpopulations, with one subpopulation actively invading the tissue and the other remaining close to the origin. However, a key difference of the nonlocal model is that it is able to generate spatially heterogeneous steady-state solutions where cell-cell and cell-matrix adhesion reach a balance. The results of the nonlocal model also demonstrated that the nonlocal term that models the differential adhesion in mixtures of different cell types (Armstrong et al., 2006) is suitable for application in a more general context. In Chaplain et al. (2011), a system of reaction-diffusion partial integro-differential equations was presented to describe interactions between cancer cells, ECM and matrix degradation enzymes, which also emphasised the importance of cell-cell and cell-matrix adhesion in cancer invasion and provided some rigorous results on the existence, regularity and uniqueness of solutions. This model was later further extended in Domschke et al. (2014) to explore the dynamics during the processes cancer invasion where cell-cell and cell-matrix adhesion is accounted for through non-local interaction terms in a system of partial integro-differential equations. The model investigated the change of adhesion properties during cancer growth and development through time-dependent adhesion characteristics within the cell population as well as those between the cells and the components of the extracellular matrix. The simulation results demonstrate a range of heterogeneous dynamics which are qualitatively similar to the invasive growth patterns observed in a number of different types of cancer, such as tumour infiltrative growth patterns (INF).

3.3 Multiscale cancer invasion modelling

As described in the previous chapter, the key factors of cancer growth and invasion are genetic mutations, molecular properties, dynamical interactions among the

cancer cells, and also mutual effects between the tumour and its microenvironment. Thus, mathematical models built at a single biological scale are insufficient to uncover the multiscale mechanisms that exist. In order to investigate the behaviour of the complex system as a whole, efforts must be made to develop models that span different biological scales (Preziosi, 2006).

3.3.1 The concept of spatial and temporal scales in biological systems and associated modelling methods

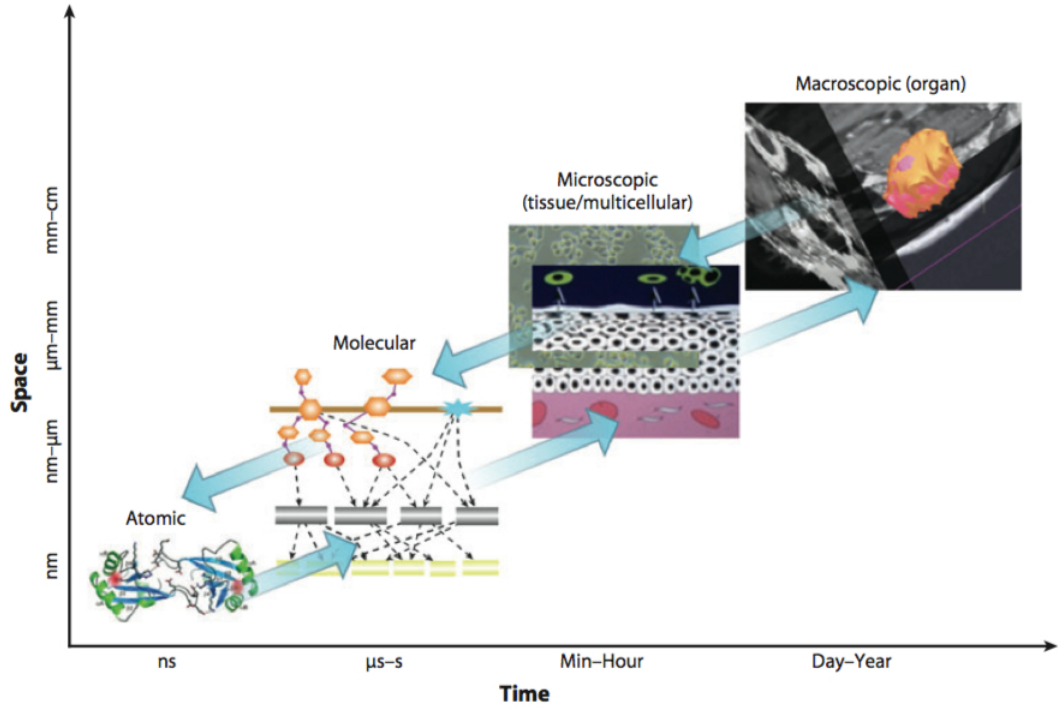

Figure 3.1: *Schematic illustration of the biological scales including atomic, molecular, microscopic (tissue/multicellular), and macroscopic (organ) scales. Copyright permission requested (Deisboeck et al., 2011).*

In the following discussions, we mainly focus on three important biological spatial scales: molecular, microscopic and macroscopic (Deisboeck et al., 2011) (Figure 3.1).

Molecular scale The molecular scale is used to study cell signalling mechanisms and intracellular regulations of biological systems. At this scale, molecular dynamics of individual proteins are not presented. Instead, an average of the properties of a population of proteins are used. The length scales at this level vary from nanometers to micrometers and time scales are on the order of microseconds to seconds. Ordinary differential equations (ODEs) are often used to represent biochemical reactions in such signalling pathways. For example, a system that represents a biological network of n species (enzymes, proteins, complex, etc.) can be described by a set of ODEs of the form:

$$\dot{\mathbf{x}} = f(\mathbf{x}, \mathbf{p}), \tag{3.46}$$

where $\mathbf{x} = (x_1, x_2, ...x_n)$ is the state vector, $x_1, x_2...x_n$ denotes the evolution of concentrations of the species in the system, and $\mathbf{p} = (p_1, p_2, ..., p_n)$ is the parameter vector (Donze et al., 2011).

Microscopic scale The microscopic scale is also called the multicellular scale, by the definition in Deisboeck et al. (2011). It includes the cellular scale, i.e., single-cell behaviours and properties. Models at this scale usually describe the process of carcinogenesis of cells, cell-cell and cell-matrix interactions and the heterogeneity of the tumour and its surrounding microenvironment, dealing with length scales from micrometers to millimetres and time scales from minutes to hours. Partial differential equations (PDEs) are usually used in the models at the microscopic scale, e.g. the reaction-diffusion system in Gatenby and Gawlinski (1996) and the continuum model proposed in Anderson et al. (2000), and the individual-based models in Turner and Sherratt (2002), Ramis-Conde et al. (2008b) and Schluter et al. (2012).

Macroscopic scale The macroscopic scale concerns the dynamics of the gross tumour behaviour, e.g., morphology, extent of vascularisation and invasion. Models

at the macroscopic scale deal with length scales from millimetres to centimetres and time scales from days to years. Since the number of cells in the model is sufficiently large, it is necessary to treat some or all of the cells as a single continuum, which allows for cell and substrate transport to be modelled with conservation laws for spatio-temporally varying densities, i.e. PDEs, and individual cell activities are not required to be tracked (Byrne and Chaplain, 1996; Anderson, 2005; Gerisch and Chaplain, 2008; Trucu et al., 2013).

Since lower-level processes are much faster, a lot of mathematical models of cancer invasion mentioned above reasonably assume that these processes are in quasi-steady-state, being included in the slower, higher-level through constitutive equations or force fields (Sloot and Hoekstra, 2009). This assumption facilitates the simplicity of the modelling by eliminating one of the differential equations from the system, and this type of multiscale modelling that couples lower-level and higher-level processes has dominated the methods used in current cancer research. However, the complexity of the disease requires more realistic and predictive multiscale models of cancer invasion. Thus, one of the motivations in this thesis is to build multiscale models that describe processes spanning different spatial and temporal scales without eliminating differential equations for the lower-level processes from the integrated system.

The majority of the models we mentioned above were formulated at single scale or eliminated differential equations that govern the dynamics at lower scales based on the assumption that lower-level processes are much faster, i.e., they are not in an integrated multiscale system. However, in the work of Trucu et al. (2013), a novel multiscale model was introduced that models the biological processes at both cellular (micoscopic) and tissue/organ (macroscopic) level with suitable numerical spatial and temporal lengths respectively. This model consists of three parts: (1)

partial differential equations modelling the dynamics of cancer cells and ECM at the macroscopic scale; (2) at the microscopic scale, the dynamics of molecular distributions of matrix degrading enzymes (which are confined around the invasive boundary of the tumour) are governed by a reaction-diffusion equation; (3) regulation mechanics of the tumour boundary acts as a link between the two scales. The details of the numerical technique (macro-microscopic technique) will be presented in the following chapter.

Other key papers in this thesis are Chaplain and Lolas (2005) and Andasari et al. (2011), which investigate the roles of the urokinase plasminogen activation (uPA) system during cancer invasion by a system of PDEs. In the following chapters of this thesis, we adapt with the macro-microscopic technique of Trucu et al. (2013) to study the phenomenon of cancer invasion at the cellular and tissue level.

Chapter 4

Mathematical modelling of cancer invasion: application of a level-set method to a moving boundary problem

4.1 Introduction

In this chapter, we use a level-set method to develop models that are motivated by our interests in modelling cancer invasion and the morphological response of a solid tumour to its microenvironment and tissue heterogeneity. As a useful and convenient tool to deal with moving boundary problems, the level-set method has been used to model tumour growth over the last ten years in the series of papers: Zheng et al. (2005), Frieboes et al. (2006), Macklin and Lowengrub (2005, 2006, 2007, 2008) and Macklin et al. (2009). Here the level-set method was used to study solid tumour morphology changes in homogeneous and heterogeneous microenvironments.

These models developed the modelling techniques of solid tumour growth that help describe the processes of different stages of tumour growth. Also they contribute to the development of the level-set method in the wider area of numerical techniques.

In this chapter, we mainly use the algorithms concerning a level-set technique introduced by Macklin and Lowengrub (2008). However, instead of using linear and nonlinear quasi-steady reaction-diffusion equations with curvature-dependent boundary conditions to model the dynamics in the tumour microenvironment, we investigate PDE systems that model the interactions in and around the tumour region and couple them with the level-set technique to describe the deformations of the tumour during invasion. The structure of the chapter is as follows: in Section 2 we introduce the numerical techniques that are applied in the level-set method; Section 3 contains the first model that we studied as a test model, including the Schnakenberg kinetics system as the description of peritumour interactions and a level-set method that involves a curvature-dependent velocity function; in Section 4, we couple the level-set method with the uPA system (Chaplain and Lolas, 2005; Andasari et al., 2011) describes the pericellular proteolysis activities and ECM degradation and remodelling during cancer invasion. A brief discussion section is given at the end.

4.2 The level-set method

Level-set methods were first developed by Osher and Sethian (1988) and have been used to study the evolution of moving surfaces that experience frequent topology changes (e.g., the merging of regions and fragmentation), particularly in the context of fluid mechanics and computer graphics (Sethian, 1999; Osher and Fedkiw, 2003; Osher and Sethian, 1988; Sethian and Smereka, 2003). The main concept of the method is that we trace the moving interface Σ *implicitly* by introducing a level set

function ϕ defined on a rectangular domain $D \supset (\Omega \cup \Sigma)$, where Ω is the moving domain that the cell is in, i.e.,

$$\phi(x) \begin{cases} < 0 & \text{if } x \in \Omega, \\ = 0 & \text{if } x \in \Sigma, \\ > 0 & \text{otherwise,} \end{cases} \qquad \text{and} \qquad |\nabla \phi| \equiv 1. \tag{4.1}$$

In this framework, we call Ω the *interior region*, $\Omega_o = D/(\Sigma \cup \Omega)$ the *exterior region*, and Σ the *interface* between the regions. Instead of capturing the position of the interface Σ explicitly and manually handling topology changes, we trace the moving boundary implicitly by updating the level set function in time. We solve a PDE equation of the type (4.2) to accomplish the updating, which automatically accounts for the interface motion and all topology changes, i.e.,

$$\phi_t + \tilde{F}|\nabla \phi| = 0, \tag{4.2}$$

where $\tilde{F}$ is an extension of F around the interface and F is the outward normal velocity of the interface (see section 4.2.4 for details about the velocity extension). Since numerical error might be introduced into the level set function by solving equation (4.2) (which perturbs it away from being a signed distance function, even for simple and special choices of $\tilde{F}$), we apply reinitialisation to the level set function at regular intervals in order to maintain it as a signed distance function. Thus, to maintain ϕ as a signed distance function, we solve the PDE below to steady state:

$$\phi_\tau = \text{sign}(\phi^0)(1 - |\nabla \phi|), \tag{4.3}$$

where τ is the so-called pseudo-time, and ϕ^0 is the original level-set function prior to the reinitialisation.

When solving equations (4.2) and (4.3), we discretise the spatial operator $|\nabla\phi|$ by a fifth-order weighted essentially non-oscillatory (WENO) method (Jiang and Peng, 2000), and we use the third order total variation-diminishing Runge-Kutta method (Gottlieb and Shu, 1997) to discretise the pseudo-time. These algorithms will be introduced in detail in the following sections.

Also, to improve computational efficiency, we adopted the narrow band/local level-set updating scheme introduced in Malladi et al. (1996). This means that we propagate the front by updating ϕ at points that lie in a narrow band in the vicinity of the interface. Since the primary purpose of a level-set function is to track the position of the interface Σ over time, its accuracy is most important on and close to the interface. In the level-set context, the narrow band can be identified by

$$\{\mathbf{x} : |\phi(\mathbf{x})| \leq R\}, \tag{4.4}$$

where $R > 0$ is a fixed constant that is chosen to suit the problem (e.g. $R = 10\Delta x$).

4.2.1 Discretisation of geometric quantities

In the level-set method, all the geometric information is encoded, which is one of advantages of this method. In particular, the outward unit normal vector $\mathbf{n}$ is given by,

$$\mathbf{n} = \frac{\nabla\phi}{|\nabla\phi|}, \tag{4.5}$$

and the mean curvature can be calculated as:

$$\kappa = \nabla \cdot \mathbf{n} = \nabla \cdot \left(\frac{\nabla\phi}{|\nabla\phi|}\right). \tag{4.6}$$

Numerically, we use a 9-point stencil with centred differences for all the partial derivatives as following:

$$\begin{aligned}
\phi_x &= \frac{\phi_{i+1,j} - \phi_{i-1,j}}{2\Delta x}, & \phi_y &= \frac{\phi_{i,j+1} - \phi_{i,j-1}}{2\Delta y}, \\
\phi_{xx} &= \frac{\phi_{i-1,j} - 2\phi i, j + \phi_{i+!,j}}{\Delta x^2}, & \phi_{xx} &= \frac{\phi_{i,j-1} - 2\phi i, j + \phi_{i,j+1}}{\Delta y^2}, \\
\phi_{xy} &= \frac{\phi_{i+1,j+1} - \phi_{i-1,j+1} - \phi_{i+1,j-1} + \phi_{i+1,j-1}}{4\Delta x \Delta y},
\end{aligned} \tag{4.7}$$

and the discretisations for the standard normal vector and curvature are:

$$\begin{aligned}
\mathbf{n} &= \frac{1}{\sqrt{\phi_x^2 + \phi_y^2 + \epsilon}}(\phi_x, \phi_y), \\
\kappa &= \frac{\phi_{xx}\phi_y^2 - 2\phi_x\phi_y\phi_{xy} + \phi_{yy}\phi_x^2}{(\phi_x^2 + \phi_y^2)^{\frac{3}{2}}}.
\end{aligned} \tag{4.8}$$

However, in many cases, the level-set function is not sufficiently smooth to use the conventional discretisation mentioned above for the normal vector and curvature. Also, when the two interfaces are very close, the discretisation of derivatives of ϕ becomes inaccurate. In order to detect and deal with this situation accurately, we use a geometry-aware curvature discretisation introduced in Macklin and Lowengrub (2006, 2008). Firstly, we define a level-set quality function by:

$$Q(\mathbf{x}) = \big|1 - |\nabla\phi(\mathbf{x})|\big|, \tag{4.9}$$

and use this function to detect singularities of ϕ whenever $Q \geq \eta$ for some threshold $\eta > 0$ ($\eta = 0.001$ in our work).

If $Q < \eta$ at each point of the nine grid points in $\{(x_{i+k}, y_{j+l}) | -1 \leq k, l \geq 1\}$, then the level set function is considered as smooth enough to calculate the curvature $\kappa_{i,j}$

and standard normal vector $\mathbf{n}_{i,j}$ using the conventional method in equations (4.7) and (4.8). If $Q > \eta$ at any of the points of the nine grid points, we construct an accurate approximation of the interface $\gamma(s) = (x(s), y(s))$ with proper orientation, where s is arc length.

In order to obtain this local approximation at an arbitrary point $\mathbf{x}_{i,j}$, first of all we need to locate five points: $\mathbf{x}_1, \mathbf{x}_2, \mathbf{x}_3, \mathbf{x}_4, \mathbf{x}_5$ (Figure 4.1). We set $\mathbf{x}_{i,j}$ be the point in the middle $\mathbf{x}_3$, and let $s_3 = 0$ such that $\gamma(0) = \mathbf{x}_3$. $\mathbf{x}_2$ and $\mathbf{x}_4$ are the points where the zero level-set (or the interface Γ) intersects the mesh immediately surrounding $\mathbf{x}_3$. In order to maintain the stability of the approximation, we need to make sure that $\mathbf{x}_2$ and $\mathbf{x}_4$ are at least $\frac{1}{10}\Delta x$ away from $\mathbf{x}_3$. Similarly, from the neighbourhood of $\mathbf{x}_2$ and $\mathbf{x}_4$ we choose $\mathbf{x}_1$ and $\mathbf{x}_5$ that intersect on the interface and at least $\frac{1}{10}\Delta x$ away from $\mathbf{x}_2$ and $\mathbf{x}_4$ accordingly.

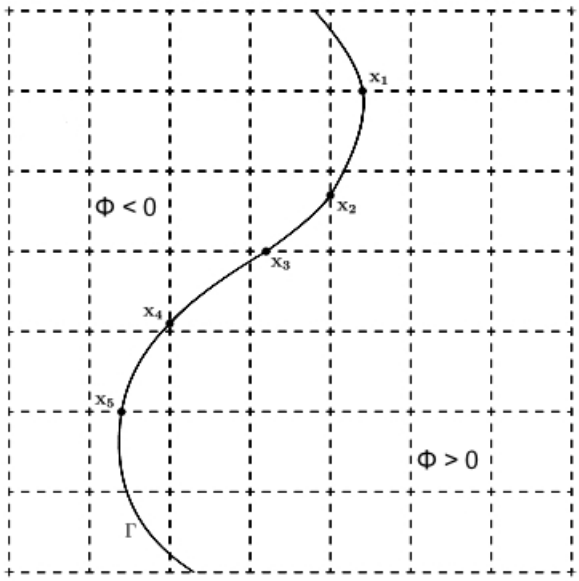

Figure 4.1: *Schematic diagram showing the choice of four points close to* $\mathbf{x_3}$

After choosing the points, we approximate the arc lengths s_i by using the linear distances between the points. That is, when moving backward along the curve from

$\mathbf{x}_3 = \gamma(s_3)$, $s_3 = 0$, $s_2 = -|\mathbf{x}_3 - \mathbf{x}_2|$, and $s_1 = s_2 - |\mathbf{x}_2 - \mathbf{x}_1|$; when moving forward along the curve from $\mathbf{x}_3$, $s_4 = |\mathbf{x}_4 - \mathbf{x}_3|$ and $s_5 = s_4 + |\mathbf{x}_5 - \mathbf{x}_4|$. Then let $x(s)$ and $y(s)$ be the least squares quadratic curves fitted to $\{(s_i, x_i)\}_{i=1}^5$ and $\{(s_i, y_i)\}_{i=1}^5$, then we obtain an approximate curve of the interface. The next step is to use this approximation of the boundary to construct a local level-set function near $\mathbf{x}_3 = (x, y)$ on the 3×3 grid $\hat{X} \times \hat{Y}$ where $\hat{X} = \{x - \delta, x, x + \delta\}$, $\hat{Y} = \{y - \delta, y, y + \delta\}$ and δ is a positive constant (here we choose $\delta = \frac{1}{1000}\Delta x$). Using this constructed local level-set function we effectively remove the influence of the nearby irregularity, and safely apply the 9-point stencil discretisation to calculate the curvature and normal vector.

4.2.2 The WENO algorithm in 2D

In this section we introduce the fifth-order weighted essentially non-oscillatory (WENO) scheme in 2D proposed by Jiang and Peng (2000) to approximate the spatial operator in the PDE for the level-set method which is a Hamilton-Jacobi equation.

Let x_i, y_j be the (i, j) node of a 2D grid with uniform spacing Δx in x-direction and Δy in y-direction. We introduce the notations:

$$\phi_{i,j} = \phi(x_i, y_j), \quad \Delta_x^+ = \phi_{i+1,j} - \phi_{i,j}, \quad \Delta_y^+ = \phi_{i,j+1} - \phi_{i,j}. \tag{4.10}$$

Here, $\phi_{x,i,j}^{\pm}$ are WENO approximations to $\dfrac{\partial \phi}{\partial x}(x_i, y_j)$, i.e.,

$$\begin{aligned}\phi_{x,i,j}^{\pm} = \frac{1}{12}\left(-\frac{\Delta_x^+\phi_{i-2,j}}{\Delta x} + 7\frac{\Delta_x^+\phi_{i-1,j}}{\Delta x} + 7\frac{\Delta_x^+\phi_{i,j}}{\Delta x} - \frac{\Delta_x^+\phi_{i+1,j}}{\Delta x}\right) \\ \pm \Phi^{WENO}\left(\frac{\Delta_x^-\Delta_x^+\phi_{i\pm2,j}}{\Delta x}, \frac{\Delta_x^-\Delta_x^+\phi_{i\pm1,j}}{\Delta x}, \frac{\Delta_x^-\Delta_x^+\phi_{i,j}}{\Delta x}, \frac{\Delta_x^-\Delta_x^+\phi_{i\mp1,j}}{\Delta x}\right).\end{aligned} \tag{4.11}$$

Similarly, $\phi^{\pm}_{y,i,j}$ are WENO approximations to $\dfrac{\partial \phi}{\partial y}(x_i, y_j)$, given by,

$$\phi^{\pm}_{y,i,j} = \frac{1}{12}\left(-\frac{\Delta^+_y \phi_{i,j-2}}{\Delta y} + 7\frac{\Delta^+_y \phi_{i,j-1}}{\Delta y} + 7\frac{\Delta^+_y \phi_{i,j}}{\Delta y} - \frac{\Delta^+_y \phi_{i,j-1}}{\Delta y}\right)$$
$$\pm \Phi^{\text{WENO}}\left(\frac{\Delta^-_y \Delta^+_y \phi_{i,j\pm 2}}{\Delta y}, \frac{\Delta^-_y \Delta^+_y \phi_{i,j\pm 1}}{\Delta y}, \frac{\Delta^-_y \Delta^+_y \phi_{i,j}}{\Delta y}, \frac{\Delta^-_y \Delta^+_y \phi_{i,j\mp 1}}{\Delta y}\right), \qquad (4.12)$$

where

$$\Phi^{\text{WENO}}(a,b,c,d) = \frac{1}{3}\omega_0(a-2b+c) + \frac{1}{6}\left(\omega_2 - \frac{1}{2}\right)(b-2c+d), \qquad (4.13)$$

and the weights ω_0, ω_2 are defined as

$$\omega_0 = \frac{\alpha_0}{\alpha_0+\alpha_1+\alpha_2}, \quad \omega_2 = \frac{\alpha_2}{\alpha_0+\alpha_1+\alpha_2}.$$

$$\alpha_0 = \frac{1}{(\epsilon + IS_0)^2}, \quad \alpha_1 = \frac{6}{(\epsilon + IS_1)^2}, \quad \alpha_0 = \frac{3}{(\epsilon + IS_2)^2}.$$

$$IS_0 = 13(a-b)^2 + 3(a-3b)^2,$$
$$IS_1 = 13(b-c)^2 + 3(b+c)^2,$$
$$IS_2 = 13(c-d)^2 + 3(3c-d)^2.$$

In this dissertation we use the WENO scheme to discretise the spatial operator $|\nabla\phi|$. In order to guarantee that our approximations of $\dfrac{\partial \phi}{\partial x}(x_i, y_j)$ and $\dfrac{\partial \phi}{\partial y}(x_i, y_j)$

are from an upwind scheme, we let,

$$|\nabla\phi_{i,j}| = \begin{cases} \sqrt{max(\phi^-_{x,i,j},0)^2 + min(\phi^+_{x,i,j},0)^2 + max(\phi^-_{y,i,j},0)^2 + min(\phi^+_{y,i,j},0)^2} \\ \text{if } \; F(i,j) > 0, \\ \\ \sqrt{min(\phi^-_{x,i,j},0)^2 + max(\phi^+_{x,i,j},0)^2 + min(\phi^-_{y,i,j},0)^2 + max(\phi^+_{y,i,j},0)^2} \\ \text{if } \; F(i,j) < 0. \end{cases} \tag{4.14}$$

4.2.3 A Third-Order TVD–Runge-Kutta Method

The time discretisation of equation (4.2) will be implemented by a third order TVD Runge-Kutta method as used in Gottlieb and Shu (1997) and Gottlieb et al. (2001) to solve the ordinary differential equation

$$\frac{du}{dt} = L(u), \tag{4.15}$$

where $L(u)$ is a discretisation of the spatial operator, the third-order TVD Runge-Kutta given by:

$$\begin{aligned} u_1 &= u_n + \Delta t L(u_n), \\ u_2 &= \frac{3}{4}u_n + \frac{1}{4}u_1 + \frac{1}{4}\Delta t L(u_1), \\ u_{n+1} &= \frac{1}{3}u_n + \frac{2}{3}u_2 + \frac{2}{3}\Delta t L(u_2). \end{aligned} \tag{4.16}$$

4.2.4 Velocity Extension

Recall that the basic idea of the level-set method, is that an interface propagating with speed F is embedded as the zero level set of the higher-dimensional level-set function ϕ, satisfying

$$\phi_t + F|\nabla\phi| = 0. \tag{4.17}$$

There is an implicit assumption that the normal velocity F is assumed to have been defined for all the level-sets and not just the zero level-set corresponding to the interface. Therefore, both the interface and the speed F are embedded in a higher-dimensional function. To be more accurate, we should write:

$$\phi_t + \widetilde{F}|\nabla\phi| = 0, \tag{4.18}$$

where

$$\widetilde{F} = F \text{ at points } (x, y), \text{ where } \phi = 0.$$

This new velocity field $\widetilde{F}$ is called the "extension velocity".

The extension velocity $\widetilde{F}$ should yield the speed F of the zero level set in the limit,

$$\lim_{\mathbf{x}\to\mathbf{a}} \widetilde{F}(\mathbf{x}) = F(\mathbf{a}), \tag{4.19}$$

where $\mathbf{a}$ is a point on the interface.

a) Identifying the closest point on the interface

   Here we use the information provided by the level-set function ϕ to make a simple, efficient operation, where no search is required. At any point $\mathbf{x}$, the outward normal vector $\mathbf{n}(\mathbf{x})$ points away from the interface, and $|\phi(\mathbf{x})|$ gives the distance to the interface. Therefore, the point is given explicitly by,

$$\mathbf{x_\Sigma} = \mathbf{x} - \phi(\mathbf{x})\mathbf{n}(\mathbf{x}), \tag{4.20}$$

where $\mathbf{x_\Sigma}$ is the closest point on the interface Σ to point $\mathbf{x}$ (Figure 4.2).

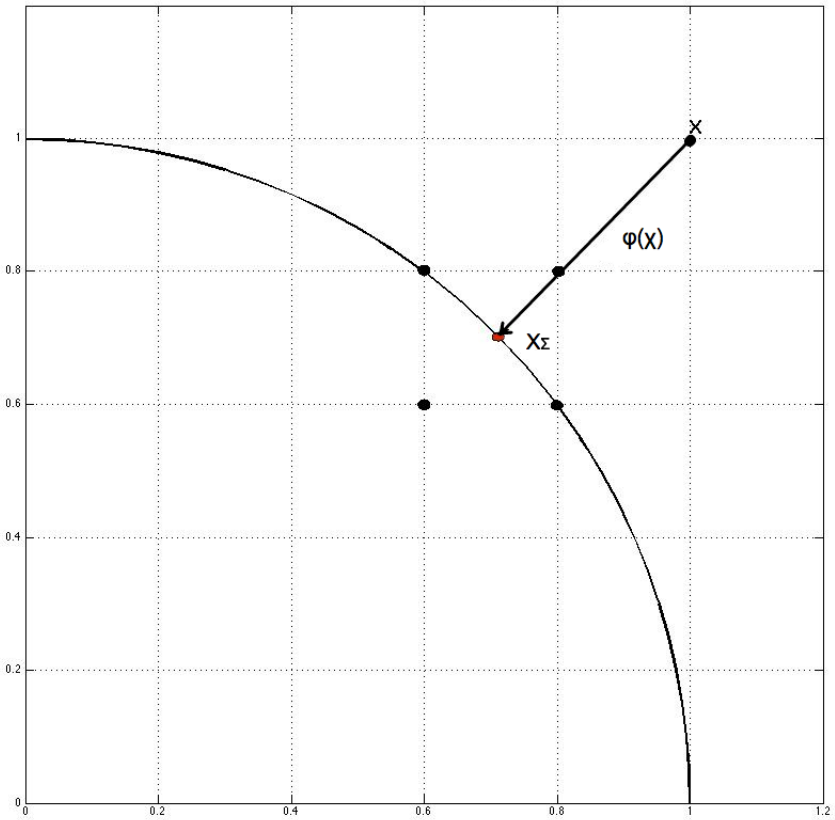

Figure 4.2: *Schematic diagram showing how to identify the closest point on the interface using the outward normal vector and signed distance function*

b) Orthogonal velocity extension

We now apply an extension routine within a band around the interface Σ to guarantee that $\nabla \widetilde{F} \cdot \mathbf{n} = 0$, which is based on a bilinear interpolation of the

velocity near the interface that has been shown to be more accurate and less computationally expensive than PDE-based techniques (Malladi et al., 1996).

Firstly, by using the technique mentioned above, we obtain the closest point $\mathbf{x_\Sigma}$ to a given point $\mathbf{x}$ on the interface. The next step is locating (x_i, y_j) such that $\mathbf{x}$ is contained in the box $[x_i, x_{i+1}] \times [y_j, y_{j+1}]$ and calculate $F(\mathbf{x}_\Sigma)$ with a bilinear interpolation of F at the corners of the box (Figure 4.2). Finally, we define $\widetilde{F}(\mathbf{x}) = F(\mathbf{x}_\Sigma)$ to obtain the extended velocity, since $\widetilde{F}$ is constant along the normal vector, i.e.,

$$\frac{\partial \widetilde{F}}{\partial \mathbf{n}} \equiv 0 \tag{4.21}$$

4.2.5 Gaussian Smoothing

When the problem to be solved is sensitive to variations in the curvature, the speed can become noisy even if small perturbations in the level set function are present. Also, grid effects such as mesh-induced anisotropies can act as sources of numerical perturbations. Although the high frequency perturbations in the speed and interface position can be damped away provided a CFL condition is satisfied, it requires a high-order time-step constraint. One way to remove the high-order time-step constraint is to use numerical diffusion to remove small, high frequency perturbations before they disturb the numerical solution. The advantage of this is that it is computationally inexpensive, and it does not degrade the accuracy of the numerical solution if done carefully. It is found that adapting a Gaussian filter (from image processing applications) to smooth the normal velocity within a certain band around the interface provides an efficient means of controlling the noise without affecting the accuracy. Additionally, Gaussian smoothing removes grid anisotropies (Macklin and Lowengrub, 2006, 2008).

In one dimension, a Gaussian filter is applied to a function f as follows:

$$\hat{f}_l = \frac{1}{\sigma\sqrt{2\pi}} \sum_i f_{l-i} \exp\left(-\frac{(i\Delta x)^2}{2\sigma^2}\right) \Delta x, \tag{4.22}$$

where σ is the standard deviation of the filter. Typically, $\sigma = M\Delta x$ for some integer M. For $|i\Delta x| \geq 3\sigma$, the exponential function in the convolution is very small, and consequently, we can truncate the sum above to

$$\hat{f}_l = \frac{1}{S} \frac{1}{M\sqrt{2\pi}} \sum_{i=-3M}^{3M} f_{l-i} \exp\left(-\frac{1}{2}\left(\frac{i}{M}\right)^2\right), \tag{4.23}$$

where S is the value of the sum for $f \equiv 1$. In order to smooth a two-dimensional data array, we use equation (4.23) first in the x-direction, and then use it again in the y-direction.

4.2.6 Convergence and Testing Results

We now present convergence results for the numerical method above. If p_h is a numerical solution of equation (4.2) computed on a computational grid with mesh length h and time step $\Delta t = \frac{1}{2}\Delta x^2$, and if the exact solution p of equation (4.2) is known, then we define,

$$\text{experimental oder of convergence} = \frac{log(\frac{||p_{h1}-p||_\infty}{||p_{h2}-p||_\infty})}{log(\frac{h_1}{h_2})}. \tag{4.24}$$

If the exact solution is unknown, we then solve on meshes with mesh lengths $h_1 = h$, $h_1 = \frac{1}{2}h$, $h_1 = \frac{1}{4}h$ and define

$$\text{experimental oder of convergence} = \frac{log(\frac{||p_h-p_{h2}||_\infty}{||p_{h2}-p_{h3}||_\infty})}{log(2)}, \tag{4.25}$$

where each norm is computed on the common grid points. In our method, we use the discrete maximum ℓ_∞ for all convergence testing.

Order of convergence of the overall algorithm

In order to test the order of convergence of the overall algorithm, first, we test it by a simple perfect unit circle with low, moderate and high resolution. Set the initial level-set function as follows:

$$\phi = \sqrt{X^2 + Y^2} - r. \tag{4.26}$$

where r is the radius of the zero contour plot of the circles and then solve the equation (4.2) with the velocity function defined as,

$$F = \kappa - \frac{1}{r} \tag{4.27}$$

where κ is the curvature.

1) $r = 1$

   Now we use the unit circle with $r = 1$ in (4.26) and velocity function $F = \kappa - 1$, to test the stability of the entire algorithm. A reasonable expectation is that the unit circle stays the same shape as it evolves, since the geometry of the interface is symmetric, meaning that the curvature $\kappa = \frac{1}{r}$ and zero contour plot of the circles gives us $r = 1$, so the speed function F should be zero, which results in a stationary circle. As can be seen from Figure 4.3 our simulation results are as expected.

   From the data we obtained, we cannot draw conclusions on the order of convergence of the method using equation (4.24) (see Table 4.1). This is probably

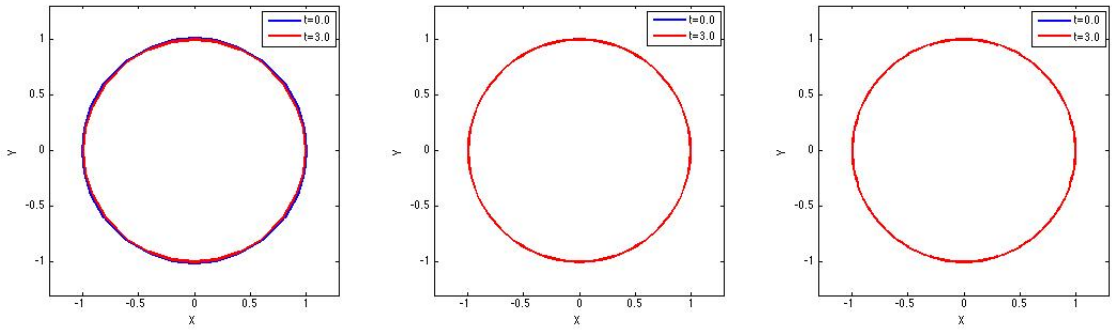

Figure 4.3: *Contour plots of tests using circle with radius $r = 1$ and speed function $F = \kappa - 1$. The bold blue curve is the initial position of the interface at $t = 0$, while the bold red curve represents the final position at $t = 3$.*

due to relatively large mesh sizes used; smaller mesh sizes could be more appropriate and this is something requiring further investigation.

dx	e_∞	order of accuracy
0.2	$1.19e^{-02}$	
0.1	$1.6725e^{-04}$	6.1561
0.05	$2.2201e^{-05}$	2.9133

Table 4.1: *Data showing the order of accuracy for the unit circle test with low, moderate and high resolution*

2) $r = 2$

Figure 4.4 shows the results of another test by using a circle with radius $r = 2$ and the velocity function $F = \kappa - \frac{1}{2}$. Similarly, we set the radius of the test circle and the speed function in a way that the interface should remain still, and once again the results are as expected.

The order of convergence given by this test is shown in Table 4.2. Again we cannot draw any precise conclusions on the order of convergence of the algorithm and this issue requires further investigation.

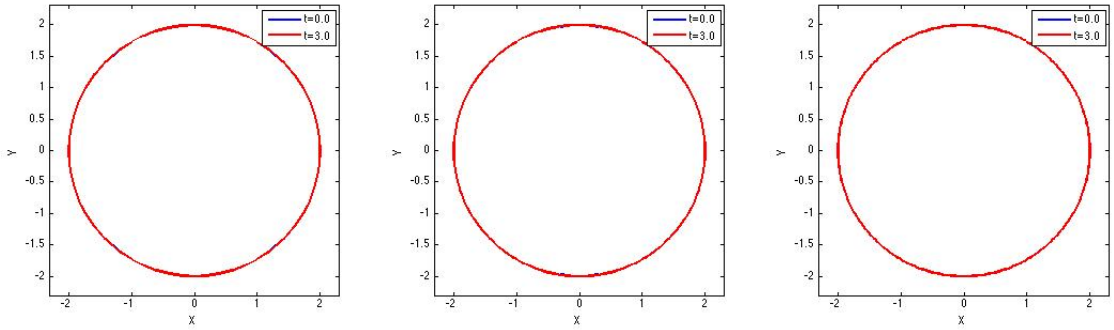

Figure 4.4: *Contour plots of tests using circle with radius $r = 2$ and speed function $F = \kappa - \frac{1}{2}$. The bold blue curve is the initial position of the interface at $t = 0$, while the bold red curve represents the final position at $t = 3$.*

dx	e_∞	order of accuracy
0.2	$2.7588e^{-04}$	
0.1	$6.2663e^{-05}$	2.1383
0.05	$2.0263e^{-06}$	1.6284

Table 4.2: *Data showing the order of accuracy for the test with low, moderate and high resolution*

4.3 Case study 1: A test model

We first introduce a test model that includes a reaction-diffusion system (the Schnakenberg system) to model the dynamics in a hypothetical peritumoural environment, and use the distribution of the determinant factor that controls the movement of cancer cells to regulate the velocity of migrating cancer cells. Using a level-set method we calculate and keep track of the precise position of the tumour boundary when the interface of the tumour deforms.

4.3.1 Analysis of the Schnakenberg system

The dimensionless Schnakenberg model, with zero-flux boundary condition is:

$$\frac{du}{dt} = \gamma f(u,v) + \nabla^2 u, \tag{4.28}$$

$$\frac{dv}{dt} = \gamma g(u,v) + d\nabla^2 v, \tag{4.29}$$

$$(\mathbf{n}\cdot\nabla)\begin{pmatrix} u \\ \\ v \end{pmatrix} = 0, \quad \mathbf{x}\ on\ \partial\mathbf{B}, \tag{4.30}$$

where,

$$f(u,v) = a - u + u^2 v, \tag{4.31}$$

$$g(u,v) = b - u^2 v, \tag{4.32}$$

and $\partial\mathbf{B}$ is the closed boundary of the domain $\mathbf{B}$ and $\mathbf{n}$ is the unit outward normal to $\partial\mathbf{B}$. Thus, the relevant homogeneous steady state is:

$$u_0 = a + b \quad v_0 = \frac{b}{(a+b)^2} \quad \text{with} \quad b > 0,\ a + b > 0. \tag{4.33}$$

It is well known (Murray, 2003) that this reaction diffusion system exhibits diffusion-driven instability (or Turing instability), i.e., the homogeneous steady state is stable to small perturbations in the absence of diffusion but unstable when diffusion is present. We derive here the necessary and sufficient conditions for diffusion-driven instability of the steady state. Consider the full system and linearise about the steady state, i.e., we set,

$$\mathbf{w} = \begin{pmatrix} u - u_0 \\ \\ v - v_0 \end{pmatrix}$$

where $|\mathbf{w}|$ is small. Then we have:

$$\mathbf{w}_t = \gamma A\mathbf{w} + D\nabla^2\mathbf{w}, \tag{4.34}$$

where A is the stability or Jacobian matrix,

$$A = \begin{pmatrix} f_u & f_v \\ g_u & g_v \end{pmatrix}_{u_0,v_0} \quad \text{and} \quad D = \begin{pmatrix} 1 & 0 \\ 0 & d \end{pmatrix}.$$

We then define $\mathbf{W}(\mathbf{r})$ to be the time-independent solution of the spatial eigenvalue problem defined by:

$$\nabla^2\mathbf{W} + k^2\mathbf{W} = 0, (\mathbf{n}\cdot\nabla)\mathbf{W} = 0 \ \text{ for } \ \mathbf{r} \ on \ \partial\mathbf{B}, \tag{4.35}$$

where k is the eigenvalue or wavenumber. Let $\mathbf{W}_k(\mathbf{r}) \propto \cos(n\pi x/a)$ be the eigenfunction corresponding to the wavenumber k. Each eigenfunction $\mathbf{W}_k(\mathbf{r})$ satisfies the zero-flux boundary conditions. Since the problem is linear, now we look for solutions $\mathbf{w}(\mathbf{r}, t)$ of (4.34) in the form:

$$\mathbf{w}(\mathbf{r}, t) = \sum_k c_k e^{\lambda t}\mathbf{W}_k(\mathbf{r}). \tag{4.36}$$

Substituting this into (4.34) and cancelling $e^{\lambda t}$, for each k, we obtain,

$$\lambda\mathbf{W}_k = \gamma A\mathbf{W}_k - Dk^2\mathbf{W}_k. \tag{4.37}$$

Since we require nontrivial solutions for $\mathbf{W}_k$, the eigenvalues are determined by the roots of the characteristic polynomial

$$|\lambda I - \gamma A + Dk^2| = 0.$$

Evaluating the determinant with A and D, we obtain the equation:

$$\lambda^2 + \lambda[k^2(1+d) - \gamma(f_u + g_v)] + h(k^2), \tag{4.38}$$

where,

$$h(k^2) = dk^4 - \gamma(df_u + g_v)k^2 + \gamma^2|A|. \tag{4.39}$$

The steady state (u_0, v_0) is linearly stable if both solutions of (4.38) and (4.38) have $Re(\lambda) < 0$. In absence of any spatial effects, i.e., $k^2 = 0$, then (4.38) becomes:

$$\lambda^2 - \gamma(f_u + g_v)\lambda + \gamma^2(f_u g_v - f_v g_u) = 0.$$

Thus linear stability is guaranteed if

$$\mathrm{tr}A = f_u + g_v < 0, \quad |A| = f_u g_v - f_v g_u > 0.$$

Meanwhile, for the steady state to be unstable to spatial disturbances we require $Re\lambda(k) > 0$, which can be satisfied if either the coefficient of λ in (4.38) is negative or if $h(k^2) < 0$ for some $k \neq 0$. However, since we already require $(f_u g_v - f_v g_u) < 0$ to guarantee stability in absence of spatial perturbations and $k^2(1+d) > 0$ for all $k \neq 0$, the coefficient of λ is always positive, namely,

$$[k^2(1+d) - \gamma(f_u + g_v)] > 0.$$

Therefore, the only way to make $Re\lambda(k^2) > 0$ is when $h(k^2) < 0$ for some k. Since we already have $|A| > 0$, it is possible for $h(k^2)$ to be negative in (4.38) if $df_u + g_v > 0$. Also, $(f_u + g_v) < 0$ implies that $d \neq 1$ and f_u and g_v must have opposite signs. Furthermore, the minimum $h_{\min}$ must be negative to ensure that $h(k^2)$ is negative

for some nonzero k. From (4.39), we have,

$$h(k^2) = d\left(k^2 - \gamma\frac{df_u + g_v}{2d}\right)^2 + \gamma^2\left[|A| - \frac{(df_u + g_v)^2}{4d}\right],$$

which gives us:

$$h_{\min} = \gamma^2\left[|A| - \frac{(df_u + g_v)^2}{4d}\right], \quad k^2 = k_m^2 = \gamma\frac{df_u + g_v}{2d}. \tag{4.40}$$

Thus, the condition that $h(k^2) < 0$ for some $k^2 \neq 0$ is:

$$|A| < \frac{(df_u + g_v)^2}{4d}. \tag{4.41}$$

At the bifurcation point, when $h_{\min} = 0$ and for fixed kinetics parameters, we define a critical diffusion coefficient ratio $d_c > 1$ as the appropriate root of

$$d_c^2 f_u^2 + 2(2f_v g_u - f_u g_v)d_c + g_v^2 = 0. \tag{4.42}$$

In this case, we obtain an expression for d_c in terms of the parameters a and b by substituting f_u and g_v as below:

$$d_c = \frac{(a+b)^2[a^2 + 3^2 + 4ab + 2(a+b)\sqrt{3b^2 - a + 3b}]}{(b-a)^2}. \tag{4.43}$$

We obtain the parameter γ from the equation:

$$\gamma \approx \frac{2d_c k_m^2}{d_c f_u + g_v}. \tag{4.44}$$

From Figure 4.5, we see that there is a wavenumber range $k_1^2 < k^2 < k_2^2$ with $h(k^2) < 0$ and $Re\lambda > 0$, and it can be obtained from solutions k_1^2 and k_2^2 of $h(k^2) = 0$

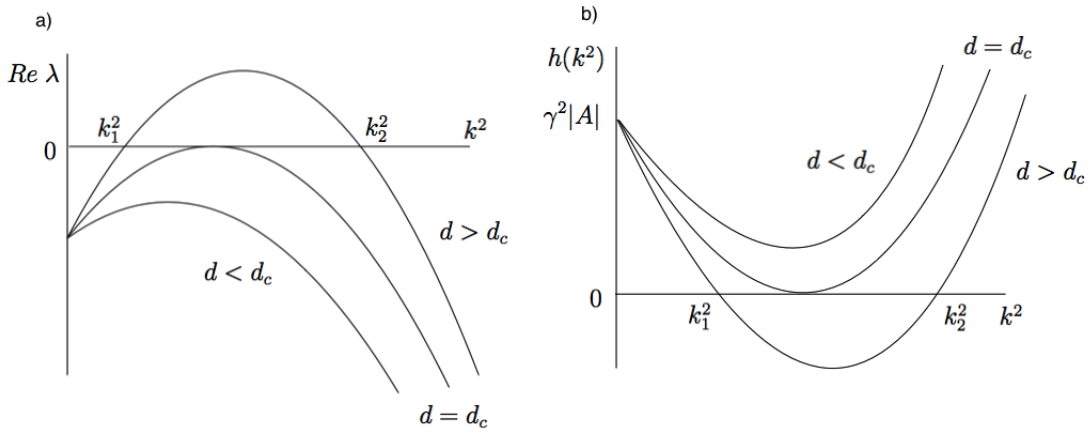

Figure 4.5: *a). Plot of* $h(k^2)$ *defined by* (4.39) *when the diffusion coefficient ratio* $d < d_c$, $d = d_c$ *and* $d > d_c$. *b).Plot of the largest of the eigenvalues* $\lambda(k^2)$ *from* (4.38) *as a function of* k^2.

(equation (4.39)), i.e.,

$$k_1^2 = \frac{\gamma\left[(df_u + g_v) - \sqrt{(df_u + g_v)^2 - 4d|A|}\right]}{2d} < k^2$$
$$< \frac{\gamma\left[(df_u + g_v) + \sqrt{(df_u + g_v)^2 - 4d|A|}\right]}{2d} = k_2^2. \tag{4.45}$$

For finite domain eigenvalue problems, the wavenumbers are discrete and so only certain k in the range are relevant. Figure 4.5 b) plots a typical $\lambda(k^2)$ against k^2 and the expression $\lambda = \lambda(k^2)$ is called dispersion relation. An analysis of the dispersion relation is crucial in order to get the information of which eigenfunctions (i.e. which spatial patterns) are linearly unstable and grow exponentially with time.

Now we consider the solution $\mathbf{w}(\mathbf{r}, t)$ given by equation (4.36). Those modes for which $Re\lambda(k^2) > 0$ make the dominant contributions as time t increases since all other modes tend to zero exponentially. Thus, we can write:

$$\mathbf{w}(\mathbf{r},t) \simeq \sum_{k_1}^{k_2} C_k e^{\lambda(k^2)t}\mathbf{W}_k(\mathbf{r}) \quad \text{for large } t, \tag{4.46}$$

with the range of wavenumbers $k_1^2 < k^2 < k_2^2$ from equation (4.45) where $h(k^2) < 0$ and hence $Re\lambda > 0$. Since we have $\mathbf{W}_k(\mathbf{r}) \propto \cos(n\pi x/a)$ from equation (4.35), in a one dimensional domain $x \in (0, p)$, the spatially heterogeneous solution which emerges is the sum of the unstable modes, i.e.,

$$\mathbf{w}(\mathbf{r},t) \simeq \sum_{n_1}^{n_2} C_n \exp\left[\lambda\left(\frac{n^2\pi^2}{p^2}\right)t\right]\cos\left(\frac{n\pi x}{p}\right), \tag{4.47}$$

where λ is given by the positive solution of equation (4.38), n_1 is the smallest integer no less than pk_1/π, n_2 the largest integer no greater than pk_2/π and C_n are the constants which are determined by the initial conditions.

Figure 4.6 shows a range of one-dimensional patterns with modes from $n = 1$ to $n = 9$ for the Schnakenberg system.

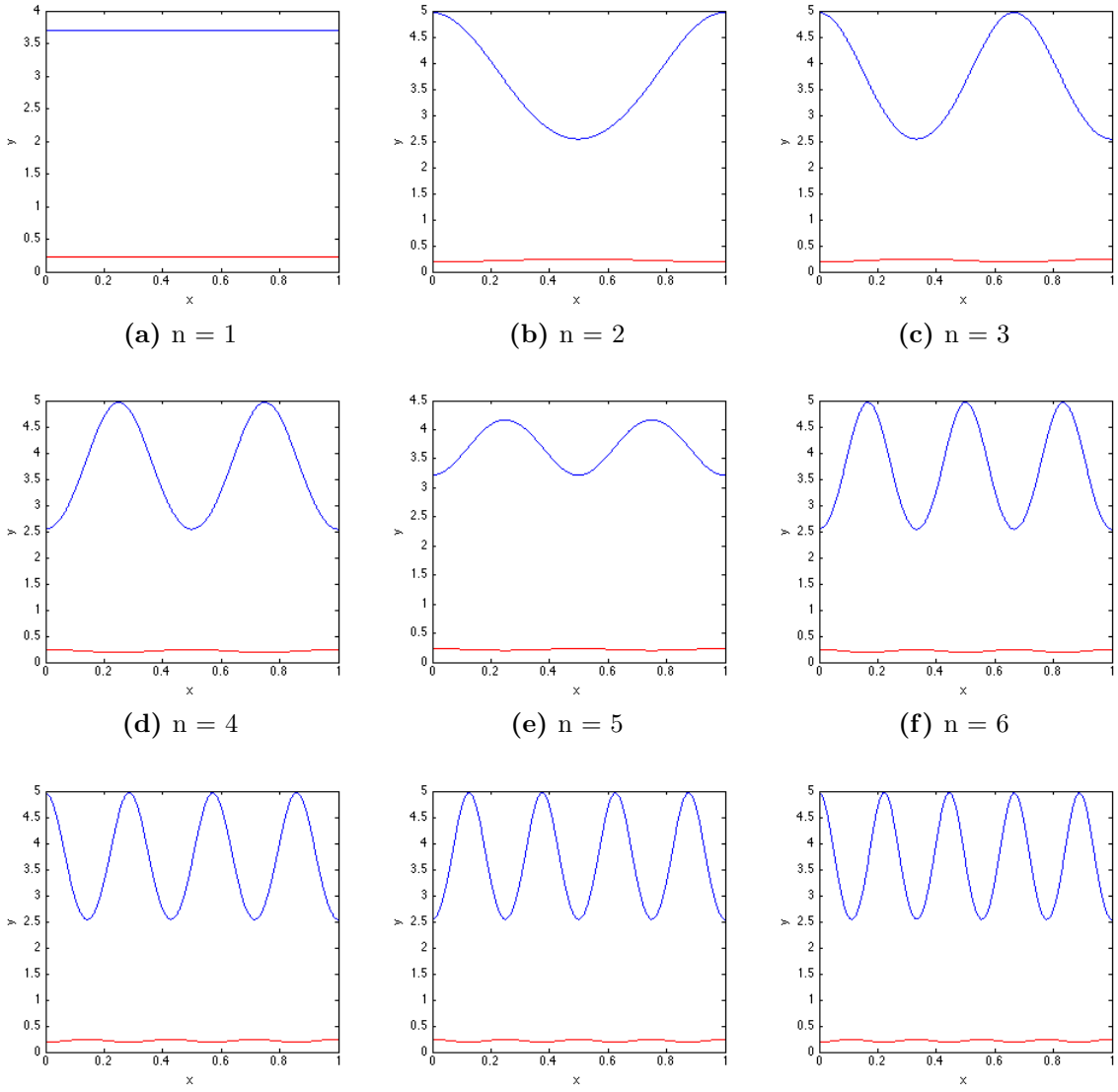

(a) n = 1 **(b)** n = 2 **(c)** n = 3

(d) n = 4 **(e)** n = 5 **(f)** n = 6

(g) n = 7 **(h)** n = 8 **(i)** n = 9

Figure 4.6: *Plots of one-dimensional patterns with modes from* $n = 1$ *to* $n = 9$ *for the Schnakenberg system. The blue curve represents the level of species* u *and red represents the level of species* v*. Parameter values are:* $a = 0.7, b = 3, d = d_c + \epsilon$*, where* $\epsilon = 10^{-6}$*; values of* d_c *and* γ *are obtained from equation* (4.43) *and* (4.44)*.*

Similarly, in a two-dimensional domain $\mathbf{x} \in [0, p] \times [0, q]$, the eigenfunctions of the spatial eigenvalue problem in equation (4.35) are:

$$\mathbf{W}_{p,q}(x, y) = C_{m,n} \cos\left(\frac{n\pi x}{p}\right) \cos\left(\frac{m\pi y}{q}\right), \tag{4.48}$$

with the corresponding spatial eigenvalues,

$$k^2 = \pi^2 \left(\frac{n^2}{p^2} + \frac{m^2}{q^2}\right), \tag{4.49}$$

where m and n are integers. These modes $\mathbf{W}_k(x, y)$ are linearly unstable with the wavenumber k lying within the unstable range. To guarantee that at least one possible mode is included in the range, we assume d is sufficiently large, or we let γ satisfy the condition in equation (4.44) and the diffusion coefficient ratio d satisfy equation (4.43). Now the unstable spatially patterned solution becomes:

$$\mathbf{w}(\mathbf{r}, t) \simeq \sum_{m,n} C_{m,n} e^{\lambda(k^2)t} \cos\left(\frac{n\pi x}{p}\right) \cos\left(\frac{m\pi y}{q}\right), \tag{4.50}$$

within the range of unstable wavenumbers.

Figure 4.7 shows the plots of different two-dimensional patterns formed by varying the values of n and m in a way that the wavenumbers remain in the unstable range.

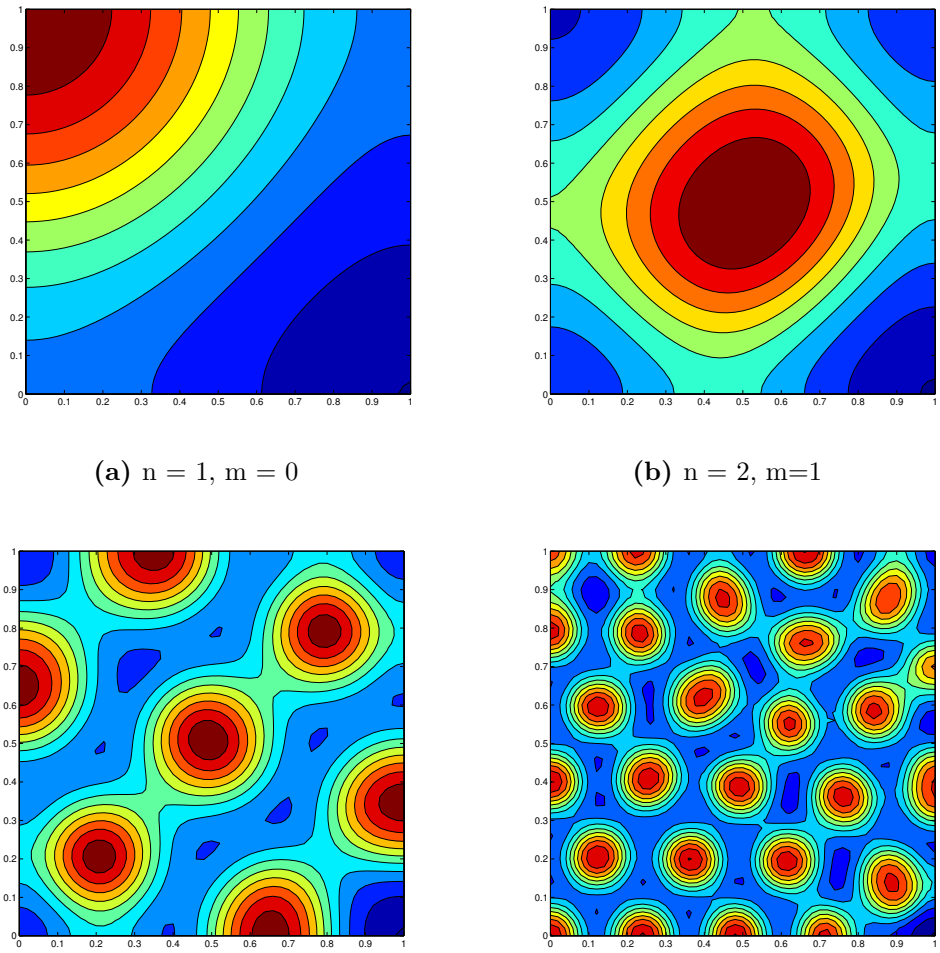

(a) n = 1, m = 0

(b) n = 2, m=1

(c) n = 4, m = 2

(d) n = 8, m=4

Figure 4.7: *Plots of different two-dimensional patterns generated by the Schnakenberg system by varying the values of n and m in a way that the wavenumbers remain in the unstable range with $dx = dy = 0.02$*

4.3.2 Regulation of deformations of the boundary

In this case study, we test the modelling idea that interactions between cancer cells and their microenvironment are modelled using reaction-diffusion equations, such as Schnakenberg kinetics that forms dynamic patterns of the distribution of species in the system, while the tumour boundary deformations are modelled as a moving boundary whose precise location will be calculated using the level-set method. We transform the front motion into an initial value problem as follows:

$$\begin{aligned} \phi_t + F|\nabla\phi| &= 0, \\ \text{given} \quad \phi(\mathbf{x}, t = 0). \end{aligned} \tag{4.51}$$

We assume that the velocity function F is determined by the local geometric character, i.e., curvature, and also by the local concentration of the species u in the Schnakenberg kinetics. If the local concentration of the species u at a point $\mathbf{x} \in \partial\mathbf{B}$ on the boundary is above some threshold value u_0, and the amount beyond the threshold is large enough to overcome the surface tension (which is proportional to the curvature at the point), then the velocity at that point is positive. Otherwise, the velocity at a point on the boundary can be zero, (when the force produced by u counterbalances the surface tension); or if the surface tension is larger than the force produced by the population of u at the point on the interface, then the velocity accordingly is negative. The equation of the velocity function at a point $\mathbf{x} \in \partial\mathbf{B}$ at time t is written as:

$$F(\mathbf{x}, t) = \alpha(u(\mathbf{x}, t) - u_0) - \tau\kappa(\mathbf{x}, t). \tag{4.52}$$

where u_0 is a threshold value that determines if the present concentration of u can overcome the pressure on the boundary and push it outward, and κ represents the

curvature of the interface. To calculate the curvature on the interface, we applied the method introduced in section 4.2.1.

4.3.3 Computational simulations

We solve the model in a rectangular region $Y := [0, 4] \times [0, 4]$ and assume that the cancer initially occupies a region $\Omega(0)$ within Y, taken to be a disc centred at $(2, 2)$. The mesh size is $\Delta x = \Delta y = 0.01325$. The initial conditions in two dimension for the Schnakenberg system are:

$$u(x, y, 0) = u_0 + 0.01 \cos(100x) \cos(100y), \tag{4.53}$$

$$v(x, y, 0) = v_0 + 0.01 \cos(100x) \cos(100y), \tag{4.54}$$

where (u_0, v_0) is the homogeneous steady states of the system.

Figure 4.8 shows us the simulation results of the evolution of the boundary deformations. We can see that coupling a reaction-diffusion system (whose solutions are spatially heterogeneous when the parameter setting satisfies the condition of diffusion-driven instability of the steady state) and the level-set method can help us to describe the boundary deformations. However, in this case, we have assumed that the surface tension of the tumour is curvature-dependent. In other words, the heterogeneity of the dynamics that models the interactions between the tumour and its microenvironment is not the main reason that triggers the deformations of the boundary. In the next study case, we will remove the effect of the curvature-dependent boundary condition.

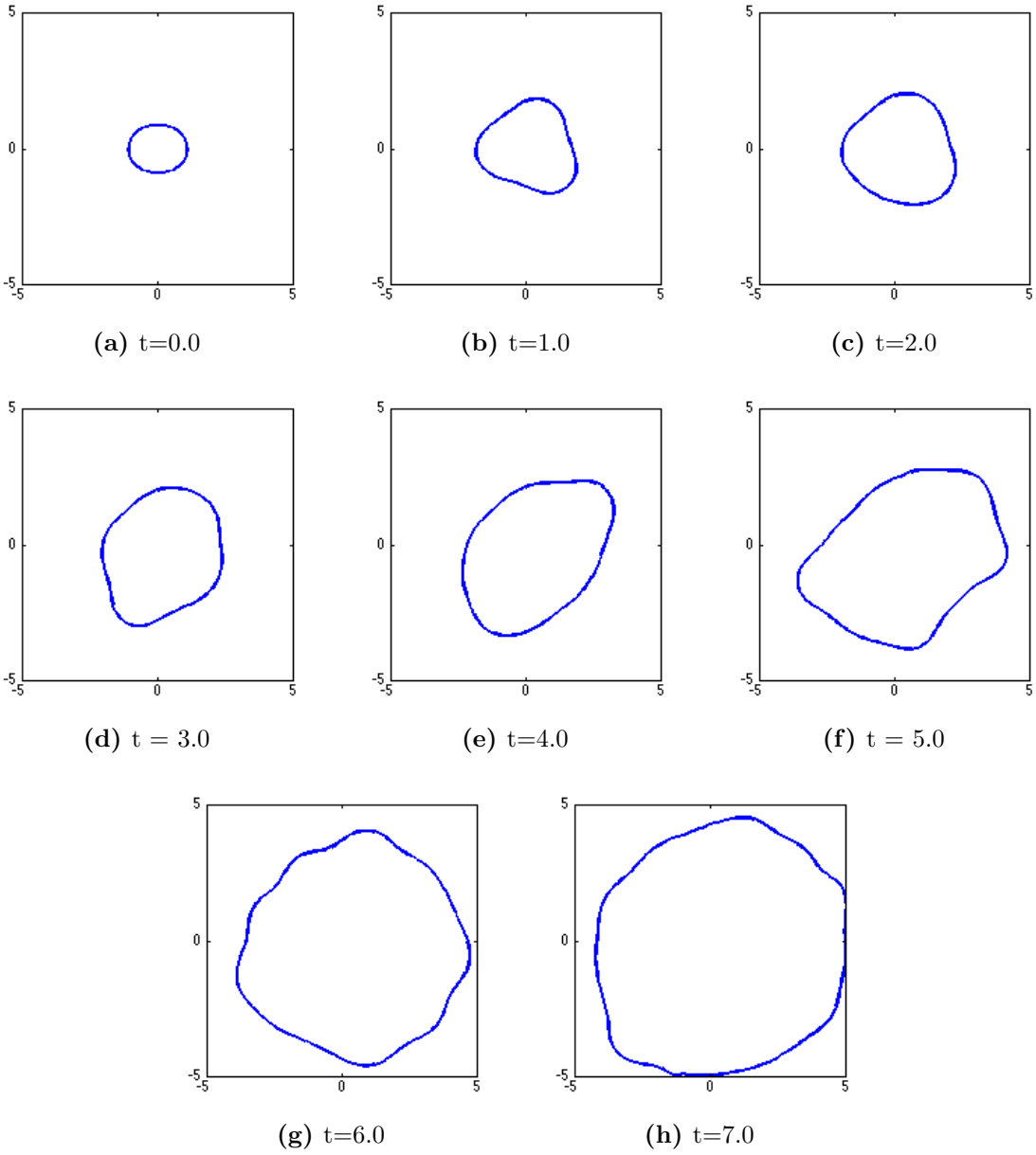

(a) t=0.0 **(b)** t=1.0 **(c)** t=2.0

(d) t = 3.0 **(e)** t=4.0 **(f)** t = 5.0

(g) t=6.0 **(h)** t=7.0

Figure 4.8: *Plots of the deformations of the interface from time* $t = 1.0$ *to* $t = 6.0$ *coupling the Schnakenberg reaction diffusion system with level-set method. The parameter values are:* $a = 0.1$, $b = 1$, $n = 8$, $m = 4$, $p = q = 1$, $d = 13.0766$, $\gamma = 2176.2$*; in the velocity function for level set method,* $\alpha = 2$,$u_0 = 0.5$ *and* $\tau = 1$.

4.4 Case study 2: The level-set method coupled with a uPA system

This case study will examine an invading cancer by coupling an urokinase plasminogen activation (uPA) system with a moving boundary that is calculated by the level-set method.

4.4.1 Components of the uPA system and their functions

Proteolytic degradation and remodelling of the extracellular matrix is essential for cancer cell invasion. It enables cancer cells to proliferate and migrate through surrounding tissue. Therefore, one of the first steps of invasion is the production and secretion of proteolytic enzymes, i.e., urokinase plasminogen activator (uPA) and matrix metalloproteinases (MMPs) by cancer cells. These enzymes regulate turnover of ECM macromolecules and pave the way for cancer invasion. The enzymatic system mainly consists of the urokinase receptor (uPAR), urokinase plasminogen activator (uPA), the matrix-like protein vitronectin (VN), plasminogen activator inhibitor type1 (PAI-1) and plasmin (a matrix degrading enzyme).

Urokinase plasminogen activator (uPA) uPA is an extracellular serine protease produced from cells. Two major functional domains of the uPA molecule are the protease domain and the growth factor domain. The protease part activates plasminogen and turns it into plasmin, which is able to digest basement membrane and extracellular matrix proteins. The growth factor domain has no protease activity but can bind a specific high affinity cell-surface receptor, uPAR. uPA has a zymogen form, pro-uPA, which can also bind to uPAR. pro-uPA can be activated by plasmin (Chaplain and Lolas, 2005; Andasari et al., 2011).

Urokinase plasminogen activator receptor (uPAR) uPAR is a high affinity cell-surface receptor of uPA (and its zymogen form pro-uPA) and by binding it localises uPA and pro-uPA to the cell surface. Importantly, uPAR contains another binding site for vitronectin, and since the vitronectin and uPA binding sites are distinct, uPAR can simultaneously bind both ligands, allowing coordinated regulation of proteolysis, cell adhesion and signalling.

uPAR expression during ECM remodelling is well controlled under normal conditions, for example, in gestational tissues during embryo implantation and placental development and in keratinocytes during epidermal would healing. uPAR is also expressed in many human cancers. It indicates poor prognosis and in some cases is predictive of invasion and metastasis. Importantly, uPAR expression in tumours can occur in tumour cells and/or tumour-associated stromal cells, such as fibroblasts and macrophages. Moreover, there is crosstalk between ligands-binding of uPA to uPAR enhances vitronectin binding by uPAR (Smith and Marshall, 2010).

Vitronectin (VN) VN is an abundant versatile glycoprotein found in serum and the extracellular matrix and promotes cell adhesion and spreading. Vitronectin binds strongly to glass surfaces, as the name indicates (*vitro* = glass), and it has binding sites for several ligands, including heparin, urokinase plasminogen activator receptor (uPAR), plasminogen activator inhibitor type-1(PAI-1), and integrins, such as $\alpha_v\beta_3$. When vitronectin binds to uPAR, it is thought to bring PAI-1 closer to uPA, thereby promoting inhibition and clearance of uPA from the receptor (Chaplain and Lolas, 2005; Andasari et al., 2011).

Urokinase plasminogen activator Inhibitor-1(PAI-1) One of the inhibitors of urokinase plasminogen activator, PAI-1, belongs to the serpin (serine protein inhibitors) family and it is believed to be the most abundant, fast-acting inhibitor of

uPA *in vivo*. It can specifically bind to soluble and membrane-bound uPA to inhibit plasminogen activation. When PAI-1 binds to the uPA/uPAR complex, it triggers the internalisation of the uPA/uPAR/PAI-1 complex by receptor-mediated endocytosis, meaning that the complex will be dissociated and PAI-1 and uPA will be digested, but the receptor will be recycled to the cell surface. This process helps with the clearance of PAI-1 from the vicinity of the cell surface. Additionally, as a major binding protein of VN, PAI-1 competes with uPAR for binding to VN (Chaplain and Lolas, 2005; Andasari et al., 2011).

Plasmin Plasmin is a widespread enzyme that cleaves many extracellular matrix proteins, such as fibronectin, laminin, vitronectin and thrombospondin. In addition, plasmin can also activate many matrix metalloproteinases (MMPs), enhancing even more the degradation of extracellular matrix. It can also influence the composition of the extracellular environment by affecting the activity of cytokines and growth factors, for example, TGF-beta (Chaplain and Lolas, 2005; Andasari et al., 2011).

Figure 4.9 shows a schematic diagram of the uPA system, which gives a clearer picture of the whole system. The effects of the plasminogen activation system in cell migration may be due to proteolytic as well as non-proteolytic mechanisms. Proteolytic mechanisms help to break physical barriers and promote detachment of the trailing edge of cells from matrix proteins by generating plasmin at focal adhesion sites, catalysed by uPAR-bound uPA. It is possible that a non-proteolytic mechanism works simultaneously in migrating cells, and in this mechanism, uPA is thought to promote cell migration by enhancing adhesion at the leading edge. The reason of this assumption is that binding of uPA to uPAR enhances VN binding by uPAR, as mentioned before.

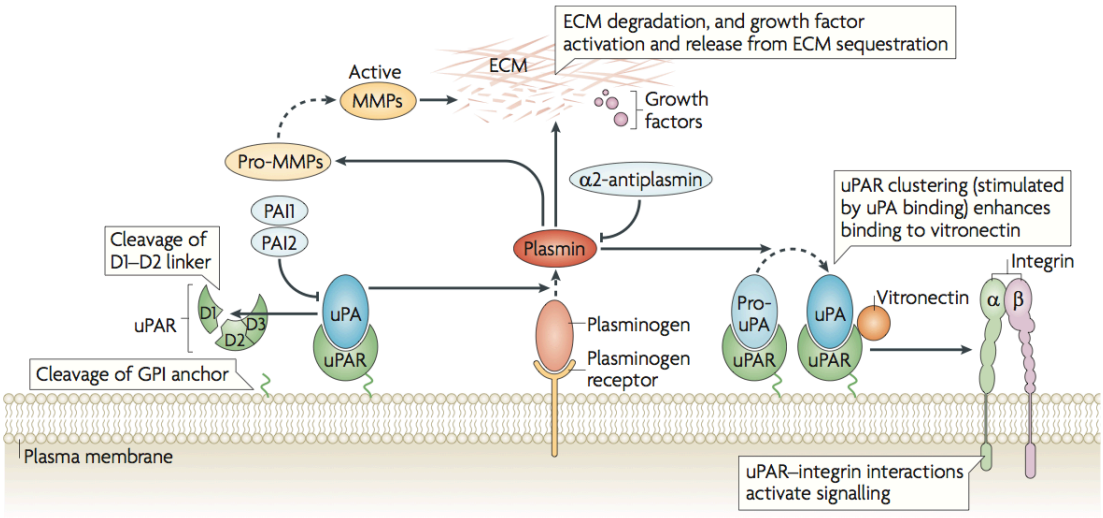

Figure 4.9: *A schematic diagram of the uPA system showing the components of the system and their functions. Copyright permission required (Smith and Marshall, 2010).*

4.4.2 Mathematical multiscale modelling of cancer invasion incorporating the uPA system

In the following descriptions, we denote the cancer cell density by c, the extracellular matrix (ECM, vitronectin) substrate density by v, the urokinase plasminogen activator (uPA) concentration by u, the plasminogen activator inhibitor (PAI-1) concentration by p and the plasmin concentration by m. There is no explicit modelling of uPAR since we assume a fixed average number of uPARs located on each cancer cell's surface. Therefore, the concentration of uPAR is proportional to the cancer cell density. Another important assumption is that the supply of plasminogen is unlimited in this model. Additionally, as well as the biological facts mentioned in the previous section, the following assumptions are made, upon which the mathematical model is built (Chaplain and Lolas, 2005; Andasari et al., 2011):

The cancer cells dynamics It is assumed that cancer cell migration is mainly governed by diffusion, chemotaxis due to uPA and PAI-1 and haptotaxis due to VN and other ECM components. Additionally, a logistic growth law is used to model cancer cell proliferation. Thus, the mathematical equation for cancer cell density is:

$$\frac{\partial c}{\partial t} = \underbrace{D_c \Delta c}_{\text{diffusion}} - \nabla \cdot [\, \underbrace{\chi_u c \nabla u}_{\text{uPA-chemo}} + \underbrace{\chi_p c \nabla p}_{\text{PAI-1-chemo}} + \underbrace{\chi_v c \nabla v}_{\text{VN-hapo}}] + \underbrace{\mu_1 c (1 - \frac{c}{c_0})}_{\text{profieration}}, \tag{4.55}$$

where D_c is the diffusion coefficient of cancer cells, χ_u and χ_p are chemotaxis coefficients relevant to uPA and PAI-1 respectively, VN-mediated haptotaxis rate is χ_v, cancer cell proliferation rate is μ_1, and c_0 is the maximum capacity for cancer cells.

The ECM/VN dynamics Since ECM does not move, we rule out any migration terms from the equation. The degradation of ECM or VN by plasmin upon contact is modelled by the term $-\delta v m$ with a degradation rate δ. This is based on the widely accepted fact that plasmin catalyses the breakdown of VN and other ECM molecules after plasminogen has been activated by the activator, uPA. However, when PAI-1 binds to uPA, it inhibits the activation of plasminogen, in such a way that VN and other ECM molecules are protected and indirectly contributes to their proliferation. This process is modelled by term $\phi_{21} u p$ with binding rate ϕ_{21}. Moreover, PAI-1 also binds to VN, leading to less binding to cell-surface receptors, e.g., uPAR, and then inhibits VN production through the regulation of cell-matrix-associated signal transduction pathways, so we include term $-\phi_{22} v p$ in the equation and ϕ_{21} is the binding rate of PAI-1 and VN. Finally, a logistic growth term describes remodelling of ECM by the cells in the tissue. We therefore have the equation as below:

$$\frac{\partial v}{\partial t} = -\underbrace{\delta v m}_{\text{degradation}} + \underbrace{\phi_{21} u p}_{\text{uPA/PAI-1}} - \underbrace{\phi_{22} v p}_{\text{PAI-1/VN}} + \underbrace{\mu_2 v (1 - \frac{v}{v_0})}_{\text{proliferation}}. \tag{4.56}$$

The uPA dynamics The evolution of uPA concentration is more straightforward than that of ECM, and consists of diffusion, a source term from production by the cancer cells, removal from the system due to binding with PAI-1 and uPAR, which yields,

$$\frac{\partial u}{\partial t} = \underbrace{D_u \Delta u}_{\text{diffusion}} - \underbrace{\phi_{31} p u}_{\text{uPA/PAI-1}} - \underbrace{\phi_{33} c u}_{\text{uPA/uPAR}} + \underbrace{\alpha_{31} c}_{\text{production}}, \tag{4.57}$$

where D_u is the diffusion coefficient, ϕ_{31} and ϕ_{33} are binding rates of uPA/PAI-1 and uPA/uPAR accordingly and α_{31} the rate of production by cancer cells.

The uPA-1 dynamics Similarly, the equation for PAI-1 simply includes a diffusion term with coefficient D_p, removal caused by binding to uPA and VN with binding rates ϕ_{41} and ϕ_{42} respectively, and production as a result of plasmin formation with coefficient α_{41}. Thus, these assumptions give us:

$$\frac{\partial p}{\partial t} = \underbrace{D_p \Delta p}_{\text{diffusion}} - \underbrace{\phi_{41} p u}_{\text{uPA/PAI-1}} - \underbrace{\phi_{42} p v}_{\text{PAI-1/VN}} + \underbrace{\alpha_{41} m}_{\text{production}}. \tag{4.58}$$

The plasmin dynamics For the evolution of plasmin concentration, we first assume that it diffuses. We also assume that binding of uPA to uPAR provides an opportunity for pericellular proteolytic activity through plasminogen activation leading to plasmin formation. Additionally, binding of PAI-1 to VN indirectly enhances the binding of uPA to uPAR and therefore helps plasmin formation as well. Finally, we include a decay term. Thus, all the assumptions yield,

$$\frac{\partial m}{\partial t} = \underbrace{D_m \Delta m}_{\text{diffusion}} + \underbrace{\phi_{52} pv}_{\text{PAI-1/VN}} + \underbrace{\phi_{53} cu}_{\text{uPA/uPAR}} - \underbrace{\phi_{54} m}_{\text{degradation}} , \tag{4.59}$$

where D_m is the diffusion coefficient, ϕ_{52} and ϕ_{53} are the binding rates of PAI-1/VN and uPAR/uPA accordingly, and ϕ_{54} is the decay rate of plasmin

To sum up, the dimensionless mathematical model of the uPA system held on spacial domain Y and temporal domain T is presented in (4.60) – (4.64) (more details about nondimensionalisation process can be found in Chaplain and Lolas (2005)):

$$\frac{\partial c}{\partial t} = \underbrace{D_c \Delta c}_{\text{diffusion}} - \nabla \cdot [\underbrace{\chi_u c \nabla u}_{\text{uPA-chemo}} + \underbrace{\chi_p c \nabla p}_{\text{PAI-1-chemo}} + \underbrace{\chi_v c \nabla v}_{\text{VN-hapo}}] + \underbrace{\mu_1 c(1-c)}_{\text{profieration}}, \ \mathbf{x} \in Y, \tag{4.60}$$

$$\frac{\partial v}{\partial t} = - \underbrace{\delta v m}_{\text{degradation}} + \underbrace{\phi_{21} up}_{\text{uPA/PAI-1}} - \underbrace{\phi_{22} vp}_{\text{PAI-1/VN}} + \underbrace{\mu_2 v(1-v)}_{\text{proliferation}}, \ \mathbf{x} \in Y, \tag{4.61}$$

$$\frac{\partial u}{\partial t} = \underbrace{D_u \Delta u}_{\text{diffusion}} - \underbrace{\phi_{31} pu}_{\text{uPA/PAI-1}} - \underbrace{\phi_{33} cu}_{\text{uPA/uPAR}} + \underbrace{\alpha_{31} c}_{\text{production}} , \ \mathbf{x} \in Y, \tag{4.62}$$

$$\frac{\partial p}{\partial t} = \underbrace{D_p \Delta p}_{\text{diffusion}} - \underbrace{\phi_{41} pu}_{\text{uPA/PAI-1}} - \underbrace{\phi_{42} pv}_{\text{PAI-1/VN}} + \underbrace{\alpha_{41} m}_{\text{production}} , \ \mathbf{x} \in Y, \tag{4.63}$$

$$\frac{\partial m}{\partial t} = \underbrace{D_m \Delta m}_{\text{diffusion}} + \underbrace{\phi_{52} pv}_{\text{PAI-1/VN}} + \underbrace{\phi_{53} cu}_{\text{uPA/uPAR}} - \underbrace{\phi_{54} m}_{\text{degradation}} , \ \mathbf{x} \in Y,. \tag{4.64}$$

where $t \in T$.

Solutions of the uPA system model in 1D and 2D

In order to investigate the behaviours of our macroscopic dynamics, we solve the mathematical model numerically in both one-dimension and two-dimensions (using the finite element package COMSOL). For the one-dimensional domain, we take $x \in [0, 10]$, and the time interval is [0,500]. The initial conditions we use are the

same as those in Chaplain and Lolas (2005), i.e.,

$$
\begin{aligned}
c(x,0) &= \exp\left(\frac{-x^2}{\varepsilon}\right), && x \in [0,10] \quad \text{and} \quad && \varepsilon > 0, \\
v(x,0) &= 1 - \frac{1}{2}\exp\left(\frac{-x^2}{\varepsilon}\right), && x \in [0,10] \quad \text{and} \quad && \varepsilon > 0, \\
u(x,0) &= \frac{1}{2}\exp\left(\frac{-x^2}{\varepsilon}\right), && x \in [0,10] \quad \text{and} \quad && \varepsilon > 0, \\
p(x,0) &= \frac{1}{20}\exp\left(\frac{-x^2}{\varepsilon}\right), && x \in [0,10] \quad \text{and} \quad && \varepsilon > 0, \\
m(x,0) &= 0, && x \in [0,10], &&
\end{aligned}
\tag{4.65}
$$

where $\varepsilon = 0.01$.

By imposing the initial conditions in this way, we assume that there is a cluster of cancer cells at the beginning and that they have penetrated a short distance into the extracellular matrix while the remaining space is occupied by ECM alone. In addition, we also assume that uPA protease and PAI-1 initial concentrations are proportional to the initial tumour density. The plasmin protease is not yet produced by the cancer cells.

In Figure 4.10, we show the plots of the spatio-temporal evolution of cancer cells invading EMC along with the other components of the model: uPA protease concentration, PAI-1 concentration and plasmin concentration at $t = 0$, $t = 75$,

$t = 150$, $t = 500$ and use the parameter set $\mathscr{P}$ for the system below:

$$\begin{aligned}
&D_n = 3.5 \cdot 10^{-4}, && \chi_u = 3.05 \cdot 10^{-2}, && \chi_p = 3.75 \cdot 10^{-2}, && \chi_v = 2.85 \cdot 10^{-2},\\
&\mu_1 = 0.25, && \delta = 8.15, && \phi_{21} = 0.75, && \phi_{22} = 0.55,\\
&\mu_2 = 0.15, && D_u = 2.5 \cdot 10^{-3}, && \phi_{31} = 0.75, && \phi_{33} = 0.3,\\
&\alpha_{31} = 0.215, && D_p = 3.5 \cdot 10^{-3}, && \phi_{41} = 0.75, && \phi_{42} = 0.55,\\
&\alpha_{41} = 0.5, && D_m = 4.91 \cdot 10^{-3}, && \phi_{52} = 0.11, && \phi_{53} = 0.75,\\
&\phi_{54} = 0.5. && && && && (4.66)
\end{aligned}$$

These plots shows us the spread of the cancer cells into the surrounding tissue in a "wave-like" manner. Since the diffusion coefficient of cancer cells that we are applying is small, so that chemotaxis and haptotaxis are the dominant mechanisms that drive the cancer cells to move. This leads to heterogeneous solutions of the uPA system. However, if we increase the diffusion rate of cancer cells the profiles to the extend that diffusion becomes dominant cell movement mechanism, then the solution of the system will lose heterogeneity.

In the two-dimensional situations, we choose three different shapes for the domain Ω: rectangular, round and "astroid". The initial conditions we use are:

$$\begin{aligned}
n(0,x,y) &= \frac{1}{2} + \frac{1}{2}\tanh(10(y-0.8)), && (x,y) \in \Omega,\\
v(0,x,y) &= \frac{1}{2} - \frac{1}{2}\tanh(10(y-0.8)), && (x,y) \in \Omega,\\
u(0,x,y) &= \frac{1}{4} + \frac{1}{4}\tanh(10(y-0.8)), && (x,y) \in \Omega, \qquad (4.67)\\
p(0,x,y) &= \frac{1}{40} - \frac{1}{40}\tanh(10(y-0.8)), && (x,y) \in \Omega,\\
m(0,x,y) &= 0, && (x,y) \in \Omega.
\end{aligned}$$

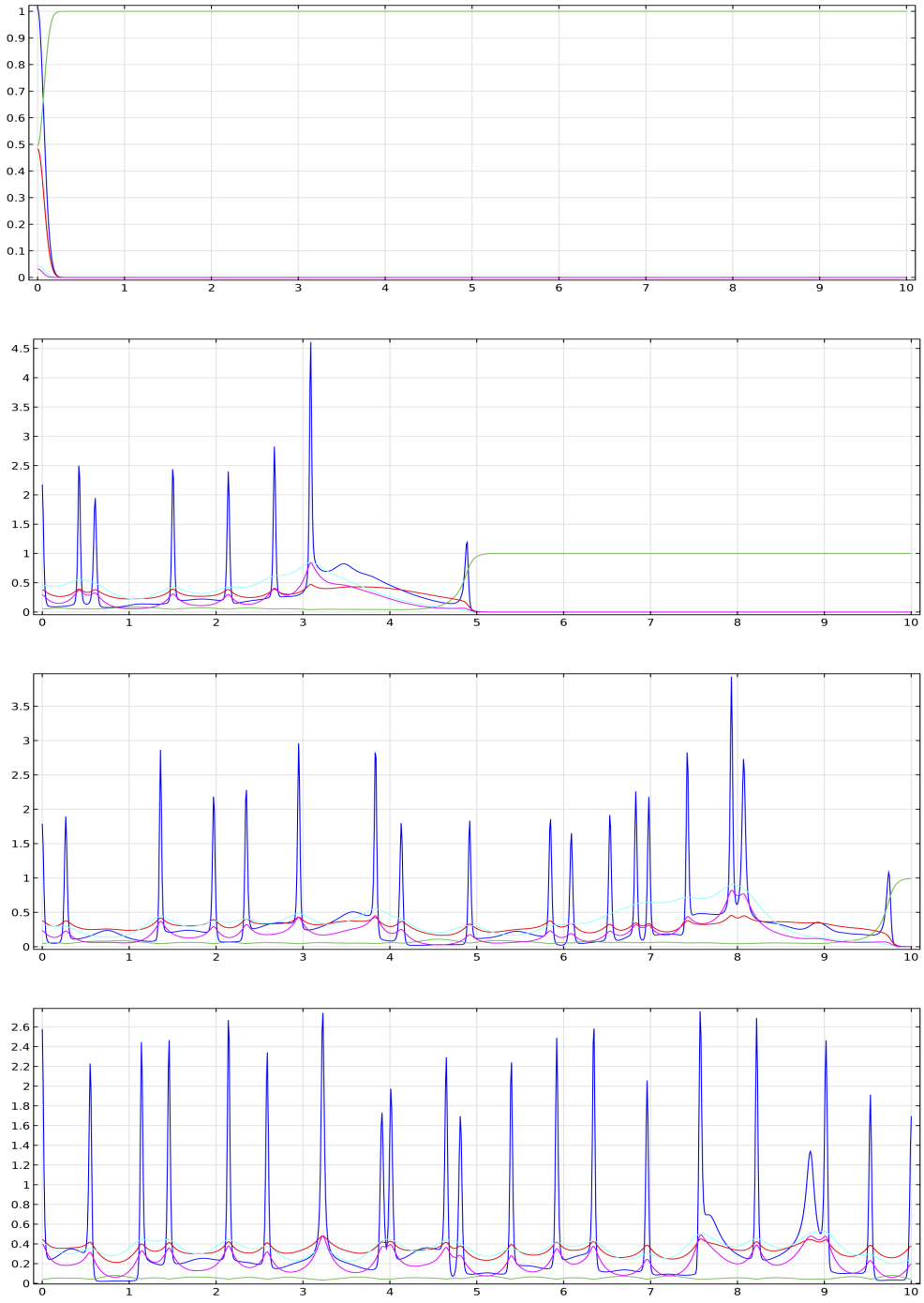

Figure 4.10: *Plots of the spatio-temporal evolution of cancer cell c (solid line) invading EMC v (dotted line) along with the other components of the model: uPA protease concentration u (thin dash-dotted line), PAI-1 concentration p (dashed line) and plasmin concentration m (dash-dotted line) with parameter set mentioned above at* $t = 0$, $t = 75$, $t = 150$, $t = 500$ *respectively.*

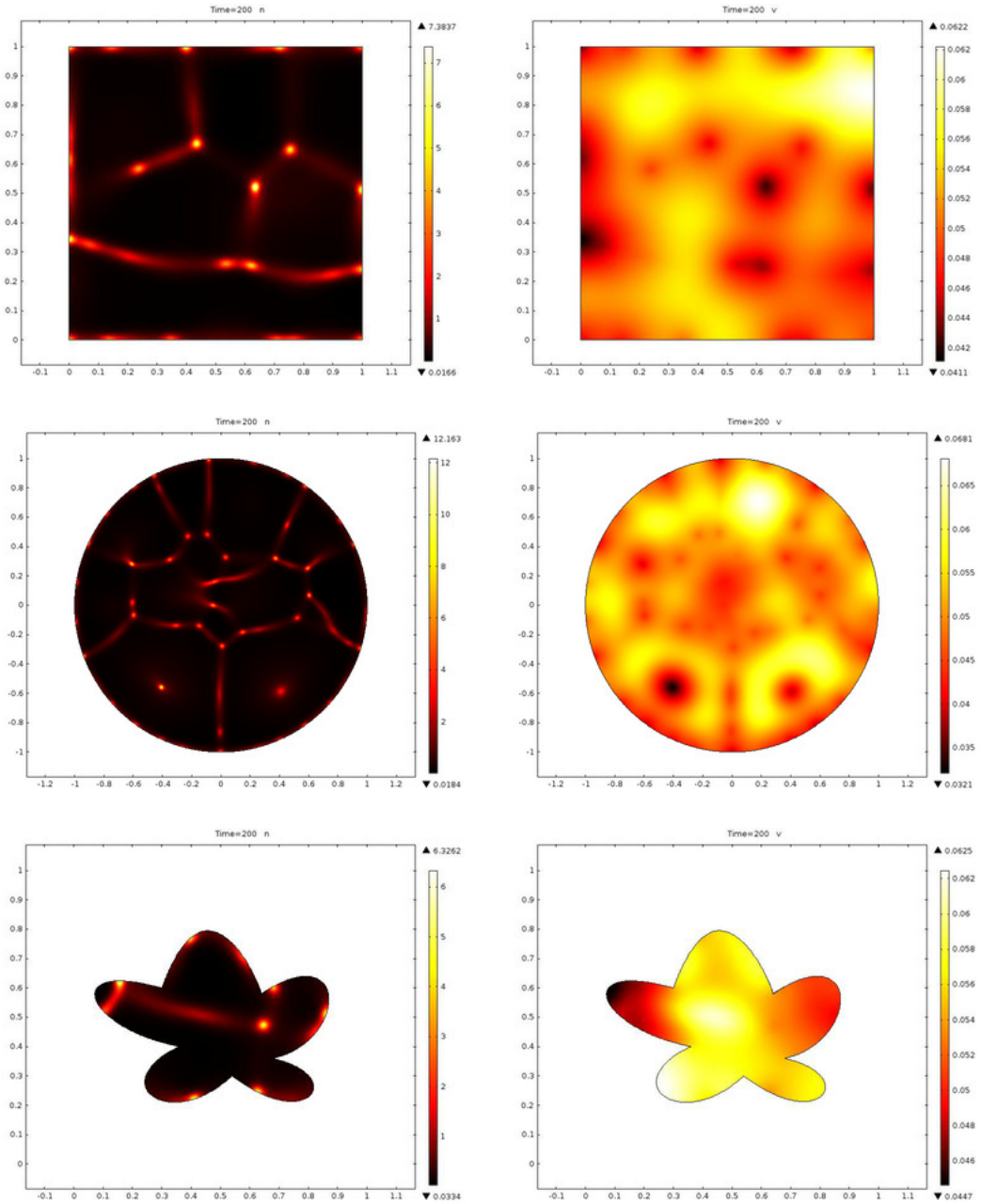

Figure 4.11: *Plots of the distribution of the cancer call n and ECM density v in in different shapes of the domain at time $t = 200$. The parameter settings are mentioned above, parameter set $\mathscr{P}$.*

We use the same parameter set as that for the one-dimensional domain. Figure 4.11 shows the two-dimensional spatio-temporal solutions of the cancer cells and ECM distribution, which renders heterogeneous patterns as we expected.

4.4.3 Incorporating a boundary boundary

In order to define the velocity of cancer cells at the invasion front, we form a group $\partial\mathbf{B}$ that includes all the points in the vicinity of the tumour boundary, i.e., $\partial\mathbf{B} := \{\mathbf{x} : |\phi(\mathbf{x})| \leq R\}$, where $R = 10\Delta x$ is the width of the narrow band around the interface. We assume that if the amount of plasmin $m(x, y)$ at a boundary point $(x, y) \in \partial\mathbf{B}$ is above the mean value (denoted by $\bar{m}$) of plasmin concentration at all the points in $\partial\mathbf{B}$, then the cancer cells at this point will invade the surrounding tissues. Whereas, if the local amount of plasmin $m(x, y)$ is no greater than the mean value, the velocity of the cancer cells at that point is zero. Therefore, we model the velocity function on point $(x, y) \in \partial\mathbf{B}$ at time t as bellow:

$$F(x,y,t) = \begin{cases} \alpha(m(x,y,t) - \bar{m})/(\max_{(x,y)\in\partial\mathbf{B}} m(x,y,t)), & \text{if } m(x,y,t) > \bar{m}, \\ \\ 0, & \text{if } m(x,y,t) \leq \bar{m}. \end{cases} \tag{4.68}$$

where $\bar{m}$ is the mean value of plasmin concentration in the vicinity of the boundary and α is a positive constant.

4.4.4 Computational simulations

We solve the model in a rectangular region $Y := [0, 4] \times [0, 4]$ and assume that the cancer initially occupies a region $\Omega(0)$ within Y, taken to be a disc centred at $(2, 2)$ with radius $r = 0.5$. The mesh size is $\Delta x = \Delta y = 0.01325$. The initial conditions

for the uPA system are:

$$c(x,0) = \frac{\exp\big(-\frac{||x-(2,2)||_2^2}{\sqrt{\Delta x \Delta y}}\big) - \exp\big(-\frac{(1-\Delta x)(1-\Delta y)}{\sqrt{\Delta x \Delta y}}\big)}{2}, \qquad x \in \Omega(0)$$
$$v(x,0) = \frac{1 + 0.3\sin\left(4\pi||x||_2\right) + \sin\left(4\pi||(4,0)-x||_2\right)}{2}, \qquad x \in Y$$

$$u(x,0) = 1 - \frac{1}{2}c(x,0), x \in Y \tag{4.69}$$
$$p(x,0) = \frac{1}{2}c(x,0), \qquad x \in Y$$
$$m(x,0) = \frac{1}{20}c(x,0), \qquad x \in Y$$

Figure 4.12 shows the initial distribution of cancer cells and ECM of the uPA system.

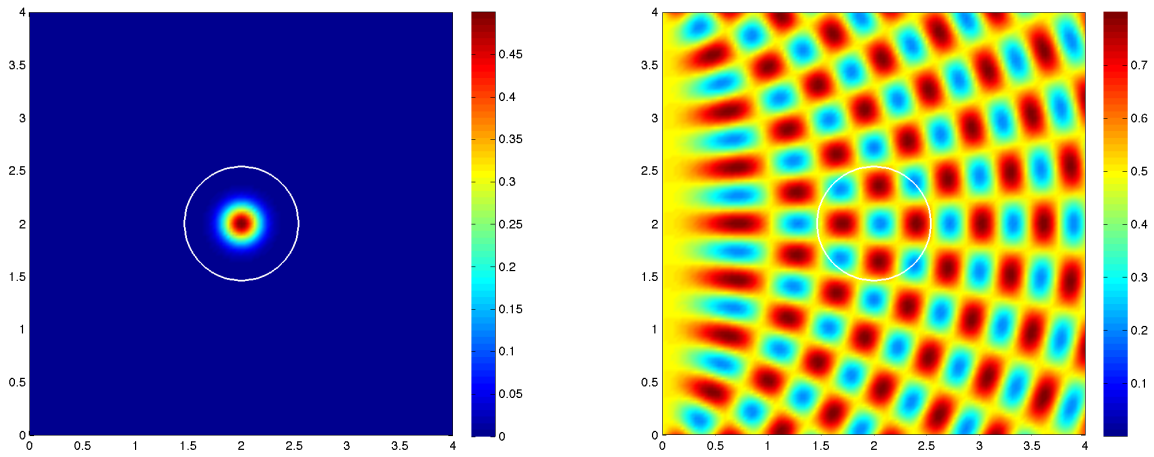

Figure 4.12: *Initial distributions of cancer cells (left column) and ECM (right column) and the invasive boundary of the tumour (white line).*

We use the first order of CFL condition for this two-dimensional case to calculate

the time step Δt for the next stage, i.e.,

$$\Delta t = \frac{\Delta x \Delta y}{\max(F)\Delta x + \max(F)\Delta y},$$

where F is the velocity function in equation (4.68). We can simplify the expression of Δt and write it as $\Delta t = \Delta x/2\max(F)$ when $\Delta x = \Delta y$. In order to obtain solutions of the uPA system we apply a finite difference scheme presented in Appendix 8.1.

The value of α in equation (4.68) controls the velocity of the boundary. For the following simulation results we use $\alpha = 5$ and $\alpha = 10$. Since in the normal velocity function (4.68) we do not include curvature-dependent terms, there is no need to use Gaussian smoothing to remove the small perturbations in the level-set function here.

Figures 4.13 to 4.18 show the simulation results of the evolution of the invasive boundary of the tumour, and distributions of cancer cells and ECM from time stages $t = 10$ to $t = 120$ with $\alpha = 5$. Figures 4.19 to 4.22 show the simulation results of the evolution of the invasive boundary of the tumour, and distributions of cancer cells and ECM from time stages $t = 10$ to $t = 80$ with $\alpha = 10$.

From these simulation results, we can see that the heterogeneity of the uPA system and the formulation of the velocity function presented above work very well together to model the interactions between cancer cells and the surrounding tissue and the deformations of the invasive tumour boundary. The parameter α introduced in (4.68) not only influences the speed of cancer cell migration but also the morphology of the tumour during its invasion and spread.

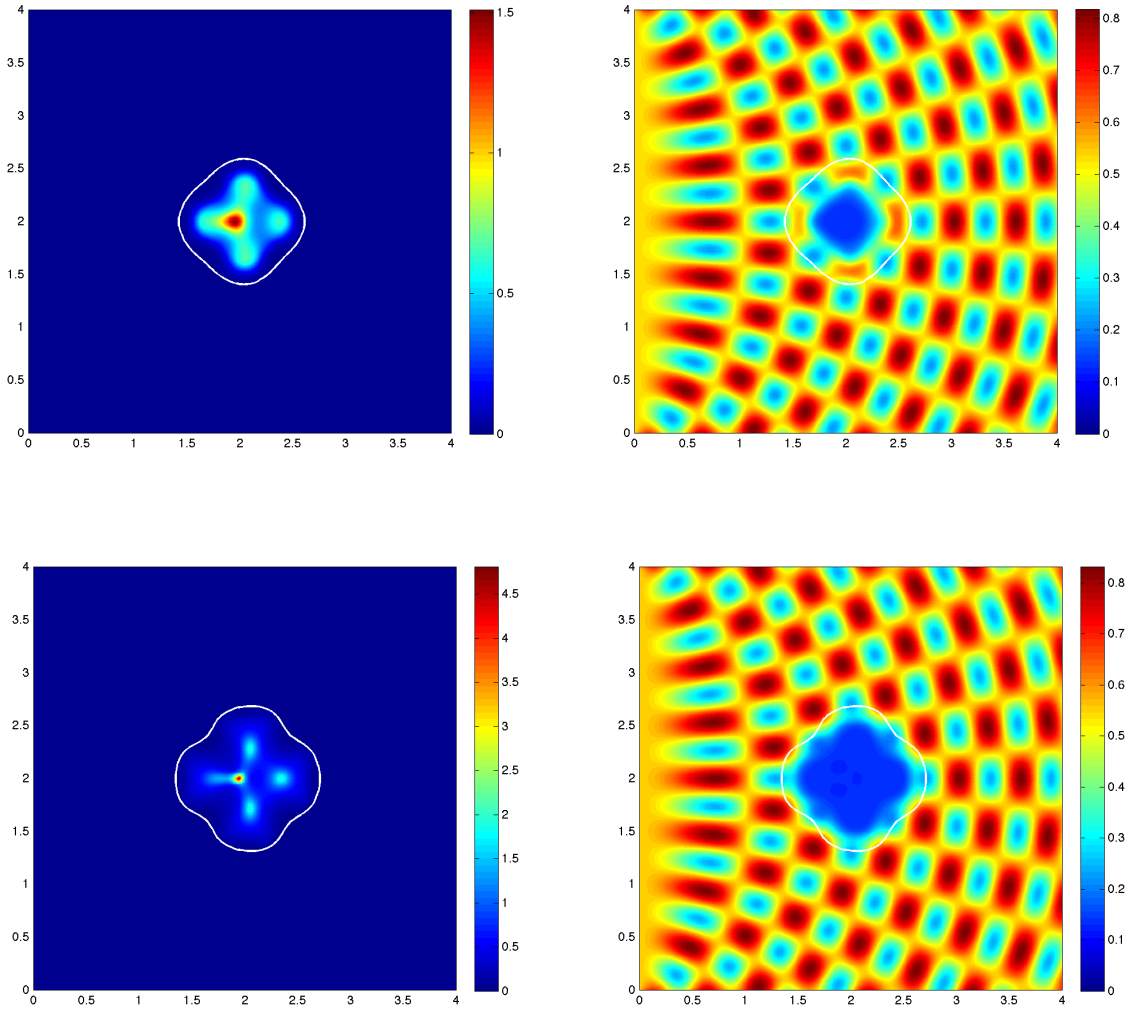

Figure 4.13: *Simulation results showing distributions of cancer cells (left column) and ECM (right column) and the invasive boundary of the tumour (white line) at time stages: Stage 10, 20. Parameter settings are as in* (5.49), $\alpha = 5$ *in* (4.68).

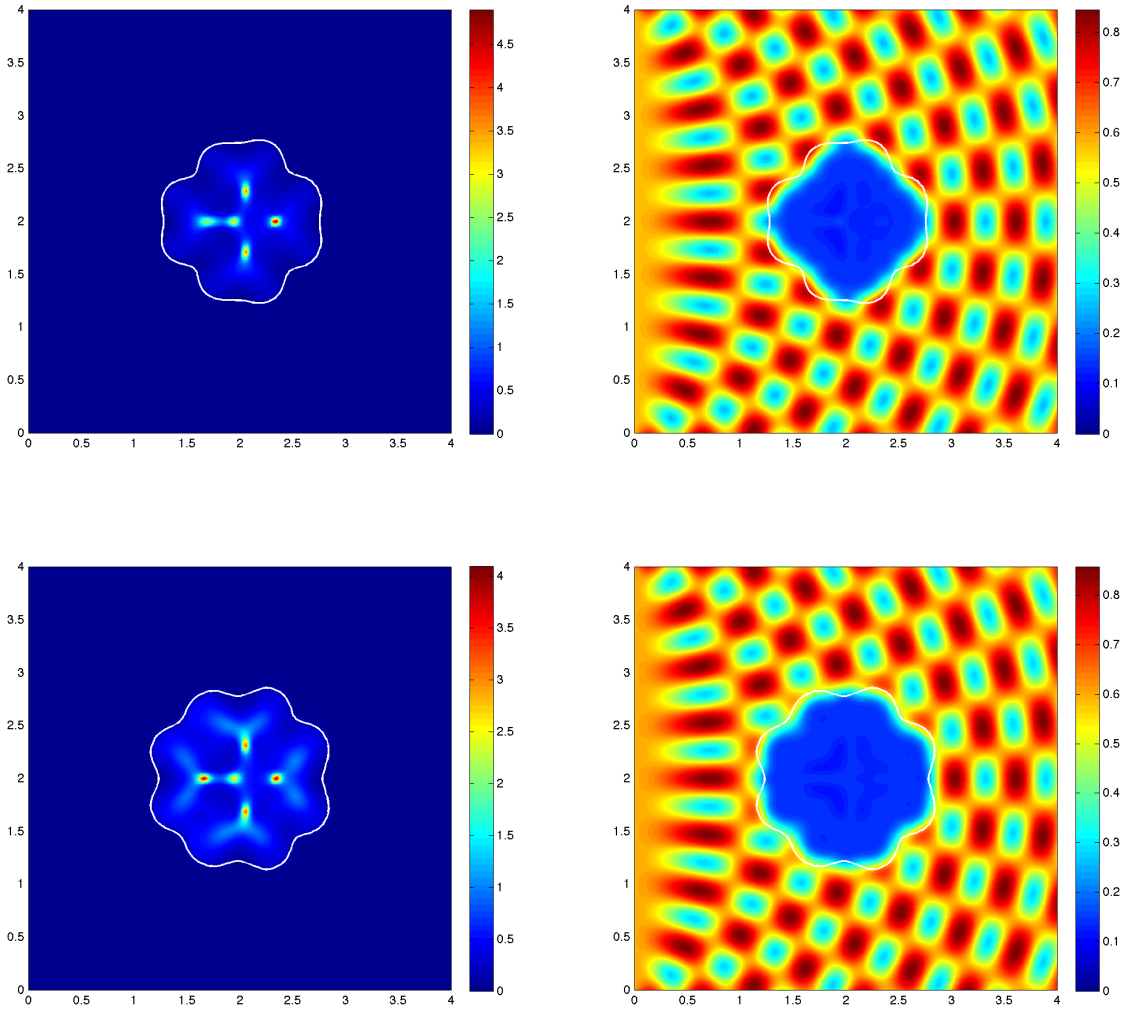

Figure 4.14: *Simulation results showing distributions of cancer cells (left column) and ECM (right column) and the invasive boundary of the tumour (white line) at time stages: Stage 30,40.Parameter settings are as in* (5.49), $\alpha = 5$ *in* (4.68).

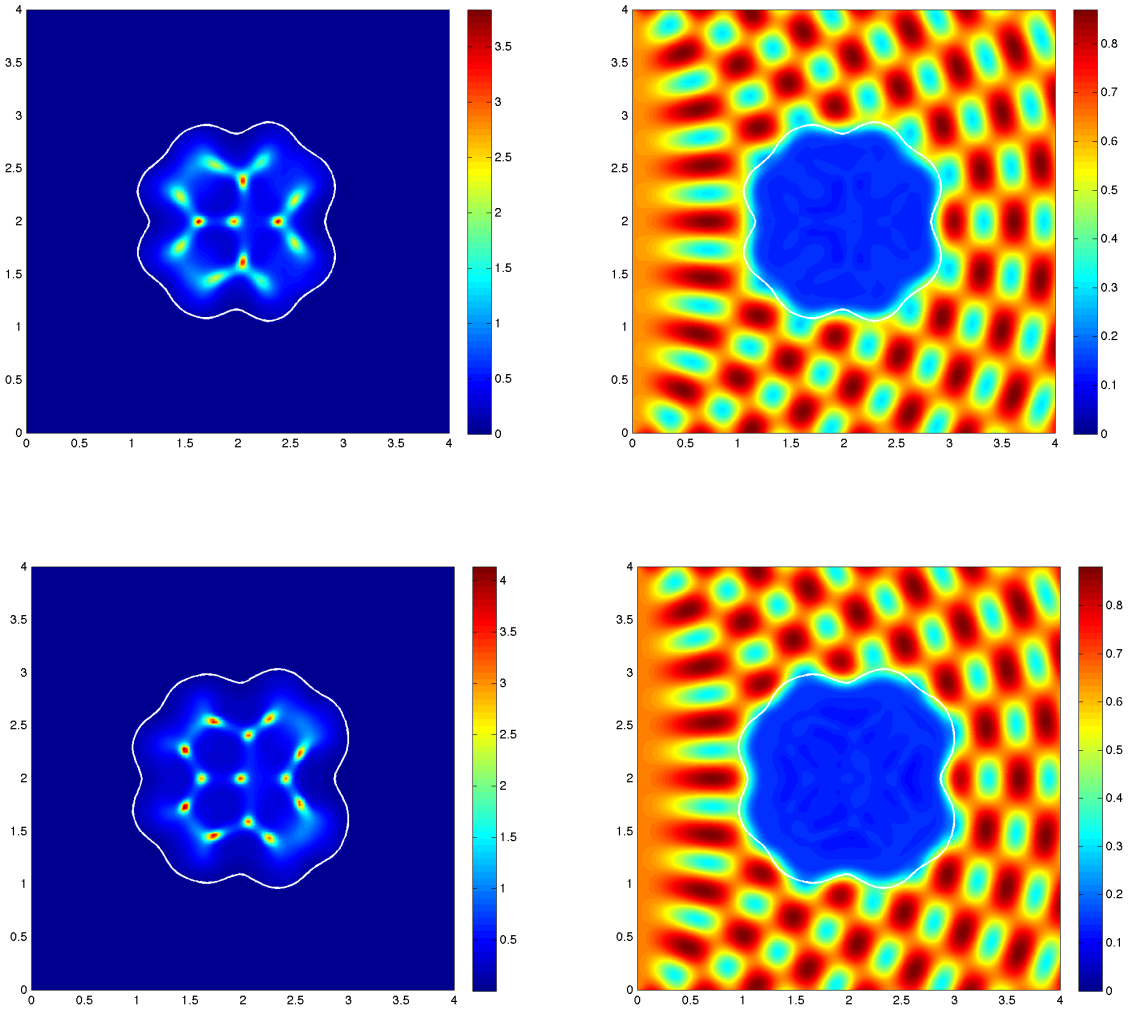

Figure 4.15: *Simulation results showing distributions of cancer cells (left column) and ECM (right column) and the invasive boundary of the tumour (white line) at time stages: Stage 50, 60. Parameter settings are as in* (5.49)*,* $\alpha = 5$ *in* (4.68)*.*

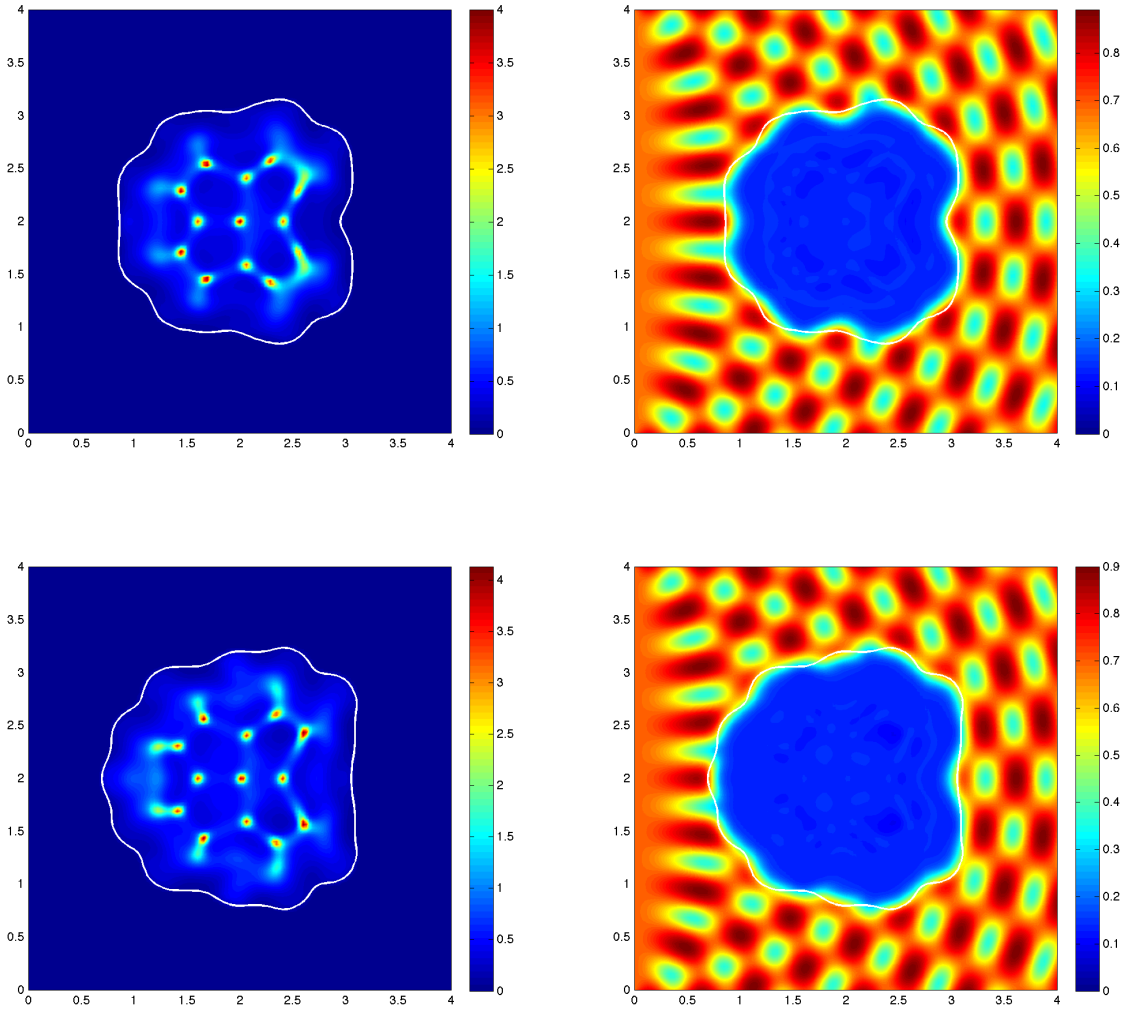

Figure 4.16: *Simulation results showing distributions of cancer cells (left column) and ECM (right column) and the invasive boundary of the tumour (white line) at time stages: Stage 70, 80. Parameter settings are as in* (5.49), $\alpha = 5$ *in* (4.68).

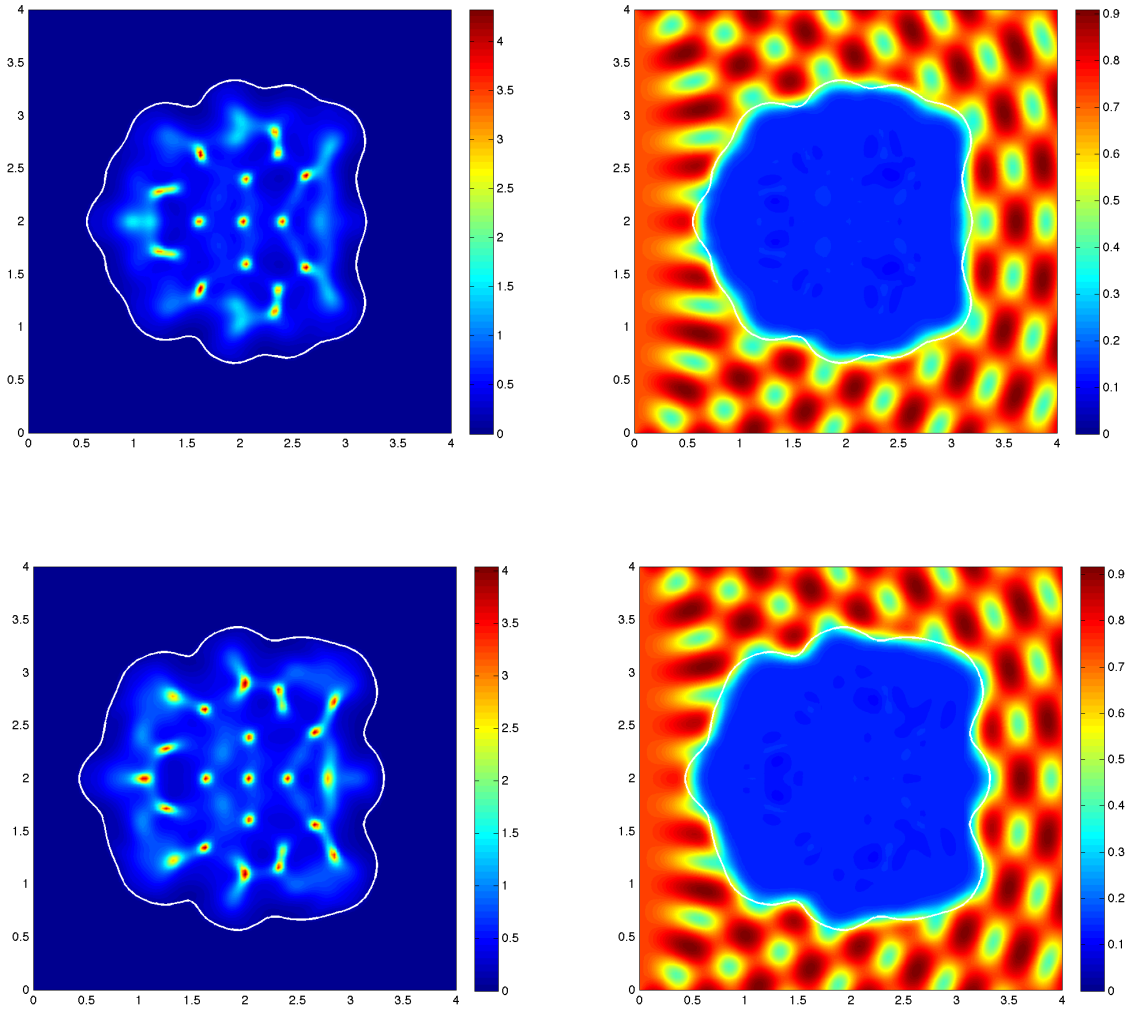

Figure 4.17: *Simulation results showing distributions of cancer cells (left column) and ECM (right column) and the invasive boundary of the tumour (white line) at time stages: Stage 90, 100. Parameter settings are as in* (5.49), $\alpha = 5$ *in* (4.68).

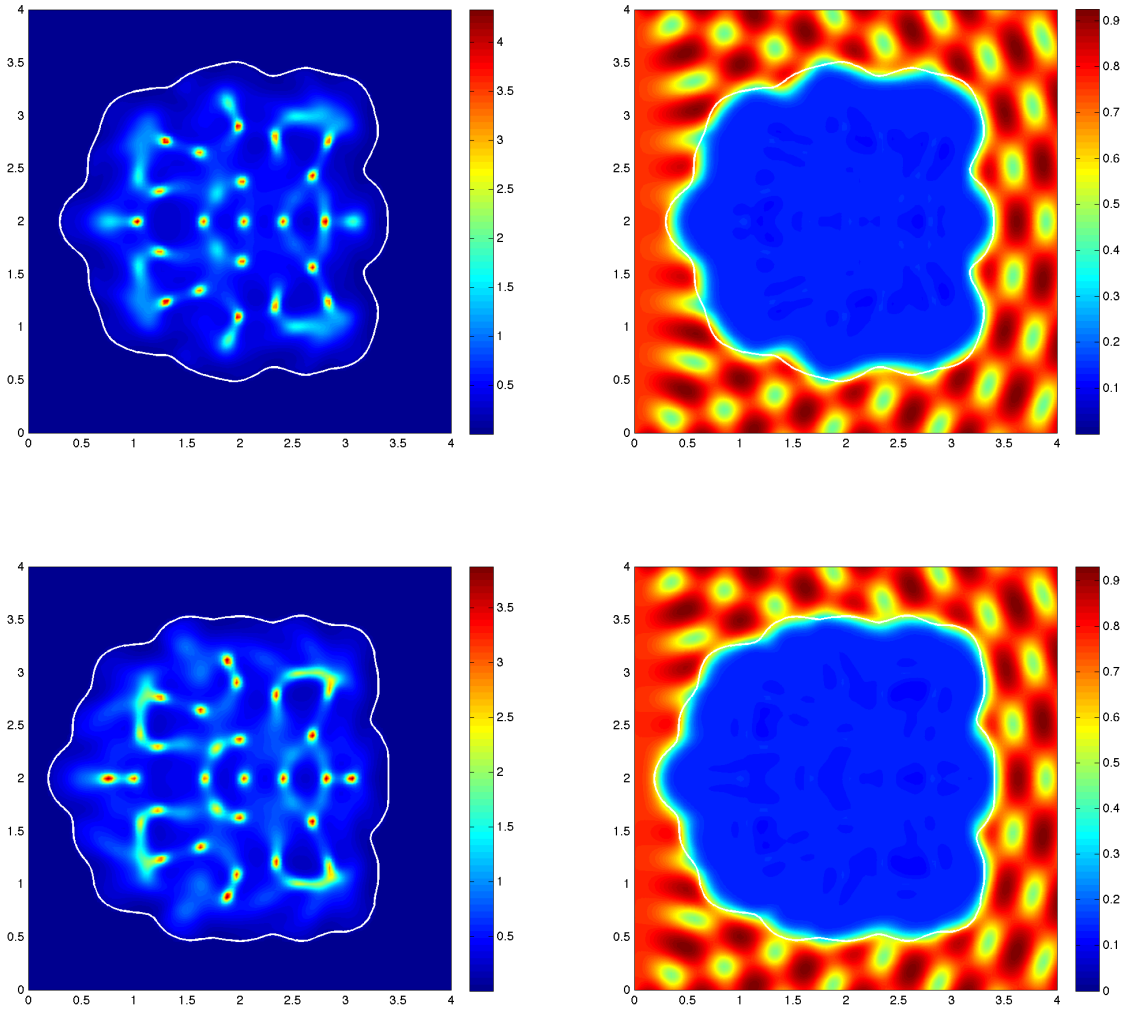

Figure 4.18: *Simulation results showing distributions of cancer cells (left column) and ECM (right column) and the invasive boundary of the tumour (white line) at time stages: Stage 110, 120. Parameter settings are as in* (5.49), $\alpha = 5$ *in* (4.68).

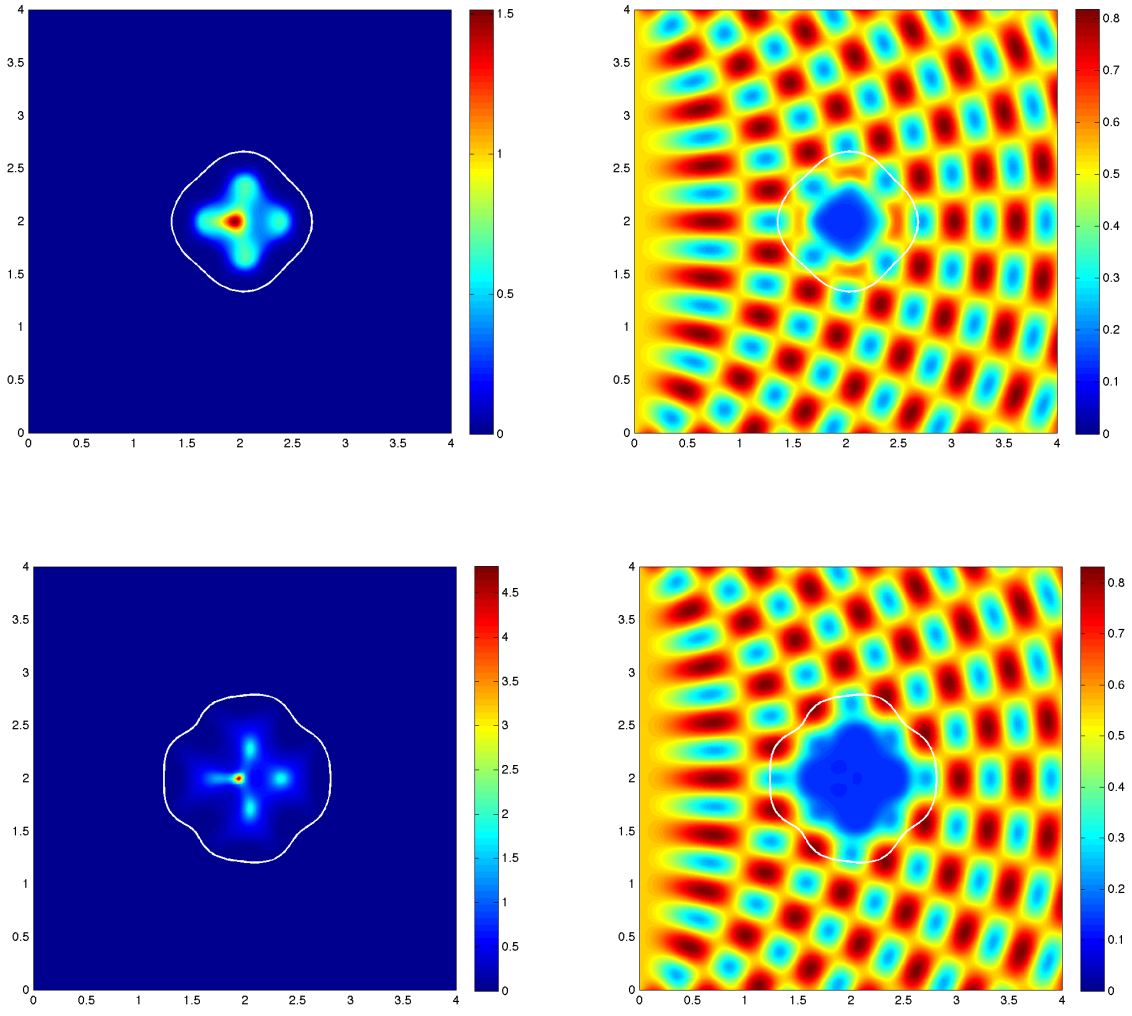

Figure 4.19: *Simulation results showing distributions of cancer cells (left column) and ECM (right column) and the invasive boundary of the tumour (white line) at time stages: Stage 10, 20.Parameter settings are as in* (5.49), $\alpha = 10$ *in* (4.68).

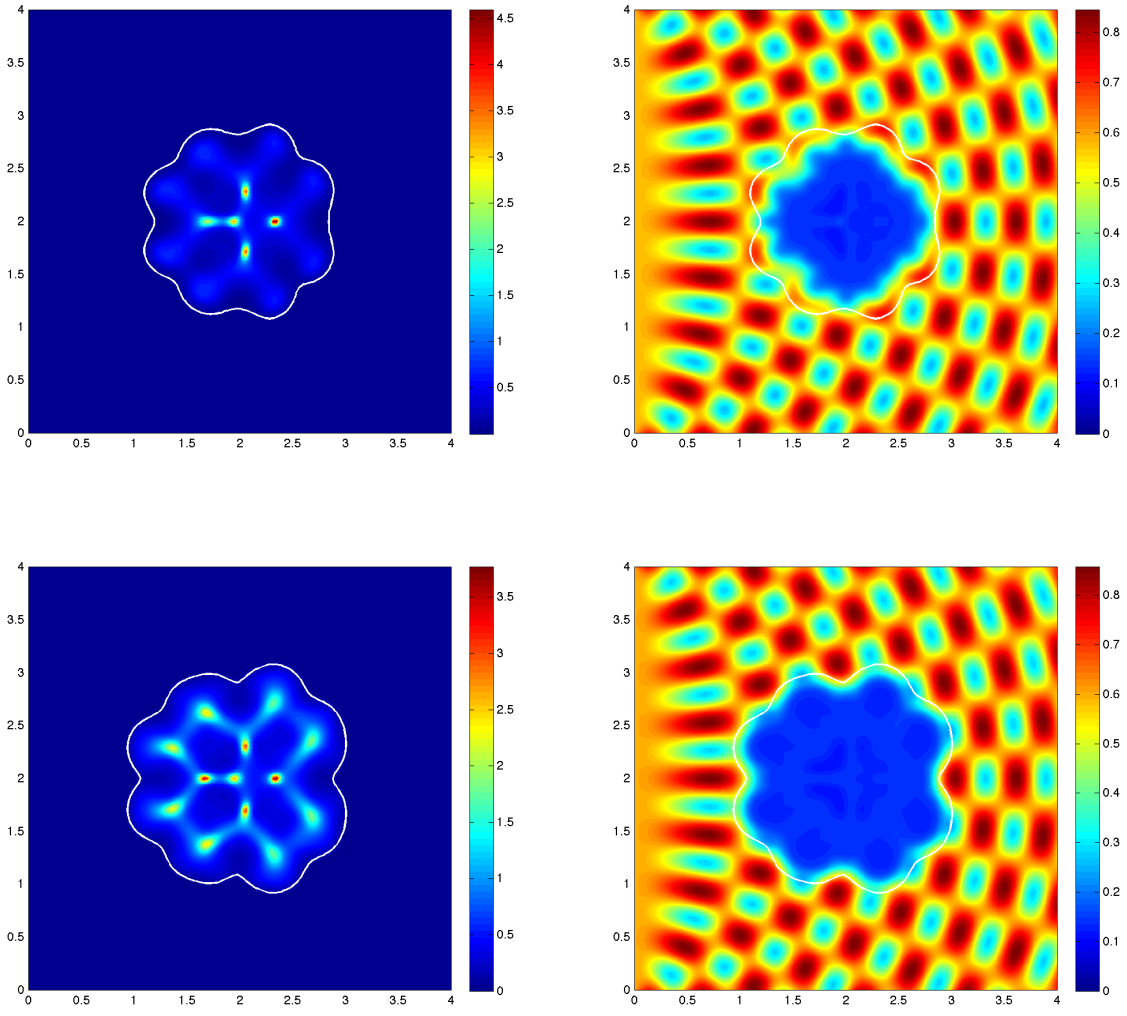

Figure 4.20: *Simulation results showing distributions of cancer cells (left column) and ECM (right column) and the invasive boundary of the tumour (white line) at time stages: Stage 30,40.Parameter settings are as in* (5.49), $\alpha = 10$ *in* (4.68).

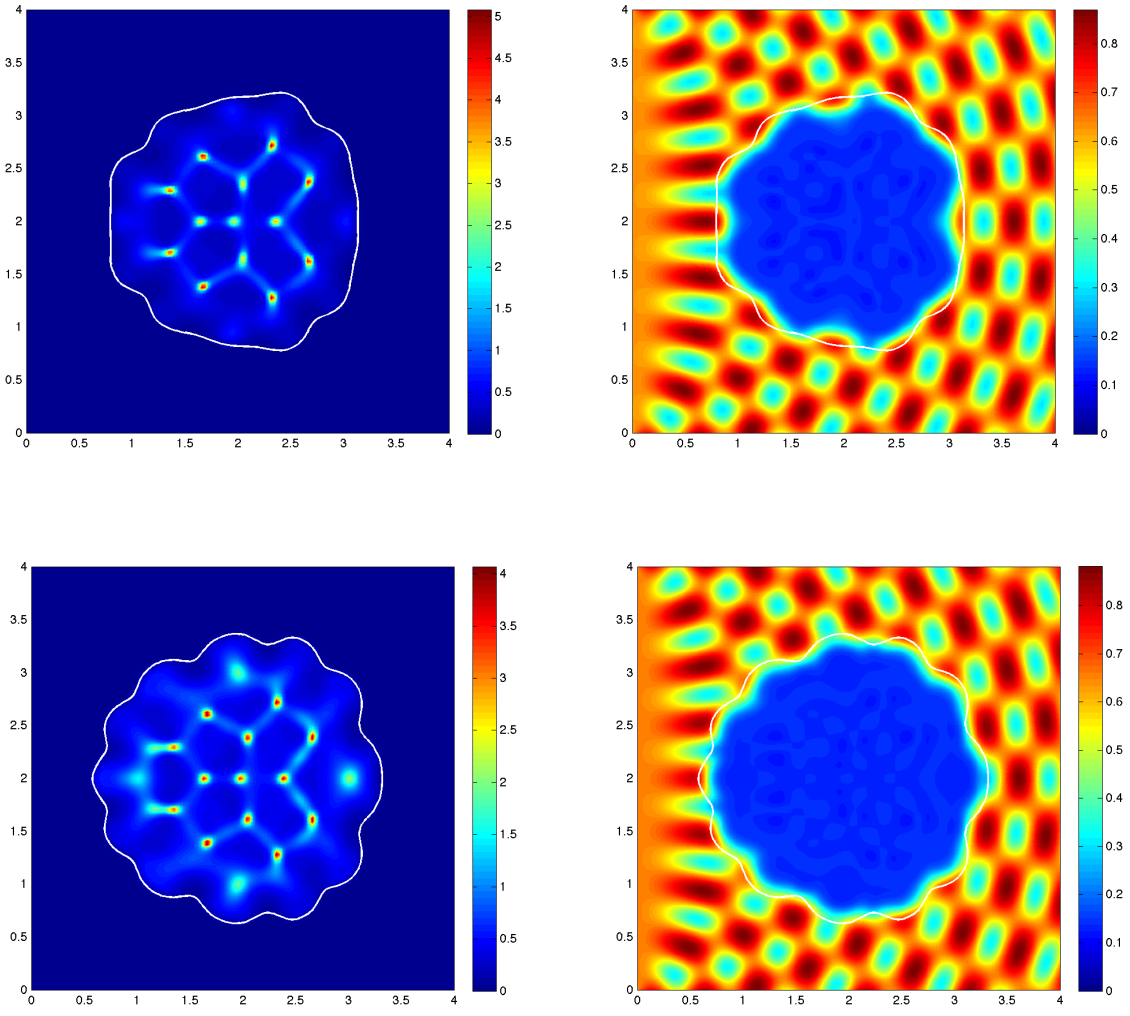

Figure 4.21: *Simulation results showing distributions of cancer cells (left column) and ECM (right column) and the invasive boundary of the tumour (white line) at time stages: Stage 50, 60. Parameter settings are as in* (5.49), $\alpha = 10$ *in* (4.68).

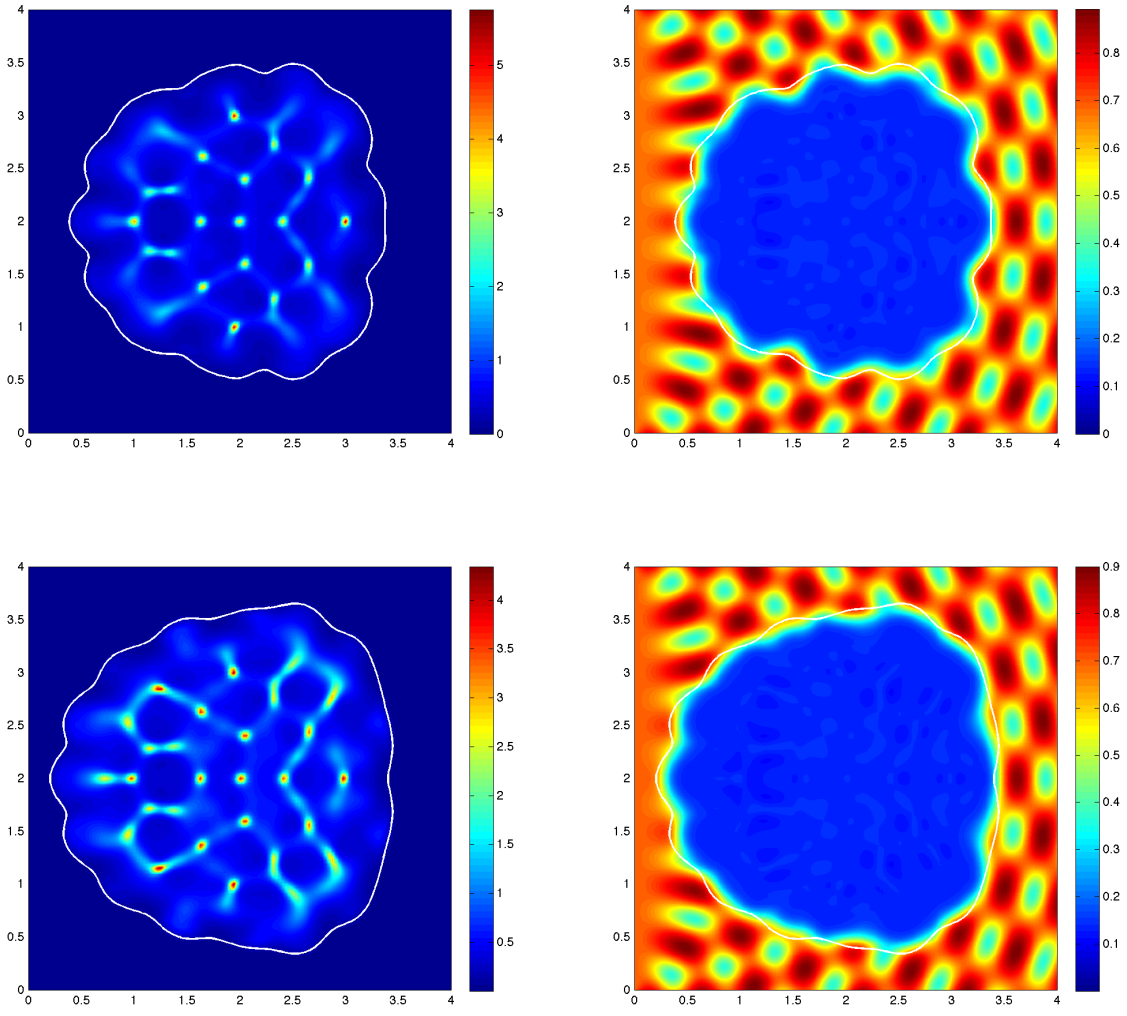

Figure 4.22: *Simulation results showing distributions of cancer cells (left column) and ECM (right column) and the invasive boundary of the tumour (white line) at time stages: Stage 70, 80.Parameter settings are as in* (5.49), $\alpha = 10$ *in* (4.68).

4.5 Discussion

In this chapter, we studied and used a level-set method coupled with two PDE systems. The modelling concept is that we use the heterogeneous patterns of the solutions of PDE systems to describe the dynamics of tumour cells, and apply the level-set method to calculate the position of the moving boundary of the tumour.

The first PDE system we used as a test was a reaction-diffusion system called the Schnakenberg system. In order to obtain a heterogeneous pattern formation, we analysed the linear stability of the steady state of the system and derived the conditions for diffusion-driven instability. Then we formulated a velocity function under the assumption that if the force generated by the growing population of one species in the system overcomes the surface tension of the boundary (which is proportional to the curvature of the interface), then the boundary of the tumour deforms. However, in this case, the curvature-dependent term is the main reason for the instability of the interface. We re-iterate that this is a test model, and we do not consider the biological relevance in this model. In the second PDE system, the uPA system, we model the interactions between cancer cells, ECM, the urokinase plasminogen activator (uPA), uPA inhibitors, and the ECM degrading enzyme plasmin. The system models the pericellular proteolytic activities which determine cancer cell migration and invasion. The formulation of the velocity function applied in the level-set technique only depended on the dynamics of the distribution of plasmin (the ECM degrading enzyme), and not on the curvature of the boundary.

Comparing the simulation results of the two test models, we conclude that a model of cancer invasion does not necessarily have to include a curvature-dependent term in the level-set method in order to model the deformations of the boundary. The heterogeneous dynamics of the uPA system alone can drive the deformations of the tumour boundary, which can exhibit a more fingering morphology seen in

pathological cases, and from experimental data.

Chapter 5

Multiscale modelling of cancer invasion: a moving boundary macro-microscopic technique

5.1 Introduction

In this chapter we study and extend a novel multiscale moving boundary modelling technique and method proposed by Trucu et al. (2013), which is very helpful and robust for multiscale mathematical PDE systems with a moving boundary. We call it a macro-microscopic technique according to its ability to deal with problems at both a macro-level and a micro-level. The formulation of the method was motivated by the complicated multiscale biological phenomenon: cancer invasion of tissue. Therefore we present and introduce the method with a general two-scale mathematical model of cancer invasion. Moreover, we extend the numerical technique by coupling the two-scale method with an enzymatic system, i.e. the urokinase plasminogen activation (uPA) system (Chaplain and Lolas, 2005; Andasari et al., 2011). This also helps us

investigate the properties of the two-scale technique.

In the following sections, first of all, some important notations and considerations will be presented in order to describe this multiscale technique. Then in the third section, we introduce the macro-microscopic method and its application to a basic cancer invasion model. In Section 5.5 we focus on computational schemes where an overall algorithm flow will be found as well. Section 5.4 will introduce the extension of the macro-microscopic technique and the properties of the two-scale method will be examined using the uPA system as a specific example. The chapter concludes with a discussion section.

5.2 Notation

In order to present the technique clearly with all the details (Trucu et al., 2013), in this section, before giving a full description of the numerical methods used at the micro- and macro-scale and the link between these two, we introduce first the necessary notations that will be referred to in the following sections (and chapters), as well as the relevant considerations and explanations.

It is assumed that the domain within which the cancer and extracellular matrix exists is a maximal reference spatial cube $Y \subset \mathbb{R}^N (N = 2, 3)$ with its centre at the origin. Given a fixed ϵ representing a negative power of 2 (*i.e.*, $0 < \epsilon < 1$), the initial Y is uniformly decomposed ϵ-size cubes, ϵY, whose union will be referred to as an ϵ-resolution of Y. For any ϵY from the decomposition, the "half-way shifted" cubes in the direction $i\bar{e}_1+j\bar{e}_2+k\bar{e}_3$ given by any triplet $(i, j, k) \in \{(i, j, k)|i, j, k \in \{-1, 0, 1\}\}$ are defined as

$$\epsilon Y_{\frac{i}{2},\frac{j}{2},\frac{k}{2}} = \epsilon Y + \frac{\epsilon(i\bar{e}_1 + j\bar{e}_2 + k\bar{e}_3)}{2}, \tag{5.1}$$

where,

$$\bar{e}_1 := e_1, \qquad \bar{e}_2 := e_2, \qquad \text{and,} \qquad \bar{e}_3 := \begin{cases} e_3 & \text{for} \quad N = 3, \\ 0 & \text{for} \quad N = 2, \end{cases} \tag{5.2}$$

and $\{e_1, e_2, e_3\}$ is the standard Euclidean basis of $\mathbb{R}^3$. The family of all these $\epsilon-$cubes is denoted by $\mathcal{F}$, i.e.,

$$\mathcal{F} := \bigcup_{i,j,k \in \{-1,0,1\}} \left\{ \epsilon Y_{\frac{i}{2},\frac{j}{2},\frac{k}{2}} \middle| \epsilon Y \text{ is in the } \epsilon\text{-resolution of } Y \right\}. \tag{5.3}$$

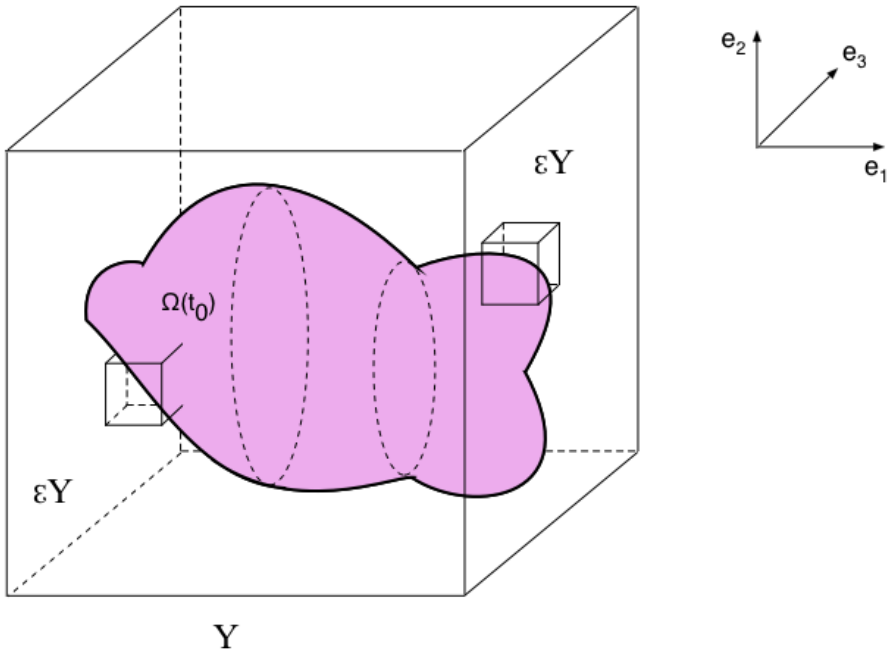

Figure 5.1: *Schematic diagram showing the cubic region Y centred at the origin $\in \mathbb{R}^3$. The dashed blue lines represent the Euclidean directions $\{e_1, e_2, e_3\}$, the pink region illustrates the cancer cluster $\Omega(t_0)$, and the solid blue line represents the family of microscopic cubic domains ϵY placed at the boundary $\partial\Omega(t_0)$.*

For any fixed time t_0, we denote the cancer affected region within Y by $\Omega(t_0)$. Therefore the cancer cell and extracellular matrix distributions can be written as $c_{\Omega(t_0)}(x,t)$ and $v_{\Omega(t_0)}(x,t)$ respectively. For simplicity, we will just use $c(x,t)$ and

$v(x,t)$ in the following context. In Figure 5.1, the notations mentioned so far are illustrated schematically.

In order to capture mathematically the microdynamics that occur in a cell-scale neighbourhood of the tumour boundary $\partial\Omega(t_0)$, out of the initial family $\mathcal{F}$, we will focus our attention of the subfamily denoted by $\mathcal{F}_{\Omega(t_0)}$ which consists of only the $\epsilon-$cubes that cross the interface $\partial\Omega(t_0)$ and have exactly one face included in the interior of $\Omega(t_0)$, namely

$$\begin{aligned}\mathcal{F}_{\Omega(t_0)} := \{\epsilon Y \in \mathcal{F} | \epsilon Y \cap (Y \backslash \Omega(t_0)) \neq \emptyset, \\ \text{and } \epsilon Y \text{ has only one face included in int}(\Omega(t_0))\},\end{aligned} \tag{5.4}$$

where $\text{int}(\Omega(t_0))$ is the topological interior of $\Omega(t_0)$ with respect to the natural topology on $\mathbb{R}^N$. In this context, for each $\epsilon Y \in \mathcal{F}_{\Omega(t_0)}$, we have the following face-notations:

$$\begin{cases} \Gamma_{\epsilon Y}^{int} \text{ denotes the face of } \epsilon Y \text{ that is included in int}(\Omega(t_0)), \\ \Gamma_{\epsilon Y}^{j,\perp}, j = 1, ..., 2^{N-1}, \text{ denote the faces of } \epsilon Y \text{ that are perpendicular to } \Gamma_{\epsilon Y}^{int} \\ \Gamma_{\epsilon Y}^{\parallel} \text{ denotes the face of } \epsilon Y \text{ that is parallel to } \Gamma_{\epsilon Y}^{int}. \end{cases} \tag{5.5}$$

These are illustrated schematically in Figure 5.2.

Furthermore, for each $\epsilon Y \in \mathcal{F}_{\Omega(t_0)}$, the topological closure of the only connected component of $\Omega(t_0) \cap \epsilon Y$ that is confined between $[\partial\Omega(t_0)]_{\epsilon Y}$ and $\Gamma_{\epsilon Y}^{int}$ is denoted by $[\Omega(t_0)]_{\epsilon Y}$. Moreover, denoting by $[\partial\Omega(t_0)]_{\epsilon Y}$ the connected component part of

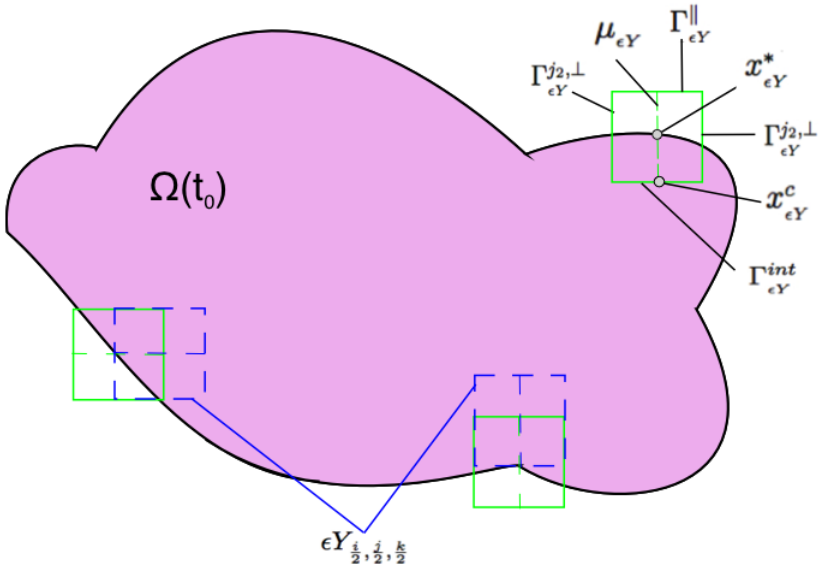

Figure 5.2: *Schematic diagram illustrating the notations introduced in* (5.5), (5.9). *For the arbitrary microdomain* $\epsilon Y \in \mathcal{P}_\epsilon$, *we indicate with a black arrow the features:* $\Gamma^{int}_{\epsilon Y}$, $\Gamma^{j_1,\perp}_{\epsilon Y}$, *and* $\Gamma^{j_2,\perp}_{\epsilon Y}$, $j_1, j_2 \in \{1, ..., 2^{N-1}\}$, $\Gamma^{\|}_{\epsilon Y}$, $x^c_{\epsilon Y}$, $\mu_{\epsilon Y}$, *and* $x^*_{\epsilon Y}$. *The arbitrary cube* $\epsilon Y \in \mathcal{P}^*_\epsilon$ *is shown in green, while the corresponding half-way shifted* $\epsilon Y^{sign}_{\frac{i}{2}} \in \mathcal{P}_\epsilon$*that are not chosen in* $\mathcal{P}^*_\epsilon$ *are shown in the blue dashed line.*

$\partial\Omega(t_0) \cap \epsilon Y$ with the property that

$$[\partial\Omega(t_0)]_{\epsilon Y} \cap \Gamma^{j,\perp}_{\epsilon Y} \neq \emptyset \qquad \text{for any } j = 1, 2, ..., 2^{N-1}, \tag{5.6}$$

we can observe that $[\partial\Omega(t_0)]_{\epsilon Y}$ represents the part of $\partial\Omega(t_0) \cap \epsilon Y$ that corresponds to $[\Omega(t_0)]_{\epsilon Y}$, and is actually the only connected component of this intersection that has property (5.6). Finally, using this observation, for the currently fixed ϵ, the subfamily denoted by $\mathcal{P}_\epsilon$ consisting of all those $\epsilon-$cubes that have $[\Omega(t_0)]_{\epsilon Y}$ not touching $\Gamma^{\|}_{\epsilon Y}$ is selected as follows:

$$\mathcal{P}_\epsilon := \{\epsilon Y \in \mathcal{F}_{\Omega(t_0)} |\ [\Omega(t_0)]_{\epsilon Y} \subset \epsilon Y \text{ and } [\partial\Omega(t_0)]_{\epsilon Y} \cap \Gamma^{\|}_{\epsilon Y} = \emptyset\}. \tag{5.7}$$

Leaving now ϵ to take all the negative powers of 2, the union

$$\bigcup_{\epsilon\in\{2^{-k}\,|\,k\in\mathbb{N}\}} \mathcal{P}_\epsilon$$

provides an infinite covering of $\partial\Omega(t_0)$. Since $\partial\Omega(t_0)$ is compact, using standard compactness arguments, a finite complete sub-covering of $\partial\Omega(t_0)$ that consist only of small cubes an equal size ϵ^* is denoted by $\mathcal{P}_\epsilon^*$, i.e.,

$$\partial\Omega(t_0) \subset \bigcup_{\epsilon Y\in\mathcal{P}_\epsilon^*} \epsilon Y. \tag{5.8}$$

Together with this finite complete covering $\mathcal{P}_\epsilon^*$ of the tumour interface $\partial\Omega(t_0)$, at each time of the tumour evolution we obtain also the size of the micro-scale ϵ^* (Trucu et al., 2013). For simplicity, for the rest of the thesis, the size of the cell-scale ϵ^* will still be denoted by ϵ. Finally, for each $\epsilon Y \in \mathcal{P}_\epsilon^*$, we distinguish the following topological details:

$$\begin{cases} x_{\epsilon Y}^c \text{ denotes the centre of the face } \Gamma_{\epsilon Y}^{int}, \\ \\ \mu_{\epsilon Y}, \text{ is the line that passes through } x_{\epsilon Y}^c \text{ and is perpendicular to } \Gamma_{\epsilon Y}^{int} \\ \\ x_{\epsilon Y}^* \in [\partial\Omega(t_0)]_{\epsilon Y} \text{ which will be referred to as the "midpoint" of } [\partial\Omega(t_0)]_{\epsilon Y}, \\ \text{represents the point from the intersection } \mu_{\epsilon Y} \cap [\partial\Omega(t_0)]_{\epsilon Y} \text{ that is located} \\ \text{at the smallest distance with respect to } x_{\epsilon Y}^c. \end{cases} \tag{5.9}$$

The well-posedness of these topological features is discussed in Trucu et al. (2013), and these are illustrated in Figure 5.2.

5.3 The multiscale moving boundary method and its application to a basic cancer invasion model

In order to introduce and discuss the multiscale moving boundary modelling method and numerical technique proposed in Trucu et al. (2013), in this section we will present a simple multiscale model, which is based on the key biological fact that during invasion cancer cells secrete various matrix degrading enzymes, e.g. MMPs (matrix metalloproteinases), and these enzymes can destroy the surrounding tissue or extracellular matrix (ECM), thus paving the way for further invasion. The concept together with the full details of this macro-micro technique will be introduced along with the description of this two-scale model (Figure 5.3).

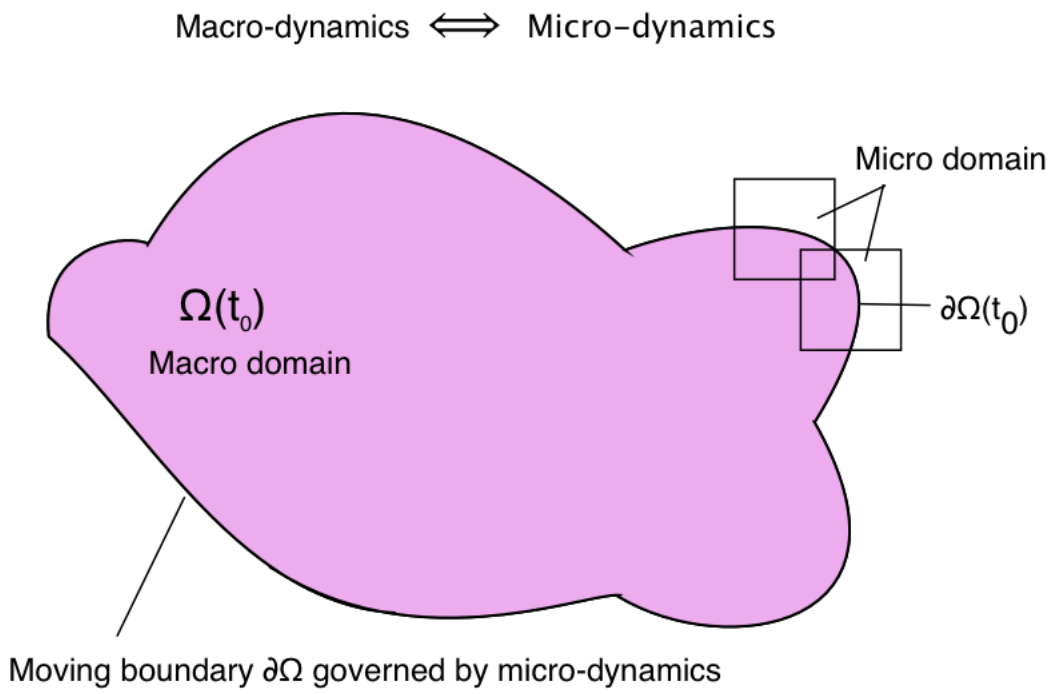

Figure 5.3: *Schematic diagram of the two-scale technique that consists of a macro domain and micro domains that covers the boundary, and the macro-dynamics and micro-dynamics link with each other through the formulation of the moving boundary.*

5.3.1 The macroscopic dynamics

At an arbitrarily chosen time t_0, in the macro domain Y, the macro dynamics of $c(x,t)$ and $v(x,t)$ occurring over the time interval $[t_0, t_0 + \Delta t]$ are governed by the following reaction-diffusion system:

$$\frac{\partial c}{\partial t} = D\Delta c - \eta\nabla \cdot (c\nabla v) + g(c,v), \quad \mathbf{x} \in Y, \tag{5.10}$$

$$\frac{\partial v}{\partial t} = -\alpha(t)cv + f(c,v), \quad \mathbf{x} \in Y, \tag{5.11}$$

where $t \in [t_0, t_0 + \Delta t]$.

In the first equation of the system, the rate of change of the cancer cell population is governed by a diffusion term as well as a haptotaxis term modelling the haptotactic movement of cancer cells to ECM, along with a proliferation term. Then, the second equation that governs the rate of change of the ECM density consists of a degradation term in the presence of the cancer cells along with a general remodelling term, where $\alpha(t)$ in the degradation term is a homogeneous time-dependent degradation factor.

The initial conditions of this macroprocess are:

$$c(\mathbf{x}, t_0) =: c_0(\mathbf{x}), \qquad \mathbf{x} \in \Omega(t_0), \tag{5.12}$$

$$v(\mathbf{x}, t_0) =: v_0(\mathbf{x}), \qquad \mathbf{x} \in Y. \tag{5.13}$$

The boundary conditions of the model in the macro-domain are zero-flux Neumann and micro-scale moving boundary conditions that are imposed by the microscopic dynamics that are described in the next subsection.

5.3.2 The microscopic dynamics

As mentioned earlier, cancer invasion is a multiscale process, including not only phenomena at the tissue level (macrodynamics) but also reactions at the molecular level (microdynamics). Between molecules around tumour boundary, we assume that some matrix degrading enzymes, i.e., MDEs secreted by cancer cells are responsible for destroying the tissue and enable the cancer cells to invade. Mathematically, this means that the macro-scale process defined by equations (5.10) - (5.11) is driven by micro-scale dynamics that cause the boundary of $\Omega(t_0)$ to advance further in the surrounding healthy tissue, namely in $Y \backslash \Omega(t_0)$.

Therefore, over the time interval $[t_0, t_0 + \Delta t]$, the macroscopic domain $\Omega(t_0)$ evolves to a new domain $\Omega(t_0 + \Delta t)$ in Y through an integrated multiscale dynamics that at cell-scale is given by the microscopic dynamics involving MDEs which arises on the micro bundle $\mathcal{P}_\epsilon^*$ that is covering the boundary $\partial\Omega(t_0)$. In the way we define this ϵ-bundle, it is sufficient to describe the governing model for the micro-process that occurs on an arbitrary ϵ-cube $\epsilon Y \in \mathcal{P}_\epsilon^*$, which we will refer to generically as the micro-domain.

In each $\epsilon Y \in \mathcal{P}_\epsilon^*$, we denote by $m(y,t)$ the MDE density on this microdomain. As the MDEs are secreted locally by the cancer cells from within $\Omega(t_0)$, the source term for the MDEs within $\epsilon Y \cap \Omega(t_0)$ can be considered to be the local mean-value of the cancer cells' spatial distribution $c(\cdot, t_0 + \tau)$ for any micro-time $\tau \in [0, \Delta t]$. Thus, on each microdomain and for any $\tau \in [0, \Delta t]$, we can write the source function $f_{\epsilon Y}(\cdot,\cdot) : \epsilon Y \to \mathbb{R}_+$ as the following :

$$f_{\epsilon Y}(y,\tau) = \begin{cases} \frac{1}{\lambda(B(y,2\epsilon)\cap\Omega(t_0))} \int\limits_{B(y,2\epsilon)\cap\Omega(t_0)} c\,(x, t_0+\tau)\,dx, & y \in \epsilon Y \cap \Omega(t_0), \\ 0, & \text{outside cancer}, \end{cases} \tag{5.14}$$

where $\lambda(\cdot)$ is the standard Lebesgue measure on $\mathbb{R}^N$ and $B(y, 2\epsilon) := \{x \in Y | ||y - x||_\infty \leq 2\epsilon\}$.

We assume that the micro dynamics on ϵY is governed by the equation (5.15), in which the change rate of the MDE distribution is determined by diffusion of MDE and its production in the presence of the source (5.14),

$$\frac{\partial m}{\partial \tau} = \Delta m + f_{\epsilon Y}(y, \tau), \quad y \in \epsilon Y, \quad \tau \in [0, \Delta t]. \tag{5.15}$$

On each micro domain ϵY, we impose zero Neumann boundary condition.

5.3.3 Regulation of the process of boundary relocation

In the following, we will explain how the set of midpoints $\{x^*_{\epsilon Y}\}_{\epsilon Y \in \mathcal{P}^*_\epsilon}$ defined on the boundary of the tumour at the current time evolves to a set of new spatial positions $\{\widetilde{x^*_{\epsilon Y}}\}_{\epsilon Y \in \mathcal{P}^*_\epsilon}$ to form the new boundary at the very next time, by describing the movement of one such midpoint $x^*_{\epsilon Y} \in [\partial\Omega(t_0)]_{\epsilon Y}$ for any $\epsilon Y \in \mathcal{P}^*_\epsilon$.

Based on biological observations that, on any micro domain ϵY, provided that a sufficient amount of MDE has been produced across the invading edge and it is the pattern of the front of the advancing spatial distribution of MDEs that characterised ECM degradation, therefore it is assumed that each boundary midpoint $x^*_{\epsilon Y} \in [\partial\Omega(t_0)]_{\epsilon Y}$ will be potentially relocated in a movement direction and by a certain displacement magnitude dictated by the spatial distribution of MDEs obtained via the micro process on ϵY at the final micro-time $\tau_f := \Delta t$, namely, $m(\cdot, \tau_f)$. In the following, we explain how the movement direction and displacement magnitude are defined for each $x^*_{\epsilon Y} \in [\partial\Omega(t_0)]_{\epsilon Y}$.

For any given threshold $\delta > 0$ and any fixed $\epsilon Y \in \mathcal{P}^*_\epsilon$, the regularity property of Lebesgue measure (Halmos, 1974) is used to select the first dyadic decomposition

$\{D_j\}_{j\in\mathcal{J}_\delta}$ of ϵY such that

$$\lambda\Bigg([\epsilon Y\backslash\Omega(t_0)]\setminus\bigcup_{\{j\in\mathcal{J}_\delta\,|\,D_j\subset\epsilon Y\backslash\Omega(t_0)\}}\mathcal{D}_j\Bigg)\leq\delta. \tag{5.16}$$

which simply means that $\epsilon Y\backslash\Omega(t_0)$ is approximated with accuracy δ by the union of all the dyadic cubes that this includes. Once this dyadic decomposition is selected, we denote by y_j the barycenters of D_j, for all $j\in\mathcal{J}_\delta$. As discussed in Trucu et al. (2013) for all $\epsilon Y\in\mathcal{P}^*_\epsilon$, this provides a resolution at which we read the further away part of the level set $\frac{1}{\lambda(\epsilon Y\backslash\Omega(t_0))}\int_{\epsilon Y\backslash\Omega(t_0)}m(y,\cdot)dy$ in the distribution of the advancing degrading enzymes $m(\cdot,\cdot)$ outside $\Omega(t_0)$ in radial direction with respect to the midpoint $x^*_{\epsilon Y}$. Therefore, this enable us to locate dyadic pixels D_l that support the peaks at the tip of the MDE front with significant contribution in degrading the ECM. Therefore, at the final microscopic time τ_f, the pixels supporting these peaks are therefore selected as

$$\mathcal{I}_\delta:=\left\{l\in\mathcal{J}_\delta\;\middle|\;\begin{array}{l}\exists r\in S^1\text{ such that, if the index }i\in\mathcal{J}_\delta\text{ has the properties:}\\ 1)\mathcal{D}_i\cap\{x\in\mathbb{R}^n\,|x=x^*_{\epsilon Y}+\alpha r,\alpha\in\mathbb{R}\}\neq\emptyset,\\ 2)\mathcal{D}_i\subset\epsilon Y\backslash\Omega(t_0),\\ 3)\frac{1}{\lambda(\mathcal{D}_i)}\int_{\mathcal{D}_i}m(y,\tau_f)dy\geq\frac{1}{\lambda(\epsilon Y\backslash\Omega(t_0))}\int_{\epsilon Y\backslash\Omega(t_0)}m(y,\tau_f)dy,\\ \text{then}\\ l=argmax\{d(x^*_{\epsilon Y},y_i)\,|\,i\in\mathcal{J}_\delta\text{ satisfies:}1),2),and3)\}\end{array}\right\}, \tag{5.17}$$

where $S^1\subset\mathbb{R}^n$ represents the unit sphere, and $d(\cdot,\cdot)$ is the Euclidean distance on $\mathbb{R}^n$.

Thus, cumulating the driving ECM degradation forces spanned by each front peak of MDEs given by the dyadic pixels $\mathcal{D}_l$ with $l\in\mathcal{I}_\delta$ in the direction of the position vectors $\overrightarrow{x^*_{\epsilon Y},y_l}$ and appropriately representing the amount of MDEs that each

D_l supports, the revolving direction of movement $\eta_{\epsilon Y}$ for the potential displacement of $x^*_{\epsilon Y}$ is given by:

$$\eta_{\epsilon Y} = x^*_{\epsilon Y} + \nu \sum_{l \in \mathcal{I}_\delta} \left(\int_{\mathcal{D}_l} m(y, \tau_f) dy \right) (y - x^*_{\epsilon Y}), \quad \nu \in [0, \infty]. \tag{5.18}$$

Further, the displacement magnitude of the point $x^*_{\epsilon Y}$ is defined as:

$$\xi_{\epsilon Y} := \sum_{l \in \mathcal{I}_\delta} \frac{\int_{\mathcal{D}_l} m(y, \tau_f) dy}{\sum\limits_{l \in \mathcal{I}_\delta} \int_{\mathcal{D}_l} m(y, \tau_f) dy} \big| \overrightarrow{x^*_{\epsilon Y} y_l} \big|. \tag{5.19}$$

Finally, as debated in Trucu et al. (2013), although a displacement magnitude and a moving direction is derived for each $x^*_{\epsilon Y}$, this will only exercise the movement if and only if the ECM degradation war of a certain local strength. The strength of ECM degradation within ϵY is explored by the transitional probability

$$q^* : \sum \left(\bigcup_{\epsilon Y \in \mathcal{P}^*_\epsilon} \epsilon Y \right) \to \mathbb{R}_+$$

defined as

$$q^*(G) := \frac{1}{\int_G m(y, \tau_f) dy} \int_{G \backslash \Omega(t_0)} m(y, \tau_f) dy, \qquad \text{for all } G \in \sum \left(\bigcup_{\epsilon Y \in \mathcal{P}^*_\epsilon} \epsilon Y \right) \tag{5.20}$$

where $\sum \left(\bigcup\limits_{\epsilon Y \in \mathcal{P}^*_\epsilon} \epsilon Y \right)$ represents the Borel $\sigma-$algebra of $\bigcup\limits_{\epsilon Y \in \mathcal{P}^*_\epsilon} \epsilon Y$.

Locally, in each ϵY, equation (5.20) is in fact a quantification of the amount of MDEs in $\epsilon Y \backslash \Omega(t_0)$ relative to the total amount of MDE concentration in ϵY. In conjunction with the local tissue conditions, this characterises whether the point $x^*_{\epsilon Y}$ is likely to relocate to the new spatial position $\widetilde{x^*_{\epsilon Y}}$ or not.

Now, by assuming that the point $x^*_{\epsilon Y}$ is moved to the position $\widetilde{x^*_{\epsilon Y}}$ if and only

if $q(x^*_{\epsilon Y})$ exceeds a certain threshold $\omega_{\epsilon Y} \in (0,1)$, we find that the new boundary $\partial\Omega(t_0+\Delta t)$ will be the interpolation of the following set of points:

$$\{x^*_{\epsilon Y} | \epsilon Y \in \mathcal{P}^*_{\epsilon Y} \text{ such that } q(x^*_{\epsilon Y}) < \omega_{\epsilon Y}\} \cup \{\widetilde{x^*_{\epsilon Y}} | \epsilon Y \in \mathcal{P}^*_{\epsilon Y} \text{ such that } q(x^*_{\epsilon Y}) \geq \omega_{\epsilon Y}\} \tag{5.21}$$

Finally before moving to the next time-step of the whole macro-micro two scale system, we replace the initial conditions of the macroscopic dynamics with the solution at the final time of the previous invasion step as follows:

$$\begin{aligned} c_{\Omega(t_0+\Delta t)}(x,t_0) &:= c(x,t_0+\Delta t)(\chi_{\Omega(t_0)\setminus \bigcup\limits_{\epsilon Y \in \mathcal{P}^*_\epsilon} \epsilon Y} * \psi_\gamma), \\ v_{\Omega(t_0+\Delta t)}(x,t_0) &:= v(x,t_0+\Delta t)\chi_{Y\setminus \bigcup\limits_{\epsilon Y \in \mathcal{P}^*_\epsilon} \epsilon Y} * \psi_\gamma). \end{aligned} \tag{5.22}$$

Here $\chi_{\Omega(t_0)\setminus \bigcup\limits_{\epsilon Y \in \mathcal{P}^*_\epsilon} \epsilon Y}$ and $\chi_{Y\setminus \bigcup\limits_{\epsilon Y \in \mathcal{P}^*_\epsilon} \epsilon Y}$ are the characteristic functions corresponding to the sets $\Omega(t_0)\setminus \bigcup\limits_{\epsilon Y \in \mathcal{P}^*_\epsilon} \epsilon Y$ and $Y\setminus \bigcup\limits_{\epsilon Y \in \mathcal{P}^*_\epsilon} \epsilon Y$, and choosing $\gamma \ll \frac{\epsilon}{3}$, $\psi_\gamma : \mathbb{R}^N \to \mathbb{R}_+$ is constructed as a smooth compact support function with $\sup(\psi_\gamma) = \{z \in \mathbb{R}^N | ||z||_2 \leq \gamma\}$. This is defined by the standard mollifier $\psi : \mathbb{R}^N \to \mathbb{R}_+$, namely,

$$\psi_\gamma(x) := \frac{1}{\gamma^N}\psi(\frac{x}{\gamma}), \tag{5.23}$$

and,

$$\psi(x) := \begin{cases} \frac{\exp(\frac{1}{x^2-1})}{\int\limits_{\{z\in\mathbb{R}^N | ||z||_2 \leq \gamma\}} \exp(\frac{1}{z^2-1})dz} & \text{if } ||x||_2 < 1, \\ 0 & \text{if } ||x||_2 \geq 1, \end{cases} \tag{5.24}$$

Then, the invasion process will continue on the new expanded domain $\Omega(t_0+\Delta t)$ with the macroscopic system and the new initial conditions in (5.22) at the macro-level followed by MDEs micro-processes around its boundary, which again governs

the movement of the boundary of the next time stage.

5.4 Extension of the macro-microscopic technique

In this section, we adapt the macro-microscopic technique mentioned above to a two-scale model which simulates the urokinase plasminogen activation (uPA) system at both the macro- and micro-scale. In addition, we investigate the properties of the numerical technique by exploring the fusing of the two solvers (i.e. macro-solver and micro-solver).

5.4.1 The macroscopic dynamics

In order to couple the uPA system with the two-scale technique, we firstly replace the equations in (5.10) and (5.11) with the five-PDE system as the macroscopic dynamics to describe the macrodynamics of cancer cells, the extracellular matrix (ECM, vitronectin), urokinase plasminogen activator (uPA), uPA inhibitor PAI-1, and matrix degrading enzyme plasmin. We recall that the equations of the dimensionless uPA system held on spacial domain Y and temporal domain T are:

$$\frac{\partial c}{\partial t} = \underbrace{D_c \Delta c}_{\text{diffusion}} - \nabla \cdot [\ \underbrace{\chi_u c \nabla u}_{\text{uPA-chemo}} + \underbrace{\chi_p c \nabla p}_{\text{PAI-1-chemo}} + \underbrace{\chi_v c \nabla v}_{\text{VN-hapo}}] + \underbrace{\mu_1 c(1-c)}_{\text{profieration}},\ \mathbf{x} \in Y, \tag{5.25}$$

$$\frac{\partial v}{\partial t} = - \underbrace{\delta v m}_{\text{degradation}} + \underbrace{\phi_{21} u p}_{\text{uPA/PAI-1}} - \underbrace{\phi_{22} v p}_{\text{PAI-1/VN}} + \underbrace{\mu_2 v(1-v)}_{\text{proliferation}},\ \mathbf{x} \in Y, \tag{5.26}$$

$$\frac{\partial u}{\partial t} = \underbrace{D_u \Delta u}_{\text{diffusion}} - \underbrace{\phi_{31} p u}_{\text{uPA/PAI-1}} - \underbrace{\phi_{33} c u}_{\text{uPA/uPAR}} + \underbrace{\alpha_{31} c}_{\text{production}}\ ,\ \mathbf{x} \in Y, \tag{5.27}$$

$$\frac{\partial p}{\partial t} = \underbrace{D_p \Delta p}_{\text{diffusion}} - \underbrace{\phi_{41} p u}_{\text{uPA/PAI-1}} - \underbrace{\phi_{42} p v}_{\text{PAI-1/VN}} + \underbrace{\alpha_{41} m}_{\text{production}}\ ,\ \mathbf{x} \in Y, \tag{5.28}$$

$$\frac{\partial m}{\partial t} = \underbrace{D_m \Delta m}_{\text{diffusion}} + \underbrace{\phi_{52} p v}_{\text{PAI-1/VN}} + \underbrace{\phi_{53} c u}_{\text{uPA/uPAR}} - \underbrace{\phi_{54} m}_{\text{degradation}}\ ,\ \mathbf{x} \in Y, \tag{5.29}$$

where $t \in T$ and we denote cancer cell density by c, ECM density by v, uPA concentration by u, PAI-1 concentration by p and plasmin concentration by m.

5.4.2 The microscopic dynamics

Secondly, for the microscopic dynamics, we use three PDE equations for uPA, PAI-1 and plasmin that describe the microdynamics of the plasminogen activation system which take place around the boundary of the tumour. The reasons that we only look into micro dynamics close to the tumour boundary are: 1) the urokinase plasminogen activator (uPA) is required to bind to the cancer surface receptor uPAR to activate plasminogen, leading to degradation of pericellular ECM through a series of proteolytic activities; and 2) membrane-bound MMPs (e.g., MT1-MMP), which play a very important role in cancer invasion, are secreted from within the tumour cell population distributed on the outer proliferating rim along the entire tumour periphery. Their region of proteolytic activities is therefore restricted around the tumour interface (Sabeh et al., 2009; Deakin and Chaplain, 2013). Thus, in the fol-

lowing, we will focus on the coupled boundary microdynamics exhibited as follows:

The uPA microdynamics. In each micro region ϵY the dynamics of uPA molecular population is governed by a diffusion process whose source is induced from the tumour cell macro-dynamics. At each point $y \in \epsilon Y$, a source of uPA arises as a collective contribution of the tumour cells distributed within a certain neighbouring area within the tumour's outer proliferating rim. Therefore, per unit time, under the presence of this source, denoted by $f_{\epsilon Y}(\cdot,\cdot) : \epsilon Y \to \mathbb{R}_+$ and defined as:

$$f_1^{\epsilon Y}(y,\tau) = \begin{cases} \frac{1}{\lambda(B(y,2\epsilon)\cap\Omega(t_0))} \int\limits_{B(y,2\epsilon)\cap\Omega(t_0)} c\,(x, t_0+\tau)\,dx, & y \in \epsilon Y \cap \Omega(t_0), \\ 0, & \text{outside cancer.} \end{cases} \tag{5.30}$$

The uPA is locally diffusing, and is binding both PAI-1 and uPAR (uPA receptor) that are uniformly expressed on the cell surface of various cell types in the tumour, and so the equation of uPA can be formally written as:

$$\frac{\partial u}{\partial \tau} = \underbrace{D_u \Delta u}_{\text{diffusion}} - \underbrace{\phi_{31} p u}_{\text{uPA/PAI-1}} + \Big(\underbrace{\alpha_{31}}_{\text{production}} - \underbrace{\phi_{33} u}_{\text{uPA/uPAR}} \Big) f_1^{\epsilon Y}(y,\tau). \tag{5.31}$$

The PAI-1 microdynamics. The equation for PAI-1 consists of diffusive motion, production due to plasmin activation and loss due to binding with uPA and VN. Specifically, we use the local mean-value of ECM distribution within the whole micro-domain ϵY to describe the binding between PAI-1 and VN, meaning we consider it as a collective effect of ECM distribution in ϵY. In a similar fashion to the source term above, we define,

$$f_2^{\epsilon Y}(y,\tau) = \frac{1}{\lambda(B(y,2\epsilon))} \int_{B(y,2\epsilon)} v\,(x, t_0+\tau)\,dx, \quad y \in \epsilon Y. \tag{5.32}$$

Therefore, the equation can be written as:

$$\frac{\partial p}{\partial \tau} = \underbrace{D_p \Delta p}_{\text{diffusion}} - \underbrace{\phi_{41} p u}_{\text{uPA/PAI-1}} - \underbrace{\phi_{42} p\ f_2^{\epsilon Y}(y,\tau)}_{\text{PAI-1/VN}} + \underbrace{\alpha_{41} m}_{\text{production}} . \tag{5.33}$$

The plasmin microdynamics. Similarly, motion of plasmin is also through diffusion. Since it has been claimed that binding of uPA to uPAR is required to provide the cell surface with a potential proteolytic activity, therefore the binding uPA/uPAR contributes to the increase of plasmin concentration. Furthermore, since PAI-1 competes with uPAR for binding to VN, the binding of PAI-1 to VN would give more opportunities to uPAR to bind with uPA, which indirectly results in more plasmin formation (Note: here we deal with binding of PAI-1/VN and uPA/uPAR in a 'collective-effect' fashion introduced in equation (6.9) and (6.10)). Also, plasmin can be deactivated either by degradation or by the action of the plasmin inhibitor α_2-antiplasmin. The equation describing these biological interactions is:

$$\frac{\partial m}{\partial \tau} = \underbrace{D_m \Delta m}_{\text{diffusion}} + \underbrace{\phi_{52} p\ f_2^{\epsilon Y}(y,\tau)}_{\text{PAI-1/VN}} + \underbrace{\phi_{53} u\ f_1^{\epsilon Y}(y,\tau)}_{\text{uPA/uPAR}} - \underbrace{\phi_{53} m}_{\text{degradation}} \tag{5.34}$$

In summary, the whole system of microdynamics on each microdomain in time interval $[0, \tau_f]$ is given as:

$$\frac{\partial u}{\partial \tau} = \underbrace{D_u \Delta u}_{\text{diffusion}} - \underbrace{\phi_{31} p u}_{\text{uPA/PAI-1}} + \Big(\underbrace{\alpha_{31}}_{\text{production}} - \underbrace{\phi_{33} u}_{\text{uPA/uPAR}} \Big) f_1^{\epsilon Y}(y,\tau), \quad \mathbf{x} \in \epsilon Y, \tag{5.35}$$

$$\frac{\partial p}{\partial \tau} = \underbrace{D_p \Delta p}_{\text{diffusion}} - \underbrace{\phi_{41} p u}_{\text{uPA/PAI-1}} - \underbrace{\phi_{42} p\ f_2^{\epsilon Y}(y,\tau)}_{\text{PAI-1/VN}} + \underbrace{\alpha_{41} m}_{\text{production}} , \quad \mathbf{x} \in \epsilon Y, \tag{5.36}$$

$$\frac{\partial m}{\partial \tau} = \underbrace{D_m \Delta m}_{\text{diffusion}} + \underbrace{\phi_{52} p\ f_2^{\epsilon Y}(y,\tau)}_{\text{PAI-1/VN}} + \underbrace{\phi_{53} u\ f_1^{\epsilon Y}(y,\tau)}_{\text{uPA/uPAR}} - \underbrace{\phi_{54} m}_{\text{degradation}} , \quad \mathbf{x} \in \epsilon Y. \tag{5.37}$$

On each micro domain ϵY, we impose zero Neumann boundary condition. The

initial conditions on ϵY are defined by the interpolation of the solutions of u, p and m on macro mesh.

5.4.3 Regulation of the tumour boundary relocation

Now we present the functions that we use to simulate the process of the boundary relocation. In order to describe how the set of points $\{x^*_{\epsilon Y}\}$ on the boundary of tumour at the current time moves towards a set of new spatial positions $\{\widetilde{x^*_{\epsilon Y}}\}$ to form the new boundary at the next time stage, we need a local transitional probability (or we could call it 'invading strength') to check if the circumstances in the microenvironment are suitable for cell movement. When this invading strength is above some threshold value, we need the direction in which the cells will move and the magnitude of the movement as well.

Similarly as stated in section 5.3.3, on any micro-domain ϵY, provided that a sufficient amount of plasmin has been produced across the invading edge, it is the pattern of the front of the advancing spatial distribution of plasmin that characterises ECM degradation. Therefore we need to obtain the spatial distribution of plasmin $m(\cdot, \tau_f)$ at the final micro-time τ_f which is obtained though the uPA microscopic dynamics, in order to define the movement direction and displacement magnitude of the invading part of the cancer interface. Then we use a weighted contribution to describe the characters of the invasive movement from all the peaks (denoted by y^*_l) located at the front of advancing plasmin that are above the mean value of the entire mass of plasmin produced on $\epsilon Y \backslash \Omega(t_0)$. These selected plasmin peaks at the front of its distribution $m(\cdot, \tau_f)$ are located at the furthest possible Euclidean distance with respect to $x^*_{\epsilon Y}$. Based on these conditions and assumptions, the moving direction $\eta_{\epsilon Y}$ is given by:

$$\eta_{\epsilon Y} = x^*_{\epsilon Y} + \nu \sum_{l \in \mathcal{I}_\delta} \Big(\int_{\mathcal{D}_l} m(y, \tau_f) dy \Big) (y_l - x^*_{\epsilon Y}), \nu \in [0, \infty]. \tag{5.38}$$

The total displacement magnitude of the point $x^*_{\epsilon Y}$ is defined as:

$$\xi_{\epsilon Y} := \sum_{l \in \mathcal{I}_\delta} \frac{\int_{\mathcal{D}_l} m(y, \tau_f) dy}{\sum\limits_{l \in \mathcal{I}_\delta} \int_{\mathcal{D}_l} m(y, \tau_f) dy} \big| \overrightarrow{x^*_{\epsilon Y} y_l} \big|. \tag{5.39}$$

Lastly, the cumulative distribution function $q^* : \sum(\epsilon Y) \to \mathbb{R}_+$ acts as the invading strength function that is written as:

$$q^*(A) := \frac{1}{\int_A m(y, \tau_f) dy} \int_{A \setminus \Omega(t_0)} m(y, \tau_f) dy, A \in \Sigma(\epsilon Y), \tag{5.40}$$

which is in fact a quantification of the amount of plasmin in $\epsilon Y \setminus \Omega(t_0)$ relative to the total amount of plasmin concentration in ϵY. Moreover, we assume that the point $x^*_{\epsilon Y}$ is moved to the position $\widetilde{x^*_{\epsilon Y}}$ if and only if $q(x^*_{\epsilon Y})$ exceeds a certain threshold $\omega(\beta, \epsilon Y) \in (0, 1)$.

5.5 Two-dimensional multiscale numerical technique for the uPA system

Building on the general implementation idea outlined in Trucu et al. (2013), in two-dimensions, we compute and solve the multiscale model by using a finite difference scheme for the macro-dynamics (as described in Appendix 8.1) and for the micro-dynamics around the boundary a finite element scheme is employed. In the following context we will introduce the computational microscopic scheme and its relation to the macroscopic level.

We describe our computational scheme for the micro scale dynamics occurring

on each micro-domain $\epsilon Y \in \mathcal{P}^*_\epsilon$, which are cubes of size ϵ located at the boundary $\partial\Omega(t_0)$, as described in section 5.2. We have each microdomain ϵY centred at a boundary point from the macroscopic mesh, with the neighbouring ϵ-cubes starting from the centre of the current one (i.e. they are appropriately "half-way shifted" copies of $\epsilon Y \in \mathcal{P}^*_\epsilon$), due to the purposely chosen macroscopic mesh size $h = \frac{\epsilon}{2}$ and the properties of the family $\mathcal{P}^*_{\epsilon Y}$. Moreover, the centre point of the microdomains are coincidentally the midpoint induced by ϵY on $[\partial\Omega(t_0)]_{\epsilon Y}$, i.e. $x^*_{\epsilon Y}$.

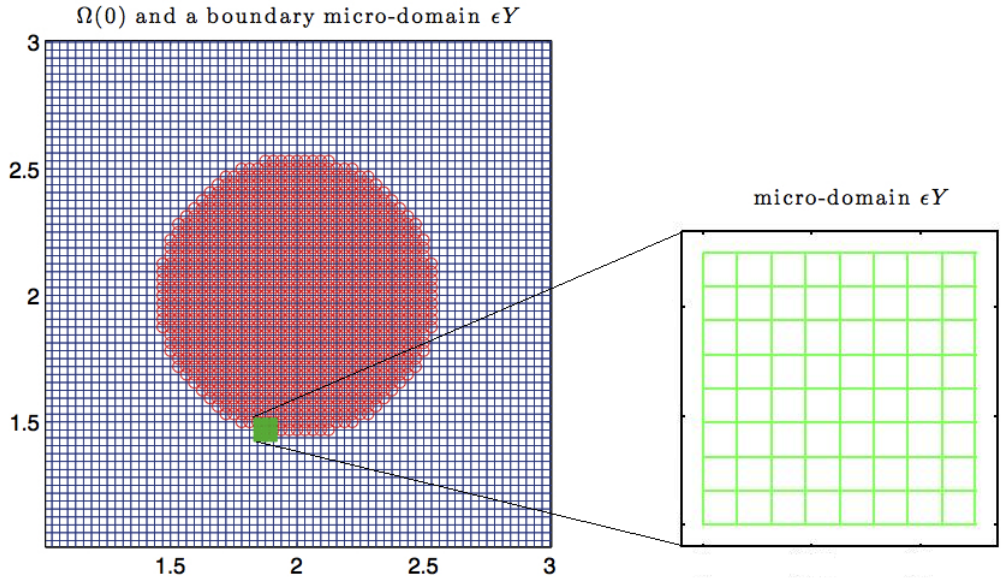

Figure 5.4: *Plots showing the macro- and microdomains used in the numerical scheme. The left figure shows the central part of the uniformly discretised domain* $Y = [0, 4] \times [0, 4]$*, which contains the initial cancer region* $\Omega(t_0)$ *(red circles). One boundary microdomain* ϵY *is shown in green, and a detailed view of this is given in the right-hand figure.*

.

In order to compute the integrals in the source terms in equation (5.30) and (5.32), a midpoint rule is proposed and the constitutive details are given below. Assuming that K denotes a generic element domain in a finite element subdivision with either triangular or square elements of a given region $A \subset \mathbb{R}^2$, this "midpoint rule" con-

sists of approximating the integral of a function g over K as the product between the value of g at the centre of mass of K, K_{centre}, and the Lebesgue measure of K (Trucu et al., 2013), namely,

$$\int_K g = g(K_{centre})\lambda(K). \tag{5.41}$$

For an arbitrarily chosen $\epsilon Y \in \mathcal{P}^*_\epsilon$, we consider a finite element approach involving triangular elements on a uniform micro-mesh, which is maintained with identical structure for all the microdomains. In order to calculate the source terms $f_1^{\epsilon Y}$ and $f_2^{\epsilon Y}$, we consider time-constant approximations $\tilde{f}_1^{\epsilon Y}$ of $f_1^{\epsilon Y}$ and $\tilde{f}_2^{\epsilon Y}$ of $f_2^{\epsilon Y}$ on the time interval $[0, \Delta t]$. We use the computed final-time values of $c(\cdot, t_0 + \Delta t)$ and $v(\cdot, t_0 + \Delta t)$ accordingly at the macro-mesh points that are included on the current microdomain, $x_1, x_2, ..., x_{P_{\epsilon Y}} \in \epsilon Y \cap \Omega(t_0)$, we can write:

$$\tilde{f}_1^{\epsilon Y}(x_s) = \frac{1}{\lambda(B(x_s, 2\epsilon) \cap \Omega(t_0))} \int\limits_{B(x_s, 2\epsilon)\cap\Omega(t_0)} c\,(x_s, t_0 + \Delta t)\,dx, \tag{5.42}$$

and

$$\tilde{f}_2^{\epsilon Y}(x_s) = \frac{1}{\lambda(B(x_s, 2\epsilon)} \int\limits_{B(x_s, 2\epsilon)} v\,(x_s, t_0 + \Delta t)\,dx, \tag{5.43}$$

where $s = 1, ..., P_{\epsilon Y}$ and the integrals are computed via the midpoint rule.

For the rest of the points y on the micro-mesh, the value of $\tilde{f}_1^{\epsilon Y}$ is obtained in terms of the set of finite element basis functions considered at the contact points, i.e. , $\{\phi_{x_s} | s = 1, ..., P_{\epsilon Y}\}$. We note that for any micro mesh point $y \in \epsilon Y$ we have two possibilities:

- Case 1: If there exists three overlapping points $x_{i_1}, x_{i_2}, x_{i_3} \in \{x_1, x_2, ..., x_{P_{\epsilon Y}}\}$ which belong to the same connected component of $\epsilon Y \cap \Omega(t_0)$ and y belongs

to the convex closure of the set, i.e. $y \in \text{Conv}\{x_{i_1}, x_{i_2}, x_{i_3}\}$, then we have:

$$\tilde{f}_1^{\epsilon Y}(y) = \tilde{f}_1^{\epsilon Y}(x_{i_1})\phi_{x_{i_1}}(y) + \tilde{f}_1^{\epsilon Y}(x_{i_2})\phi_{x_{i_2}}(y) + \tilde{f}_1^{\epsilon Y}(x_{i_3})\phi_{x_{i_3}}(y). \tag{5.44}$$

- Case 2: If y does not satisfy the conditions in Case 1, then we have,

$$\tilde{f}_1^{\epsilon Y}(y) = 0. \tag{5.45}$$

Since the source $f_2^{\epsilon Y}$ is produced by ECM on the entire micro-mesh ϵY, we only need to consider one case to calculate $\tilde{f}_1^{\epsilon Y}$ at any micro mesh point $y \in \epsilon Y$, i.e.,

$$\tilde{f}_2^{\epsilon Y}(y) = \tilde{f}_2^{\epsilon Y}(x_{i_1})\phi_{x_{i_1}}(y) + \tilde{f}_2^{\epsilon Y}(x_{i_2})\phi_{x_{i_2}}(y) + \tilde{f}_2^{\epsilon Y}(x_{i_3})\phi_{x_{i_3}}(y), \tag{5.46}$$

where $x_{i_1}, x_{i_2}, x_{i_3}$ are three overlapping points in the set $\{x_1, x_2, ..., x_{P_{\epsilon Y}}\}$ on the micro-mesh and y satisfies $y \in \text{Conv}\{x_{i_1}, x_{i_2}, x_{i_3}\}$.

From the descriptions above, now we can calculate the source terms $\tilde{f}_1^{\epsilon Y}$ and $\tilde{f}_2^{\epsilon Y}$ on each microdomain ϵY. In order to solve the reaction-diffusion system (5.35) - (5.37), we impose Neumann boundary conditions for these equations on the boundary of each microdomain ϵY, and the initial conditions are determined by the solutions of u, p and m in the macroscopic dynamics. Then we use the finite element method to solve the microscopic dynamic system on ϵY over the time interval $[0, t_0+\Delta t]$. Then, using bilinear elements on a square mesh, the numerical scheme for the micro-processes occurring on each ϵY is finally obtained by using a trapezoidal predictor-corrector method for the time integration.

After we obtain the distribution of plasmin at the final micro-time $m(\cdot, \tau_f)$ on microdomain ϵY, we then use the midpoint rule to compute the transitional probability described in (5.40). For simplicity, now the numerical implementation of

the multiscale model for cancer invasion proposed above is slightly simplified in the following way: provided that the transitional probability exceeds an associated threshold $\omega_{\epsilon Y} \in (0,1)$, the boundary mesh-point $x^*_{\epsilon Y}$ will move in direction $\eta_{\epsilon Y}$ to the macro-mesh point from $\partial\epsilon Y \backslash [\Omega(t_0)]_{\epsilon Y}$ that is closest (in Euclidean distance) to $x^*_{\epsilon Y}$. If the threshold is not satisfied, then $x^*_{\epsilon Y}$ remains at the same spatial location. Therefore, the new boundary $\partial\Omega(t_0 + \Delta t)$ is now obtained by the interpolation of the set of points given in (5.21), and the computational process is continued on the new domain $\Omega(t_0 + \Delta t)$ by imposing a new initial condition for the macroscopic dynamics, i.e.,

$$c(x_{i,j}, t_0 + \Delta t) = \begin{cases} c^k_{i,j}, & x_{i,j} \in \overline{\Omega(t_0)}, \\ \frac{1}{4}(c^k_{i-1,j} + c^k_{i+1,j} + c^k_{i,j-1} + c^k_{i,j+1}), & x_{i,j} \in \overline{\mathbf{B}(\overline{\Omega(t_0)}, h)} \backslash \overline{\Omega(t_0)}, \\ 0, & x_{i,j} \notin \overline{\mathbf{B}(\overline{\Omega(t_0)}, h)}, \end{cases}$$

$$\begin{aligned} v(x_{i,j}, t_0 + \Delta t) &= v^k_{i,j}, \\ u(x_{i,j}, t_0 + \Delta t) &= u^k_{i,j}, \\ p(x_{i,j}, t_0 + \Delta t) &= p^k_{i,j}, \\ m(x_{i,j}, t_0 + \Delta t) &= m^k_{i,j}, \end{aligned} \tag{5.47}$$

where $\{x_{i,j} | i, j = 1, ..., q\}$ is the macroscopic mesh in Y, $\overline{\Omega(t_0)}$ is the topological closure of $\Omega(t_0)$, and $\overline{\mathbf{B}(\overline{\Omega(t_0)}, h)}$ represents the topological closure of the h-bundle of $\overline{\Omega(t_0)}$., i.e., $\overline{\mathbf{B}(\overline{\Omega(t_0)}, h)} := \{x \in Y | \exists z_x \in \overline{\Omega(t_0)} \text{ such that } ||x - z_x||_2 \leq h\}$.

5.6 Computational simulation results

The complete multiscale model of cancer invasion was numerically solved in a rectangular region $Y := [0,4] \times [0,4]$ and it was assumed that the cancer initially occupies a region $\Omega(0)$ within Y, taken to be a disc centred at $(2,2)$ with radius $r = 0.5$. We use the discretisation of the entire domain Y that applies the uniform spatial mesh size $h = 0.03125$ and $\epsilon = 2h = 0.0625$, which gives us a mesh of Y with 64×64 elements and each element is a microdomain ϵY. All the effort in assessing the microdynamics is aimed at ultimately describing the potential spatial movement of this midpoint $x^*_{\epsilon Y}$. The initial conditions for the macroscopic uPA system are:

$$\begin{aligned}
c(x,0) &= \frac{\exp\big(-\frac{||x-(2,2)||_2^2}{\sqrt{\Delta x \Delta y}}\big) - \exp(-\frac{(1-\Delta x)(1-\Delta y)}{\sqrt{\Delta x \Delta y}})}{2},\ x \in \Omega(0),\\
v(x,0) &= \frac{1 + 0.3\sin\left(4\pi||x||_2\right) + \sin\left(4\pi||(4,0)-x||_2\right)}{2},\ x \in Y,\\
u(x,0) &= 1 - \frac{1}{2}c(x,0),\ x \in Y,\\
p(x,0) &= \frac{1}{2}c(x,0), \qquad x \in Y,\\
m(x,0) &= \frac{1}{20}c(x,0), \qquad x \in Y.
\end{aligned} \tag{5.48}$$

Meanwhile, the parameters of the uPA system are given below and these are used in all the simulation results presented in this section (unless stated otherwise):

$$
\begin{aligned}
&D_n = 4.25 \cdot 10^{-3}, \quad \chi_u = 3.05 \cdot 10^{-2}, \quad \chi_p = 3.75 \cdot 10^{-2}, \quad \chi_v = 2.85 \cdot 10^{-2},\\
&\mu_1 = 0.25, \quad \delta = 8.15, \quad \phi_{21} = 0.75, \quad \phi_{22} = 0.55,\\
&\mu_2 = 0.15, \quad D_u = 2.5 \cdot 10^{-3}, \quad \phi_{31} = 0.75, \quad \phi_{33} = 0.3,\\
&\alpha_{31} = 0.215, \quad D_p = 3.5 \cdot 10^{-3}, \quad \phi_{41} = 0.75, \quad \phi_{42} = 0.55,\\
&\alpha_{41} = 0.5, \quad D_m = 4.91 \cdot 10^{-3}, \quad \phi_{52} = 0.11, \quad \phi_{53} = 0.75,\\
&\phi_{54} = 0.5.
\end{aligned} \tag{5.49}
$$

Since the threshold, which controls whether or not a point on the boundary can move, depends on the local composition of the ECM, thus we define our threshold function $\omega(\beta, \epsilon Y)$ as follows:

$$
\omega(\beta, \epsilon Y) := \begin{cases} \sin\left(\frac{\pi}{2}\left(1 - \frac{1}{\beta}\frac{v_{\omega(t_0)}(x^*_{\epsilon Y}, t_0+\Delta t)}{\sup\limits_{\xi\in\partial\Omega(t_0)} v_{\Omega(t_0)}(\xi, t_0+\Delta t)}\right)\right), & \text{if } \frac{v_{\omega(t_0)}(x^*_{\epsilon Y}, t_0+\Delta t)}{\sup\limits_{\xi\in\partial\Omega(t_0)} v_{\Omega(t_0)}(\xi, t_0+\Delta t)} \leq \beta, \\ \sin\left(\frac{\pi}{2(1-\beta)}\left(\frac{v_{\omega(t_0)}(x^*_{\epsilon Y}, t_0+\Delta t)}{\sup\limits_{\xi\in\partial\Omega(t_0)} v_{\Omega(t_0)}(\xi, t_0+\Delta t)} - \beta\right)\right), & \text{if } \frac{v_{\omega(t_0)}(x^*_{\epsilon Y}, t_0+\Delta t)}{\sup\limits_{\xi\in\partial\Omega(t_0)} v_{\Omega(t_0)}(\xi, t_0+\Delta t)} > \beta, \end{cases} \tag{5.50}
$$

where $\beta \in (0, 1)$ is a parameter that controls the "optimal level" of EMC density and consider this as being the indicator of the most favourable invasion conditions at the level of tumour and tissue microenvironment.

The following figures show the simulation results of the evolving cancer cell and ECM spatial distributions and of the invasive tumour boundary at time stages 0, 20, 40, 60. For micro-solver, we set the length of runtime is 0.1 (i.e., we solve the microscopic dynamics on the microdomain in the time interval $[0, 0.1]$ and $\tau_f = 0.1$) and the time step $\Delta\tau = 10^{-9}$. In order to investigate the effect that macro-solver runtime has on the simulation results and choose the best timing, we use four groups of values for the macro-time step Δt and the total iteration number N (thus the

runtime of the macro-solver is $N\Delta t$). They are: 1) $\Delta t = 0.001,\ N = 100$; 2) $\Delta t = 0.0025,\ N = 250$; 3) $\Delta t = 0.005,\ N = 500$; 4) $\Delta t = 0.01,\ N = 1000$.

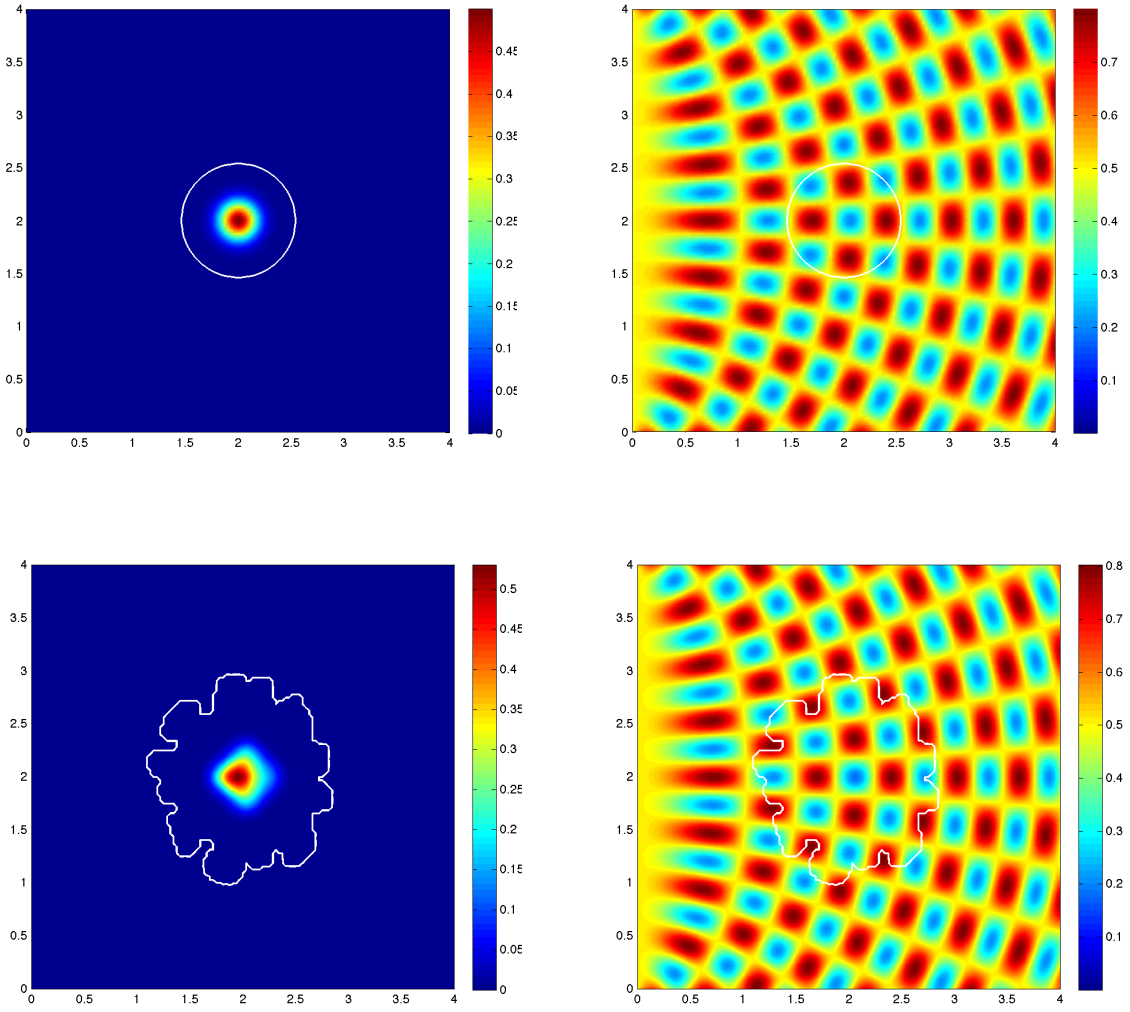

Figure 5.5: *Simulation results showing distributions of cancer cells (left column) and ECM (right column) and the invasive boundary of the tumour (white line) at various macro-micro stages: Stage 0, 20. Macro-solver:* $\Delta t = 0.001,\ N = 100$.

From Figures 5.5 - 5.6, Figures 5.7 - 5.8, Figures 5.9 - 5.10, Figures 5.11 - 5.12, we see that the longer we allow the macro-solver to run, the higher is the degree of heterogeneity of the cancer cell distribution inside the tumour. It make sense that

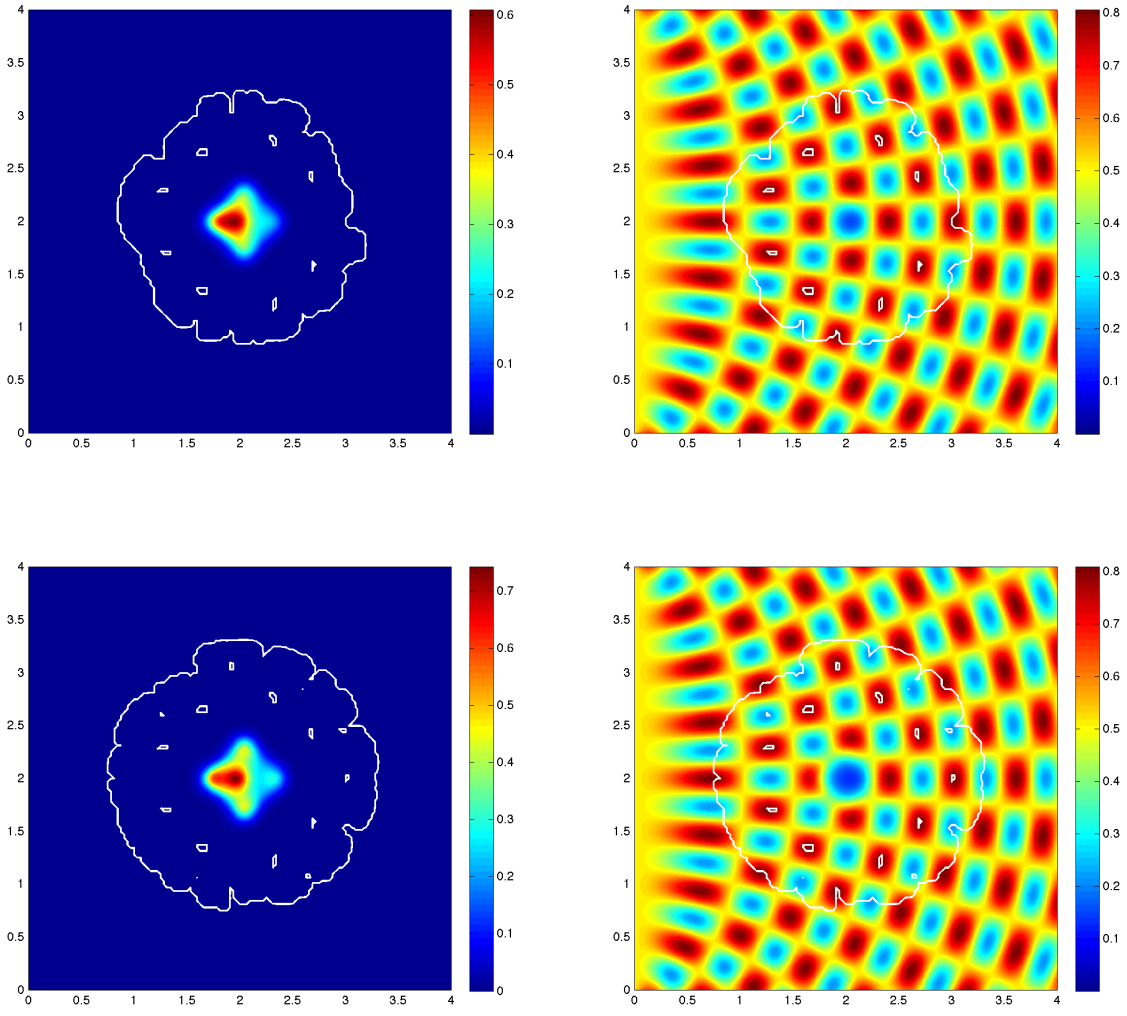

Figure 5.6: *Simulation results showing distributions of cancer cells (left column) and ECM (right column) and the invasive boundary of the tumour (white line) at various macro-micro stages: Stage 40, 60. Macro-solver:* $\Delta t = 0.001,\ N = 100.$

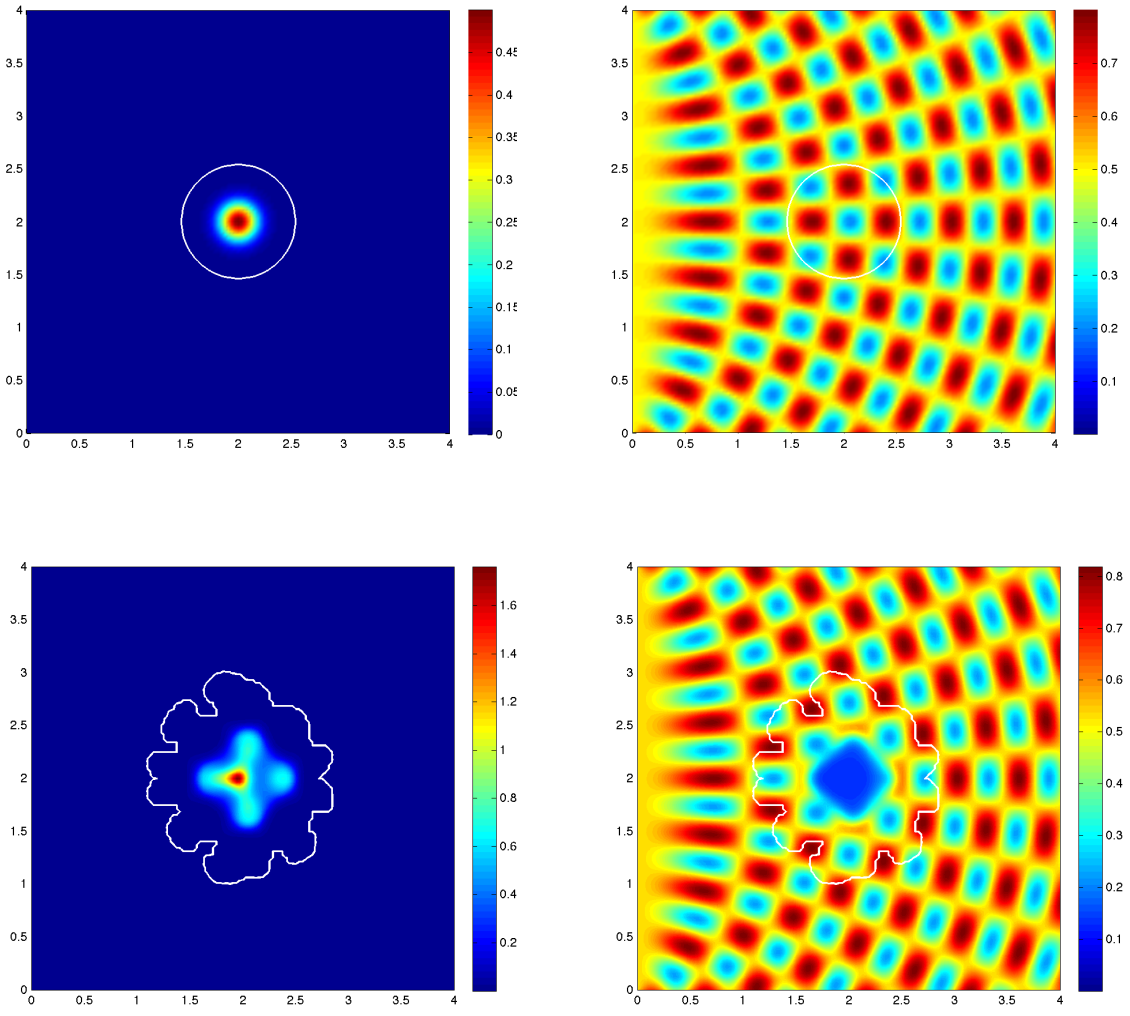

Figure 5.7: *Simulation results showing distributions of cancer cells (left column) and ECM (right column) and the invasive boundary of the tumour (white line) at various macro-micro stages: Stage 0, 20. Macro-solver:* $\Delta t = 0.0025,\ N = 250.$

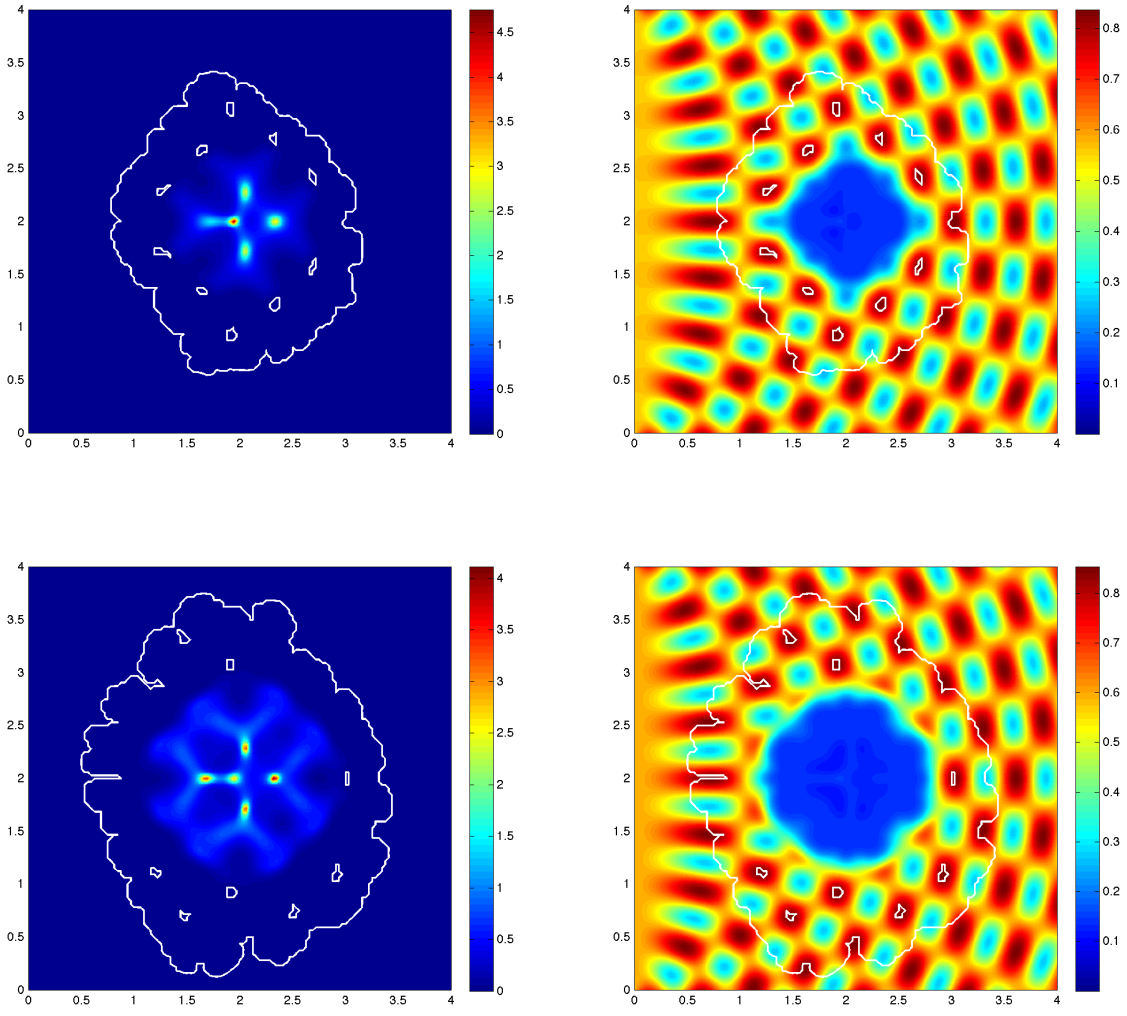

Figure 5.8: *Simulation results showing distributions of cancer cells (left column) and ECM (right column) and the invasive boundary of the tumour (white line) at various macro-micro stages: Stage 40, 60. Macro-solver:* $\Delta t = 0.0025,\ N = 250$.

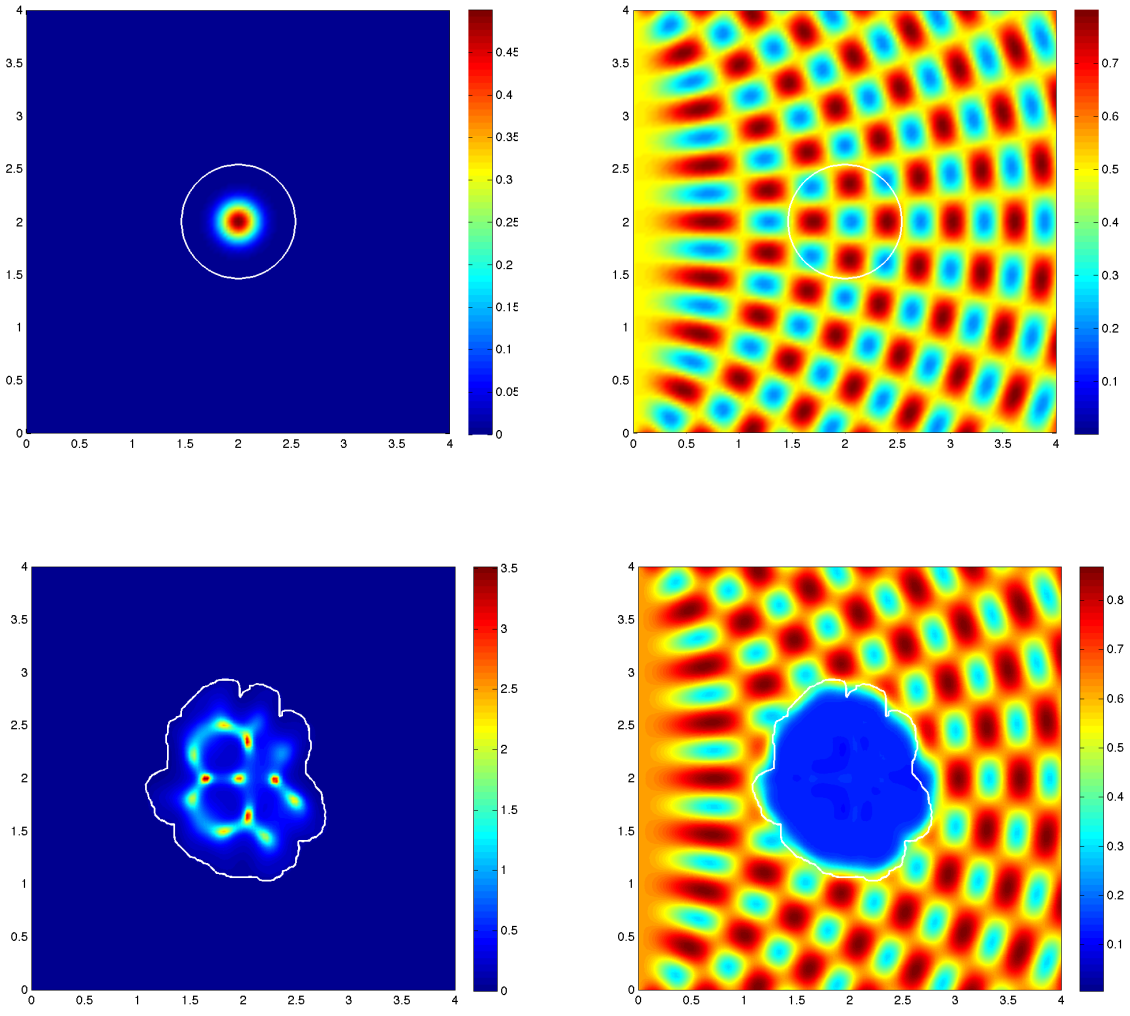

Figure 5.9: *Simulation results showing distributions of cancer cells (left column) and ECM (right column) and the invasive boundary of the tumour (white line) at various macro-micro stages: Stage 0, 20. Macro-solver:* $\Delta t = 0.005,\ N = 500.$

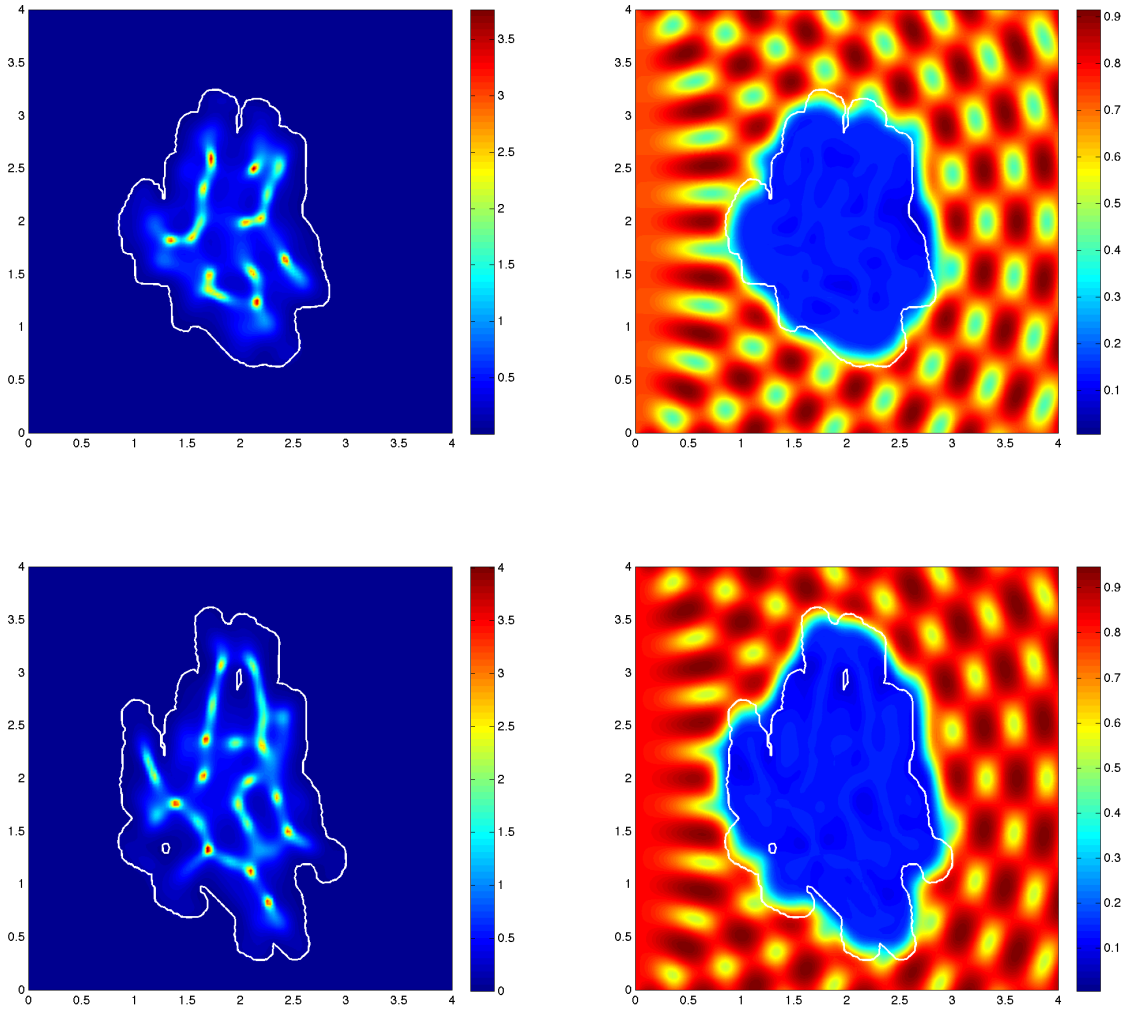

Figure 5.10: *Simulation results showing distributions of cancer cells (left column) and ECM (right column) and the invasive boundary of the tumour (white line) at various macro-micro stages: Stage 40, 60. Macro-solver:* $\Delta t = 0.005,\ N = 500.$

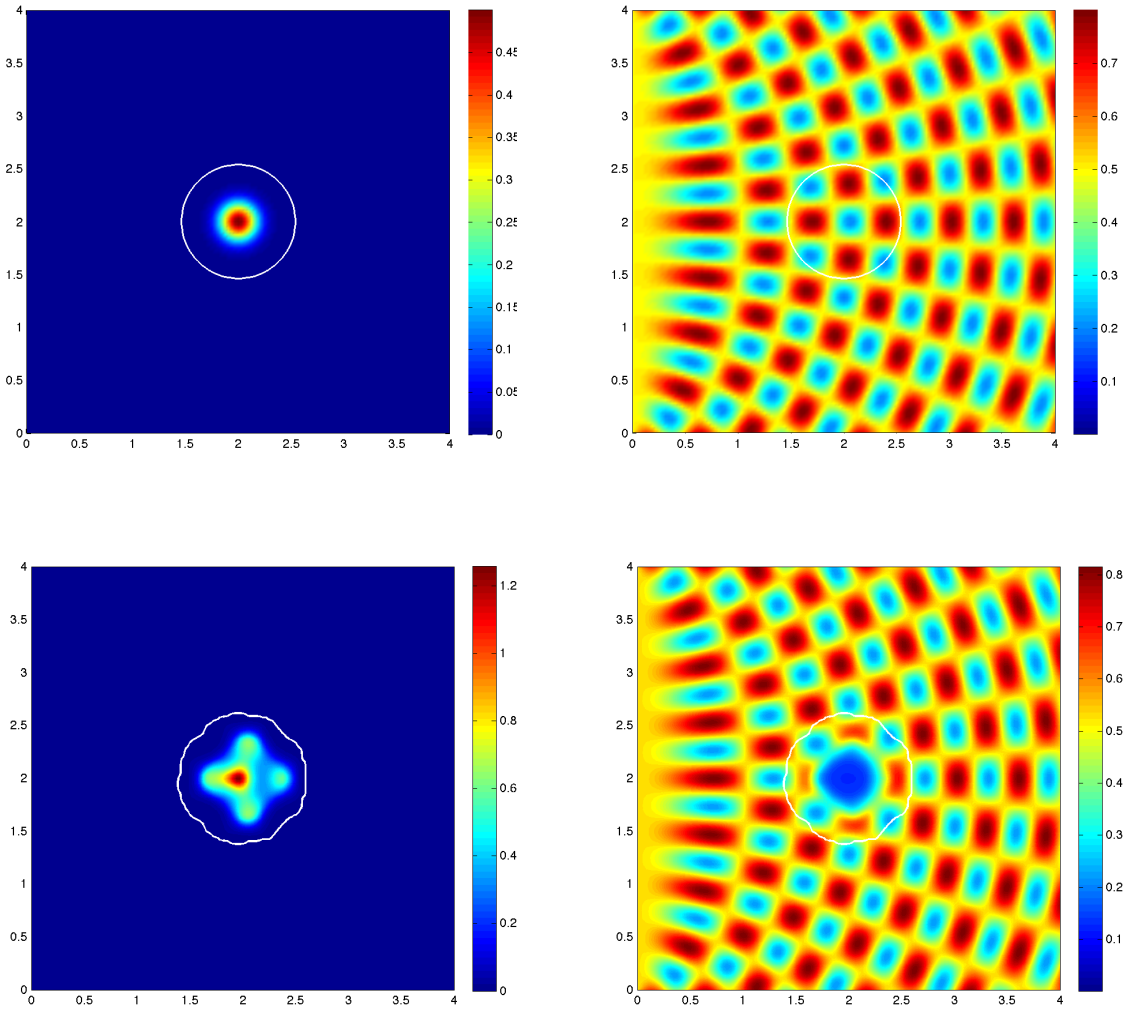

Figure 5.11: *Simulation results showing distributions of cancer cells (left column) and ECM (right column) and the invasive boundary of the tumour (white line) at various macro-micro stages: Stage 0, 1. Macro-solver:* $\Delta t = 0.01,\ N = 1000.$

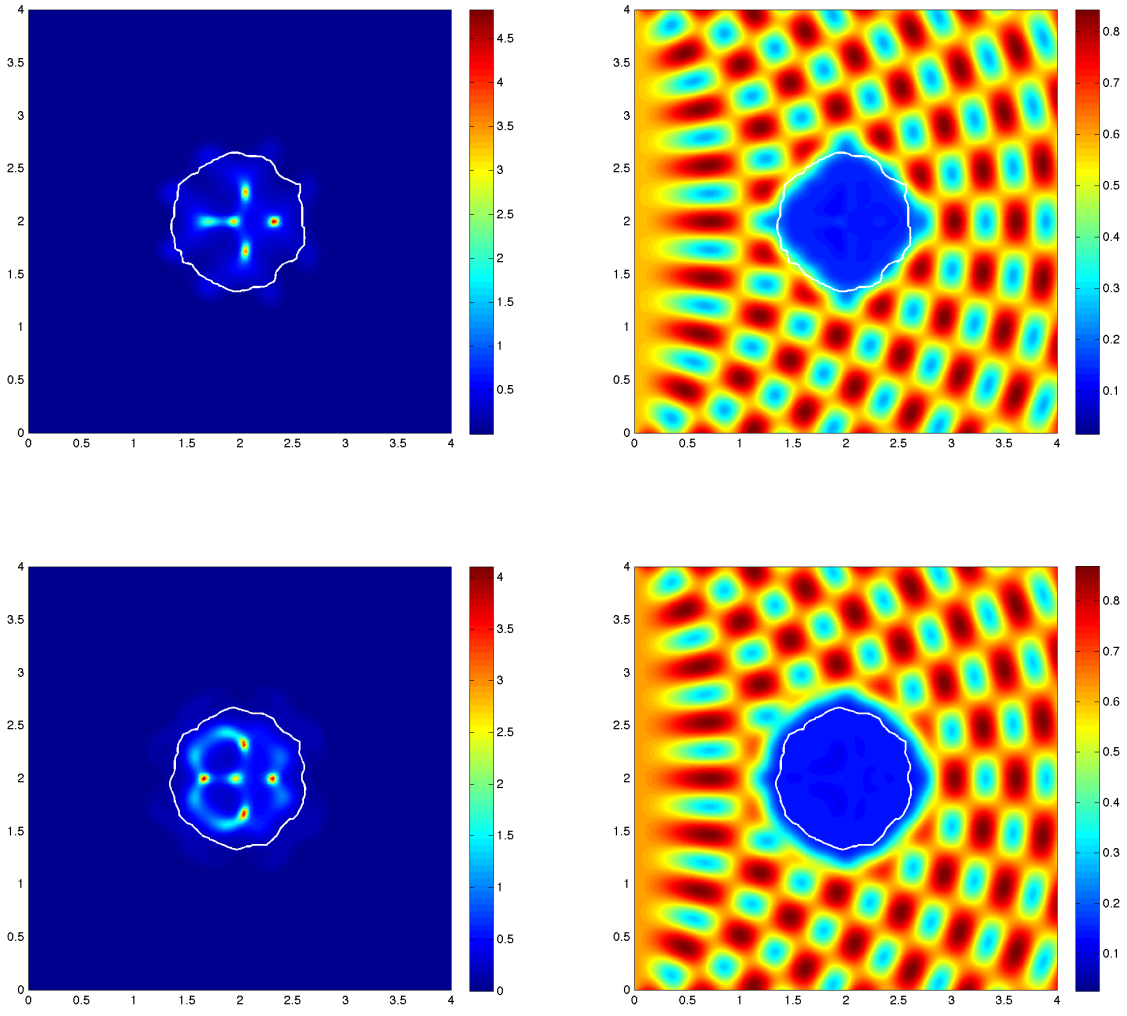

Figure 5.12: *Simulation results showing distributions of cancer cells (left column) and ECM (right column) and the invasive boundary of the tumour (white line) at various macro-micro stages: Stage 3,5. Macro-solver:* $\Delta t = 0.01,\ N = 1000.$

when the runtime of macro-solver is short the uPA system does not have enough time to form heterogeneous patterns (Figures 5.5 - 5.6). However, we cannot allow the macro-solver to run for too long either. Otherwise, the cancer cells will diffuse much faster than the velocity of the boundary, which will lead to a disconnection between the macro-solver and the micro-solver (Figures 5.11 - 5.12). Therefore, it is very important to choose a proper length of the runtime of the macro-solver. From our computational experiment results, we choose $\Delta t = 0.005,\ N = 500$ in our model.

5.7 Discussion

In this chapter, we have introduced and extended a sophisticated numerical method proposed in Trucu et al. (2013), which is referred to as the macro-microscopic technique. It has proven to be a robust and powerful tool to investigate multiscale PDE systems at both macro- and micro-level involved with a moving boundary problem.

As stated in the introduction, this technique was motivated by modelling the phenomenon of cancer invasion of tissue. A basic model of cancer invasion presented firstly (Trucu et al., 2013) consists of three main parts: 1) the macroscopic dynamics of the spatio-temporal distributions of cancer cells and ECM taking place on a macroscopic domain $\Omega(t_0)$; 2) the microdynamics of matrix degrading enzymes developed on the microscopic scale in the vicinity of the cancer interface $\partial\Omega(t_0)$, based on the biological background that cancer cells secrete various matrix degrading enzymes, e.g. MMPs (matrix metalloproteinases), and these enzymes helps pave the way for cancer invasion by destroying the surrounding tissue or extracellular matrix (ECM); 3) the regulation of the process of boundary relocation, governed by the microscopic dynamics and which determine the new initial conditions for the macroscopic dynamics at the next time step, which links the two scales together.

Furthermore, we extended the basic model by coupling the two-scale technique with a cancer invasion model introduced in Chaplain and Lolas (2005) and Andasari et al. (2011). It also consists of three main parts: the macroscopic dynamics, the microscopic dynamics, and the regulation of boundary relocation. However, instead of using a two-equation reaction diffusion system shown in equations (5.10) and (5.11), we applied a five PDE reaction-diffusion-taxis system shown in equations (5.25) to (5.29), the uPA system, as our macroscopic dynamics. Also, we replaced the simple reaction diffusion equation (equation (5.15)) with a system of three equations (5.35) to (5.37) in order to model the interactions and movement of the molecules involved in the proteolytic activities around the tumour boundary. This uPA system helps us simulate regulations and interactions between cancer cells, ECM molecules and cancer associated matrix degrading enzymes and describes more diverse dynamics at both the macroscopic and the microscopic scale, which is more biologically relevant and realistic. Through the simulation results, we confirm that the macro-microscopic technique has the ability to model tumour infiltrative growth patterns when coupled with proper macrodynamics and the microdynamics system.

In addition, we also discovered that this two-scale model has the property that changing the runtime of the macro-solver would affect not only the degree of heterogeneity of cancer cell distribution inside the tumour but also the deformations of the tumour boundary. In order to model the integrated process of cancer invasion at the tissue level and cellular level properly, we should be careful in choosing the right length of the total runtime and the time step of the macro-solver. For the specific problem we are trying to solve in this chapter (i.e. using uPA system to model the macroscopic dynamics and the microdynamics around the boundary, and link these two solvers by the regulation of the boundary movement), we set $\Delta t = 0.005,\ N = 500$ as an appropriate choice based on the computational experi-

ments we obtained so far.

Apart from the modelling point of view, another aspect of this technique is that we apply different numerical schemes on domains at different levels: a finite-difference scheme for the macrodynamics (macro-solver) and for the microdomain around the boundary a finite element scheme is employed (micro-solver). In this way, we could maintain the simplicity at the macro-level, and also the difficulty of dealing with a deformed geometry is overcome by computing functions element-by-element of the microdomains around the irregular interface.

Chapter 6

Modelling of cancer cell invasion: using the uPA system coupled with the macro-microscopic technique

6.1 Introduction

In the previous chapter, a two-scale mathematical model of cancer invasion was introduced which used the uPA system (i.e. urokinase plasminogen activation system) of Chaplain and Lolas (2005) and Andasari et al. (2011). We applied the extended macro-microscopic technique to investigate the protease-dependent invasion not only at the macroscopic level, but also at the microscopic level, simulating the two-scale model on both a macro-mesh and a micro-mesh in close proximity to the cancer interface. A very important discovery of the two-scale technique is that we need to choose the right timing to weld the macro-solver and micro-solver to model the

multiscale process of cancer invasion properly. In order to continue to explore this two-scale model, in this chapter we will focus on the effects that other parameters in the system have on the dynamics at both scales and the morphology of the tumour boundary.

In the following sections, we will first recall the two-scale model that coupled the uPA system with the macro-microscopic technique, presented without either the technical details, or explained notations, but with the key modelling concepts to give us a complete picture of the whole model. In Section 6.3, the adapted overall algorithm flow for the model will be given. Section 6.4 will show us the computational simulations that help us to analyse the effect of each variable, namely, ECM initial condition, the cancer cell diffusion coefficient, the threshold coefficient, and ECM proliferation & degradation rates. Finally, there is a discussion section.

6.2 The two-scale model of cancer invasion

As introduced in the previous chapter, the two-scale model consists mainly of three parts: the macroscopic dynamics, the microscopic dynamics, and the regulation of the boundary relocation as a link between the macrodynamics and microdynamics.

The uPA macrodynamics We recall that the dimensionless form of the equations of the uPA system held on spacial domain Y and temporal domain T are:

$$\frac{\partial c}{\partial t} = \underbrace{D_c \Delta c}_{\text{diffusion}} - \nabla \cdot [\ \underbrace{\chi_u c \nabla u}_{\text{uPA-chemo}} + \underbrace{\chi_p c \nabla p}_{\text{PAI-1-chemo}} + \underbrace{\chi_v c \nabla v}_{\text{VN-hapo}}] + \underbrace{\mu_1 c(1-c)}_{\text{profieration}},\ \mathbf{x} \in Y, \tag{6.1}$$

$$\frac{\partial v}{\partial t} = - \underbrace{\delta v m}_{\text{degradation}} + \underbrace{\phi_{21} u p}_{\text{uPA/PAI-1}} - \underbrace{\phi_{22} v p}_{\text{PAI-1/VN}} + \underbrace{\mu_2 v(1-v)}_{\text{proliferation}},\ \mathbf{x} \in Y, \tag{6.2}$$

$$\frac{\partial u}{\partial t} = \underbrace{D_u \Delta u}_{\text{diffusion}} - \underbrace{\phi_{31} p u}_{\text{uPA/PAI-1}} - \underbrace{\phi_{33} c u}_{\text{uPA/uPAR}} + \underbrace{\alpha_{31} c}_{\text{production}},\ \mathbf{x} \in Y, \tag{6.3}$$

$$\frac{\partial p}{\partial t} = \underbrace{D_p \Delta p}_{\text{diffusion}} - \underbrace{\phi_{41} p u}_{\text{uPA/PAI-1}} - \underbrace{\phi_{42} p v}_{\text{PAI-1/VN}} + \underbrace{\alpha_{41} m}_{\text{production}},\ \mathbf{x} \in Y, \tag{6.4}$$

$$\frac{\partial m}{\partial t} = \underbrace{D_m \Delta m}_{\text{diffusion}} + \underbrace{\phi_{52} p v}_{\text{PAI-1/VN}} + \underbrace{\phi_{53} c u}_{\text{uPA/uPAR}} - \underbrace{\phi_{54} m}_{\text{degradation}},\ \mathbf{x} \in Y, \tag{6.5}$$

where $t \in T$ and we denote cancer cell density by c, ECM density by v, uPA concentration by u, PAI-1 concentration by p and plasmin concentration by m. This reaction-diffusion-taxis system helps us to capture the main characteristic effects of the system in cancer progression and invasion by coupling the cancer cell migration with interactions of the components of the uPA system. The movements of the cancer cells are governed by diffusion, chemotaxis due to the presence of uPA (u) and the PAI-1(p) and haptotaxis due to vitronectin and other ECM components (v).

The uPA microdynamics Along the boundary of the tumour, we define a certain number of micro-domains that cover all the points on the interface. In order to investigate the process of cancer invasion at the cellular level, in each micro-domain ϵY on time interval $\tau \in [0, \tau_f]$, we use a system of three reaction-diffusion equations to model the interactions between the plasminogen activator uPA, the uPA inhibitor

PAI-1, and the proteolytic enzyme plasmin, namely,

$$\frac{\partial u}{\partial \tau} = \underbrace{D_u \Delta u}_{\text{diffusion}} - \underbrace{\phi_{31} p u}_{\text{uPA/PAI-1}} + \Big(\underbrace{\alpha_{31}}_{\text{production}} - \underbrace{\phi_{33} u}_{\text{uPA/uPAR}} \Big) f_1^{\epsilon Y}(y,\tau), \quad \mathbf{x} \in \epsilon Y, \tag{6.6}$$

$$\frac{\partial p}{\partial \tau} = \underbrace{D_p \Delta p}_{\text{diffusion}} - \underbrace{\phi_{41} p u}_{\text{uPA/PAI-1}} - \underbrace{\phi_{42} p \, f_2^{\epsilon Y}(y,\tau)}_{\text{PAI-1/VN}} + \underbrace{\alpha_{41} m}_{\text{production}}, \quad \mathbf{x} \in \epsilon Y, \tag{6.7}$$

$$\frac{\partial m}{\partial \tau} = \underbrace{D_m \Delta m}_{\text{diffusion}} + \underbrace{\phi_{52} p \, f_2^{\epsilon Y}(y,\tau)}_{\text{PAI-1/VN}} + \underbrace{\phi_{53} u \, f_1^{\epsilon Y}(y,\tau)}_{\text{uPA/uPAR}} - \underbrace{\phi_{54} m}_{\text{degradation}}, \quad \mathbf{x} \in \epsilon Y, \tag{6.8}$$

where,

$$f_1^{\epsilon Y}(y,\tau) = \begin{cases} \frac{1}{\lambda(B(y,2\epsilon) \cap \Omega(t_0))} \int\limits_{B(y,2\epsilon)\cap\Omega(t_0)} c\,(x, t_0+\tau)\, dx, & y \in \epsilon Y \cap \Omega(t_0) \\ 0, & \text{outside the cancer} \end{cases} \tag{6.9}$$

and,

$$f_2^{\epsilon Y}(y,\tau) = \frac{1}{\lambda(B(y,2\epsilon))} \int_{B(y,2\epsilon)} v\,(x, t_0+\tau)\, dx, \quad y \in \epsilon Y. \tag{6.10}$$

In the source terms above, $B(y,2\epsilon) := \{x \in Y | \, ||y-x||_\infty \leq 2\epsilon\}$ and $\lambda(\cdot)$ is the standard Lebesgue measure on $\mathbb{R}^N$. At this microscopic scale, the macroscopic dynamics of the cancer cells and ECM components were involved in the definition of source terms $f_1^{\epsilon Y}$ and $f_2^{\epsilon Y}$. In these source terms, we model the collective contribution of the cancer cells and ECM components distributed close to the boundary.

Regulation of the moving boundary There are three aspects of the process of the boundary relocation we consider in this model: 1) whether the microenvironment around the tumour boundary is suitable for cancer cells to migrate; 2) at the points on the boundary that certain conditions are satisfied for cell migration,

which direction they will move in; 3) and what is the magnitude of the velocity of the movement.

In order to determine whether a point in the set of boundary points $\{x^*_{\epsilon Y}\}$ will migrate or not, we define a local invading strength function as below:

$$q^*(A) := \frac{1}{\int_{\epsilon Y} m(y,\tau_f)dy}\int_A m(y,\tau_f)dy,\ A \in \Sigma(\epsilon Y)\ , \tag{6.11}$$

where $m(\cdot,\tau_f)$ represents the spatial distribution of plasmin at the final micro time τ_f after solving the microscopic uPA system (6.6)-(6.8). Actually $q^*(A)$ is a quantification of the amount of the matrix degrading enzyme plasmin in $\epsilon Y \backslash \Omega(t_0)$ relative to the total amount of plasmin concentration in ϵY. When this invading strength $q^*(A)$ at a point $x^*_{\epsilon Y}$ is below some threshold value $\omega(\beta, \epsilon Y) \in (0,1)$, then the point does not move. If $q^*(A) > \omega$ at a certain point $x^*_{\epsilon Y}$, we need the direction in which the cells would move and the magnitude of the movement as well.

Following the same line of arguments as the ones described in section 5.3.3, the formulation of the moving direction $\eta_{\epsilon Y}$ and the total displacement magnitude of the point $x^*_{\epsilon Y}$ are defined accordingly as:

$$\eta_{\epsilon Y} = x^*_{\epsilon Y} + \nu\sum_{l\in\mathcal{I}_\delta}\Big(\int_{\mathcal{D}_l} m(y,\tau_f)dy\Big)(y^*_l - x^*_{\epsilon Y}),\ \nu \in [0,\infty]\ , \tag{6.12}$$

and,

$$\xi_{\epsilon Y} := \sum_{l\in\mathcal{I}_\delta}\frac{\int_{\mathcal{D}_l} m(y,\tau_f)dy}{\sum\limits_{l\in\mathcal{I}_\delta}\int_{\mathcal{D}_l} m(y,\tau_f)dy}\big|\overrightarrow{x^*_{\epsilon Y}y_l}\big|\ , \tag{6.13}$$

where y_l denotes the front peaks of plasmin distribution at the final micro-time τ_f which is obtained though the uPA microscopic dynamics.These selected plasmin peaks at the front of its distribution $m(\cdot,\tau_f)$ are located at the furthest possible Euclidean distance with respect to $x^*_{\epsilon Y}$ and the concentration of plasmin at peak

points is above the mean value of the entire mass of plasmin produced on $\epsilon Y \backslash \Omega(t_0)$.

6.3 The overall computational algorithm

- **Step 1.** At the initial time t_0, first of all, we discretise the macrodomain $[a, b] \times [c, d]$ by

$$a = x_0, \ldots, x_i = a + i\Delta x, \ldots, x_m = a + m\Delta x = b,$$
$$c = y_0, \ldots, y_j = c + j\Delta y, \ldots, y_n = c + n\Delta y = d.$$

  where $\Delta x = \Delta y = h$, $\epsilon = 2h$ and let $a = c = 0, c = d = 4$. Also, we number each point on the macrodomain, record their coordinates all sorts of data of the domain that might be used later.

- **Step 2.** Define initial conditions for components in the uPA system on the macro-domain including cancer cells c, ECM and its components v, the plasminogen activator u, the uPA inhibitor p and plasmin m, namely,

$$\begin{aligned}
c(\mathbf{x}, t_0) &=: c_0(\mathbf{x}), && \mathbf{x} \in \Omega(t_0),\\
v(\mathbf{x}, t_0) &=: v_0(\mathbf{x}), && \mathbf{x} \in Y,\\
u(\mathbf{x}, t_0) &=: v_0(\mathbf{x}), && \mathbf{x} \in Y,\\
p(\mathbf{x}, t_0) &=: v_0(\mathbf{x}), && \mathbf{x} \in Y\\
m(\mathbf{x}, t_0) &=: v_0(\mathbf{x}), && \mathbf{x} \in Y,
\end{aligned}$$

- **Step 3.** Start the main time loop (from time stage 1 to certain time stage

N), and at the current time stage,

a) Run the macro-solver, which applies the finite difference scheme as in Appendix 8.1, to solve the equations (6.1) to (6.5) of uPA system by using the values at the current time $c^n_{i,j}$, $v^n_{i,j}$, $u^n_{i,j}$, $p^n_{i,j}$ and $m^n_{i,j}$, where $i, j = 1, ...q$ to obtain the solution of the system at the next time step $c^{n+1}_{i,j}$, $v^{n+1}_{i,j}$, $u^{n+1}_{i,j}$, $p^{n+1}_{i,j}$, and $m^{n+1}_{i,j}$, where $i, j = 1, ...q$. The choices of the runtime length of the macro-solver and the size of the time step is important, in this model, we choose $\Delta t = 0.005,\ N = 500$.

b) Run the micro-solver, in which we loop over each point that is on the boundary of the tumour at the previous time, and at an arbitrary boundary point,

   i. Define the micro-domain ϵY centring at the current point on the boundary, which consists of nine points on macrodomain. For simplicity, we first construct the domain on $[0, \epsilon] \times [0, \epsilon]$ and we uniformly decompose the domain into sixty-four square elements consists of eighty-one points in total. On this micro-domain we compute the source terms $f_1^{\epsilon Y}$ and $f_2^{\epsilon Y}$ values for the points that are also on macro mesh first, and then by interpolation, we obtain the source term values and the spatial distributions of u, p and m in the uPA system on a finer mesh. (See Figure 6.1).

   ii. On the microdomain ϵY, apply the finite element method to solve the microscopic dynamics equations (6.6) to (6.8), to obtain the spatial distribution of the matrix degrading enzyme plasmin at the final microtime $m(\cdot, \tau_f)$ (involving a proposed midpoint rule formula for the integral source terms, and for time integration a trapezoidal predictor-corrector) , which will be used later in the regulation func-

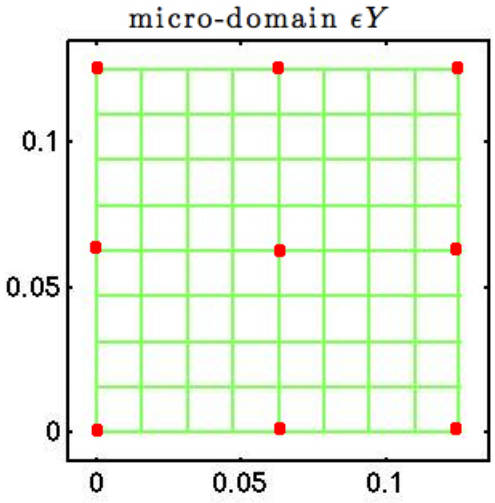

Figure 6.1: *Plots showing the microdomain ϵY used in the numerical scheme and each microdomian contains eighty-one points in total and gives us sixty-four square elements. The red points are the nine points that are also on macrodomain, the solutions of the macrodynamics are known on these points by running macro-solver. We calculate the spacial distribution of components in uPA system on other points in this microdomain by interpolation.*

tions of cancer cells' movement. For micro-solver, we set the length of runtime is 0.1 (i.e., we solve the microscopic dynamics on the microdomain in the time interval $[0, 0.1]$ and $\tau_f = 0.1$) and the time step $\Delta\tau = 10^{-9}$.

iii. Translocate the coordinates of this microdomain $[0, \epsilon] \times [0, \epsilon]$ back to where the micro spatial position was before.

iv. Compute the probability function $q(x^*_{\epsilon Y})$ introduced in equation (6.11), which is crucial for determining the relocation of the new boundary.

v. Check if the microenvironment induced probability $q^*(x^*_{\epsilon Y})$ is greater than some threshold value $\omega_{\epsilon Y} \in (0, 1)$, we furthermore compute the direction $\eta_{\epsilon Y}$ and magnitude $\xi_{\epsilon Y}$ of the movement as mentioned in equation (6.12) and (6.13) if needed.

c) After running both the macro-solver and micro-solver at the current time stage, we obtain a new macroscopic distribution for uPA system components, $c^{n+1}_{i,j}$, $v^{n+1}_{i,j}$, $u^{n+1}_{i,j}$, $p^{n+1}_{i,j}$, and $m^{n+1}_{i,j}$, where $i, j = 1, ...q$. Also for each midpoint $x^*_{\epsilon Y}$ on the tumour boundary, we have the possibility $q^*(x^*_{\epsilon Y})$, direction $\eta_{\epsilon Y}$ and magnitude $\xi_{\epsilon Y}$ of their movement, therefore we

could use all these information to determine the new position $\widetilde{x^*_{\epsilon Y}}$ and the points remain where they were on the cancer interface $\partial\Omega(t_0 + \Delta t)$. This is schematically shown in Figure 6.2.

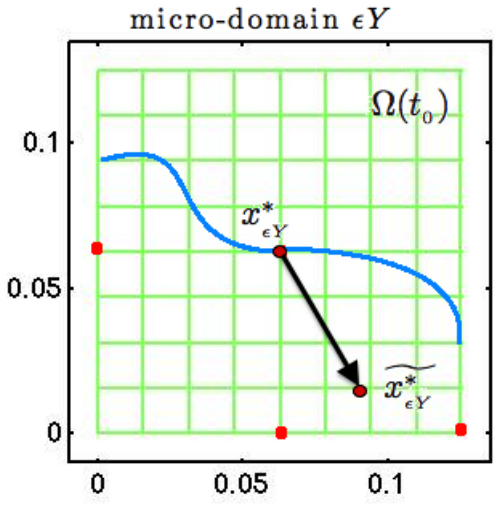

Figure 6.2: *Plot shows the relocation of one point on the boundary moves to a new spatial position in the microdomain ϵY.*

d) Finally, by using the approximations below, replace the initial values of cancer and ECM distribution in macroscopic dynamics with the solutions $c^{n+1}_{i,j}$, $v^{n+1}_{i,j}$, $u^{n+1}_{i,j}$, $p^{n+1}_{i,j}$, and $m^{n+1}_{i,j}$, where $i, j = 1, ...q$.

$$c(x_{i,j}, t_0 + \Delta t) = \begin{cases} c^{n+1}_{i,j}, & x_{i,j} \in \overline{\Omega(t_0)}, \\ \frac{1}{4}(c^{n+1}_{i-1,j} + c^{n+1}_{i+1,j} + c^{n+1}_{i,j-1} + c^{n+1}_{i,j+1}), & x_{i,j} \in \overline{\mathbf{B}(\overline{\Omega(t_0)}, h)} \backslash \overline{\Omega(t_0)}, \\ 0, & x_{i,j} \notin \overline{\mathbf{B}(\overline{\Omega(t_0)}, h)}, \end{cases}$$

$$
\begin{aligned}
v(x_{i,j}, t_0 + \Delta t) &= v_{i,j}^{n+1}, \\
u(x_{i,j}, t_0 + \Delta t) &= u_{i,j}^{n+1}, \\
p(x_{i,j}, t_0 + \Delta t) &= p_{i,j}^{n+1}, \\
m(x_{i,j}, t_0 + \Delta t) &= m_{i,j}^{n+1},
\end{aligned}
\tag{6.14}
$$

- **Step 4.** Using the new initial conditions for macroscopic dynamics, continue the invasion process by coupling the new macroprocess on the expand domain $\Omega(t_0 + \Delta t)$ with the corresponding of MDEs micro processes occurring on its boundary, which means repeating the Step 3 above with new initial conditions for macroscopic dynamics and new boundary of cancer.

6.4 Computational simulation results

The complete multiscale model of cancer invasion is numerically solved in a rectangular region $Y := [0, 4] \times [0, 4]$ and it was assumed that the cancer initially occupied a region $\Omega(0)$ within Y, taken to be a disc centred at $(2, 2)$ with the radius $r = 0.5$. We use the discretisation of the entire domain Y that applies the uniform spatial mesh size $h = 0.03125$ and $\epsilon = 2h = 0.0625$, which gives us a mesh of Y with 64×64 elements and each element is a microdomain ϵY. Figure (6.3) shows the central part of the domain Y, containing the cancer region $\Omega(0)$, and the macroscopic uniformly discretised mesh on domain Y. One of the overlapping microdomains ϵY along the boundary is shown in green, in the right-hand side of the figure. All the effort in assessing the microdynamics is aimed at ultimately describing the potential spatial movement of this midpoint $x^*_{\epsilon Y}$.

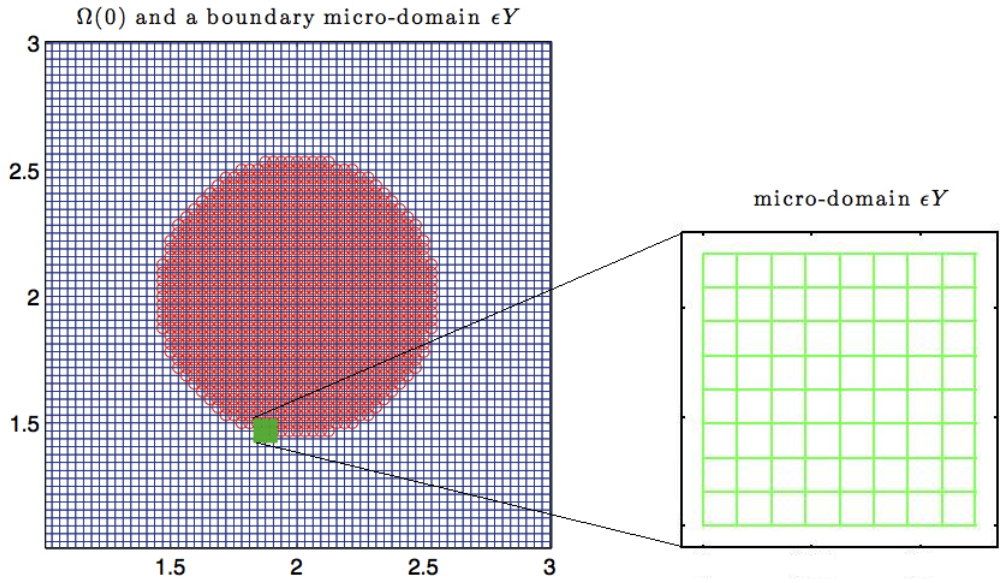

Figure 6.3: *Plots showing the macro- and microdomains used in the numerical scheme. The left figure shows the central part of the uniformly discretised domain* $Y = [0,4] \times [0,4]$*, which contains the initial cancer region* $\Omega(0)$ *(red circle). One boundary micro-domain* ϵY *is shown in green, and a detailed view of this is given in the right-hand figure. This is adapted from the original paper Trucu et al. (2013).*

The initial conditions for the macroscopic uPA system are:

$$\begin{aligned} c(x,0) &= \frac{\exp\big(-\frac{||x-(2,2)||_2^2}{\sqrt{\Delta x \Delta y}}\big) - \exp\big(-\frac{(1-\Delta x)(1-\Delta y)}{\sqrt{\Delta x \Delta y}}\big)}{2}, && x \in \Omega(0), \\ u(x,0) &= 1 - \frac{1}{2}c(x,0), && x \in Y, \\ p(x,0) &= \frac{1}{2}c(x,0), && x \in Y, \\ m(x,0) &= \frac{1}{20}c(x,0), && x \in Y. \end{aligned} \tag{6.15}$$

We applied two types (i.e., homogeneous and heterogeneous) of initial condition of

ECM in our model as following,

Homogeneous: (6.16)

$$v(x,0) = 1 - c(x,0), \qquad x \in Y.$$

Heterogeneous: (6.17)

$$v(x,0) = \frac{1 + 0.3\sin\left(4\pi||x||_2\right) + \sin\left(4\pi||(4,0) - x||_2\right)}{2}, \qquad x \in Y.$$

Since the threshold, which controls whether or not a point on the boundary can move, depends on the local composition of the ECM, thus we define our threshold function $\omega(\beta, \epsilon Y)$ as follows:

$$\omega(\beta,\epsilon Y) := \begin{cases} \sin\left(\frac{\pi}{2}\left(1 - \frac{1}{\beta}\frac{v_{\omega(t_0)}(x^*_{\epsilon Y}, t_0+\Delta t)}{\sup\limits_{\xi\in\partial\Omega(t_0)} v_{\Omega(t_0)}(\xi, t_0+\Delta t)}\right)\right), & \text{if } \frac{v_{\omega(t_0)}(x^*_{\epsilon Y}, t_0+\Delta t)}{\sup\limits_{\xi\in\partial\Omega(t_0)} v_{\Omega(t_0)}(\xi, t_0+\Delta t)} \leq \beta, \\ \sin\left(\frac{\pi}{2(1-\beta)}\left(\frac{v_{\omega(t_0)}(x^*_{\epsilon Y}, t_0+\Delta t)}{\sup\limits_{\xi\in\partial\Omega(t_0)} v_{\Omega(t_0)}(\xi, t_0+\Delta t)} - \beta\right)\right), & \text{if } \frac{v_{\omega(t_0)}(x^*_{\epsilon Y}, t_0+\Delta t)}{\sup\limits_{\xi\in\partial\Omega(t_0)} v_{\Omega(t_0)}(\xi, t_0+\Delta t)} > \beta, \end{cases} \tag{6.18}$$

where $\beta \in (0,1)$ is a parameter that controls the 'optimal level' of EMC density and consider this as being the indicator of the most favourable invasion conditions at the level of tumour and tissue microenvironment. For a homogeneous ECM initial condition, when the ratio between local ECM density at midpoint $x^*_{\epsilon Y}$ and the maximum level of ECM is larger than parameter β, then we reduce by 60% of the threshold function presented in equation (6.18).

The following figures show the simulation results of the evolving cancer cell and ECM spatial distributions and of the invasive tumour boundary at time stages 0, 20, 40, 60. The images are presented in two columns: the left columns are for the cancer cell distribution and the right ones for that of ECM, but all of them include the tumour boundary. The parameter set in the uPA system we are using is the same one mentioned previously, parameter set $\mathscr{P}$ (see (5.49)). However we

do change the diffusion coefficient of cancer cells D_n, ECM proliferation rate μ_2 and ECM degradation rate δ which give us different deformation dynamics. Also, we use several values of β, the parameter that controls the 'optimal level' of ECM density, to regulate the conditions of cancer invasion imposed on the microenvironment. We will split the results into four groups to analyse the effect of each variable, namely, ECM initial condition, cancer cell diffusion coefficient, threshold coefficient, and ECM proliferation & degradation rates.

ECM initial condition. In order to investigate what effect different ECM initial conditions have on the dynamics of the model, we apply the same reduced threshold function for both homogeneous and heterogeneous ECM scenario. From the results in Figures 6.4 - 6.5 and Figures 6.6 - 6.7, we can see that the heterogeneous ECM initial condition leads to a more 'fingered' spreading of the tumour compared with what we have in the homogeneous ECM.

Cancer cell diffusion coefficient D_c**.** As was demonstrated in Hillen and Painter (2013) and Painter and Hillen (2011), the chemotaxis terms in the cancer cell equation (4.60) are the main causes of the occurrence of heterogeneous patterns. Therefore, if the cancer cell diffusion coefficient D_c is increased to one order magnitude larger than the chemotaxis coefficients (χ_u and χ_p), which becomes the dominant mechanism of cell movement, then no heterogeneous dynamics will occur inside the tumour as shown in Figures 6.8 - 6.9. In Figures 6.10 - 6.11, the chemotaxis coefficients are one order of magnitude larger than the diffusion coefficient, and we obtain a heterogeneous pattern formation of cancer cells, which leads to a more dynamic boundary deformation of the tumour.

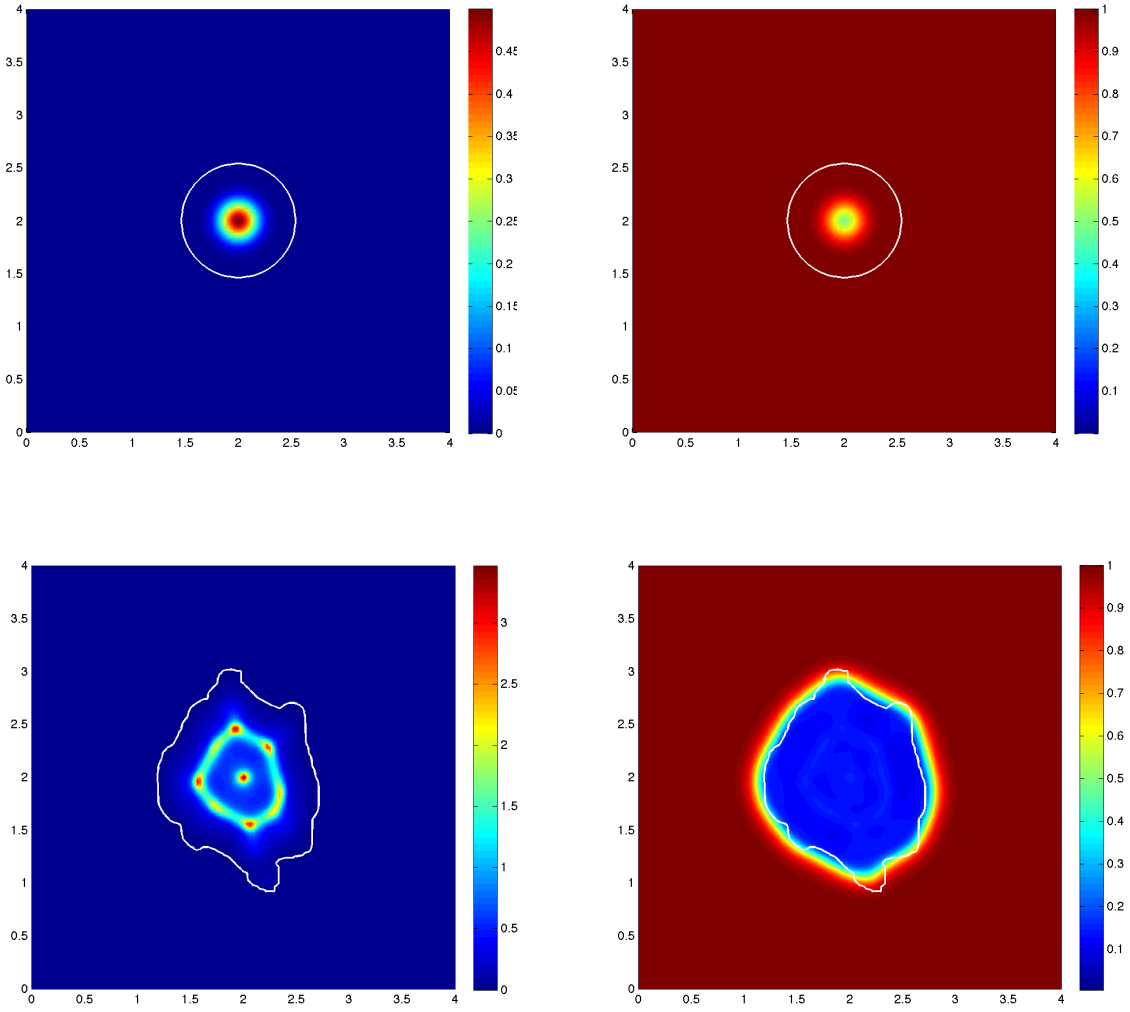

Figure 6.4: *Simulation results showing distributions of cancer cells (left column) and ECM (right column) and the invasive boundary of the tumour (white line) at various macro-micro stages: Stage 0, 20.* $D_c = 4.3 \times 10^{-3}$, $\beta = 0.775$, $\mu_2 = 0.01$ *and* $\delta = 1.5$.

Threshold coefficient β**.** Figure 6.12 to Figure 6.21 shows us the results of varying the threshold coefficient $\beta \in (0.75, 0.8)$ accordingly. Since β controls the 'optimal level' of EMC density for cancer cells to migrate, its variation gives us different invasion morphologies as expected. The comparison between Figures 6.12

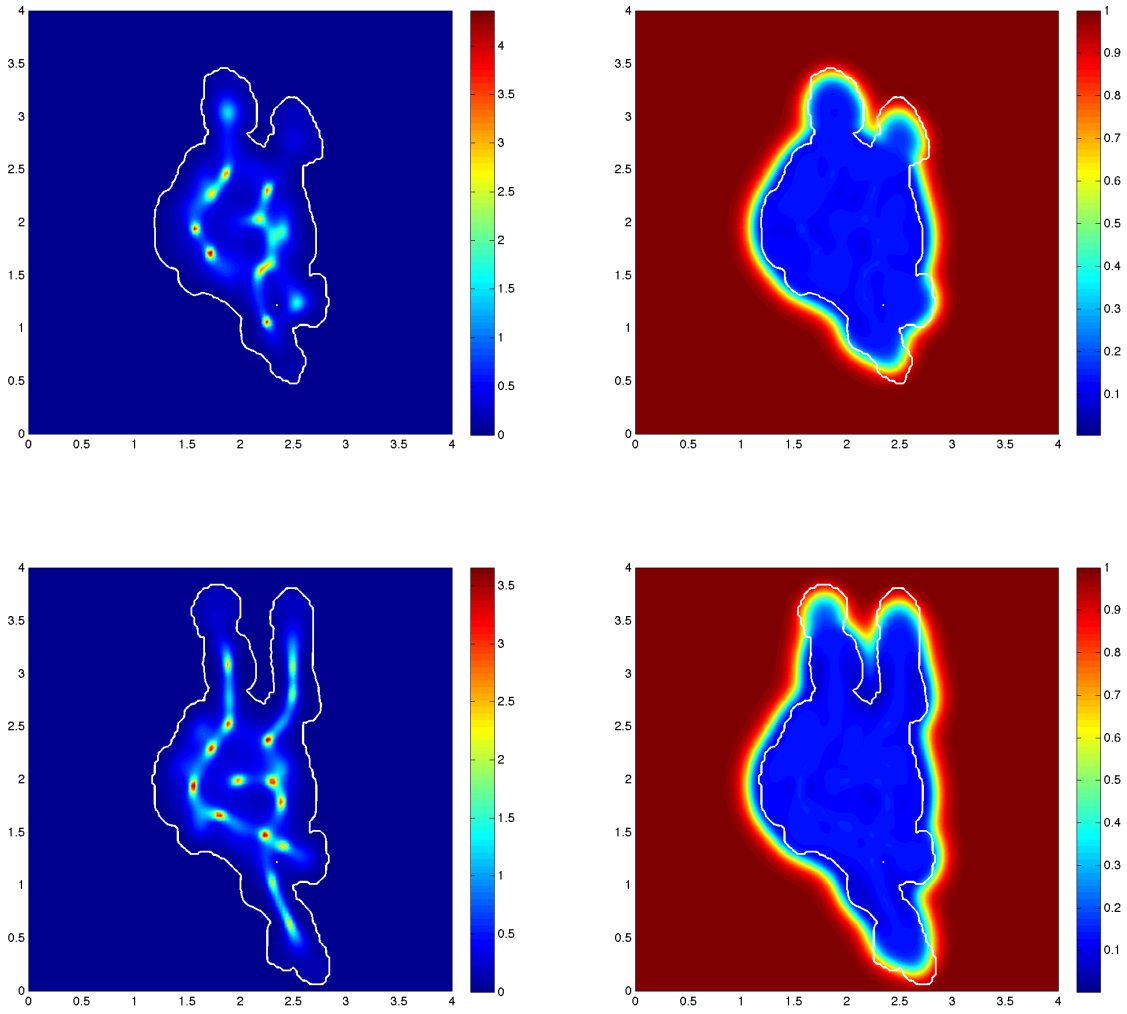

Figure 6.5: *Simulation results showing distributions of cancer cells (left column) and ECM (right column) and the invasive boundary of the tumour (white line) at various macro-micro stages: Stage 40, 60.* $D_c = 4.3 \times 10^{-3}$, $\beta = 0.775$, $\mu_2 = 0.01$ *and* $\delta = 1.5$.

- 6.13, Figures 6.16 - 6.17, Figures 6.18 - 6.19 and Figures 6.20 - 6.21 give us a clue that an increase in β very likely reduces the number of 'roads' that cancer cells will invade into. However, this is not always the case. Figures 6.14 - 6.15 and Figures 6.16 - 6.17 show us that although β is larger, it is still possible that more

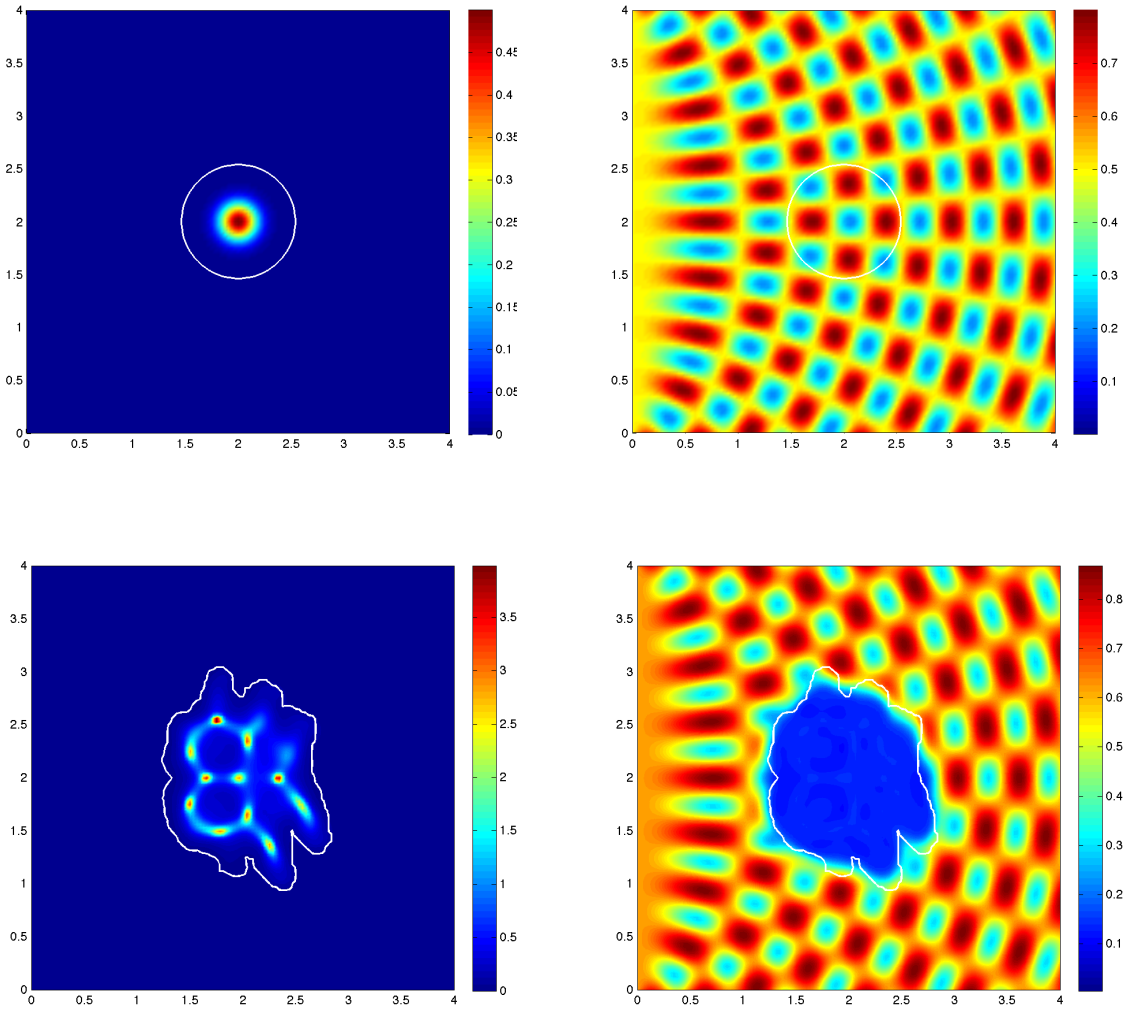

Figure 6.6: *Simulation results showing distributions of cancer cells (left column) and ECM (right column) and the invasive boundary of the tumour (white line) at various macro-micro stages: Stage 0, 20.* $D_c = 4.3 \times 10^{-3}$, $\beta = 0.775$, $\mu_2 = 0.01$ *and* $\delta = 1.5$.

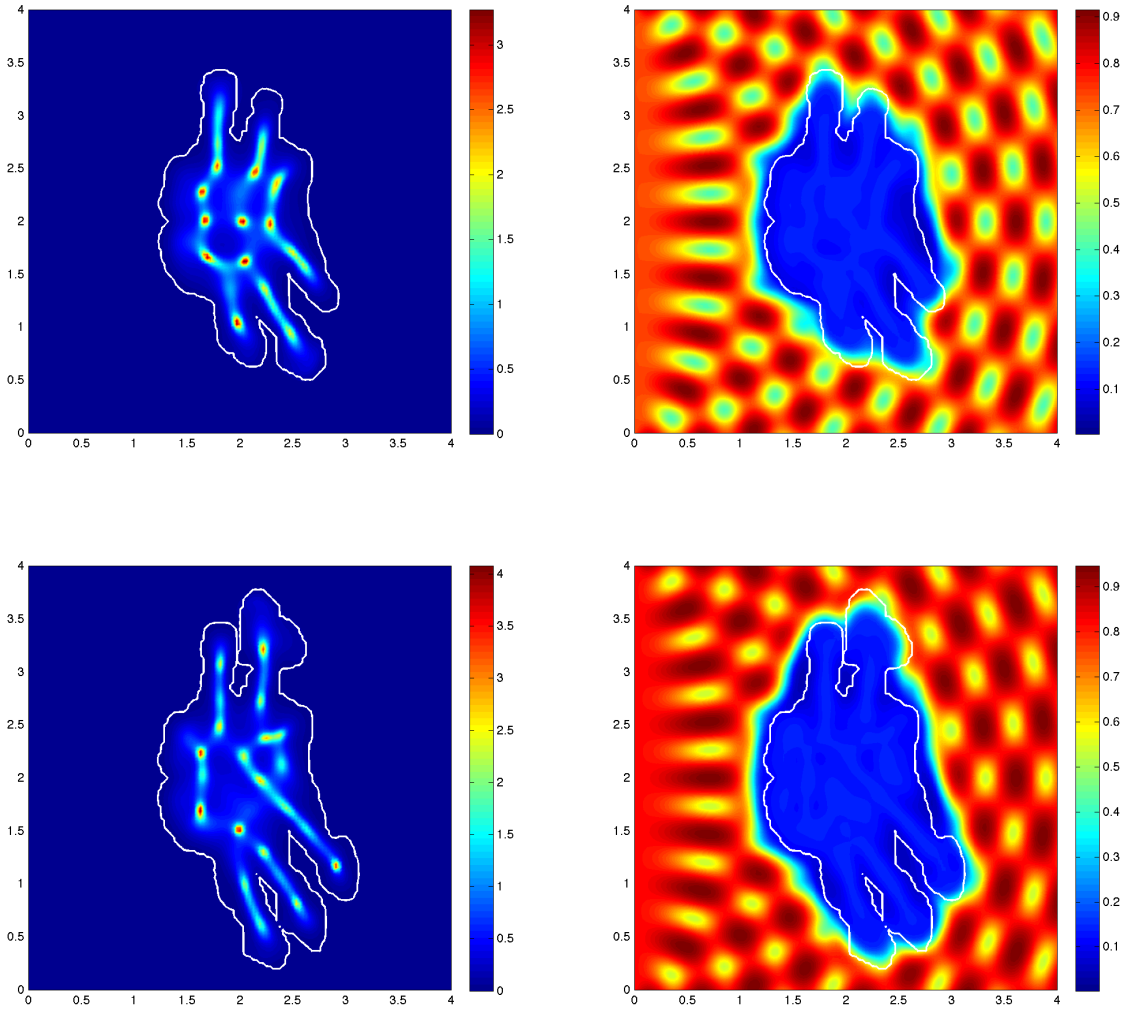

Figure 6.7: *Simulation results showing distributions of cancer cells (left column) and ECM (right column) and the invasive boundary of the tumour (white line) at various macro-micro stages: Stage 40, 60.* $D_c = 4.3 \times 10^{-3}$, $\beta = 0.775$, $\mu_2 = 0.01$ *and* $\delta = 1.5$.

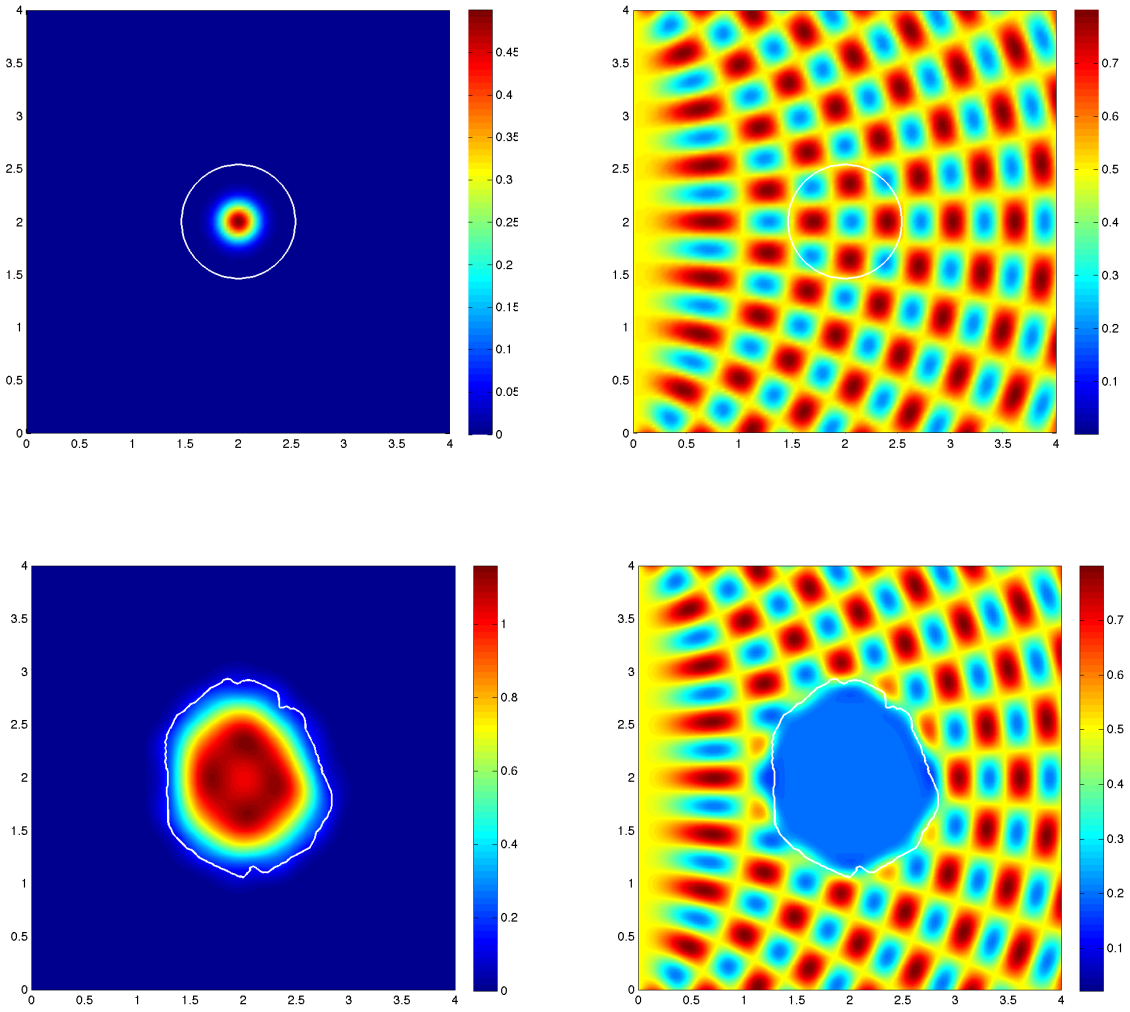

Figure 6.8: *Simulation results showing distributions of cancer cells (left column) and ECM (right column) and the invasive boundary of the tumour (white line) at various macro-micro stages: Stage 0, 20.* $D_c = 1.4 \times 10^{-2}$, $\beta = 0.775$, $\mu_2 = 0$ *and* $\delta = 0.75$.

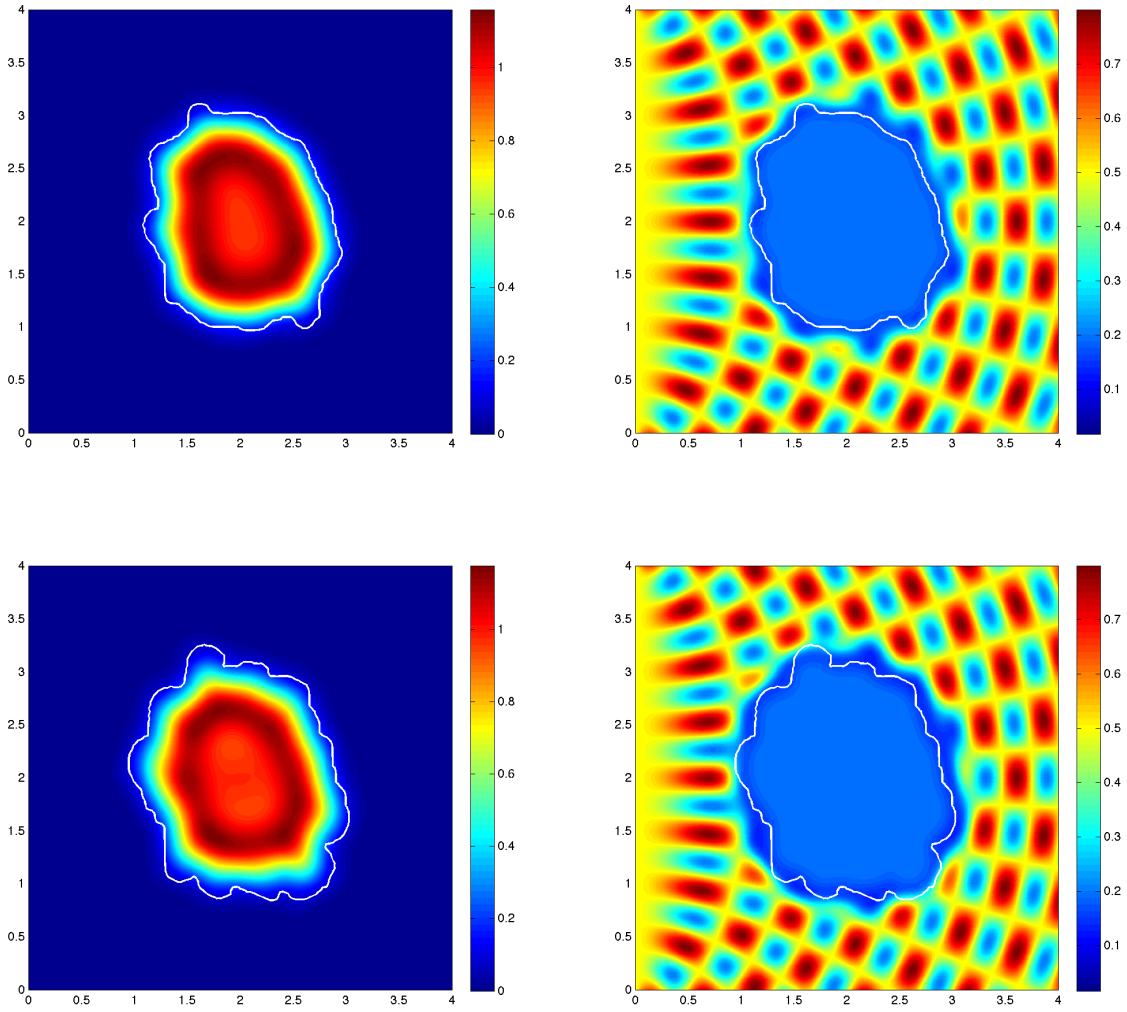

Figure 6.9: *Simulation results showing distributions of cancer cells (left column) and ECM (right column) and the invasive boundary of the tumour (white line) at various macro-micro stages: Stage 40, 60.* $D_c = 1.4 \times 10^{-2}$, $\beta = 0.775$, $\mu_2 = 0$ *and* $\delta = 0.75$.

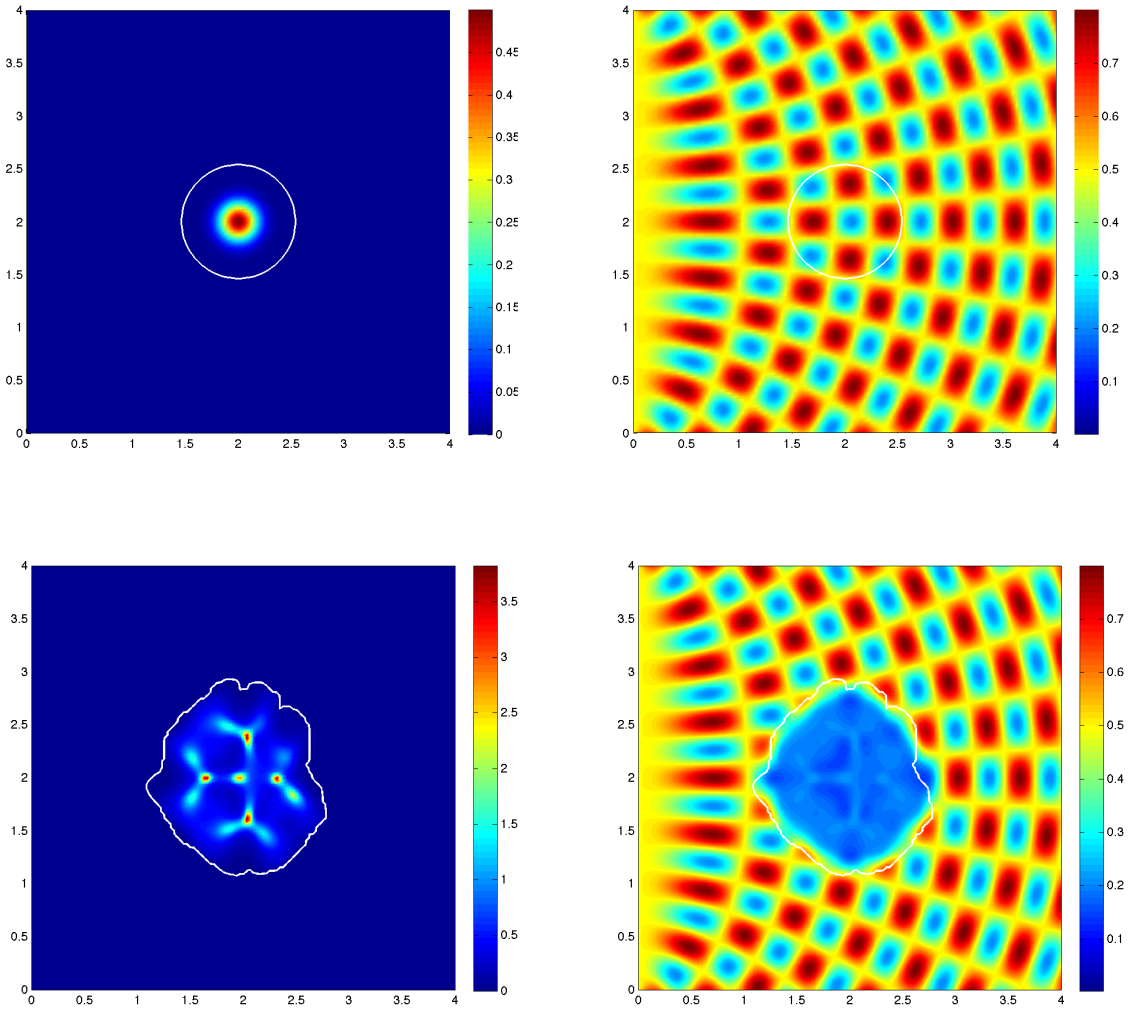

Figure 6.10: *Simulation results showing distributions of cancer cells (left column) and ECM (right column) and the invasive boundary of the tumour (white line) at various macro-micro stages: Stage 0, 20.* $D_c = 4.3 \times 10^{-3}$, $\beta = 0.775$, $\mu_2 = 0$ *and* $\delta = 0.75$.

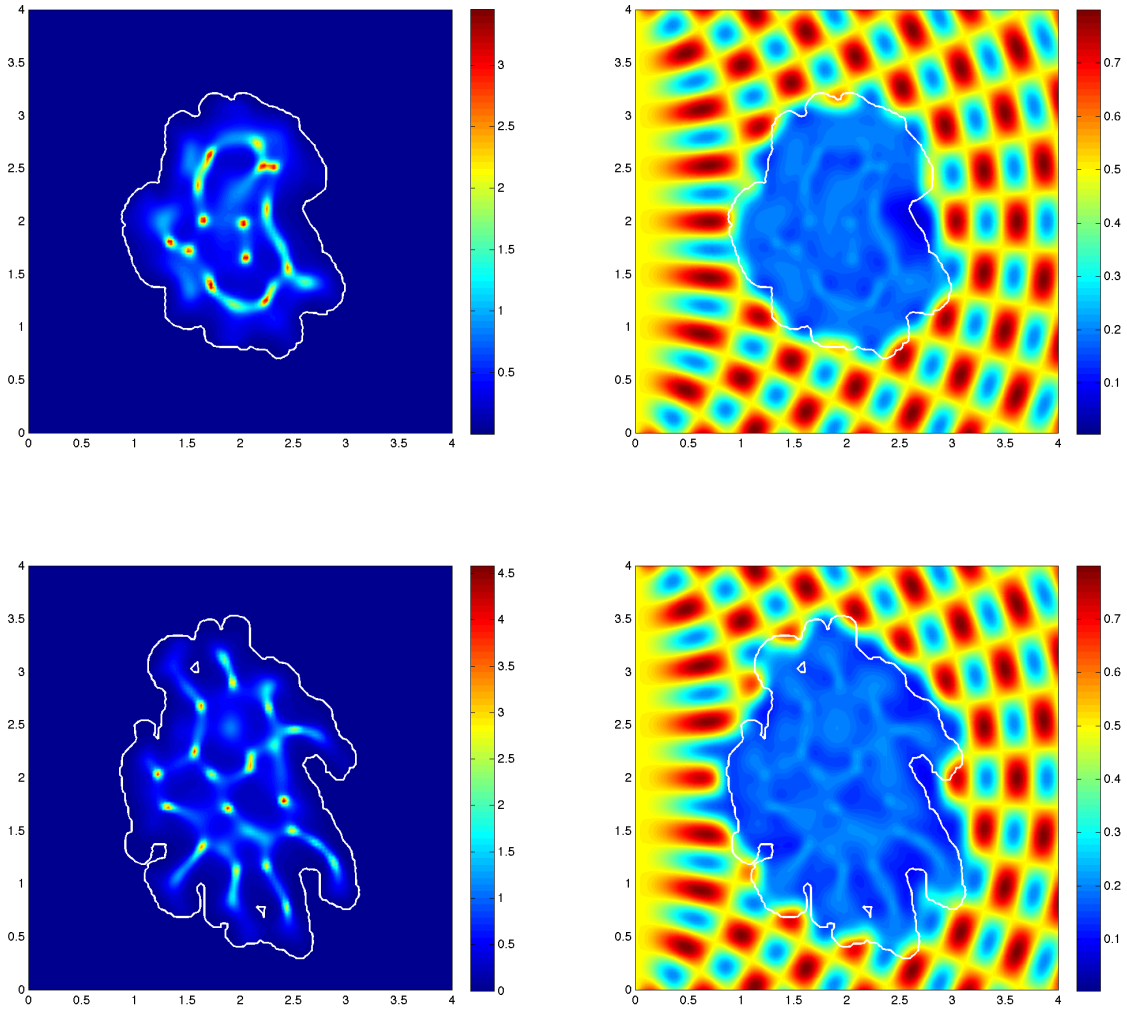

Figure 6.11: *Simulation results showing distributions of cancer cells (left column) and ECM (right column) and the invasive boundary of the tumour (white line) at various macro-micro stages: Stage 40, 60.* $D_c = 4.3 \times 10^{-3}$, $\beta = 0.775$, $\mu_2 = 0$ *and* $\delta = 0.75$.

'fingers' will occur during the boundary deformation.

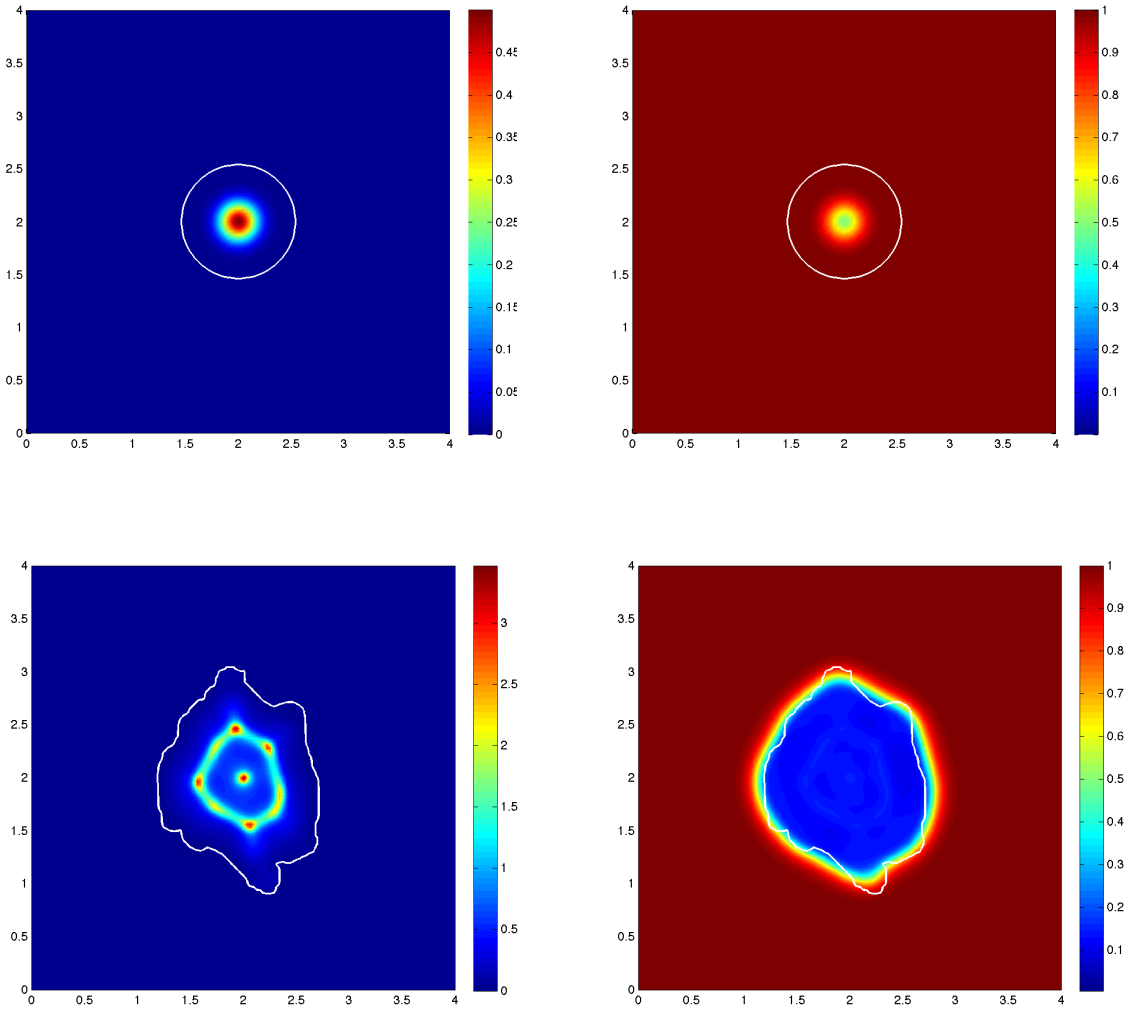

Figure 6.12: *Simulation results showing distributions of cancer cells (left column) and ECM (right column) and the invasive boundary of the tumour (white line) at various macro-micro stages: Stage 0, 20.* $D_c = 4.3 \times 10^{-3}$, $\beta = 0.75$, $\mu_2 = 0.01$ *and* $\delta = 1.5$.

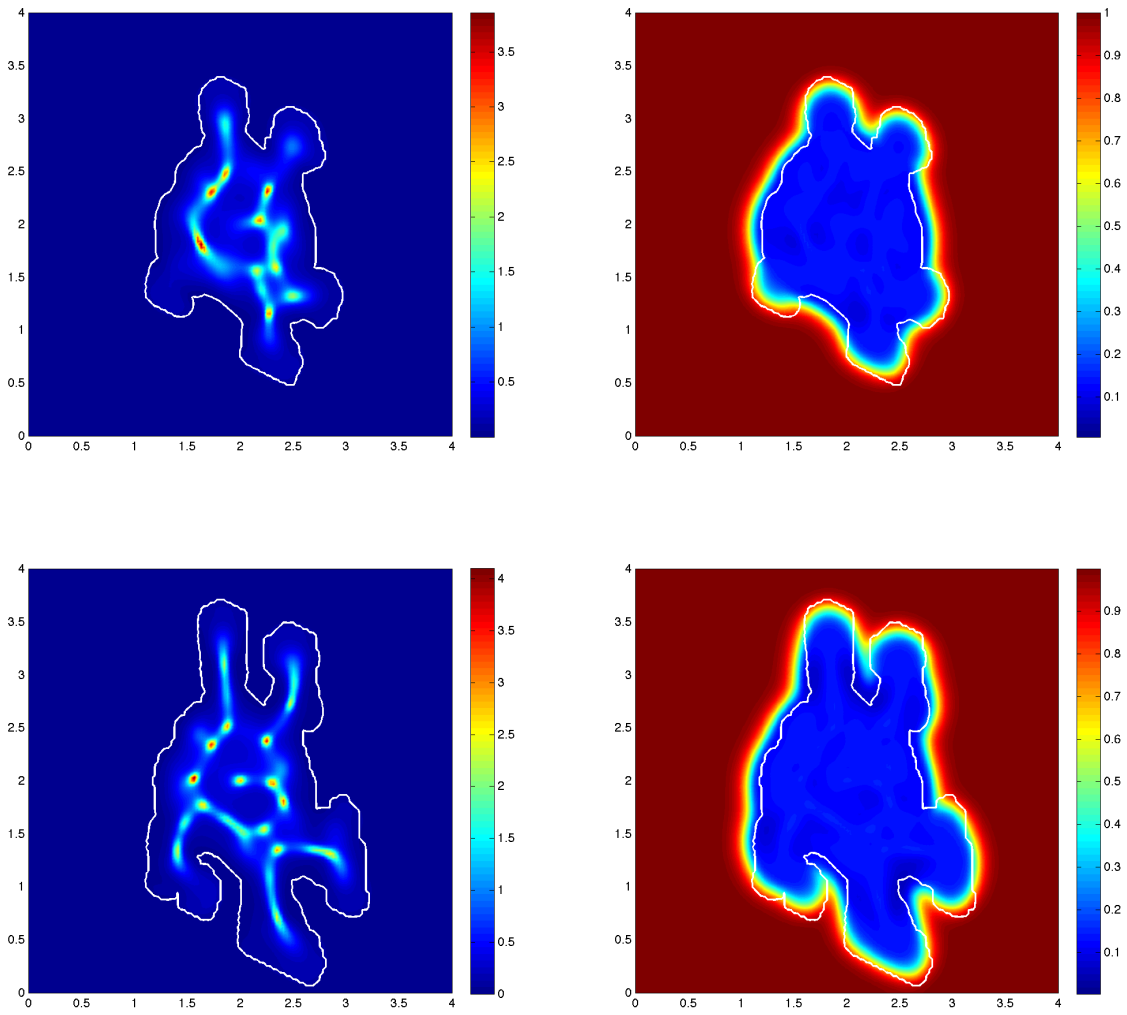

Figure 6.13: *Simulation results showing distributions of cancer cells (left column) and ECM (right column) and the invasive boundary of the tumour (white line) at various macro-micro stages: Stage 40, 60.* $D_c = 4.3 \times 10^{-3}$, $\beta = 0.75$, $\mu_2 = 0.01$ *and* $\delta = 1.5$.

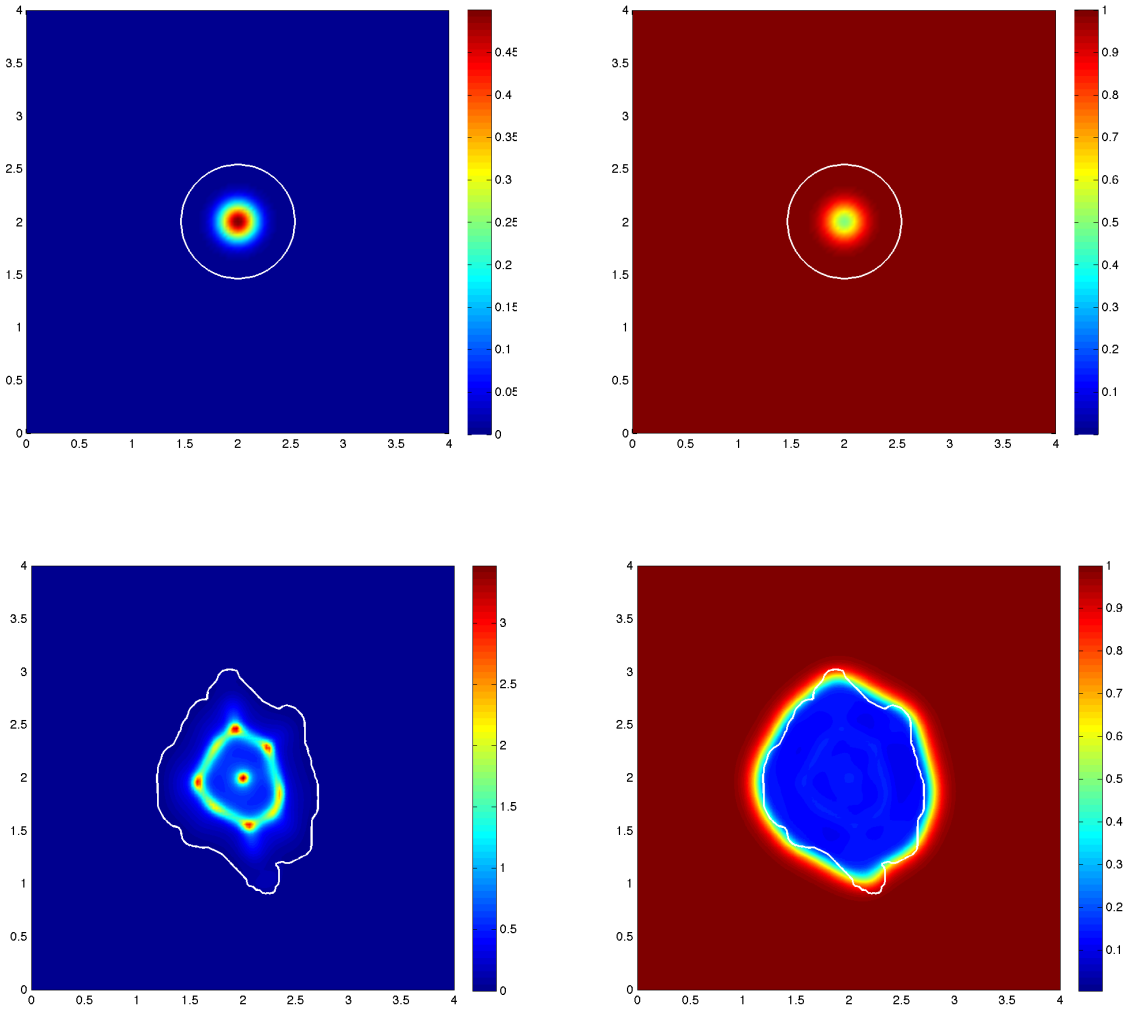

Figure 6.14: *Simulation results showing distributions of cancer cells (left column) and ECM (right column) and the invasive boundary of the tumour (white line) at various macro-micro stages: Stage 0, 20.* $D_c = 4.3 \times 10^{-3}$, $\beta = 0.7625$, $\mu_2 = 0.01$ *and* $\delta = 1.5$.

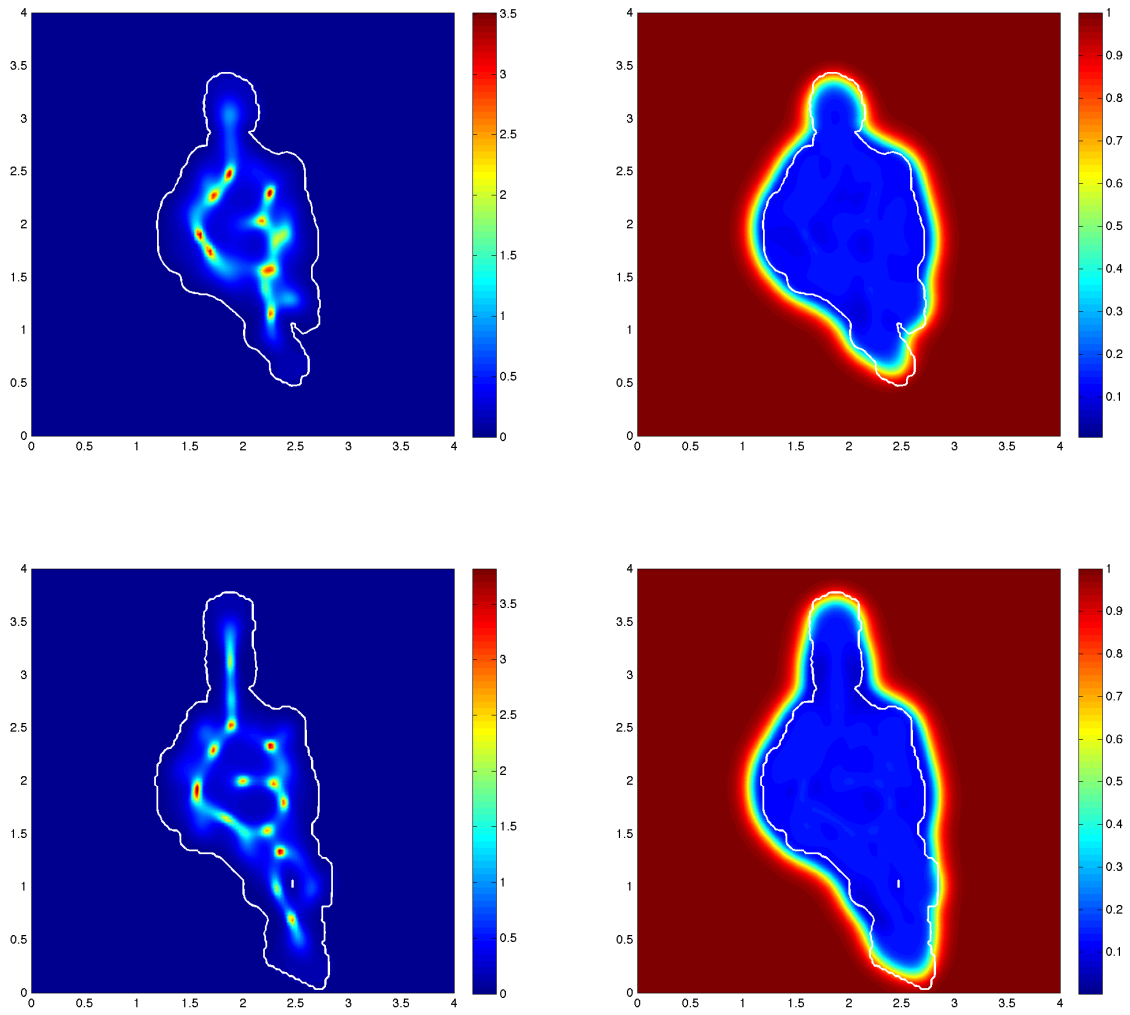

Figure 6.15: *Simulation results showing distributions of cancer cells (left column) and ECM (right column) and the invasive boundary of the tumour (white line) at various macro-micro stages: Stage 40, 60.* $D_c = 4.3 \times 10^{-3}$, $\beta = 0.7625$, $\mu_2 = 0.01$ *and* $\delta = 1.5$.

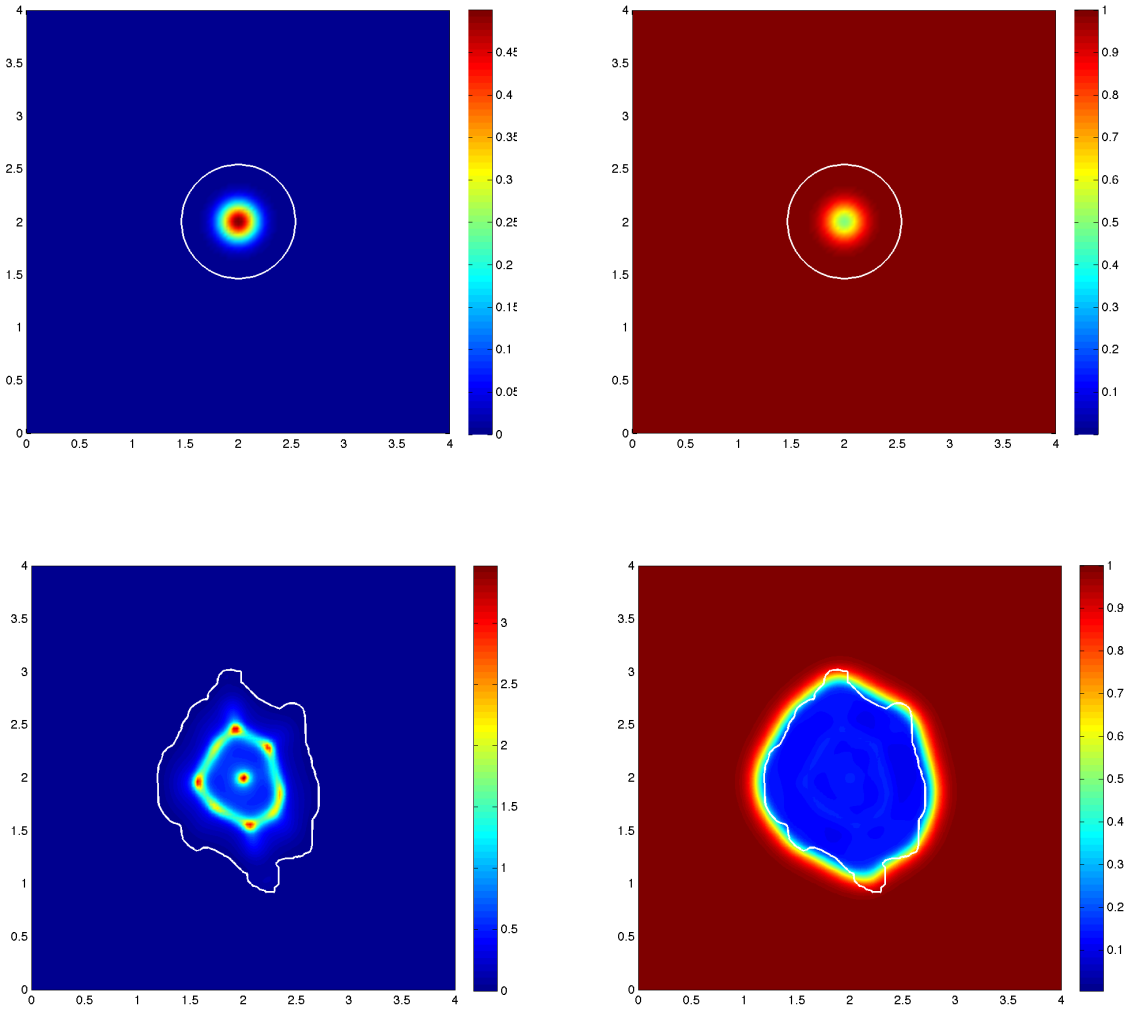

Figure 6.16: *Simulation results showing distributions of cancer cells (left column) and ECM (right column) and the invasive boundary of the tumour (white line) at various macro-micro stages: Stage 0, 20.* $D_c = 4.3 \times 10^{-3}$, $\beta = 0.775$, $\mu_2 = 0.01$ *and* $\delta = 1.5$.

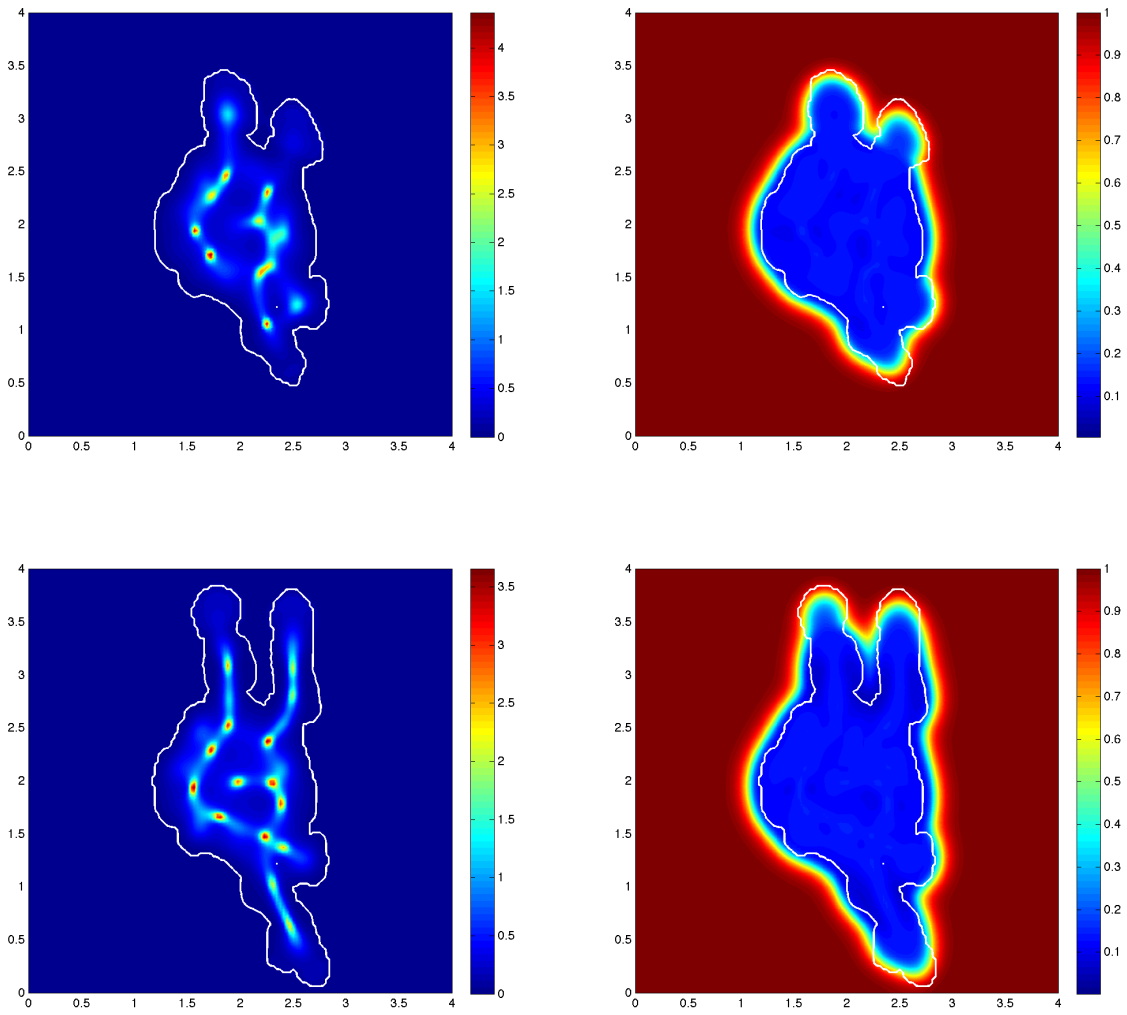

Figure 6.17: *Simulation results showing distributions of cancer cells (left column) and ECM (right column) and the invasive boundary of the tumour (white line) at various macro-micro stages: Stage 40, 60.* $D_c = 4.3 \times 10^{-3}$, $\beta = 0.775$, $\mu_2 = 0.01$ *and* $\delta = 1.5$.

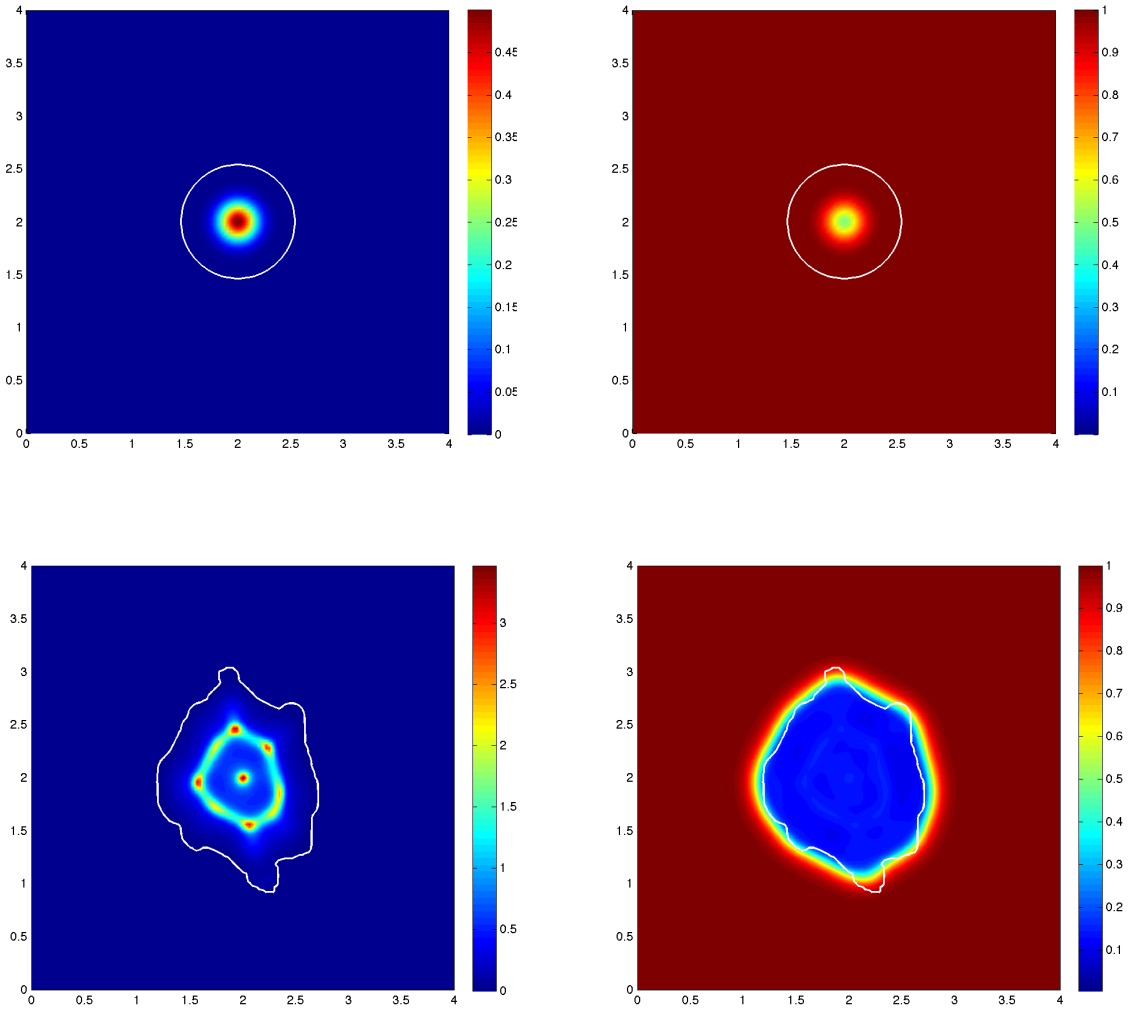

Figure 6.18: *Simulation results showing distributions of cancer cells (left column) and ECM (right column) and the invasive boundary of the tumour (white line) at various macro-micro stages: Stage 0, 20.* $D_c = 4.3 \times 10^{-3}$, $\beta = 0.7875$, $\mu_2 = 0.01$ *and* $\delta = 1.5$.

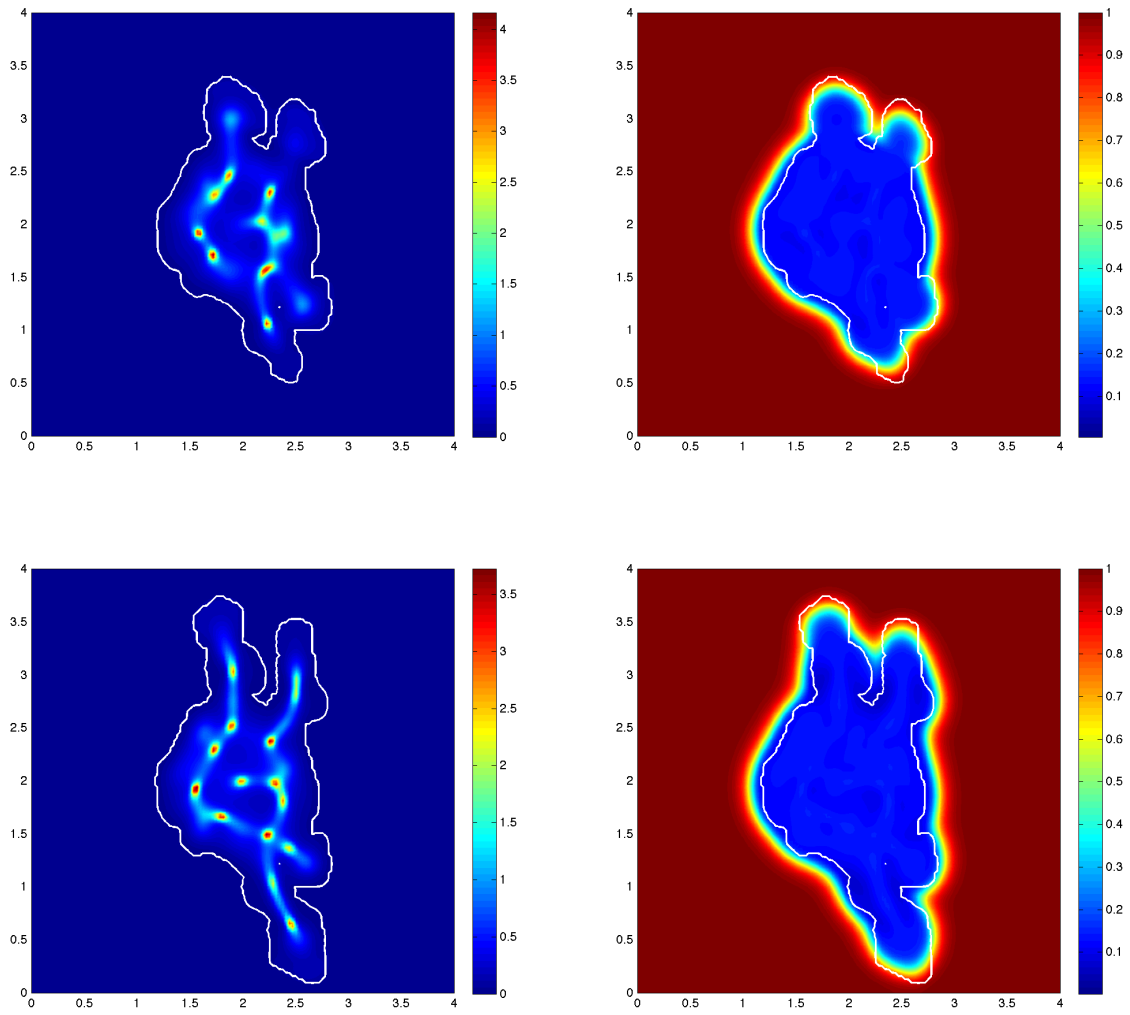

Figure 6.19: *Simulation results showing distributions of cancer cells (left column) and ECM (right column) and the invasive boundary of the tumour (white line) at various macro-micro stages: Stage 40, 60.* $D_c = 4.3 \times 10^{-3}$, $\beta = 0.7875$, $\mu_2 = 0.01$ *and* $\delta = 1.5$.

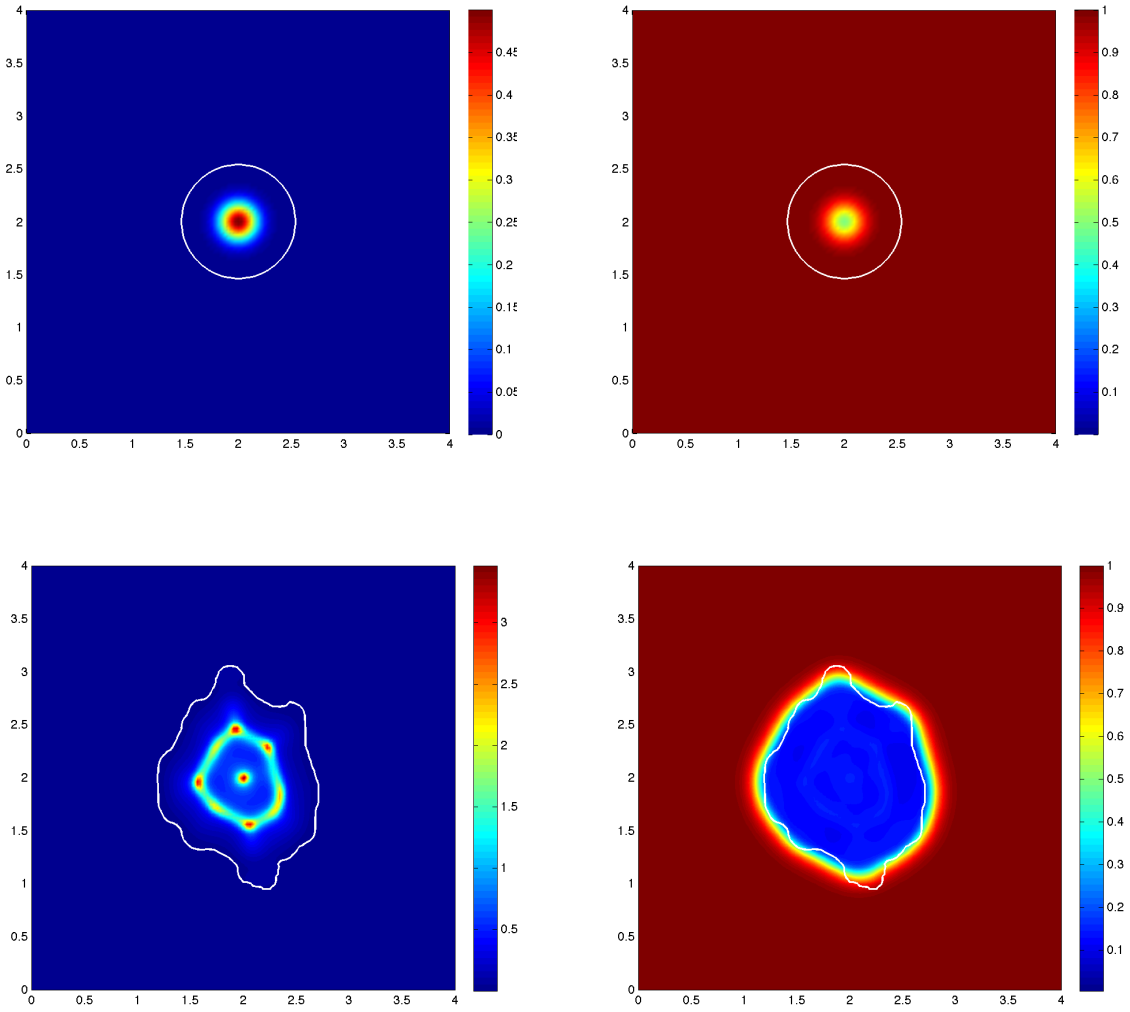

Figure 6.20: *Simulation results showing distributions of cancer cells (left column) and ECM (right column) and the invasive boundary of the tumour (white line) at various macro-micro stages: Stage 0, 20.* $D_c = 4.3 \times 10^{-3}$, $\beta = 0.8$, $\mu_2 = 0.01$ *and* $\delta = 1.5$.

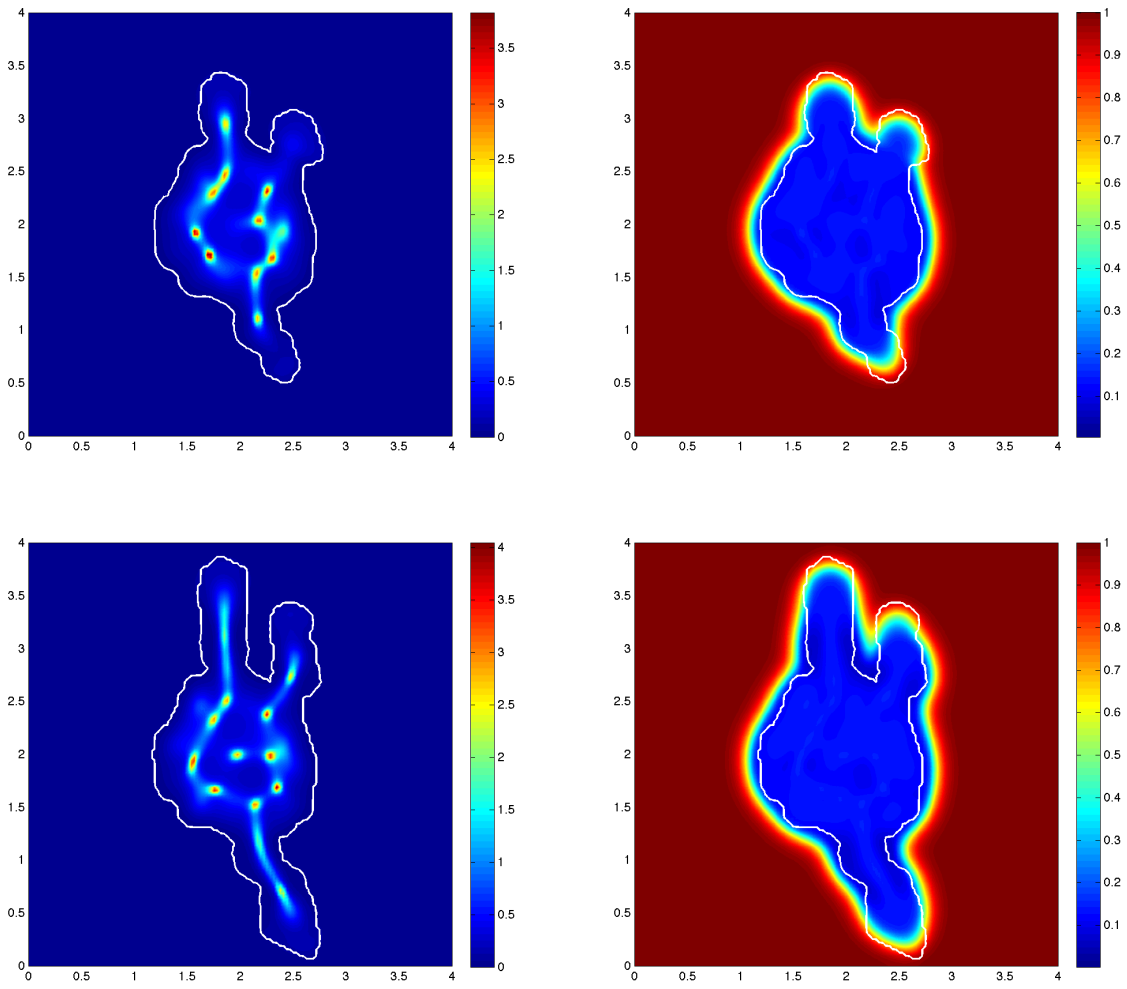

Figure 6.21: *Simulation results showing distributions of cancer cells (left column) and ECM (right column) and the invasive boundary of the tumour (white line) at various macro-micro stages: Stage 40, 60.* $D_c = 4.3 \times 10^{-3}$, $\beta = 0.8$, $\mu_2 = 0.01$ *and* $\delta = 1.5$.

ECM proliferation rate μ_2 & degradation rate δ. From all the simulation results, we conclude that the degradation of ECM facilitates cancer invasion. However, the invasion process will stop where ECM is degraded a lot. This captures the biological scenario in 2D that when cell-matrix adhesion is too low, no focal adhesions or stress fibres are formed, and the cells do not move (Friedl and Wolf, 2010; Weaver, 2006; Alberts et al., 2008; Ridley et al., 2003). In order to investigate the effect of ECM proliferation and degradation on the invasion process, we compare two groups of parameters: 1) $\mu_2 = 0.01$, $\delta = 1.5$ (non-zero proliferation rate with relatively large degradation rate, Figures 6.22 - 6.23); 2) $\mu_2 = 0$, $\delta = 0.75$ (no proliferation with relatively small degradation rate, Figures 6.24 - 6.25). From these two groups of images, we observe that when proliferation is present and the degradation rate is relatively large, deformations of the boundary is not as dynamic as that when the proliferation term is absent with a relatively small degradation rate. The reason could be that the proliferation term will reduce the degree of heterogeneity of the distribution of ECM, which leads to a less fingered spreading of the cancer cells.

6.5 Discussion

In this chapter we introduced a further extension of the two-scale mathematical model of cancer invasion that was based on the previous works in Chaplain and Lolas (2005), Andasari et al. (2011) and Trucu et al. (2013), which originally simulates the process of cancer invasion by investigating the link between the macroscopic dynamics of the spatio-temporal distribution of cancer cells and ECM taking place on a macroscopic domain, and the microdynamics of the matrix degrading enzymes developed on the microscopic domains that are in close proximity to tumour boundary.

We already extended the two-scale technique in Trucu et al. (2013) in the pre-

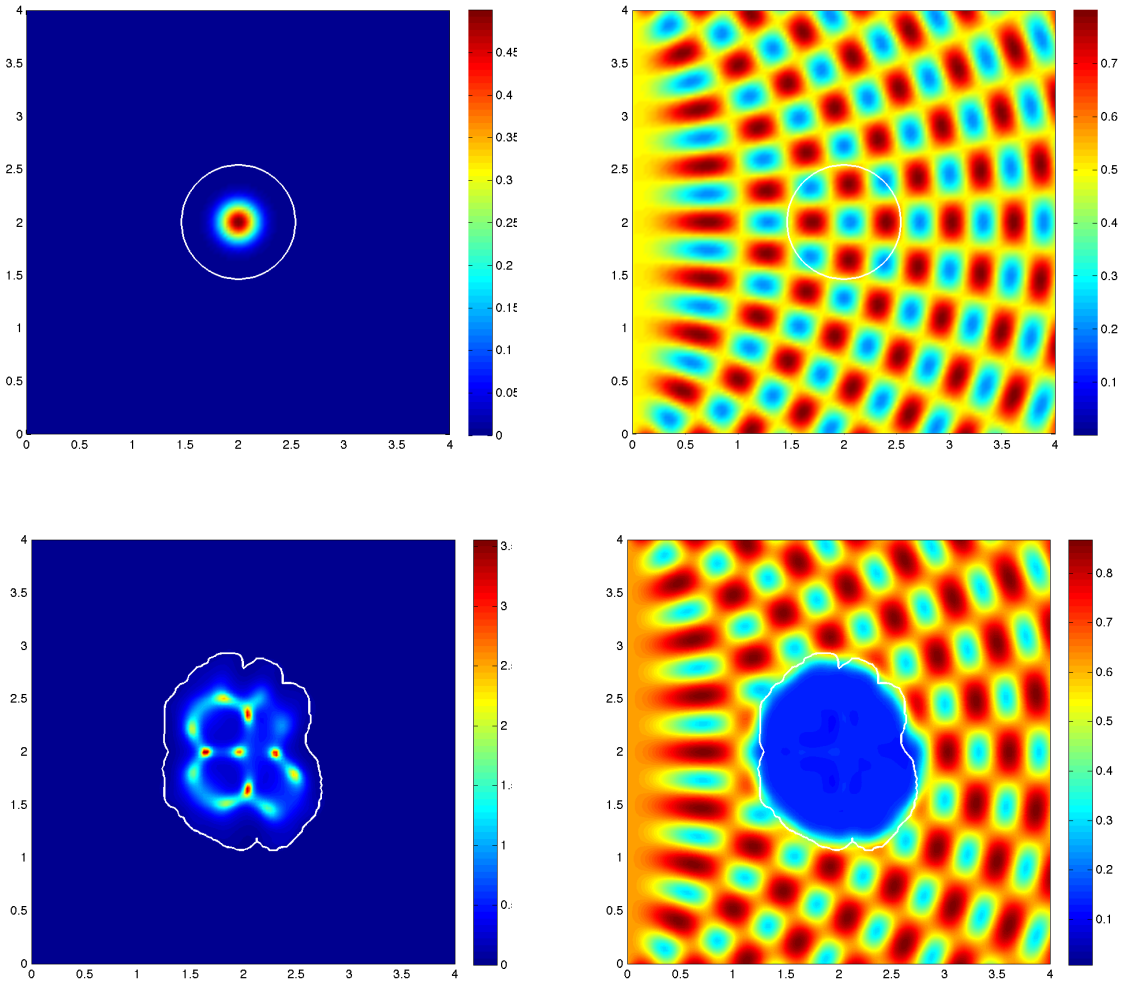

Figure 6.22: *Simulation results showing distributions of cancer cells (left column) and ECM (right column) and the invasive boundary of the tumour (white line) at various macro-micro stages: Stage 0, 20.* $D_c = 4.3 \times 10^{-3}$, $\beta = 0.7625$, $\mu_2 = 0.01$ *and* $\delta = 1.5$.

vious chapter that coupled a well-established model of the uPA system and cancer invasion from Chaplain and Lolas (2005) and Andasari et al. (2011) with the macro-microscopic technique. This consists of a system of five reaction-diffusion-taxis partial differential equations. Also, we discovered that we need to choose the right timing to weld the macro-solver and micro-solver to model the multiscale process of

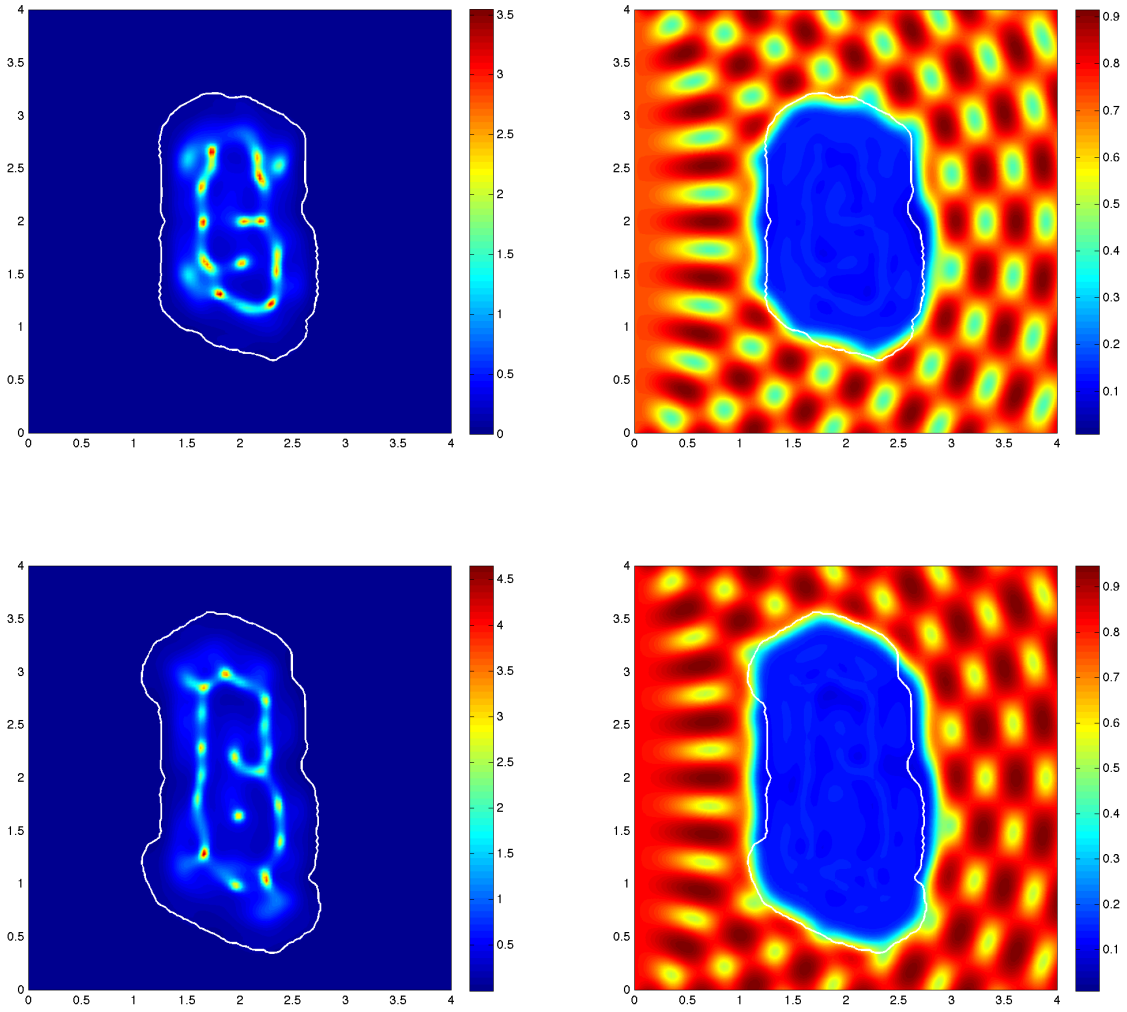

Figure 6.23: *Simulation results showing distributions of cancer cells (left column) and ECM (right column) and the invasive boundary of the tumour (white line) at various macro-micro stages: Stage 40, 60.* $D_c = 4.3 \times 10^{-3}$, $\beta = 0.7625$, $\mu_2 = 0.01$ *and* $\delta = 1.5$.

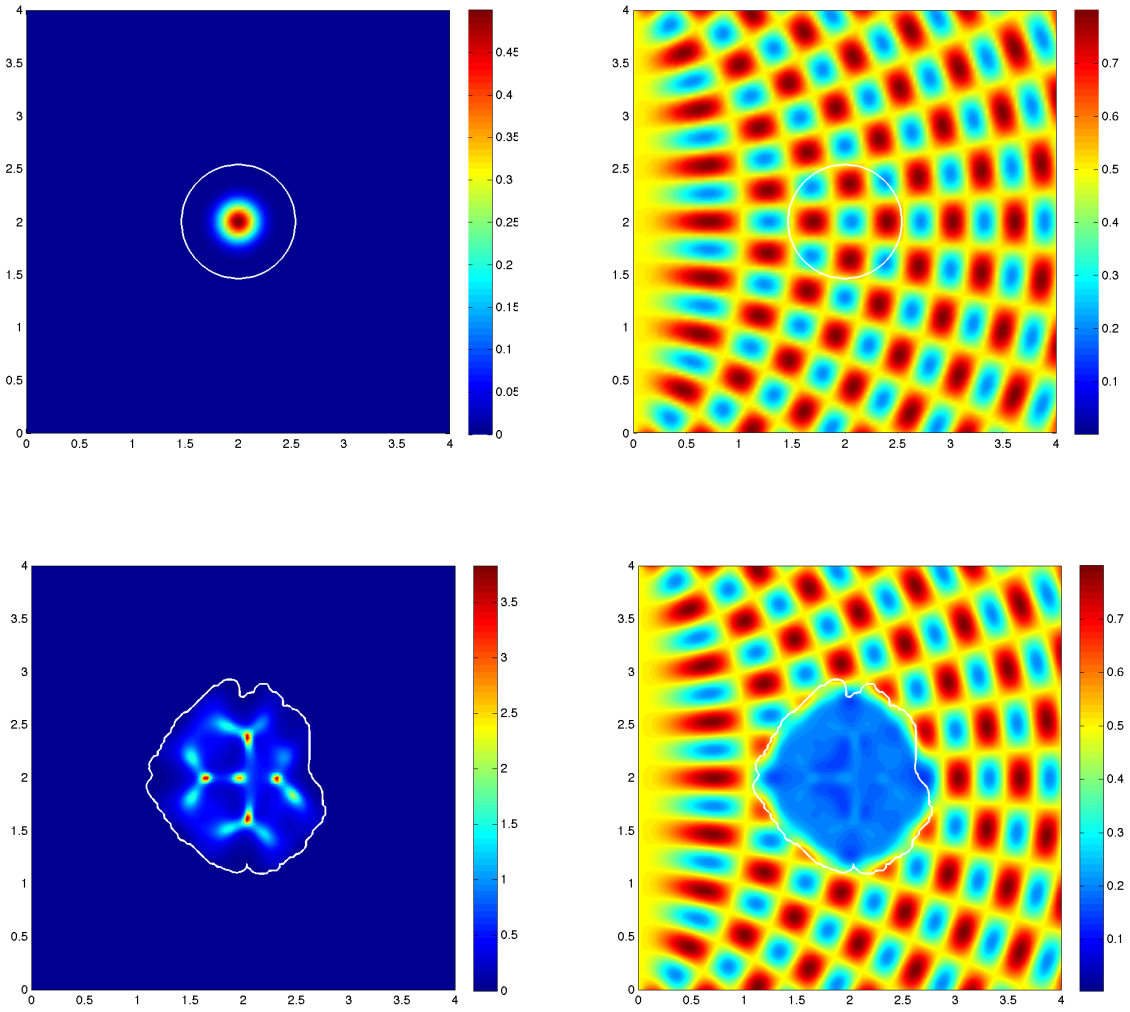

Figure 6.24: *Simulation results showing distributions of cancer cells (left column) and ECM (right column) and the invasive boundary of the tumour (white line) at various macro-micro stages: Stage 0, 20.* $D_c = 4.3 \times 10^{-3}$, $\beta = 0.7625$, $\mu_2 = 0$ *and* $\delta = 0.75$.

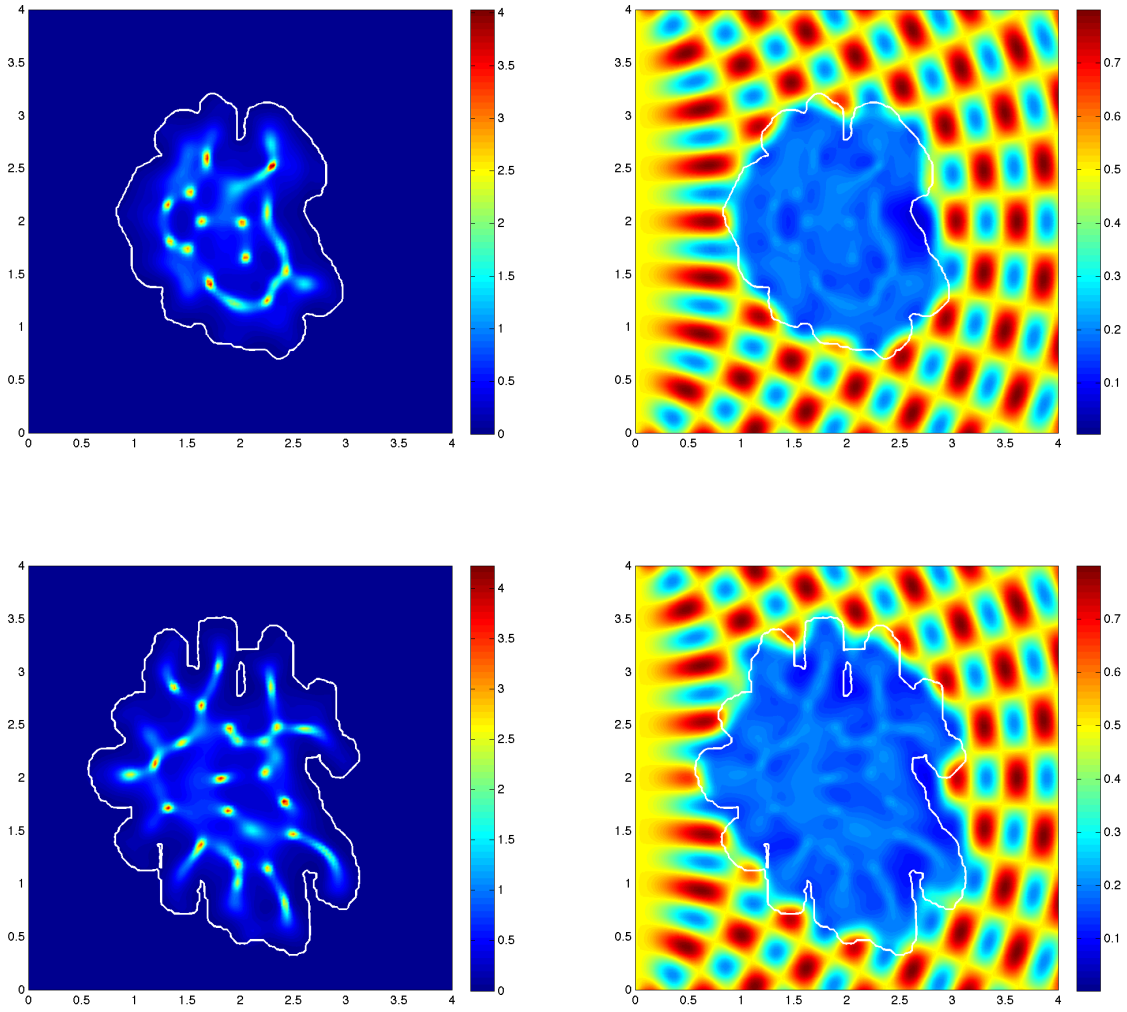

Figure 6.25: *Simulation results showing distributions of cancer cells (left column) and ECM (right column) and the invasive boundary of the tumour (white line) at various macro-micro stages: Stage 40, 60.* $D_c = 4.3 \times 10^{-3}$, $\beta = 0.7625$, $\mu_2 = 0$ *and* $\delta = 0.75$.

cancer invasion properly. In this chapter, we explored how the other parameters in the system influence the solution of the two-scale model.

From the computational simulation results of our model, we can see that the extended two-scale technique coupled with the uPA system and more specific modelling of the pericellular proteolytic activities, gives more adverse dynamics in the invading cancer. Settings of ECM initial condition, cancer cell diffusion coefficient, threshold coefficient, and ECM proliferation & degradation rates all have an impact on the deformations of the tumour boundary. The conclusions which can be made from the results are: 1) the heterogeneous ECM initial condition leads to more fingered spreading of the tumour compared with the homogeneous ECM initial condition; 2) in order to obtain heterogeneous patterns of cancer cells inside the tumour region, chemotaxis must be dominant to drive the cells migration; 3) the changes of threshold coefficient will definitely affect the boundary deformations, and there is a tendency that the increase of β reduces the number of 'fingers' of the interface. However, there may be exceptions; 4) without a proliferation term of ECM coupled with a relatively small degradation rate, deformations of the boundary show more fingering.

The two-scale modelling technique is a useful tool to capture processes at different levels during cancer invasion. However, we need further details to explain the dynamics and interactions of the tumour cell community at the macro-level and the micro-level. We could also extend our model by exploring other ways to determine the movement of cancer cells (for example, change the definition of the threshold function ω) or a new method to link the macro-solver and the micro-solver together.

Chapter 7

Conclusion and future directions

The aim of this thesis was to develop multiscale mathematical models of cancer cell migration and invasion in order to gain a better understanding of the processes of cancer growth and invasion, thereby helping to facilitate cancer research and strategies of treatment. As mentioned in the biological background chapter, invasion of the surrounding tissue is one of the hallmarks of cancer, and also a landmark event that transforms a localised solid tumour into a systemic, metastatic and fatal disease (Hanahan and Weinberg, 2011, 2000). Solid tumours have a reciprocal relationship with the surrounding microenvironment, a complex tissue composed of extracellular matrix and other multiple distinct cell types. The extracellular matrix especially not only plays the role of a scaffold for tissues and cells and acts as a physical barrier during cell migration, but also provides biological signals that, together with soluble factors, may create distinct cellular micro-environments that locally regulate cell migration, proliferation and differentiation (Wolf et al., 2013; Wolf and Friedl, 2011; Papini et al., 2007). Thus, proteolytic degradation and remodelling of the extracellular matrix is essential for cancer cells to be able to invade. Important matrix degrading enzymes include the matrix metalloproteases (MMP) and the urokinase

plasminogen activation system (uPA).

Chapter 4 studied and extended a level-set method (Macklin and Lowengrub, 2008) which was used to calculate the position of the moving boundary of the tumour, and to describe the dynamics of the tumour cell community we used PDE systems that have heterogeneous solutions. The first PDE system we used as a test model was a reaction-diffusion system called the Schnakenberg system. In order to obtain the heterogeneous pattern formation, we analysed the linear stability of the steady state of the system and derived conditions for diffusion-driven instability. Then we formulated a velocity function under the assumption that if the force generated by the growing population of one species in the system overcomes the surface tension of the boundary, which is proportional to the curvature of the interface, then the boundary of the tumour deforms. However, in this case, the curvature-dependent term was the dominant cause that drives the instability of the interface. The second PDE system test model, the urokinase plasminogen activation (uPA) system, modelled the interactions between cancer cells, ECM, the urokinase plasminogen activator (uPA), uPA inhibitors, and the ECM degrading enzyme plasmin (Chaplain and Lolas, 2005; Andasari et al., 2011). The system modelled pericellular proteolysis activities which determines cancer cell migration and invasion. The formulation of the velocity function which was applied in the level-set technique only depended on the dynamics of distribution of plasmin, the ECM degrading enzyme, and not on the curvature of the boundary. Comparing the simulation results of the two models, we concluded that it does not necessarily have to include a curvature-dependent term in the level-set method to model the deformations of the boundary. The heterogeneous dynamics of the uPA system alone can drive the deformations of the tumour boundary, which can render more fingering morphology when compared with the first test model.

Chapter 5 presented a multi-scale mathematical model of cancer invasion by coupling the urokinase plasminogen activation (uPA) system with the two-scale computational modelling technique recently introduced in Trucu et al. (2013). In this model, we investigated the protease-dependent cancer invasion not only on the macroscopic (tissue) level, but also on the microscopic (cellular) level, simulating the two-scale model on both a macro-mesh and a micro-mesh in close proximity to the cancer interface. It consisted of three main parts: the macroscopic uPA dynamics, the microscopic uPA dynamics, and the regulation of boundary relocation. The uPA system helped simulate regulations and interactions between cancer cells, ECM molecules and cancer associated matrix degrading enzymes and describe a more diverse dynamics at both the macroscopic and microscopic scale. Our computational simulation results (see Figure 7.1) demonstrated a range of heterogeneous dynamics which were qualitatively similar to the invasive growth patterns observed in a number of different types of cancer known as tumour infiltrative growth patterns (INF) (see Figure 2.5).

From our simulation results we also discovered that this two-scale model has a property that changing the total runtime of the macro-solver affects not only the degree of heterogeneity of the cancer cell distribution inside the tumour but also the deformations of the tumour boundary. In order to model the integrated process of cancer invasion at tissue level and cellular level properly, we must be careful in choosing the right timing to weld the macro-solver and micro- solver together. Apart from the modelling point of view, another aspect of this technique is that we apply different numerical schemes on domains at different levels: a finite-difference scheme for the macrodynamics (macro-solver) and for the microdomain around the boundary a finite-element scheme is employed (micro-solver). In this way, we were able to maintain the simplicity at the macro-level, and also the difficulty of dealing

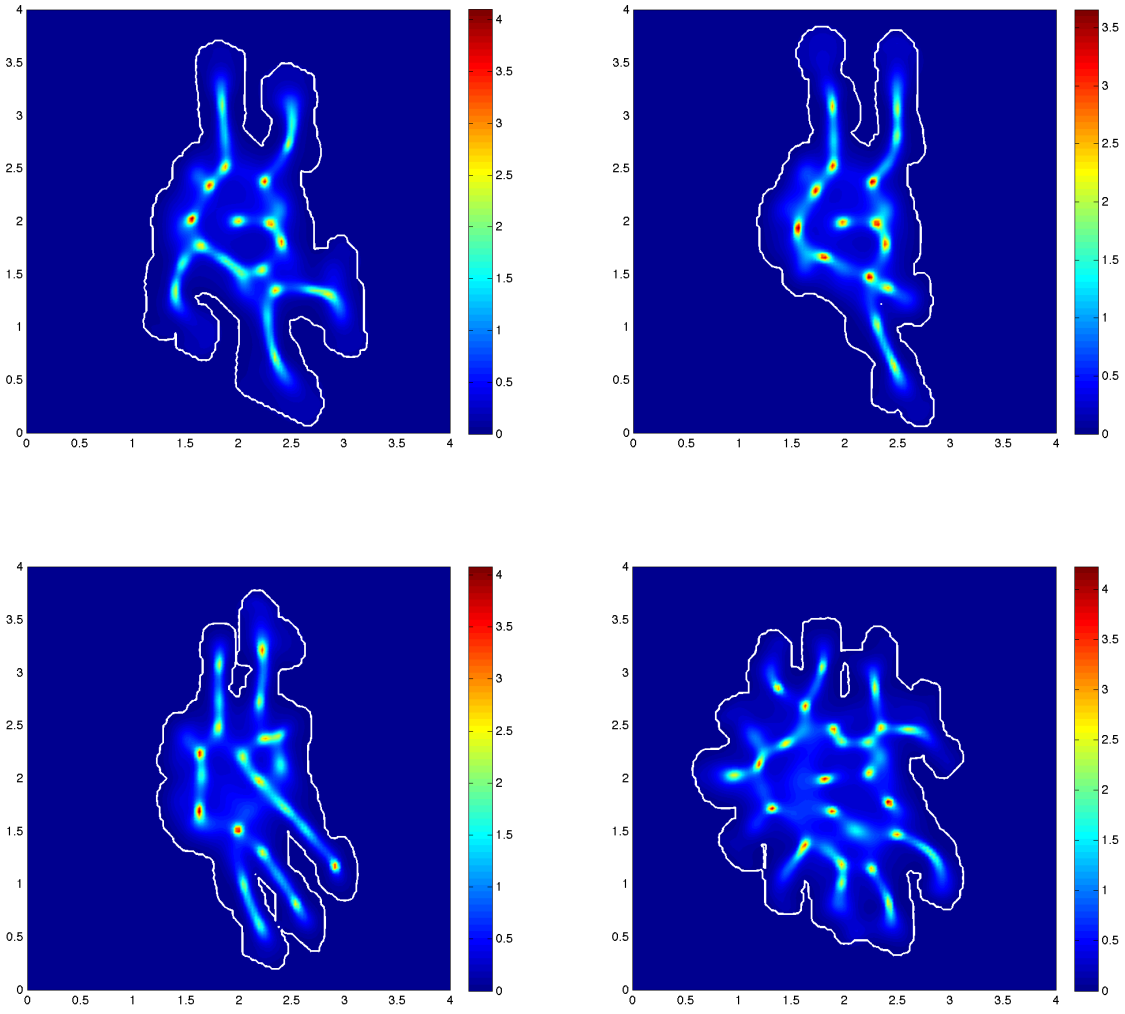

Figure 7.1: *Simulation results showing distributions of cancer cells and the invasive boundary of the tumour (white line) at macro-micro stage 60 using different parameter settings.*

with a deformed geometry was overcome by computing functions element-by-element of the microdomains around the irregular interface.

Chapter 6 showed an extension to the work of the two-scale model in Chapter 5, which focused on the effects that some key parameters in the system have on the dynamics at both scales and the morphology of the tumour boundary. From the computational simulation results of our model, we observed that the extended two-scale technique coupled with the uPA system and a more detailed modelling of pericellular proteolytic activities, the deformations of tumour rendered diverse dynamics. Settings of ECM initial condition, cancer cell diffusion coefficient, threshold coefficient, and ECM proliferation & degradation rates had an impact on the deformations of the tumour cell community. The conclusions that can be made from the results are: 1) a heterogeneous ECM initial condition leads to more fingered spreading of the tumour compared with that in the homogeneous ECM; 2) in order to obtain heterogeneous patterns of cancer cells inside the tumour region, chemotaxis must be dominant to drive cell migration; 3) the changes of threshold coefficient will definitely affect the boundary deformations, and there is a tendency that the increase of β reduces the number of 'fingers' of the interface. However, there might be exceptions; 4) without the proliferation term of ECM coupled with a relatively small degradation rate, deformations of the cancer boundary show more fingering.

The two-scale modelling technique is a useful tool to capture processes at different levels during cancer invasion. However, we need further details to explain the dynamics and interactions of the tumour cell community at both the macro-level and the micro-level. We could improve our model by exploring other ways to determine the movement of cancer cells. For instance, we could change the definition of the threshold function which determines whether the microenvironment is suitable

for cells to move; we could explore new methods to link the macro-solver and micro-solver together; and take into account other physical and molecular determinants of cell migration in the model, for example, Rac activity and Rho/ROCK signalling and actin polymerisation-driven propulsion and actomyosin-based contractility, etc. Another direction to extend the current model is that we could include other biological scales, such as the genetic and the molecular scale. We also could extend the 2D multiscale model to a 3D model, in order to describe the processes of cancer cell invasion in the human body more realistically.

Although we have focused on the collective migration of cancer cells, we could also use the macro-microscopic modelling technique or level-set method to model single cell migration. It is known that the actin cytoskeleton plays an essential role in eukaryotic cell motility and the regulation of the actin cytoskeleton dynamics is mainly conducted by the actin nucleating complex, Arp2/3, and the small G-proteins: Cdc42, Rac and Rho. Therefore, we could develop a mathematical model of the dynamics of crosstalk between the Rho-family GTPases, then couple it with the two-scale technique or level-set method to simulate the deformations of a cell membrane. For example, in Maree et al. (2006), a mathematical model was proposed to describe the interactions between the key proteins in the Rho-family GTPases as follows:

$$\frac{\partial C}{\partial t} = \frac{I_C}{1+(\rho/\beta_\rho)^n}(C_i/C_{total}) - d_C C + D_m \Delta C, \tag{7.1}$$

$$\frac{\partial R}{\partial t} = (I_R + \alpha_C C)(R_i/R_{total}) - d_R R + D_m \Delta R, \tag{7.2}$$

$$\frac{\partial \rho}{\partial t} = \frac{(I_\rho + \alpha_R R)}{1+(C/\beta_C)^n}(\rho_i/\rho_{total}) - d_\rho \rho + D_m \Delta \rho, \tag{7.3}$$

$$\frac{\partial C_i}{\partial t} = -\frac{I_C}{1+(\rho/\beta_\rho)^n}(C_i/C_{total}) + d_C C + D_c \Delta C_i, \tag{7.4}$$

$$\frac{\partial R_i}{\partial t} = -(I_R + \alpha_C C)(R_i/R_{total}) + d_R R + D_c \Delta R_i, \tag{7.5}$$

$$\frac{\partial \rho_i}{\partial t} = -\frac{(I_\rho + \alpha_R R)}{1+(C/\beta_C)^n}(\rho_i/\rho_{total}) + d_\rho \rho + D_c \Delta \rho_i, \tag{7.6}$$

where C, R, ρ represents concentration of active Cdc42, Rac, Rho, and C_i,R_i,ρ_i are their inactive forms of the G-proteins accordingly. n is a Hill coefficient. Some of the simulation results in 1D and 2D of the whole system are shown in Figure 7.2 and 7.3.

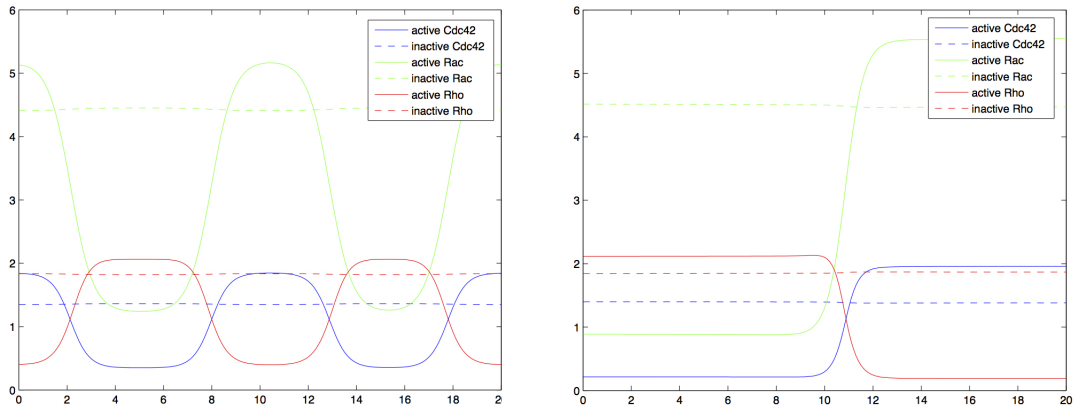

(a) n=3 **(b)** n=4

Figure 7.2: *Plots of the equilibrium distribution of active and inactive Cdc42, Rac and Rho in 1D. Solid lines represents active forms of Cdc42 (blue), Rac (green) and Rho (red) and dash lines are the inactive forms respectively. (a) Hill coefficient $n = 3$ (b) Hill coefficient $n = 4$.*

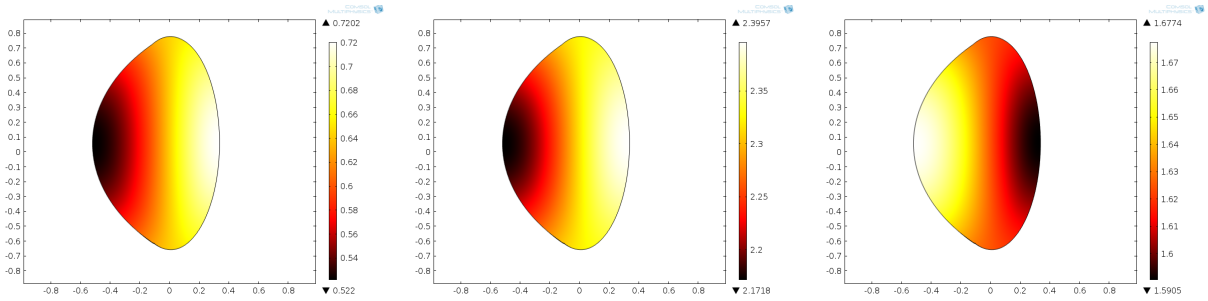

(a) Cdc42 **(b)** Rac **(c)** Rho

Figure 7.3: *Distribution of the active forms of small G-proteins in 2D. (a) Cdc42, (b) Rac, (c) Rho, showing the relative concentrations inside the cell from low(dark) to high(light) concentration values. Hill coefficient here is* $n = 4$.

Once we obtain the distribution of active forms of the key small G-proteins that regulates the signalling pathways controlling cell migration, such as active Cdc42 (which is able to simulate actin polymerisation by activating Arp2/3 complex), then we could formulate a velocity function that is governed by the distribution of the key proteins, and use the level-set method to calculate the changing positions of the cell membrane.

Also, we could apply the macro-microscopic technique to model single cell migration and the three parts of the model could be: 1) the macroscopic dynamics modelling the system of the Rho-family GTPases; 2) the microscopic dynamics describing the actin polymerisation and depolymerisation close to the cell membrane; 3) regulation of the deformations of the cell membrane which is governed by the distribution of actin filaments.

In conclusion, the work presented in this thesis has sought to study the process of cancer growth and invasion through mathematical modelling. More efforts are needed to make these models more biologically relevant in order to fully validate the results. Since the model concepts and modelling techniques are at an early stage of development, there is a lot of potential for the current work to be improved and

extended. Thus, we believe that the work in this thesis will open more doors for researchers to investigate cancer invasion in the future.

Chapter 8

Appendix

8.1 A Finite-difference method applied to solve uPA system

Assume that uPA system dynamics are taking place in the cube Y, we discretise the entire Y by considering a uniform spatial mesh of size $h := \frac{\epsilon}{2}$, i.e., $\Delta x = \Delta y = h$. And, the time interval $[t_0, t_0 + \Delta t]$ split by the uniform time step $\delta\tau := \frac{\Delta t}{k}$. The temporal discretisation of the reaction-diffusion system that we used here is a first-order scheme, while the diffusion term and haptotactic terms are approximated with a second-order midpoint rule. The notations for the midpoint approximations in equation (4.60) and (4.61) are:

$$\begin{cases} c^n_{i,j+\frac{1}{2}} & := \frac{c^n_{i,j}+c^n_{i,j+1}}{2}, \\ c^n_{i,j-\frac{1}{2}} & := \frac{c^n_{i,j}+c^n_{i,j-1}}{2}, \\ c^n_{i+\frac{1}{2},j} & := \frac{c^n_{i,j}+c^n_{i+1,j}}{2}, \\ c^n_{i-\frac{1}{2},j} & := \frac{c^n_{i,j}+c^n_{i-1,j}}{2}, \end{cases}$$

and those for the central difference are:

$$\begin{cases} (c_y)^n_{i,j+\frac{1}{2}} & := \frac{c^n_{i,j+1}-c^n_{i,j}}{\Delta y}, \\ (c_y)^n_{i,j-\frac{1}{2}} & := \frac{c^n_{i,j}-c^n_{i,j-1}}{\Delta y}, \\ (c_x)^n_{i+\frac{1}{2},j} & := \frac{c^n_{i+1,j}-c^n_{i,j}}{\Delta x}, \\ (c_x)^n_{i-\frac{1}{2},j} & := \frac{c^n_{i,j}-c^n_{i-1,j}}{\Delta x}, \end{cases}, \quad \text{and} \quad \begin{cases} (v_y)^n_{i,j+\frac{1}{2}} & := \frac{v^n_{i,j+1}-v^n_{i,j}}{\Delta y}, \\ (v_y)^n_{i,j-\frac{1}{2}} & := \frac{v^n_{i,j}-v^n_{i,j-1}}{\Delta y}, \\ (v_x)^n_{i+\frac{1}{2},j} & := \frac{v^n_{i+1,j}-v^n_{i,j}}{\Delta x}, \\ (v_x)^n_{i-\frac{1}{2},j} & := \frac{v^n_{i,j}-v^n_{i-1,j}}{\Delta x}, \end{cases}$$

Using the approximation notations mentioned so far, the approximation for $\nabla \cdot (\nabla c)^n_{i,j}$ and $\nabla \cdot (c\nabla v)^n_{i,j}$ are constructed as follows:

$$\begin{aligned} \nabla \cdot (\nabla c)^n_{i,j} &= \operatorname{div}(\nabla c)^n_{i,j} \\ &\simeq \frac{(c_x)^n_{i+\frac{1}{2},j} - (c_x)^n_{i-\frac{1}{2},j}}{\Delta x} + \frac{(c_y)^n_{i,j+\frac{1}{2}} - (c_y)^n_{i,j-\frac{1}{2}}}{\Delta y} \end{aligned}$$

and,

$$\begin{aligned} \nabla \cdot (c\nabla v)^n_{i,j} &= \operatorname{div}(c\nabla v)^n_{i,j} \\ &=\simeq \frac{c^n_{i+\frac{1}{2},j}(v_x)^n_{i+\frac{1}{2},j} - c^n_{i-\frac{1}{2},j}(v_x)^n_{i-\frac{1}{2},j}}{\Delta x} + \frac{c^n_{i,j+\frac{1}{2}}(v_y)^n_{i,j+\frac{1}{2}} - c^n_{i,j-\frac{1}{2}}v_y)^n_{i,j-\frac{1}{2}}}{\Delta y} \end{aligned}$$

Note that $n = 0, 1, ..., k$ are index of time step, and (i, j) are spatial nodes where $i = 1, ...q$ are the indices for the x-direction and $j = 1, ...q$ are the indices for the y-direction. The diffusion terms in equations (4.62) -(4.64) are approximated in the same way as it is in equation (4.60).

Bibliography

Adam, J.A., 1986. A simplified mathematical model of tumour growth. *Math. Biosci.* **81**(2), 229–244.

Adam, J.A., 1987a. A mathematical model of tumour growth 2: Effects of geometry and spatial nonuniformity on stability. *Math. Biosci.* **86**(2), 183–211.

Adam, J.A., 1987b. A mathematical model of tumour growth 3: Comparison with experiment. *Math. Biosci.* **86**(2), 213–227.

Akgu, B., Garcia-Escudero, R., Ghali, L., Pfister, H.J., Fuchs, P.G., Navsaria, H., Storey, A., 2005. The e7 protein of cutaneous human papillomavirus type 8 causes invasion of human keratinocytes into the dermis in organotypic cultures of skin. *Cancer Res.* **65**(6), 2216–2223.

Alberts, B., Johnson, A., Lewis, J., Raff, M., Roberts, K., Walter, P. (Eds.), 2008. Molecular Biology of The Cell. fifth edition ed., Garland Science, New York, USA.

Andasari, V., Gerisch, A., Lolas, G., South, A., Chaplain, M.A.J., 2011. Mathematical modeling of cancer cell invasion of tissue: biological insight from mathematical analysis and computational simulation. *J. Math. Biol.* **63**(1), 141–171.

Anderson, A., Chaplain, M., Newman, E., Steele, R., Thompson, A., 2000. Mathe-

matical modelling of tumour invasion and metastasis. *J. Theorl. Medic.* **2**, 129–154.

Anderson, A.R.A., 2005. A hybrid mathematical model of solid tumour invasion: the importance of cell adhesion. *Math. Medic. Biol.* **22**, 163–186.

Araujo, R.P., Mcelwain, D.L.S., 2004. A history of the study of solid tumour growth: The contribution of mathematical modelling. *Bull. Math. Biol.* **66**, 1039–1091.

Armstrong, N.J., Painter, K.J., Sherratt, J.A., 2006. A continuum approach to modelling cell-cell adhesion. *J. Theor. Biol.* **243**(1), 98–113.

Burton, A., 1966. Rate of growth of solid tumours as a problem of diffusion. *Growth* **30**(2), 157–176.

Byrne, H., Chaplain, M., Pettet, G., Mcelwain, D.L.S., 2001. A mathematical model of trophoblast invasion. *Appl. Math. Lett.* **14**(8), 1005–1010.

Byrne, H., Preziosi, L., 2003. Modelling solid tumour growth using the theory of mixtures. *Math. Medic. Biol.* **20**, 341–366.

Byrne, H.M., Chaplain, M., 1995a. Growth of nonnecrotic tumours in the presence and absence of inhibitors. *Math. Biosci.* **130**, 151–181.

Byrne, H.M., Chaplain, M., 1995b. Mathematical models for tumour angiogenesis: numerical simulations and nonlinear wave solutions. *Bull. Mathe. Biol.* **57**(3), 461–486.

Byrne, H.M., Chaplain, M., 1997. Free boundary value problems associated with the growth and development of multicellular spheroids. *Euro. J. Appl. Math.* **8**, 639–658.

Byrne, H.M., Chaplain, M., 1998. Necrosis and apoptosis: Distinct cell loss mechanisms in a mathematical model of avascular tumour growth. *J. Theor. Medic.* **1**, 223–235.

Byrne, H.M., Chaplain, M.A., 1996. Modelling the role of cell-cell adhesion in the growth and developement of carcinoma. *Math. Comput. Model.* **24**(12), 1–17.

Chaplain, M., Ganesh, M., Graham, I., 2001. Spatio-temporal pattern formation on spherical surfaces: numerical simulation and application to solid tumour growth. *J. Math. Biol.* **42**, 387–423.

Chaplain, M., Graziano, L., Preziosi, L., 2006a. Mathematical modelling of the loss of tissue compression responsiveness and its role in solid tumour development. *Math. Medic. Biol.* **23**, 197–229.

Chaplain, M., Graziano, L., Preziosi, L., 2006b. Mathematical modelling of the loss of tissue compression responsiveness and its role in solid tumour development. *Math. Medic. Biol.* **23**, 197–229.

Chaplain, M., Lachowicz, M., Szymanska, Z., Wrzosek, D., 2011. Mathematical modelling of cancer invasion: The importance of cell-cell adhesion and cell-matrix adhesion. *Math. Model. Meth. Appl. Sci.* **21**(4), 719–743.

Chaplain, M., Lolas, G., 2005. Mathematical modelling of cancer cell invasion of tissue: the role of the urokinase plasminogen activation system. *Math. Model. Meth. Appl. Sci.* **15**(11), 1685–1734.

Chaplain, M., McDougal, S., Anderson, A., 2006c. Mathematical modeling of tumor-induced angiogenesis. *Annu. Rev. Biomed. Eng.* **8**, 233–257.

Chaplain, M., Stuart, A., 1993. A model mechanism for chemotactic response of endothelial cells to tumour angiogenesis factor. *J. Math. Appl. Medic. Biol.* **10**, 149–168.

Chaplain, M.A., 1996. Avascular growth, angiogenesis and vascular growth in solid tumours: The mathematical modelling of the stages of tumour development. *Math. Comput. Model.* **23**(6), 47–87.

Chaplain, M.A., Anderson, A., 1996. Mathematical modelling, simulation and prediction of tumour-induced angiogenesis. *Invas. Metast.* **16**(4-5), 222–234.

Chaplain, M.A., Benson, D., Maini, P., 1994. Nonlinear diffusion of a growth-inhibitory factor in multicell spheroids. *Math. Biosci.* **121**(1), 1–13.

Cristini, V., Lowengrub, J., Nie, Q., 2003. Nonlinear simulation of tumour growth. *J. Math. Biol.* **46**, 191–224.

Deakin, N.E., Chaplain, M.A.J., 2013. Mathematical modelling of cancer cell invasion: the role of membrane-bound matrix metalloproteinases. *Front. Oncol.* **3**(70), 1–9.

Deisboeck, T.S., Wang, Z., Macklin, P., Cristini, V., 2011. Multiscale cancer modeling. *Annu. Rev. Biomed. Eng.* **13**, 127–155.

Devreotes, P., Zigmond, S., 1988. Chemotaxis in eukaryotic cells - a focus on leukocytes and dictyostelium. *Annul. Rev. Cel. Biol.* **4**, 649–686.

Domschke, P., Trucu, D., Gerisch, A., Chaplain, M., 2014. Mathematical modelling of cancer invasion: Implications of cell adhesion variability for tumour infiltrative growth patterns. *J. Theor. Biol.* **361**, 41–60.

Donze, A., Fanchon, E., Gattepaille, L.M., Maler, O., Tracqui, P., 2011. Robustness analysis and behavior discrimination in enzymatic reaction networks. *PLoS ONE* **6**(9), e24246.

Drasdo, D., 2003. On selected individual-based approaches to the dynamics in multicellular systems. Mathematics and Biosicences in Interaction, Birkhauser Verlag AG., Basel, Switzerland.

Estecha, A., Sanchez-Martin, L., Puig-Kroger, A., Bartolome, R., Teixido, J., Samaniego, R., Sanchez-Mateos, P., 2009. Moesin orchestrates cortical polarity of melanoma tumour cells to initiate 3d invasion. *J. Cell. Sci.* **122**(19), 3492–3501.

Ewald, A., Brenot, A., Duong, M., Chan, B., Werb, Z., 2008. Collective epithelial migration and cell rearrangements drive mammary branching morphogenesis. *Developm. Cel.* **14**(4), 570–581.

Firtel, R., Meili, R., 2000. Dictyostelium: a model for regulated cell movement during morphogenesis. *Curr. Opin. Genet. Developm.* **10**(4), 421–427.

Frieboes, H.B., Jin, F., Chuang, Y.L., Wise, S.M., Lowengrub, J.S., Cristini, V., 2010. Three-dimensional multispecies nonlinear tumor growth—ii: Tumor invasion and angiogenesis. *J. Theor. Biol.* **264**, 1254–1278.

Frieboes, H.B., Zheng, X., Sun, C.H., Tromberg, B., Gatenby, R., Cristini, V., 2006. An integrated computational/experimental model of tumor invasion. *Cancer Res.* **66**, 1597–1604.

Friedl, P., Alexander, S., 2011. Cancer invasion and the microenvironment: Plasticity and reciprocity. *Cell* **147**, 992–1009.

Friedl, P., Borgmann, S., Brocker, E.B., 2001. Amoeboid leukocyte crawling through extracellular matrix: lessons from the dictyostelium paradigm of cell movement. *J. Leukoc. Biol.* **70**(4), 491–509.

Friedl, P., Gilmour, D., 2009. Collective cell migration in morphogenesis, regeneration and cancer. *Nat. Rev. Mol. Cel. Biol.* **10**, 445–457.

Friedl, P., Maaser, K., Klein, C., Niggemann, B., Krohne, G., Zanker, K., 1997. Migration of highly aggressive mv3 melanoma cells in 3-dimensional collagen lattices results in local matrix reorganization and shedding of alpha 2 and beta 1 integrins and cd44. *Cancer Res.* **57**(10), 2061–2070.

Friedl, P., Wolf, K., 2003. Tumour cell invasionand migration: Diversity and escape mechanisms. *Nat. Rev. Cancer.* **3**, 362–374.

Friedl, P., Wolf, K., 2008. Tube travel: The role of proteases in individual and collective cancer cell invasion. *Cancer Res.* **68**(18), 7247–7249.

Friedl, P., Wolf, K., 2009. Proteolytic interstitial cell migration: a five-step process. *Cancer Metast. Rev.* **28**, 129–135.

Friedl, P., Wolf, K., 2010. Plasticity of cell migration: a multiscale tuning model. *J. Cell Biol.* **188**(1), 11–19.

Gatenby, R., Gawlinski, E., 2003. The glycolytic phenotype in carcinogenesis and tumor invasion: Insights through mathematical models. *Cancer Res.* **63**(14), 3847–3854.

Gatenby, R.A., Gawlinski, E.T., 1996. A reaction-diffusion model of cancer invasion. *Cancer Res.* **56**, 5745–5753.

Gatenby, R.A., Gawlinski, E.T., Gmitro, A.F., Kaylor, B., Gillies, R.J., 2006. Acid-mediated tumor invasion: a multidisciplinary study. *Cancer Res.* **66**, 5216–5223.

Gerisch, A., 2010. On the approximation and efficient evaluation of integral terms in pde models of cell adhesion. *IMA J. Numer. Anal.* **30**(1), 173–194.

Gerisch, A., Chaplain, M., 2008. Mathematical modelling of cancer cell invasion of tissue: Local and non-local models and the effect of adhesion. *J. Theor. Biol.* **250**, 684–704.

Gottlieb, S., Shu, C., 1997. Total variation diminishing runge-kutta schemes. *Math. Comput.* **67**(221), 73–85.

Gottlieb, S., Shu, C., Tadmor, E., 2001. Strong stability-preserving high order time discretisation methods. *SIAM Rev.* **43**(1), 89–112.

Greenspan, H.P., 1976. On the growth and stabiligy of cell cultures and solid tumours. *J. Theor. Biol.* **56**, 229–242.

Halmos, P., 1974. Measure Theory. Springer-Verlag, New York, USA.

Hanahan, D., Weinberg, R.A., 2000. The hallmarks of cancer. *Cell* **100**, 57–70.

Hanahan, D., Weinberg, R.A., 2011. The hallmarks of cancer: The next generation. *Cell* **144**, 646–674.

Hillen, T., Painter, K.J., 2013. Convergence of a cancer invasion model to a logistic chemotaxis model. *Math. Model. Meth. Appl. Sci.* **23**(1), 165–198.

Inaba, H., Sugita, H., Kuboniwa, M., Iwai, S., Hamada, M., Noda, T., Morisaki, I., Lamont, R.J., Amano, A., 2014. Porphyromonas gingivalis promotes invasion of oral squamous cell carcinoma through induction of prommp9 and its activation. *Cellular Microbiol.* **16**(1), 131–145.

Jiang, G., Peng, D., 2000. Weighted eno schems for hamilton-jacobi equations. *SIAM J. Sci. Comput.* **21**(6), 2126–2143.

Joyce, J.A., Pollard, J., 2009. Microenvironmental regulation of metastasis. *Nat. Rev. Cancer.* **9**(4), 239–252.

Kalluri, R., Zeisberg, M., 2006. Fibroblasts in cancer. *Nat. Rev. Cancer.* **6**(5), 392–401.

Kim, Y., M.A., S., Othmer, H., 2007. A hybrid model for tumor spheroid growth in vitro: I.theoretical development and early results. *Math. Methods Appl. Sci.* **17**, 1773–1798.

Kim, Y., Othmer, H.G., 2013. A hybrid model of tumor-stromal interactions in breast cancerß. *Bull. Math. Biol.* **75**(8), 1304–1350.

Lauffenburger, D.A., Horwitz, A.F., 1996. Cell migration: A physically integrated molecular process. *Cell* **84**, 359–369.

Lowengrub, J.S., Frieboes, H.B., Jin, F., Chuang, Y.L., Li, X., Macklin, P., Cristini, S.M.W.V., 2010. Nonlinear modelling of cancer: bridging the gap between cells and tumours. *Nonlinearity* **23**, R1–R91.

Macklin, P., Lowengrub, J., 2005. Evolving interfaces via gradients of geometry-dependent interior poisson problems: application to tumor growth. *J. Comput. Phys.* **203**(1), 191–220.

Macklin, P., Lowengrub, J., 2006. An improved geometry-aware curvature discretization for level set methods: application to tumor growth. *J. Comput. Phys.* **215**(2), 392–401.

Macklin, P., Lowengrub, J., 2007. Nonlinear simulation of the effect of microenvironment on tumor growth. *J. Theor. Biol.* **245**(4), 677–704.

Macklin, P., Lowengrub, J., 2008. A new ghost cell/level set method for moving boundary problems: Application to tumor growth. *J. Sci. Comput.* **35**, 266 – 299.

Macklin, P., McDougall, S., Anderson, A.R.A., Chaplain, M.A.J., Cristini, V., Lowengrub, J., 2009. Multiscale modelling and nonlinear simulation of vascular tumour growth. *J. Math. Biol.* **58**, 765–798.

Malladi, R., Sethian, J., Vemuri, B., 1996. A fast level set based algorithm for topology-independent shape modeling. *J. Math. Imag. Vis.* **6**(2-3), 269–289.

Maree, A.F., Jikine, A., Dawes, A., A.Grieneisen, V., Edelstein-Keshet, L., 2006. Polarization and movement of keratocytes: A multiscale modelling approach. *Bull. Math. Biol.* **68**, 1169–1211.

Mason, S.D., Joyce, J.A., 2011. Proteolytic networks in cancer. *Tren. Cel. Biol.* **21**(4), 228–237.

Mikala, E., S., N.E., Zena, W., 2010. Tumors as organs: Complex tissues that interface with the entire organism. *Developm. Cel.* **18**(6), 884–901.

Murray, J., 2003. Mathematical Biology 2: Spatial Models and Biomedical Applications. 3rd ed., Springer, New York.

Ordoñez, R., Carbajo-Pescador, S., Prieto-Dominguez, N., Garca-Palomo, A., Gonzalez-Gallego, J., Mauriz, J.L., 2014. Inhibition of matrix metalloproteinase-9 and nuclear factor kappa b contribute to melatonin prevention of motility and invasiveness in hepg2 liver cancer cells. *J. Pineal Res.* **56**, 20–30.

Orme, M., Chaplain, M.A., 1996. A mathematical model of the first steps of tumour-related angiogenesis: Capillary sprout fromation and secondary branching. *J. Math. Appl. Medic. Biol.* **13**(2), 73–98.

Osher, S., Fedkiw, R., 2003. Level Set Methods and Dynamic Implicit Surfaces. Springer-Verlag, New York, USA.

Osher, S., Sethian, J., 1988. Fronts propagating with curvature-dependent speed: algorithms based on hamilton-jacobi formulations. *J. Comput. Phys.* **79**(1), 12–49.

Painter, K.J., Hillen, T., 2011. Spatio-temporal chaos in a chemotaxis model. *Physica D.* **240**, 363–375.

Papini, S., Rosellini, A., Matteis, A.D., Campani, D., Selli, C., Caporalic, A., Bettuzzi, S., Revoltella, R.P., 2007. Establishment of an organotypic in vitro culture system and its relevance to the characterization of human prostate epithelial cancer cells and their stromal interactions. *Pathol. Res. Pract.* **203**, 209–216.

Perumpanani, A., Simmons, D., Gearing, A., Miller, K., Ward, G., Norbury, J., Schneemann, M., Sherratt, J., 1998. Extracellular matrix-mediated chemotaxis can impede cell migration. *Proceed. Royal Soci. Biol. Sci.* **265**(1413), 2347–2352.

Perumpanani, A.J. Sherratt, J., Norbury, J., Byrne, H., 1996. Biological inferences from a mathematical model for malignant invasion. *Invas. Metast.* **16**(4-5), 209–221.

Poincloux, R., Collin, O., Lizarraga, F., Romao, M., Debray, M., Piel, M., Chavrier, P., 2011. Contractility of the cell rear drives invasion of breast tumor cells in 3d matrigel. *Proceed. Nation. Acad. Sci. U. S. A.* **108**(5), 1943–1948.

Preziosi, L., 2006. Hybrid and multiscale modelling. *J. Math. Biol.* **53**, 977–978.

Preziosi, L., Tosin, A., 2009. Multiphase modelling of tumour growth and extracellular matrix interaction: mathematical tools and applications. *J. Math. Biol.* **58**, 625–656.

Qian, B.Z., Pollard, J.W., 2010. Macrophage diversity enhances tumor progression and metastasis. *Cell* **141**(1), 39–51.

Ramis-Conde, I., Chaplain, M., Anderson, A., 2008a. Mathematical modelling of tumour invasion and metastasis. *Math. Comput. Model.* **47**(5-6), 533–545.

Ramis-Conde, I., Drasdo, D., Anderson, A.R., Chaplain, M.A., 2008b. Modeling the influence of the e-cadherin-beta-catenin pathway in cancer cell invasion: a multiscale approach. *Biophys. J.* **95**(1), 155–165.

Ridley, A.J., Schwartz, M.A., Burridge, K., Firtel, R.A., Ginsberg, M.H., Borisy, G., Parsons, J.T., Horwitz, A.R., 2003. Cell migration: Integrating signals from front to back. *Science* **302**, 1704–1709.

Rowe, R.G., Weiss, S.J., 2009. Navigating ecm barriers at the invasive front: The cancer cell–stroma interface. *Annu. Rev. Cell. Dev. Biol.* **25**, 567–595.

Sabeh, F., Shimizu-Hirota, R., Weiss, S.J., 2009. Protease-dependent versus -independent cancer cell invasion programs: three-dimensional amoeboid movement revisited. *J. Cell Biol.* **185**(1), 11–19.

Sahai, E., 2007. Illuminating the metastatic process. *Nat. Rev. Cancer.* **7**(10), 737–749.

Sahai, E., Marshall, C., 2003. Differing modes of tumour cell invasion have distinct requirements for rho/rock signalling and extracellular proteolysis. *Nat. Cel. Biol.* **5**(8), 711–719.

Sanz-Moreno, V., Gadea, G. Ahn, J., Paterson, H., Marra, P., Pinner, S., Sahai, E., Marshall, C., 2008. Rac activation and inactivation control plasticity of tumor cell movement. *Cell* **135**(3), 510–523.

Sanz-Moreno, V., Marshall, C., 2010. The plasticity of cytoskeletal dynamics underlying neoplastic cell migration. *Curr. Opin. Cell. Biol.* **22**(5), 690–696.

Schluter, D.K., Ramis-Conde, I., Chaplain, M., 2012. Computational modeling of single cell migration: the leading role of extracellular matrix fibers. *Biophys. J.* **103**(6), 1141–1151.

Scianna, M., Preziosi, L., 2012. A hybrid model describing different morphologies of tumor invasion fronts. *Math. Model. Nat. Phenom.* **7**(1), 78–104.

Sethian, J., 1999. Level Set Methods and Fast Marching Methods: Evolving Interfaces in Computational Geometry, Fluid Mechanics, Computer Vision, and Materials Science. second edition ed., Cambridge University Press, New York, USA.

Sethian, J., Smereka, P., 2003. Level set methods for fluid interfaces. *Ann. Rev. of Fluid Mech.* **35**(1), 211–259.

Sheetz, M.P., Felsenfeld, D., Galbraith, C.G., Choquet, D., 1999. Cell migration as a five-step cycle. *Biochem. Soci. Sympo.* **65**, 233–243.

Sloot, P.M.A., Hoekstra, A.G., 2009. Multi-scale modelling in computational biomedicine. *Brief. Bioinforma.* **11**, 142–152.

Smith, H.W., Marshall, C.J., 2010. Regulation of cell signalling by upar. *Nat. Rev. Mol. Cel. Biol.* **11**, 23–36.

Stolarska, M.A., Kim, Y., Othmer, H.G., 2009. Multi-scale models of cell and tissue dynamics. *Philos. Trans. A. Math. Phys. Eng. Sci.* **367**(1902), 3525–3553.

Thomlinson, R.H., Gray, L.H., 1955. The histological structure of some human lung cancers and the possible implications for radiotherapy. *Brit. J. Cancer.* **9**(4), 539–549.

Trucu, D., Lin, P., Chaplain, M.A.J., Wang, Y., 2013. A multiscale moving boundary model arising in cancer invasion. *Multiscale Model. Simul.* **11**(1), 309–335.

Turner, S., Sherratt, J., 2002. Intercellular adhesion and cancer invasion: A discrete simulation using the extended potts model. *J. Theor. Biol.* **216**(1), 85–100.

Vitorino, P., Meyer, T., 2008. Modular control of endothelial sheet migration. *Gen. Develop.* **22**(23), 3268–3281.

Weaver, A.M., 2006. Invadopodia: specialised cell structures for cancer invasion. *Clin. Exp. Metast.* **23**, 97–105.

Webb, S., Sherratt, J., Fish, R., 1999. Alterations in proteolytic activity at low ph and its association with invasion: a theoretical model. *Clin. Experim. Metast.* **17**(5), 397–407.

Wise, S., Lowengrub, J., Friebose, H., Cristini, V., 2008. Three-dimensional multi-species nonlinear tumor growth - i - model and numerical method. *J. Theor. Biol.* **253**(3), 524–543.

Wise, S.M., Lowengrub, J., v. Christini, 2011. An adaptive multigrid algorithm for simulating solid tumor growth using mixture models. *Math. Comput. Model.* **53**, 1–20.

Wolf, K., Friedl, P., 2011. Extracellular matrix determinants of proteolytic and non-proteolytic cell migration. *Tren. Cel. Biol.* **21**(12), 736–744.

Wolf, K., te Lindert, M., Krause, M., Alexander, S., te Riet, J., Willis, A.L., Hoffman, R.M., Figdor, C.G., Weiss, S.J., Friedl, P., 2013. Physical limits of cell migration: Control by ecm space and nuclear deformation and tuning by proteolysis and traction force. *J. Cell Biol.* **201**(7), 1069–1084.

Wolf, K., Wu, Y.I., Liu, Y., Geiger, J., Tam, E., Overall, C., Stack, M.S., Friedl, P., 2007. Multi-step pericellular proteolysis controls the transition from individual to collective cancer cell invasion. *Nat. Rev. Cancer.* **9**(8), 893–904.

Zheng, X., Wise, S., Cristini, V., 2005. Nonlinear simulation of tumor necrosis, neo-vascularization and tissue invasion via an adaptive finite-element/level-set method. *Bull. Math. Biol.* **67**(2), 211–259.